

**STRESS-STRAIN CHARACTERISATION OF
SEEBODENLEHM**

A dissertation submitted to the
SWISS FEDERAL INSTITUTE OF TECHNOLOGY ZURICH

for the degree of

Doctor of Technical Sciences

presented by

JOLANDA LUISA TRAUSCH - GIUDICI

Dipl. Bauingenieur ETH

born March 11, 1973

citizen of Arzo, Ticino

accepted on the recommendation of

Prof. Dr. Sarah M. Springman, examiner

Prof. Dr. Simon J. Wheeler, co-examiner

Prof. Dr. Jitendra Sharma, co-examiner

Zurich, 2004

Contents

| | |
|---|--------------|
| Abstract | v |
| Zusammenfassung | vii |
| Ringraziamenti | ix |
| List of Figures | xi |
| List of Tables | xxi |
| List of Symbols | xxiii |
| Introduction | 1 |
| 1.1 Objectives of the project | 2 |
| 1.2 Outline of the thesis | 3 |
| Literature Review | 5 |
| 2.1 Soft lacustrine soils | 5 |
| 2.1.1 Natural soft lacustrine clays | 5 |
| 2.1.2 Reconstituted material | 15 |
| 2.2 Factors affecting the deformation behaviour | 16 |
| 2.3 Soil models | 28 |
| 2.4 Summary from the literature review | 34 |
| Testing Material: Seebodenlehm | 37 |
| 3.1 Site description | 37 |
| 3.1.1 Kreuzlingen | 38 |
| 3.1.2 Reconstituted Kreuzlingen clay | 39 |
| 3.1.3 Birmensdorf | 40 |

| | | |
|-------|---|-----------|
| 3.2 | Stratigraphy | 43 |
| 3.3 | Engineering geology | 45 |
| 3.4 | Composition, state and index properties | 48 |
| 3.4.1 | Composition | 48 |
| | Methods | 48 |
| | Results | 49 |
| 3.4.2 | State and index properties | 52 |
| 3.4.3 | Structure | 55 |
| | In situ testing | 57 |
| 4.1 | In situ testing programme | 57 |
| 4.2 | Cone penetration testing | 58 |
| 4.2.1 | Introduction | 58 |
| 4.2.2 | Interpretation procedures | 60 |
| 4.2.3 | Results | 61 |
| | Kreuzlingen | 61 |
| | Birmensdorf | 65 |
| 4.3 | Seismic tomography | 68 |
| 4.3.1 | Introduction | 68 |
| 4.3.2 | Transmission experiment | 68 |
| 4.3.3 | Results | 70 |
| | Laboratory testing | 73 |
| 5.1 | Triaxial stress path tests | 73 |
| 5.1.1 | Testing equipment | 73 |
| | Mechanical set up | 74 |
| | Electronic set up | 77 |
| | Software set up | 77 |
| | Bender element test | 80 |
| 5.1.2 | Testing procedures | 86 |
| | Sample preparation | 86 |
| | Testing programme | 88 |
| | Interpretation procedures | 91 |
| 5.1.3 | Results | 103 |

| | | |
|-------|--|------------|
| | Kreuzlingen clay | 103 |
| | Reconstituted Kreuzlingen clay | 108 |
| | Birmensdorf clay | 112 |
| 5.2 | One-dimensional compression tests | 117 |
| 5.2.1 | Oedometer testing equipment | 117 |
| 5.2.2 | Testing procedures | 118 |
| | Sample preparation | 118 |
| | Testing programme | 118 |
| | Interpretation procedures | 124 |
| 5.2.3 | Results | 128 |
| | Kreuzlingen | 131 |
| | Reconstituted Kreuzlingen clay | 136 |
| | Birmensdorf | 140 |
| | CG tests | 143 |
| | Stress - strain- strain rate relationship | 144 |
| | Data Analysis | 147 |
| 6.1 | Introduction | 147 |
| 6.2 | Plasticity index | 147 |
| 6.3 | Determination and comparison of the undrained shear strength s_u from laboratory triaxial tests and from in situ piezocone tests CPTU .. | 150 |
| 6.4 | Determination and comparison of the shear modulus G from laboratory triaxial tests and from in situ seismic tests | 157 |
| 6.5 | Determination of yield from TSPT and comparison with the predicted yield loci from S-CLAY1 | 166 |
| 6.6 | In situ settlement: the Birmensdorf test fill | 173 |
| | Numerical Analysis | 181 |
| | Summary and conclusions | 193 |
| 7.1 | Summary | 193 |
| 7.2 | Conclusions | 197 |
| | References | 201 |
| | Curriculum Vitae | 215 |

Seite Leer /
Blank leaf

Abstract

The stress-strain and permeability properties of Swiss post-glacial lacustrine clays have been investigated using various in situ and laboratory tests. These deposits of soft varved lacustrine clays stretch along the highly populated Swiss Mittelland from the SW to the NE of the country. Two sites in Kreuzlingen (on the shore of Lake Constance) and Birmensdorf (near Zürich) have been investigated, where extensive and complicated construction activity needed an improved site characterisation.

The mineralogical composition, the state and structure as well as the index properties of the soft varved clays from both sites have been characterised and discussed. The main difference between the two clays is the higher clay mineral content and the distinct macro-fabric of the Birmensdorf clay. The influence of structure on the properties of the varved clays has been investigated by comparing the composition and the mechanical behaviour in triaxial and oedometer tests of the natural Kreuzlingen clay to those of the reconstituted Kreuzlingen clay. The reconstituted clay was very homogeneous and had equivalent index properties to the natural Kreuzlingen clay, but a lower sensitivity (2.1) and lower undrained shear strength, as expected from the effects of reconstitution.

The strength properties of these Swiss soft clays have been investigated in situ using the piezocone technique (CPTU), to give an estimate of the undrained shear strength s_u . The CPTU constitutes a high-quality in situ test, which is often cheaper than drilling and sampling and its results offer the interpretation of various soil parameters. Standard and stress path triaxial tests were carried out to determine the undrained shear strength s_u and the angle of shearing resistance ϕ' . Based on correlation of CPTU results to borehole vane and field vane tests, it was possible to give equations relating the variation of s_u with effective vertical stress σ'_{v0} for each site, which would represent a lower bound and a safe assumption for design, providing a reasonable fit to the triaxial test results for stresses up to a depth of 30m.

The compressibility and the permeability of Kreuzlingen and Birmensdorf clays has been investigated using continuous loading oedometer tests. No satisfactory correlation could be found between the compressibility and the plasticity of these soils. For these varved clays, the plasticity index should be determined for every soil specimen, whose dimensions should be chosen according to thickness and spacing between the varves present in the soil. Birmensdorf clay shows a higher scatter in the results, largely because of greater heterogeneity of the natural samples.

The influence of loading rate has been investigated by varying the strain rate within the continuous loading oedometers. The mean effective stress σ'_m to normalised void ratio e/e_0 curves do not show a sharp bend when reaching the vertical yield stress, which is therefore difficult to determine exactly. It could be concluded that the strain rate dependency of Seebodenlehm cannot be investigated with tests on different natural samples, therefore, strain rate stepping tests

on the same specimen should be carried out in future, in order to compare the effect of rate on the same specimen. In addition, the strain rates should be varied over at least 2 or 3 orders of magnitude.

Values of the dynamic small strain shear modulus G_{\max} were obtained from a seismic surface-to-borehole transmission experiment in Kreuzlingen (Maurer et al., 1998) and from bender elements tests during triaxial tests. The correlation between these different measurements of the small-strain stiffness G_{\max} shows that the values of G_{\max} measured with the bender elements are not influenced by the general strain level in the specimen, but only by the stress state during the test. The dynamic shear stiffness measured with the bender element is lower than the value measured with the seismic test in situ. The Kondner hyperbola was used to model the static shear stiffness-shear strain behaviour during a triaxial shear test. The static stiffness measurement gives an estimate of the modulus reduction curve, which tends asymptotically to the maximum shear stiffness measured in situ.

One of the main goals of the triaxial investigation was the determination of the yield surfaces for the clays investigated and investigation into the applicability of an anisotropic elasto-plastic model with rotational hardening (SCLAY1) for Swiss soft clays. The investigation of yield during triaxial drained loading on different stress paths η was carried out on the basis of different strain and stiffness variables, to deliver a more sensitive indication of the occurrence of yield. The tests on Swiss varved clay confirmed that the first loading path has to be continued much further in extension than in compression to rotate the yield surface completely to the new inclination. It was observed that the total strain vectors of similar tests (with the same stress path history η_1 and η_2) on different specimens are parallel, and that the total strain vectors seem to have the same inclination as the approaching stress path.

A simple numerical analysis with the Modified Cam Clay model has been carried out to model the behaviour under a test embankment in Birmensdorf.

Zusammenfassung

Das Spannungsdehnungsverhalten und die Permeabilitätseigenschaften von schweizerischen Seebodenlehm wurden in der vorliegenden Arbeit, mittels in-situ und Laborprüfungen untersucht. Seebodenablagerungen befinden sich in dem dicht besiedelten Mittelland vom Südwesten bis zum Nordosten der Schweiz. Der Seebodenlehm von zwei Baustellen, in Kreuzlingen (am Ende des Bodensees) und in Birmensdorf (in der Nähe von Zürich), konnte untersucht werden. Die komplexen Bauvorhaben in Birmensdorf und Kreuzlingen benötigten eine eingehende Prüfung der Bodeneigenschaften.

Die mineralische Zusammensetzung, der Zustand und die Struktur sowie die Index Eigenschaften der vorgefundenen Seebodenlehm wurden charakterisiert und diskutiert. Der Hauptunterschied zwischen den beiden Böden ist der höhere Anteil an Tonmineralien und dem typische Makrostruktur des Birmensdorfer Seebodenlehms. Der Einfluss der Struktur auf die Bodeneigenschaften wurde untersucht, indem die Zusammensetzung und das mechanische Verhalten von natürlichen und wiederhergestellten Proben aus Kreuzlingen in Triax- und Oedometerversuchen untereinander verglichen wurden. Der wiederhergestellte Seebodenlehm war sehr homogen und besass nährungsweise die gleichen Index Eigenschaften wie der natürliche Kreuzlinger Seebodenlehm, aber eine geringere Sensitivität und eine geringere undrainierte Scherfestigkeit, so wie es aufgrund der Wiederherstellung der Proben zu erwarten war.

Die Schichtung der Seebodenlehm wurde in-situ mittels der CPTU Technik untersucht. Der CPTU Versuch ist eine qualitativ hochwertige in-situ Methode, welche wirtschaftlicher als Bohrproben ist. Die Interpretation von mehreren Bodeneigenschaften ist dabei möglich. Die Durchführung von standard und dehnungsgesteuerten triaxialen Scherversuchen ergaben die undrainierten Scherfestigkeiten s_u und der Scherwinkel ϕ' . Durch die Korrelation der CPTU Versuche mit Bohr- und Felduntersuchungen war es möglich, eine Gleichung für die Variation der Scherfestigkeit s_u mit der effektive Vertikalspannung σ'_{v0} für den Böden anzugeben. Es wurde gezeigt, dass diese Gleichungen eine verbesserte Angabe für die Bemessung von Tragwerken in diesen Böden sind.

Die Zusammendrückung und die Permeabilität der Seebodenlehme wurden mit Hilfe von dehnungsgesteuerten Oedometer Versuchen bestimmt. Eine befriedigende Korrelation zwischen den Zusammendrückungseigenschaften und der Plastizitätszahl für diese Böden konnten nicht gefunden werden. Bei dieser Art von Seebodenlehm sollte bei jeder Probe die Plastizität überprüft werden. Dabei muss die Probengrösse in Funktion der in den Böden vorhandenen Siltschichten bestimmt werden. Der Seebodenlehm aus Birmensdorf weist eine höhere Streuung in den Ergebnissen, vor allem aufgrund der höheren Heterogenität der natürlichen Proben.

Der Einfluss der Belastungsgeschwindigkeit wurde untersucht, indem man die Dehngeschwindigkeit der dehnungsgesteuerten Oedometer variierte. Die Kurven der effektiven mittleren Spannung σ'_m versus der normalisierten Porenzahl e/e_0 , zeigen keine eindeutige Fließspannung. Daraus kann geschlossen werden, dass die Abhängigkeit von Seebodenlehm von der Dehngeschwindigkeit

keit nicht mit Versuchen anhand von unterschiedlichen natürlichen Proben ermittelt werden kann. Deshalb sollten in Zukunft Versuche mit variierender Dehngeschwindigkeit am gleichen Probekörper durchgeführt werden. Zusätzlich müssen die Dehngeschwindigkeiten über 2 bis 3 Größenordnungen variiert werden.

Ein seismisches Oberfläche-zu-Bohrloch Transmissionsexperiment in Kreuzlingen sowie Versuche mit piezocheramischen Messelementen (Bender) während den triaxialen Versuchen, lieferten die Werte für den dynamischen Schermodul bei kleinen Dehnungen G_{max} . Die Korrelation zwischen der unterschiedlichen Messmethoden für den Schermodul G_{max} zeigt, dass die Bender Messelemente nicht durch die Dehnungen im Probekörper beeinflusst werden, sondern nur durch den Spannungszustand während dem Versuch. Die anhand der Bender gemessene dynamische Schersteifigkeit ist geringer als die, die mit der seismischen in-situ Methode ermittelt wurde. Die Variation der statischen Schersteifigkeit mit den Scherdehnungen während eines undrainierten triaxialen Kompressionsversuch wurde mittels der Kondner Hyperbel modelliert.

Einer der Hauptziele der triaxialer Scherversuche war die Bestimmung der Fließoberflächen der untersuchten Seebodenlehm sowie die Überprüfung der Verwendbarkeit von eines anisotropischen elasto-plastischen Modells mit Verfestigung und Rotation der Fließoberflächen (SCLAY1). Die Bestimmung des Fließpunktes während der drainierte Spannungspfade der triaxialen Scherversuchen wurde mittels unterschiedlicher Dehnungs- und Steifigkeitsvariablen ermitteln, um eine bessere Empfindlichkeit für das Stattfinden des Fließens zu liefern. Die Versuche an den schweizerischen Seebodenlehm bestätigten, dass die Belastung aus einem neuen Spannungspfad in Extension wesentlich weiter als in Kompression geführt werden muss, um die vollständige Rotation der Fließoberfläche zu erreichen. Es wurde beobachtet, dass die Vektoren der totalen Dehnungsincrementen von ähnlichen Versuchen (mit gleichen Spannungsgeschichte) aber unterschiedlicher Probekörper parallel sind und dass sie die gleiche Neigung wie die Spannungspfade besitzen.

Eine einfache numerische Analyse aufgrund des Modified Cam Clay Model wurde für die Modellierung des Verhaltens einer Testschüttung in Birmensdorf durchgeführt.

Ringraziamenti

La professoressa Sarah Springman merita il primo sincero ringraziamento oltre che per il suo supporto scientifico, per aver saputo accettare tutti i miei doveri di mamma senza mai battere ciglio (o quasi), e quindi essersi dimostrata un datore di lavoro moderno a tutti gli effetti. Un secondo e non minore ringraziamento a mio marito Jean-Luc per essersi sobbarcato la maggior parte delle cene e dei turni "lava piatti" degli ultimi mesi, e per aver soprattutto ascoltato le mie lamentele, impedendomi così di perdere il senno completamente! Un pensiero infinito va ai miei genitori Annamaria e Roberto, e ai miei suoceri Josette e Dominique per tutte le volte che sono venuti ad aiutarci come super nonni per i nostri bambini e poi per tutte le torte, le marmellate e le varie squisitezze che ci hanno sempre sollevato il morale. L'ingegnere cantonale Heim ha permesso che il mio lavoro iniziasse, stanziando i fondi necessari per le prove in situ a Kreuzlingen. A lui riconoscenza e rispetto. L'ufficio cantonale delle costruzioni di Zurigo ha permesso e sovvenzionato tutte le prove in situ a Birmensdorf. I coreferenti Prof. Dr. Wheeler (Glasgow University) e Prof. Dr. Sharma (University of Saskatchewan) hanno lavorato intensamente alla correzione di questo manoscritto e portato critiche e suggerimenti preziosi. Dr. Maurer ha eseguito le prove dinamiche in situ a Kreuzlingen, dandomi modo di prendere visione delle tecniche sismiche.

Lungo tempo è passato da quando ho cominciato il mio lavoro all'istituto di geotecnica del politecnico di Zurigo e sulla mia strada ho incontrato molte persone formidabili che mi hanno in un modo o nell'altro aiutato nel mio lavoro e che ricorderò sempre con affetto. A tutti loro il mio sincero ringraziamento:

A Pierre Mayor per avermi fatto parte dei segreti delle analisi numeriche, per tutte le pause caffè e per la sua amicizia.

A Lukas Arenson per avermi sopportato quale collega d'ufficio per tanti anni, per il suo supporto informatico e per tanti discorsi divertenti e seri. Lukas è stato sostituito da una non meno formidabile collega Karin Frey.

A Marco Sperl che ha messo mano a tutti i miei esperimenti o quasi, per la sua irrefrenabile voglia di aiutarmi e per averci portato sull'Insla.

A Ernst Bleiker che con la sua impagabile calma mi ha sempre soccorso quando i programmi di laboratorio non funzionavano più.

A Heinz Buschor e Alfred Ehrbar che hanno avvitato e svitato le mie celle triassiali mille volte.

A Thomas Weber che ha contribuito con il suo lavoro alla riuscita degli esperimenti odometrici e che sa sempre farmi ridere.

A Philippe Nater, compagno di questa lunga avventura, di cui a volte ci siamo presi beffe.

A Michael Plötze per non aver mai riso delle mie lacune in chimica e per aver sempre saputo spiegare in modo sorprendentemente chiaro.

A Mengia Amberg per l'enorme lavoro che si è sobbarcata per me, per la sua affidabilità e precisione.

A Michael Heil, in ricordo dei primi tempi all'istituto, quando mi fece imparare le tecniche di sondaggio CPTU e i primi rudimenti degli esperimenti triassiali.

Anche tutti gli altri colleghi dell'istituto di geotecnica, dottorandi, tecnici o collaboratori scientifici hanno preso parte alla mia vita all'istituto, non fosse altro che per le pause caffè prese insieme.

Al Dr. Luigi Burlini va uno speciale ringraziamento per essersi letto la tesi e per avermi sempre fatto coraggio.

È stato bello passare questo tempo all'istituto, sono contenta di partire ora. Ai miei figli Liam e Cedric chiedo scusa per il tempo che questo lavoro ci ha rubato. D'ora in poi i fine settimana saranno di nuovo nostri!

List of Figures

- Figure 2-1 Deposition of varved clays: in proglacial lakes by turbidity currents (summer, a) and settling (winter, b), in post glacial lakes by overflows and interflows (summer, c) and by thermal stratification (winter, d) where C_s = concentrated suspended solids and T = temperature in °C. (Kenney, 1976 and Smith, 1978 as reported by Quigley, 1980). 7
- Figure 2-2 Deposits in the lakebed off Richterswil, canton Zürich, Switzerland (Gyger et al., 1976), (translation of key terms can be found in List of Symbols). 9
- Figure 2-3 Characteristic range of grain size distribution (Korn-durchmesser) for the glacio-lacustrine deposits in lake Zürich (Gyger et al., 1976)..... 10
- Figure 2-4 Comparison of oedometer compression curves for Athlone laminated clay (Long, 2003): in void ratio-mean effective stress plane (above), in normalised plane intrinsic void index I_v - mean effective stress (below). [SCL = sedimentation compression curve, ICL = intrinsic compression curve, e^*_{100} and C^*_c = intrinsic constant of compression (Burland, 1990)]. ... 12
- Figure 2-5 One dimensional consolidation curves showing influence of remoulding and ageing on Mexico City soil (Mesri et al., 1975) 13
- Figure 2-6 One dimensional compression curves on Fucino clay, represented in: a) standard $e-\sigma'_v$ plot; and b) normalised $I_v-\sigma'_v$ plot (Soccodato, 2003). 13
- Figure 2-7 Stress path during sampling for the Lower Limavady clay (Cummings et al., 2003) 14
- Figure 2-8 The effects of stress, time and structure history on the stress void ratio relationship of clays, as reported by Länsivaara (1999). 17
- Figure 2-9 Yield curves of natural clays grouped according to their friction angles (ϕ' in degrees) as reported by Länsivaara (1999). ... 18
- Figure 2-10 Possible differences in the effective stress paths between laboratory and in situ K_0 loading, after Länsivaara (1999) 19
- Figure 2-11 Normalized effective stress-strain curves for Bäckebo clay (Sällfors, 1975) and Mascouche clay from oedometer tests, from Leroueil et al. (1985). [CRS: constant rate of strain, CG: controlled gradient] 20
- Figure 2-12 Normalized preconsolidation pressure - strain rate relationship for a) Champlain sea clay (Leroueil et al., 1983 and 1985) and for b) Finnish clays (Länsivaara, 1995b), both after Länsivaara (1999). [$\sigma'_p(4 \times 10^{-4} \text{ s}^{-1})$ = reference preconsolidation pressure

σ'_p measured in a test carried out with strain rate $4 \times 10^{-4} \text{ s}^{-1}$].
21

| | | |
|-------------|---|----|
| Figure 2-13 | The dependence of the viscous strain of the primary deformation properties assuming that Equation 2-1 is valid (after Län-sivaara, 1999) ($m = \text{modulus number} = 1/C_c$)..... | 22 |
| Figure 2-14 | Measured and computed settlements near the excavation of the New Palace Yard car park (Simpson et al., 1979)..... | 23 |
| Figure 2-15 | Normalized apparent secant modulus versus load factor for various boundary value problems, analysed with a non-linear model (Jardine et al., 1986)..... | 24 |
| Figure 2-16 | Results of triaxial stress path tests obtained by Richardson (1988) a) stress paths, b) tangential stiffness for path OX. . | 25 |
| Figure 2-17 | Typical variation of stiffness with stress change observed in laboratory tests (Atkinson and Stallebrass, 1991)..... | 25 |
| Figure 2-18 | The effect of stress, preconsoli-dation pressure and time on the value of shear stiffness G_{max} (Drammen clay after Dyvik and Olsen (1989))..... | 25 |
| Figure 2-19 | Determination of the parameter a and b from the Kondner hy-perbolic stress- strain relationship. | 27 |
| Figure 2-20 | Yield data of a) Winnipeg clay by Graham et al. (1983b) and b) Champlain Sea clay by Wong and Mitchell (1975). | 29 |
| Figure 2-21 | The non-uniqueness of plastic strain increment vectors for two yield points P1 and P2 (Newson, 1992)..... | 30 |
| Figure 2-22 | S-Clay1 yield surface a) in triaxial stress space and b) in 3D stress space (Wheeler et al., 2003a)..... | 31 |
| Figure 2-23 | S-Clay1S yield surfaces in triaxial stress spaces (Wheeler et al., 2003 a)..... | 32 |
| Figure 2-24 | a) Basic features of the 3-SKH model, b) Kinematics of the yield and history surfaces following a rotation of the stress path (Atkinson and Stallebrass, 1991)..... | 33 |
| Figure 3-1 | Location of the test sites in Switzerland..... | 37 |
| Figure 3-2 | Link road underpass in Kreuzlingen; a) plan; b) deepest sec-tion through closed box construction. | 38 |
| Figure 3-3 | Layout plan of the highway intersections in Birmensdorf..... | 40 |
| Figure 3-4 | Sketch of the highway intersection with position of the bore-holes and piezocone test site CPTU..... | 41 |
| Figure 3-5 | Borehole log at B1 in Kreuzlingen. | 43 |
| Figure 3-6 | Borehole logs PWGD10, PWGD11 and PW6/99 at Bir-mensdorf (after Geotechnisches Institut, 1994-1999). Depth of samples see Chapter 5..... | 44 |

| | | |
|-------------|--|----|
| Figure 3-7 | Ice sheet over the Swiss Mittelland during the Würm ice-age (Geotechnische Karte der Schweiz, 1:1000000). Contours show ice surface as masl..... | 45 |
| Figure 3-8 | Geology charts: left at Birmensdorf (Geologischer Atlas der Schweiz, 1:25000); right at Kreuzlingen (Geologische Generalkarte der Schweiz, 1:200000). | 46 |
| Figure 3-9 | Picture of Seebodenlehm samples showing a clear varving pattern for Birmensdorf and a more homogeneous material for Kreuzlingen..... | 47 |
| Figure 3-10 | Grain size distribution: above by sedimentation analysis, left by MICROTRAC FRA..... | 49 |
| Figure 3-11 | Kreuzlingen soil profile: bulk soil grain size distribution and Atterberg limits..... | 53 |
| Figure 3-12 | Birmensdorf soil profile: bulk soil grain size distribution and Atterberg limits..... | 53 |
| Figure 3-13 | Plasticity chart after USCS. | 54 |
| Figure 3-14 | Activity chart. | 55 |
| Figure 3-15 | SEM pictures of layers in varved clay body from Birmensdorf after triaxial testing (Plötze et al., 2003) | 56 |
| Figure 4-1 | Position of the boreholes and CPTU sites in Birmensdorf. ... | 58 |
| Figure 4-2 | Occurrence of fine grained and soft clayey and peaty deposits in Switzerland (Amann & Heil, 1995)..... | 59 |
| Figure 4-3 | Correlation between the undrained shear strength s_u and the effective overburden pressure σ'_{v0} for the Kreuzlingen Seebodenlehm from Heil et al., 1997..... | 60 |
| Figure 4-4 | CPTU at B1 in Kreuzlingen: a) shaft friction f_s ; b) total pressure on tip q_T ; c) normalized friction ratio R_{FT} ; d) pore pressure ratio B_q | 62 |
| Figure 4-5 | CPTU characterisation charts for B1 (Kreuzlingen) based on Robertson (1990)..... | 63 |
| Figure 4-6 | Undrained shear strength profile with effective overburden pressure from CPTU at B1 | 64 |
| Figure 4-7 | CPTUs in Birmensdorf: a) shaft friction f_s ; b) total pressure on tip q_T ; c) normalized friction ratio R_{FT} ; d) pore pressure ratio B_q . 65 | 65 |
| Figure 4-8 | CPTU characterisation charts for depth 4.3m to 11.5m based on Robertson (1990) from results of the first CPTU measurement in Birmensdorf..... | 66 |
| Figure 4-9 | Undrained shear strength profile with effective overburden pressure from CPTU1 in Birmensdorf (Panduri, 2000)..... | 67 |
| Figure 4-10 | a) Preparation for the seismic experiment, b) Seismic source | |

| | | |
|-------------|--|----|
| | in place, in preparation for the hammer blow..... | 69 |
| Figure 4-11 | Schematic overview of the seismic transmission experiment. The expanded view shows the source, the force directions of the hammer blows (F_L and F_R) and the resulting force vectors for added and subtracted signals (Maurer et al., 1998)..... | 69 |
| Figure 4-12 | Seismographs recorded with a source at 10 m distance and 4 m depth. a) normal-component seismographs from the left and the right hammer blows, b) addition of the normal components, c) equivalent transverse-component seismographs, d) subtraction of the transverse components (Maurer et al., 1998)... | 70 |
| Figure 4-13 | Wave velocity-depth functions and elastic parameters from seismic experiment, stratigraphy from borehole log at B1 in Kreuzlingen (Chapter 3.2) (Maurer et al., 1998)..... | 71 |
| Figure 5-1 | Triaxial test apparatus: mechanical set up | 74 |
| Figure 5-2 | Triaxial test apparatus: test control set up..... | 75 |
| Figure 5-3 | Mount for the correct positioning of the sample..... | 76 |
| Figure 5-4 | Cell base and bottom platten with piezoceramic elements.. | 77 |
| Figure 5-5 | Schematic set up of bender test equipment | 80 |
| Figure 5-6 | Typical oscilloscope signals from a bender element test a) with a square pulse excitation and b) with a sine pulse excitation (Viggiani and Atkinson, 1995)..... | 82 |
| Figure 5-7 | ... Two oscilloscope signals from a bender element test with a square pulse excitation (above) and with a sine pulse excitation (below), for Kreuzlingen clay samples..... | 83 |
| Figure 5-8 | Extrusion of test sample | 86 |
| Figure 5-9 | Extruded sample, cut and sealed specimen | 86 |
| Figure 5-10 | a) Trimming the triaxial specimen; b) weighing the triaxial specimen | 87 |
| Figure 5-11 | Drainage bands along sides of the sample..... | 88 |
| Figure 5-12 | Principal illustration of the triaxial testing programme a) test series 1, b) test series 2 (not scaled)..... | 89 |
| Figure 5-13 | Example of TSPT of series 2..... | 89 |
| Figure 5-14 | Various stress-strain and work input plots used to determine the yield stress during test 46471/1..... | 95 |
| Figure 5-15 | Various stress-strain and work input plots used to determine the yield stress during test 46216/2..... | 96 |
| Figure 5-16 | Deformation behaviour during undrained shear in Birmensdorf clay (Fleischer, 2000) a) ductile, barrelling b) brittle, slip plane. | 99 |

| | | |
|-------------|--|-----|
| Figure 5-17 | Barrelling deformation of undrained compression test specimen (Head, 1985)..... | 100 |
| Figure 5-18 | Area correction due to single plane slip (Head, 1985): a) mechanism of slip, b) area of contact between the two portions of the sample, c) projected area of contact, d) displacement along slip surface related to vertical deformation. | 101 |
| Figure 5-19 | q-p' diagrams for Kreuzlingen clay: undrained shear stage to failure, series 1 (dashed line) and 2 (full line)..... | 103 |
| Figure 5-20 | Excess pore water pressures and deviator stress development du-ring shearing: typical test..... | 104 |
| Figure 5-21 | q-p' diagrams for Kreuzlingen clay: stress path controlled conso-lidation in series 2. | 104 |
| Figure 5-22 | Strain paths for Kreuzlingen clay during stress controlled con-solidation stages in series 2. Points A to B refer to stress reversal points as shown in Figure 5-12. | 105 |
| Figure 5-23 | Trend between the λ values and the inclination η of the stress path during which λ was measured. | 107 |
| Figure 5-24 | a) q-p' diagram for reconstituted Kreuzlingen clay: undrained shear stage to failure, b) v-lnp' diagram of the consolidation and creep stage..... | 108 |
| Figure 5-25 | a) q-p' diagrams for reconstituted Kreuzlingen clay: undrained shear stage to failure, b) excess pore water pressures and deviator stress development during shearing..... | 109 |
| Figure 5-26 | Comparison between natural and reconstituted Kreuzlingen clay: tests with same stress path history. | 110 |
| Figure 5-27 | Comparison between natural and reconstituted Kreuzlingen clay: tests with same stress path history. | 110 |
| Figure 5-28 | Comparison of the strain paths of reconstituted and natural Kreuzlingen clay during stress controlled consolidation stages on the same stress paths. Points A to B refer to stress reversal points as shown in Figure 5-12..... | 111 |
| Figure 5-29 | Failure points in effective stress space for Birmensdorf clay, series 1 and 2. | 112 |
| Figure 5-30 | Stress paths in p'-q space: a) undisturbed samples (Panduri, 2000, and Giudici), b) drilled core samples (Fleischer, 2000). 113 | |
| Figure 5-31 | Pictures of sheared specimens of undis-turbed Birmensdorf samples. | 115 |
| Figure 5-32 | Stress paths during consolidation and shearing for specimens 46297/2 and 46297/3..... | 115 |
| Figure 5-33 | v-lnp' and strain path graphs for specimens 46297/2 and 46297/3 during stress controlled consolidation. Points A to B | |

| | | |
|-------------|--|-----|
| | refer to stress reversal points as shown in Figure 5-12..... | 116 |
| Figure 5-34 | a) NGI oedometer device, b) Wille oedometer device | 117 |
| Figure 5-35 | Boundary conditions for a CRS-Oedometer test. | 124 |
| Figure 5-36 | Correlations between ICL and CRS-oedometer results for Kreuzlingen clay. (bold: ICL lines; full lines: natural samples; dashed lines: reconstituted)..... | 129 |
| Figure 5-37 | Correlations between ICL and CRS-oedometer results for Birmensdorf clay (Messerklinger, 2003, pers. comm.). (bold: ICL lines; full lines: $3 \cdot 10^{-6}$ 1/s; dashed lines: $6 \cdot 10^{-6}$ 1/s; full symbols: $1 \cdot 10^{-5}$ 1/s) | 130 |
| Figure 5-38 | Results from tests with strain rate = $3 \cdot 10^{-6}$ 1/s. Sample 46217 comes from Kreuz1, whereas samples 46476 and 46488 come from Kreuz2. | 131 |
| Figure 5-39 | Results from tests with strain rate = $6 \cdot 10^{-6}$ 1/s. Sample 46217 comes from Kreuz1, whereas samples 46476, 46474 and 46483 originate from Kreuz2. | 132 |
| Figure 5-40 | Results from tests with strain rate = $1 \cdot 10^{-5}$ 1/s. Sample 46217 comes from Kreuz1, whereas sample 46474 originates from Kreuz2. | 133 |
| Figure 5-41 | Comparison of strain rates for Kreuz1..... | 134 |
| Figure 5-42 | Comparison of strain rates for Kreuz2..... | 134 |
| Figure 5-43 | Influence of strain rate on σ'_{vy} and C_c : a) Kreuz1 b) Kreuz2. . | 135 |
| Figure 5-44 | Results from tests on reconstituted Kreuzlingen clay with strain rate = $3 \cdot 10^{-6}$ 1/s..... | 136 |
| Figure 5-45 | Results from tests on rec. Kreuz. clay with strain rate = $6 \cdot 10^{-6}$ 1/s. | 137 |
| Figure 5-46 | Results from tests on rec. Kreuz. clay with strain rate = $1 \cdot 10^{-5}$ 1/s. | 137 |
| Figure 5-47 | Reconstituted Kreuzlingen clay: comparison of strain rates.... | 138 |
| Figure 5-48 | Influence of strain rate on σ'_{vy} and C_c for reconstituted Kreuzlingen clay..... | 139 |
| Figure 5-49 | Comparison between natural and reconstituted Kreuzlingen clay: a) = $1.8 \cdot 10^{-7}$ [1/s], b) = $3 \cdot 10^{-6}$ [1/s], c) = $6 \cdot 10^{-6}$ [1/s], d) = $1 \cdot 10^{-5}$ [1/s]..... | 139 |
| Figure 5-50 | Results from tests on Birmensdorf clay with strain rate = $3 \cdot 10^{-6}$ 1/s | 140 |
| Figure 5-51 | Results from tests on Birmensdorf clay with strain rate = $6 \cdot 10^{-6}$ 1/s | 141 |

| | | |
|-------------|---|-----|
| Figure 5-52 | Results from tests on Birmensdorf clay with strain rate = $1 \cdot 10^{-5}$ 1/s..... | 142 |
| Figure 5-53 | Birmensdorf: comparison of strain rates (46295 and 46292).. | 142 |
| Figure 5-54 | Influence of strain rate on σ'_{vy} and C_c for samples 46292 and 46295 (same depth, different boreholes)..... | 143 |
| Figure 5-55 | Strain rates measured during CG tests on Birmensdorf clay as a function of axial strain. | 143 |
| Figure 5-56 | Normalized vertical yield stress-strain rate plot for Swiss Seebodenlehm (after Leroueil et al., 1985)..... | 144 |
| Figure 6-1 | C_c - I_p graph for CRS and CG tests on Birmensdorf, Kreuzlingen and Belp natural clay and the reconstituted material from Kreuzlingen (Giudici Trausch et al., 2003). The dotted line "Fit" represents Equation 6-2. | 148 |
| Figure 6-2 | C_c - I_p graph for all oedometer tests..... | 149 |
| Figure 6-3 | $s_u - \sigma'_{v0}$ from CPTU at B1 in Kreuzlingen with $N_{KT} = 17$, with results from triaxial tests. | 152 |
| Figure 6-4 | $s_u - \sigma'_{v0}$ from CPTU in Birmensdorf with $N_{KT} = 17$, with results from triaxial tests..... | 154 |
| Figure 6-5 | $s_u - \sigma'_{v0}$ from CPTU at B1 in Kreuzlingen, with $N_{KT} = 14$.. | 156 |
| Figure 6-6 | Variation of G_{max} measured with the bender element method during consolidation and during undrained shearing of two typical tests (a: Birmensdorf clay, b: reconstituted Kreuzlingen clay). | 157 |
| Figure 6-7 | Variation of G_{max} measured with the bender element method during a constant stress stage on two reconstituted specimens..... | 159 |
| Figure 6-8 | Stiffness-strain relationship during typical undrained triaxial shear tests on Kreuzlingen (46471/1, 46472/2 and 46473/2) and Birmensdorf (46297/2) Seebodenlehm: comparison between the calculated tangential shear modulus G_{tan} , the Kondner hyperbola approximation of maximum shear stiffness $G_{max,calc}$, of the modulus reduction curve $G_{Kondner}$ and the small strain shear modulus from bender element tests G_{bender} . | 160 |
| Figure 6-9 | Stiffness-strain relationship during typical undrained shear tests on reconstituted Kreuzlingen Seebodenlehm: comparison between the calculated tangential shear modulus G_{tan} , the Kondner hyperbola approximation of $G_{max,calc}$ and of the modulus reduction curve $G_{Kondner}$ and the small strain shear modulus from bender element tests G_{bender} | 161 |
| Figure 6-10 | Normalized Kondner hyperbolae for all tests in series 2. . | 162 |

| | | |
|-------------|--|-----|
| Figure 6-11 | Comparison of the maximum deviatoric stress during undrained shear q_{max} and from the Kondner hyperbola..... | 162 |
| Figure 6-12 | Maximum shear modulus $G_{max,calc}$ from the Kondner hyperbola compared to Equations 2-4 and 2-7 from Hardin (1978) and Kagawa (1992). | 163 |
| Figure 6-13 | Shear stiffness - shear strain plot normalized with undrained shear strength s_u . Modulus reduction curves from measured tangential stiffness of test series 1, compared with the in situ stiffness from the seismic experiment..... | 164 |
| Figure 6-14 | Shear stiffness - shear strain plot normalized with undrained shear strength s_u . Modulus reduction curves from measured tangential stiffness of test series 2, compared with the in situ stiffness from the seismic experiment..... | 164 |
| Figure 6-15 | Comparison between the G values normalized with s_u from the Bender measurement and from the in situ measurement with Equation 2-7..... | 165 |
| Figure 6-16 | Yield points and maximum load stress obtained during triaxial stress path tests, estimated in situ stress and inclined yield surfaces estimated from S-CLAY 1: a) Kreuz1 - 46216, 3 specimens, b) Birm2 - 46297, 2 specimens, c) Kreuz2 - 46471 and 46474, d) Kreuz2 - 46472 and 46475. | 167 |
| Figure 6-17 | Yield points and maximum load stresses obtained during triaxial stress path tests for the reconstituted specimens 46496/56 and 46496/57 are compared to the relative tests on natural samples 46472/2 and 46471/1 respectively (Kreuz2)..... | 168 |
| Figure 6-18 | Experimental versus theoretical values of α/M at equilibrium, data from series 2 for Swiss Seebodenlehm (Diagram as presented in Wheeler et al., 2003b)..... | 170 |
| Figure 6-19 | Picture of two of the test fill embankments in Birmensdorf (Tiefbauamt des Cantons Zürich, 1996) | 173 |
| Figure 6-20 | Sketch of the Birmensdorf test fill: a) section, b) plan..... | 174 |
| Figure 6-21 | Applied load, settlement evolution, measured pore water pressure and calculated excess pore water pressure. (Technical failure of piezometers at 12m and 22m depth after 260 days) | 175 |
| Figure 6-22 | Isochrones of the measured excess porewater pressure with depth: a) during construction period, b) during consolidation time | 176 |
| Figure 6-23 | Pore pressure development during loading phases | 177 |
| Figure 6-24 | Vertical effective stress-vertical strain curves for in situ boundary conditions under the Birmensdorf test fill (8m depth) and for three CRS oedometer tests on Birmensdorf clay specimens from 8m depth..... | 178 |

| | | |
|-------------|--|-----|
| Figure 6-25 | In situ vertical strain rate under Birmensdorf test fill..... | 179 |
| Figure 6-26 | a) Measured differential horizontal displacements with depth and b) integrated horizontal displacements at the inclinometer location (Figure 6-20) by end of observation period. | 180 |
| Figure 6-27 | Geometry, boundary conditions and mesh of soil model used (scale in m). | 182 |
| Figure 6-28 | a) OCR values before loading, calculated on the basis of the POP values of Table 6-4 and the PLAXIS generated in situ stresses; b) Earth pressure coefficient at rest calculated with Equation 6-19. | 186 |
| Figure 6-29 | OCR values calculated at the end of the consolidation period (Scale from 1.0 to 1.425) and calculated as defined by Equation 6-17: | 186 |
| Figure 6-30 | Principal direction of effective stresses before loading..... | 187 |
| Figure 6-31 | Principal direction of effective stresses at the end of the observation period. | 188 |
| Figure 6-32 | Horizontal displacements at the end of the observation period. | 188 |
| Figure 6-33 | Horizontal displacements at inclinometer location A in m.. | 189 |
| Figure 6-34 | Evolution of cumulative settlements with time under the centre of the embankments at points A, B, C and D (respectively 4, 8, 12 and 18m depth) (the load phase number is encircled). | 190 |
| Figure 6-35 | Evolution of excess pore pressures with time under the centre of the embankments at points A, B, C and D (respectively 4, 8, 12 and 18m depth) (the load phase number is encircled). | 190 |
| Figure 6-36 | Plastic points in the Seebodenlehm deposit at the end of load stage 5 and 7 and at the end of the consolidation phases 6 and 8; a) phase 5; b) phase 6; c) phase 7; d) phase 8 (blue: "cap" points; red: Mohr Coulomb points)..... | 191 |
| Figure 6-37 | Stress paths followed by points E, F, and G..... | 192 |

Seite Leer /
Blank leaf

List of Tables

| | | |
|------------|---|-----|
| Table 2-1 | Type of soft clayey deposits after Quigley (1980)..... | 6 |
| Table 2-2 | Typical average values of state and index properties (Gyger et al., 1976)..... | 8 |
| Table 3-1 | Mineralogical composition of the bulk material (Plötze et al., 2003)..... | 50 |
| Table 3-2 | Mineralogical composition of the decarbonised fraction <2 μm (Plötze et al., 2003)..... | 50 |
| Table 3-3 | Cation exchange and water uptake capacity, average values (Plötze et al., 2003)..... | 51 |
| Table 3-4 | Pore water chemistry (nd = not detected)..... | 52 |
| Table 3-5 | Typical average values of state and index properties..... | 52 |
| Table 5-1 | Triaxial test apparatus: instrumentation..... | 79 |
| Table 5-2 | Details of the stepper motors, type DCX-AT200..... | 79 |
| Table 5-3 | Excess pore water pressure development with loading rate 90 | |
| Table 5-4 | Overview of test series 1, part 1: tests on Kreuzlingen clay. | 91 |
| Table 5-5 | Overview of test series 1, part 2: tests on Birmensdorf clay. a) Panduri (2000), b) Fleischer (2000)..... | 92 |
| Table 5-6 | Overview of test series 2. | 93 |
| Table 5-7 | Determination of a yield point from different stress-strain plots for specimen 46471/1. | 98 |
| Table 5-8 | Results of triaxial stress path tests, series 2..... | 106 |
| Table 5-9 | Results of triaxial stress path tests on Birmensdorf clay, series 1 and 2..... | 114 |
| Table 5-10 | Overview of CL-oedometer test series | 119 |
| Table 5-11 | Overview of CL-oedometer test series Fleischer (2000) ... | 123 |
| Table 6-1 | Parameters for Equation 6-3 from Mayne (2003) (I_p in%) | 151 |
| Table 6-2 | Values of initial yield curve inclination α_{K0} and yield curve inclination after first loading α_1 | 169 |
| Table 6-3 | Stage data set..... | 182 |
| Table 6-4 | Soil data set..... | 184 |

Seite Leer /
Blank leaf

List of Symbols

| | |
|----------------|---|
| A | non dimensional soil parameter in Equation 2-4 |
| A | area |
| A_c | corrected cross sectional area of a triaxial specimen after consolidation |
| A_s | corrected cross sectional area of a triaxial specimen during shearing by ductile behaviour of the specimen |
| B | exponent of the relationship between yield stress and effective stresses obtained at different strain rates (Equation 2-2, 2-3) |
| \bar{B} | ratio between excess pore water pressure and total applied vertical stress (embankment loading) (Equation 6-15) |
| B_q | pore pressure ratio from CPTU |
| C_α | secondary compression index |
| C_c | compression index |
| C_c^* | intrinsic compression index |
| C_s | swelling index |
| D | diameter |
| D_{slip} | diameter of a triaxial specimen at start of slip |
| E | Young's modulus |
| E_r | radial stiffness modulus |
| F(e) | expression based on void ratio e in Equation 2-4 |
| G | shear modulus |
| G_{bender} | shear modulus measured with the bender element test |
| $G_{Kondner}$ | Kondner approximation of the modulus reduction curve |
| $G_{max,calc}$ | Kondner approximation of the maximum shear stiffness |
| G_{tan} | tangential shear modulus |
| H | height |
| I_A | activity index |
| I_L | liquidity index |
| I_P | plasticity index |
| I_r | rigidity index |
| I_v | intrinsic void index |
| J | stress distribution factor |
| K | earth-pressure coefficient: ratio between horizontal and vertical effective stress |

| | |
|------------|--|
| K | bulk modulus |
| K_0 | coefficient of the earth-pressure at rest |
| L_0 | initial length of a specimen |
| L_{s0} | reference length of a specimen after consolidation |
| L_{slip} | length of a triaxial specimen at start of slip |
| M | inclination of the critical state line in p' - q space (critical state soil mechanics) |
| M | P wave modulus |
| M_E | one-dimensional modulus |
| N | axial force |
| N_{KT} | cone factor |
| N_S | spherical expanding cavity factor |
| P-wave | compression wave |
| PW | porewater |
| PWP | porewater pressure |
| R_{ft} | normalised friction ratio |
| S | soil parameter in 3-SKH model linking the size of the inner surfaces to the boundary surface |
| S_t | sensitivity index |
| S-wave | shear wave |
| T | temperature |
| T | soil parameter in 3-SKH model linking the size of the inner surfaces to the boundary surface |
| V | volume |
| V_w | volume of water |
| $V_{w,c}$ | volume of water in the triaxial cell |
| $V_{w,p}$ | volume of water in the pore pressure measurement system |
| V_0 | initial volume of a specimen |
| V_{s0} | reference volume of a specimen after consolidation |
| W | work/energy needed to deform a specimen |
| a | interception of the Kondner hyperbola with the y-axis in a γ/τ - γ plot |
| a | net area ratio of CPTU |
| a | parameter in Equation 6-6 |
| a_{rate} | parameter describing the strain rate effect on s_u/σ'_{v0} (Equation 6-3) |

| | |
|--------------|--|
| a_{OCR} | parameter describing the effect of OCR on s_u/σ'_{v0} (Equation 6-3) |
| a_{cont} | parameter describing the effect of fissuration on s_u/σ'_{v0} (Equation 6-3) |
| b | parameter in Equation 6-6 |
| b | inclination of the Kondner hyperbola in a $\gamma/\tau-\gamma$ plot |
| c' | cohesion |
| c_v | consolidation index |
| d | diameter |
| e | void ratio |
| e_L | void ratio at liquid limit w_L |
| e_{100}^* | intrinsic void ratio at $\sigma'_v = 100$ kPa |
| e_{1000}^* | intrinsic void ratio at $\sigma'_v = 1000$ kPa |
| f_s | local friction on the sleeve of CPTU |
| f_s | slip area factor |
| h_m | organic content |
| k | parameter in Equation 2-4 |
| k | soil permeability |
| l | effective travel time of a seismic wave from transmitter to receiver element |
| n | parameter in Equation 2-4 |
| n_{qT} | normalised cone resistance |
| p_a | atmospheric pressure |
| p | hydrostatic pressure: $\frac{J_1}{3} = \frac{1}{3}(\sigma_1 + \sigma_2 + \sigma_3)$ under conditions of triaxial compression, $\sigma_c = \sigma_2 = \sigma_3$, $p = \text{mean stress: } (\sigma_1 + 2\sigma_3)/3$ |
| p' | mean effective triaxial stress |
| p'_{of} | equivalent mean effective isotropic consolidation stress at failure |
| p'_m | initial size of the yield curve for S-Clay1 model |
| ppm | parts per million |
| q | second invariant of stress: $\sqrt{3J_{2D}} = \frac{3}{\sqrt{2}}\tau_{oct} = \sqrt{\frac{1}{2}[(\sigma_1 - \sigma_2)^2 + (\sigma_2 - \sigma_3)^2 + (\sigma_3 - \sigma_1)^2]}$ under conditions of triaxial compression, $\sigma_c = \sigma_2 = \sigma_3$, $q = \text{deviator stress: } \sigma_1 - \sigma_3$ |
| q_c | cone resistance of CPTU |

| | |
|--------------------|---|
| q_{\max} | peak deviatoric stress |
| q_{res} | residual deviatoric stress |
| q_T | total pressure acting on the tip of CPTU (cone resistance) |
| $q_{T,\text{net}}$ | net cone resistance |
| r | radius |
| r | ratio between the equivalent mean effective isotropic consolidation stress at failure p'_{of} (i.e. the value of p' (> 0) at $q = 0$, due to the yield surface at failure) and the effective mean stress at the critical state p'_f |
| s | length of a stress path |
| s_u | undrained shear strength: $= \tau_f$ |
| t | time |
| t | travel time of a seismic wave from transmitter to receiver |
| t_{cr} | duration of a creep stage |
| u | pore pressure |
| u_{bt} | pore pressure measurement behind tip of CPTU |
| v | specific volume |
| v_E | Raleigh wave velocity |
| v_s | shear wave velocity |
| v_P | compression wave velocity |
| v_0 | initial velocity |
| w | water content |
| w_L | liquid limit |
| w_P | plastic limit |
| x | parameter defining the current state of bonding in S-Clay1S model |
| \bar{y}_i | calculated value |
| z | displacement along the slip area of a triaxial specimen |
| Γ | function of ζ and G_i of the components to calculate the Hashin-Shtrikman stiffness bounds for a mixture of grains and fluids |
| Δ | increment |
| Δ | in situ stress distribution factor |
| ΔL | change in length of a triaxial specimen |
| ΔV_T | change involume of a triaxial specimen due to temperature effects |
| Δu | excess pore pressure |

| | |
|---|--|
| Δu_B | imposed excess pore pressure at the base during a CG oedometer test |
| Δu_m | mean excess pore pressure |
| Λ | plastic volumetric strain ratio $=(\lambda - \kappa)/\lambda$ |
| Λ | function of G and K to calculate the Hashin- Shtrikman stiffness bounds for a mixture of grains and fluids |
| α | orientation/inclination of the yield curve in S-Clay1 model |
| α_f | adhesion factor of cone face |
| α_s | adhesion factor of cone shaft |
| β | soil parameter for the rotational hardening law in S-Clay1 |
| γ | engineers' shear strain |
| ε | strain |
| ε_a | axial strain |
| ε_n | natural strain: $-\ln(1-\varepsilon)$ |
| $\varepsilon_{r,n}$ | natural radial strain |
| ε_s | true shear strain |
| $\varepsilon_{s,n}$ | natural true shear strain |
| ε_v | volumetric strain |
| $\varepsilon^\circ = \dot{\varepsilon}$ | strain rate |
| ζ | function of G and K to calculate the Hashin- Shtrikman stiffness bounds for a mixture of grains and fluids |
| η | stress ratio q/p' |
| η | inclination of a stress path in $q-p'$ space |
| η_{K0} | stress ratio q/p' corresponding to K_0 conditions |
| κ | inclination of the URL in $v-\ln p'$ plot |
| λ | inclination of the NCL in $v-\ln p'$ plot |
| μ | soil parameter for the rotational hardening law in S-Clay1 |
| ρ | soil density |
| ρ_s | bulk density |
| σ | stress |
| σ' | effective stress: $\sigma - u$ |
| σ'_c | effective confining pressure in triaxial apparatus |
| σ'_c | consolidation pressure (Equation 2-7) |
| σ'_{cv} | effective vertical preconsolidation pressure |
| σ'_{cr} | effective vertical stress in an oedometer test by which a creep stage is carried out |

| | |
|----------------|--|
| σ'_m | mean effective stress |
| σ'_p | effective preconsolidation pressure |
| σ'_{v0} | effective overburden pressure |
| σ'_{vy} | effective yield stress |
| τ | shear stress: $q/2$ |
| ϕ' | effective friction angle |
| ϕ'_{res} | residual effective friction angle |
| ϕ'_{mob} | mobilised effective friction angle |
| $\chi_s(\eta)$ | target value of η for shear strains in S-Clay1 |
| $\chi_v(\eta)$ | target value of η for volumetric strains in S-Clay1 |
| ψ | exponent in the hardening modulus of the 3-SKH model |

Subscripts

| | |
|----------|---|
| <i>C</i> | <i>compression</i> |
| <i>E</i> | <i>extension</i> |
| <i>a</i> | axial |
| bender | stiffness measured with bender elements |
| <i>c</i> | consolidation |
| <i>h</i> | horizontal |
| Kondner | stiffness estimated by means of the Kondner hyperbola |
| max | maximum |
| min | minimum |
| <i>p</i> | preconsolidation |
| <i>r</i> | radial |
| tan | tangential |
| <i>v</i> | vertical |
| <i>u</i> | undrained |
| <i>y</i> | yield |
| 0 | initial state |

Abbreviations

| | |
|-------|---|
| Birm1 | label for undisturbed samples taken from Borehole PWDG10 in Birmensdorf |
|-------|---|

| | |
|--------------------|--|
| Birm2 | label for undisturbed samples taken from Borehole PWDG11 in Birmensdorf |
| Birm3 | label for samples taken from Borehole PW6/99 in Birmensdorf (undisturbed and drilled core) |
| BP | back pressure |
| carb. | total carbonate content |
| CAUC | anisotropically consolidated undrained compression test |
| CEC | cation exchange capacity |
| CF | clay fraction <2 μ m |
| CG | controlled gradient test |
| CIUC | isotropically consolidated undrained compression test |
| CIUE | isotropically consolidated undrained extension test |
| CK ₀ UC | K ₀ -consolidated undrained compression test |
| CK ₀ UE | K ₀ -consolidated undrained extension test |
| CL | continuous loading |
| CPTU | piezocone penetration test (U: measurement of porewater pressure) |
| CRL | constant rate of loading |
| CRS | constant rate of strain |
| CSL | critical state line |
| dc | drilled core samples |
| DSS | direct simple shear test |
| e.g. | for example |
| etc. | et cetera |
| ETH | Eidgenössische Technische Hochschule: Swiss Federal Institute of Technology |
| ICL | intrinsic consolidation line |
| i.e. | <i>id est</i> (that is) |
| IG | Institute of Geophysics: Institut für Geophysik |
| IGT | Institute for Geotechnical Engineering: Institut für Geotechnik |
| Kreuz1 | label for undisturbed samples taken at Kreuzlingen1 site |
| Kreuz2 | label for undisturbed samples taken at Kreuzlingen2 site |
| n/a: | not available |
| NC | normally consolidated |
| NCL | normal consolidation line |
| O | particle surface |

OC overconsolidated
OCR overconsolidation ratio
PW: porewater
PWP: porewater pressure
rec label for undisturbed samples of reconstituted Kreuzlingen clay
SEM scanning electron microscope
SN: Swiss code
3-SKH three-surface kinematic hardening model
TSPT triaxial stress path test
u undisturbed
URL unload-reload-line
USCS unified soil classification system
wt weight
XRD X-ray diffraction

Introduction

The lack of urban space in built up areas and the increasing demand for mobility, with the consequent need for supporting infrastructure, have led to increased construction activities in the last decade and these have been focused on potentially troublesome sites for foundations, which have been avoided until now. These activities may include underground construction for large service buildings, new construction or widening of roads and railways, new traffic intersections with excavations for underpasses or embankments for reaching higher elevations. Soft clays deposited under post-glacial lacustrine conditions in the Swiss Mittelland represent such potential high risk sites. These soft, varved clays are called "Seebodenlehm" in Switzerland. Their deposition stretches all along the Swiss Mittelland from the SW to the NE of the country (e.g. Belp, Zug, Rapperswil, Birmensdorf, Kloten and Kreuzlingen).

The main features of Seebodenlehm are the low stiffness and the alternating layers of clay and silt-fine sand, as in most varved glacial deposits. The layered nature of these soils requires special design considerations for geotechnical problems. The strength of the soil for shearing along the varves can be much less than that for shearing across them (mechanical anisotropy). Because of the silt layers, the horizontal hydraulic conductivity can be far greater than that in the vertical direction (anisotropy of permeability). Laboratory testing of varved clay is problematic because results depend greatly on specimen size and the relative proportions of the silt and clay layers in the test specimens, as the properties of these individual layers are significantly different. Thus directly relating laboratory test results to anticipated field behaviour could be misleading (DeGroot and Lutenecker, 2003, Long, 2003). This offers a challenge for geotechnical engineers, who have to consider many different aspects of design, beginning from determination of appropriate soil parameters, over to the choice of an appropriate constitutive model, to eventually the design of new construction methods. The proximity of neighbouring structures in urban areas, particularly of ancient buildings, constitutes another restrictive boundary condition for design.

Current practice routinely relies on simplified theories at both ultimate and serviceability limit states, which leads to conservative design of structures. However, engineers are under severe pressure to develop more economical and safer solutions. This should encourage innovative design and cooperation

between practice and research. An improved characterisation of the founding soil stratum, and the resulting more sophisticated constitutive modelling, can reduce costs and improve performance. This approach is now required for Seebodenlehm, a soil which has not been considered for design in such detail until recently.

1.1 Objectives of the project

The Institute for Geotechnical Engineering has had a long term scientific interest in the classification and mechanical properties of Seebodenlehm. Gyger et al. (1976) investigated the sedimentation of soft deposits in the lake of Zürich at the end and after the last glaciation. Müller -Vonmoos et al. (1988) reviewed the mineralogical aspects of Swiss clays and linked them to practical challenges in soil mechanics. In the middle 90's, research and teaching projects have been developed from links with geotechnical engineers from industry and from county and council transportation authorities (i.e. Dreifaltigkeitskirche in Constance, Kloten Airport).

Giudici-Trausch has been involved into two of the subsequent projects: the railway underpass in Kreuzlingen and the highway bypass in Birmensdorf, which has been built on high embankments. These projects present two types of problems related to the design on or in soft clays. In the first case, the question arises about whether there is any influence of strain and stress path on stiffness for this n.c. clay, which might improve the accuracy of the modelling, leading to more economic design. In the latter case, the onset of large plastic strains and the subsequent pattern of plastic straining are of interest, as well as the permeability properties of the layered soil.

This thesis deals with the in situ and laboratory characterisation of the two soft clays present as foundation soils at these sites. The specific goals of the research are:

- Determination of soil parameters from in situ and laboratory tests for Kreuzlingen and Birmensdorf Seebodenlehm, as well as for the reconstituted Kreuzlingen clay.
- Comparison of composition and mechanical behaviour between the two natural clays to investigate the geographical variation in properties along the Swiss Mittelland, and to investigate correlation between mechanical properties and plasticity index, or any other appropriate parameter (liquidity index I_L).
- Comparison of composition and mechanical behaviour between the natural and the reconstituted Kreuzlingen clay to investigate the influence of structure on properties.
- Determination of strain rate dependence relating to one dimensional consolidation.
- Comparison of results between in situ and laboratory tests.
- Investigation of applicability of an anisotropic elasto-plastic model with rotational hardening for Swiss soft clays.

1.2 Outline of the thesis

The thesis covers 7 main chapters and an additional reference section.

The thesis starts with an introduction that outlines the background, the goals and content organisation of the project.

Chapter 2 presents a review of the relevant literature pertaining to soft soils, deformation behaviour of soils and soil models.

The Seebodenlehm is introduced and described in detail in Chapter 3. First the technical and geographical details of the sites are described, then the borehole logs are presented. The engineering geology of both types of Seebodenlehm is discussed, based on the geological and geotechnical charts of Switzerland. The last part of the chapter is dedicated to the mineralogical composition, the state and structure as well as the index properties of the Seebodenlehm.

The in situ testing, incorporating piezocone testing at both sites as well as a geophysical experiment in Kreuzlingen, are summarized in Chapter 4.

Chapter 5 is dedicated to the laboratory tests. The chapter is divided into two main sections, which present the laboratory devices and the tests results of the triaxial stress path tests and of the continuous loading oedometer tests respectively.

The interpretation of the results and the comparisons between the soils tested and between field and laboratory tests are discussed in Chapter 6. The one dimensional compression of the clays is compared in Section 6.2 with the plasticity and liquidity indices of the clays. Sections 6.3 and 6.4 compare the undrained shear strength and the shear stiffness of the clays determined with in situ and laboratory tests. In Section 6.5 the yield curves of the two Seebodenlehm and their changes due to stress path history are estimated by the constitutive model S-CLAY1 and compared with the yield points determined from the triaxial stress path tests. Finally, the measurements of settlements, horizontal displacements and porewater pressures performed at the test fill embankment in Birmensdorf are analysed in Section 6.6.

The summary in Chapter 7 presents the main results and observations of the thesis.

Seite Leer /
Blank leaf

Literature Review

2.1 Soft lacustrine soils

2.1.1 Natural soft lacustrine clays

Deposits of compressible soils of recent geological origin (last phase of the Pleistocene, during the past 20000 years) are found in all continents and in all regions of the world (Leroueil et al., 1990). The physical and mechanical properties of clay soils are the result of the succession and interaction of many geological processes from the sedimentation to the geological changes in situ, including erosion or chemical modification. The particles, that make up the clay soils, contain fine particles of quartz, feldspar and clay minerals and have been produced by abrasion and chemical alteration from the parent rock. The clay minerals are hydrated aluminium silicates containing Mg, K, Ca, Na, and Fe ions and can be grouped into illites, chlorites, kaolinites and montmorillonites. The particular properties of the clays are influenced therefore by the nature of the parent rock, the climatic conditions and the mode of abrasion, transportation and deposition (Leroueil et al., 1990). During the Pleistocene period, roughly 30% of the land surface of the world was covered with glaciers. In Europe, this period is called the Würm, whereas in North America it is called the Wisconsin period. At the maximum state of the last glacial advance, the thickness of the ice sheet could have been of the order of 2 to 4 km in the centre of the Scandinavian glaciers, and the sea level was about 120 m below the present sea level (Leroueil et al., 1990). Since about 20000 years ago, the melting and progressive retreat of the glaciers have led to a general rise of the sea level and to a rebound of the earth's crust and mantle. In Scandinavia, Bjerrum (1954) estimates the uplift around Oslo at around 220 m.

The retreat of the Würm glacier in northern and continental Europe occurred more recently than in Canada, so that the isostatic uplift of the earth's crust is still continuing at a significant rate (several mm/y, (Leroueil et al., 1990)). The deposits of marine or lacustrine clays are thus of very recent origin and therefore nearly always quasi normally consolidated. Many fluvial and lacustrine deposits of soft clays are found particularly in the alpine countries of Switzerland, Germany, France and Austria. These deposits are localized formations with high

variability in physical properties and marked stratification. They can have a high organic content, with low overconsolidation ratios, thus even higher compressibility than the Seebodenlehm without organic matter.

Quigley (1980) presented an overview of the geology, mineralogy and physico-chemistry of soft soils, particular in a Canadian context. However the differing processes of sedimentation, which control the stratigraphy of soft soil deposits, are valid for all lacustrine deposits. The main type of soft clay deposits that can be encountered in geotechnical practice are listed in Table 2-1. Varved freshwater clays are layered sediments deposited in glacial freshwater lakes. They can represent proximal or distal facies, according to the distance from the source.

| Type of deposit | Origin |
|----------------------------|--|
| Waterlaid tills | Unsorted lacustrine sedimentation below floating ice |
| Lacustrotills | Sub aqueous, proximal, flow deposits in proglacial lakes |
| Mud flow deposits | Sub aerial and submarine flows |
| Turbidity current deposits | Heavy-density current deposits generated by mud flow dilution, floods, ice calving, slumping, etc. |
| Varved clays | Turbidity current summer deposits and winter clay deposition by settling |
| Marine clays | Salt-water flocculation and sedimentation |

Table 2-1: *Type of soft clayey deposits after Quigley (1980).*

The three major types of sedimentological processes, which are related to the formation of lacustrine varved clays, are the heavy density turbidity current, interflows and low-density overflow in the lakes (Kenney, 1976 as reported by Quigley, 1980) (Figure 2-1).

In proglacial lakes, where the water front was still in contact with the ice front, heavy density turbidity currents controlled the deposition of the summer silt varves, while overflows were characteristic of winter conditions. Thus the slow settling of clay particles to form the winter layer was relatively undisturbed. Current regimes and sedimentary conditions are quite different in post glacial freshwater lakes, which are no longer in contact with the ice front. Suspended sediment loads are far less than in proglacial lakes, and amount to less than 0.1 g/L. Since sediments loads are so low, the thermal density stratification becomes significant. Therefore, varved clays become laminated clays with distance from the source becoming significant in post glacial lakes. Heavy density bottom flows would only occur during erosive floods, probably in the spring or as products of under water slumping (Figure 2-1).

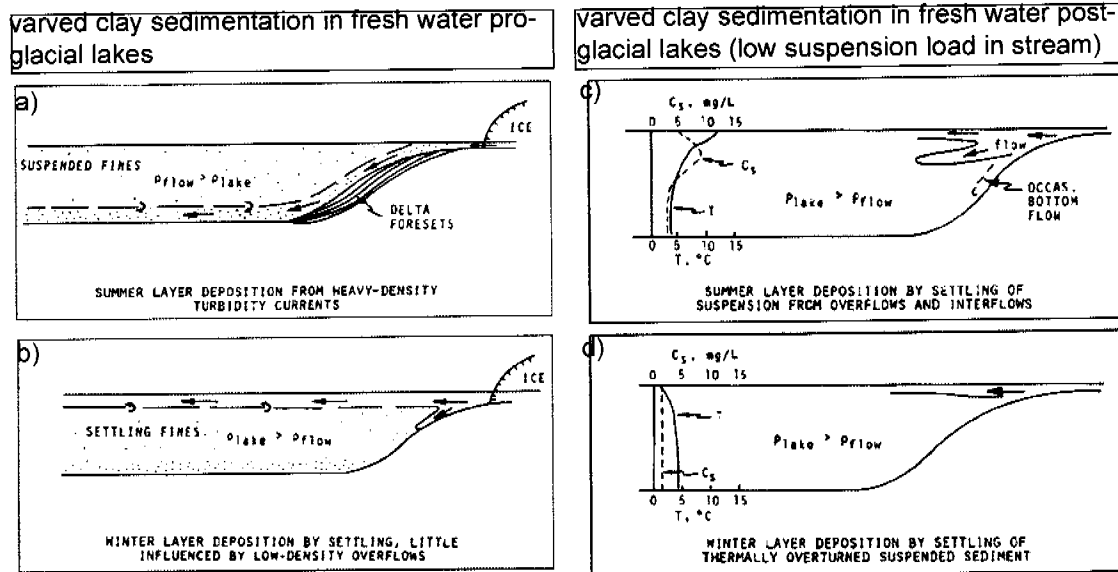


Figure 2-1: Deposition of varved clays: in proglacial lakes by turbidity currents (summer, a) and settling (winter, b), in post glacial lakes by overflows and interflows (summer, c) and by thermal stratification (winter, d) where C_s = concentrated suspended solids and T = temperature in °C. (Kenney, 1976 and Smith, 1978 as reported by Quigley, 1980).

Rey (1994) describes the geology and formation of varved clays in Flurlingen-Schaffhausen and in Dietlikon, two regions of the Swiss Mittelland. Such varved or laminated clays deposited in a glacio-lacustrine milieu are labelled as Seebodenlehm(e) in Switzerland. The Seebodenlehm from Flurlingen-Schaffhausen represents a mix of proximal and distal facies in a proglacial lake and shows the characteristic interlayering with sand and gravels of fluvial or turbidity origin and even with glacial till associated with glacial pulses. Laminated or varved clays with a chaotic layering of the laminae are characteristic of deposition on the sides of the sedimentation area, where erosive floods and slumping can occur. Rey (1994) assesses that although the Seebodenlehme from Flurlingen-Schaffhausen and Dietlikon were not overconsolidated by an overrun of the glacier, they show features of light overconsolidation (OCR up to ca. 6). He explains this with horizontal forces from the glacier front, which could have compacted and consolidated the Seebodenlehm deposits. These shearing loads have led to the formation of shingling and dislodging of entire clay layers.

Gyger et al. (1976) give a general view of the sedimentation in the lake of Zürich at the end of, and after, the last glaciation. The paper describes conditions based on data of unit weight, granulometry, plasticity, failure conditions and sensitivity for the three main deposits found in boreholes in the lakebed, which are, from the lake bottom with depth, lacustrine chalk (Seekreide), lake bottom loam (Faulschlamm) and laminated clays such as Seebodenlehm. The laminated clays found here have settled out in a post glacial lake, when the climate was still cold and icebergs floated on the lake surface. The Seebodenlehm contains boulders and glacial tills, which had run off into the upper, younger layers. On the sides of the deposition area, these lacustrine deposits can have been mixed up by strong river currents and therefore contain coarse grained sediments transported by rivers. The results of the investigation on a borehole core from the

lakebed off Richterswil (south of Zürich) are summarized in Table 2-2 and Figure 2-2 (Gyger et al., 1976). Clear deposit boundaries are detectable on the basis of the grain size distribution, the natural water content and the Atterberg limits, as well as the undrained shear strength s_u from borehole vane tests (Figure 2-2). The three types of lakebed deposits show a characteristic grain size distribution (Figure 2-3), and the clays studied in this Thesis fall in the range for Seebodenlehm (See Chapter 3). Although the Seebodenlehm contains a higher clay fraction, the Atterberg limits are far below the values for lacustrine chalk. The liquid limit of Seebodenlehm and lake bottom loam show the expected dependence upon the clay fraction content, whereas the lacustrine chalk shows an apparently high liquid limit, which is due to the high roughness of its particles (Gyger et al., 1976). Dumbleton and West (1966) stated that roughness and form of the particles have a great influence on the Atterberg limits. For the same grain size distribution, the Atterberg limits increase with increasing roughness and from spherical to angular to platelet form of the particles.

| Site | CF <2 μ m | w | w _L | w _P | I _P | O | ρ_s | carb. | clay minerals |
|---------------------|--------------------------|-----|----------------|----------------|----------------|---------------------|---------------------|-------|------------------|
| | [%] | [%] | [%] | [%] | [%] | [m ² /g] | [t/m ³] | % | % |
| lacustrine chalk | 18 | 85 | 44 | 32 | 12 | 2.8 | 2.63 | 86 | 5 |
| lake bottom loam | 46 | 30 | 32 | 20 | 12 | 7.9 | 2.74 | 41 | 17 |
| Seeboden- lehm | 52 | 41 | 38 | 19 | 19 | 15.6 | 2.76 | 37 | 35 |
| CF | Clay fraction <2 μ m | | | | | | | | |
| O | particle surface | | | | | | | | |
| carb. | total carbonate content | | | | | | | | |

Table 2-2: Typical average values of state and index properties (Gyger et al., 1976).

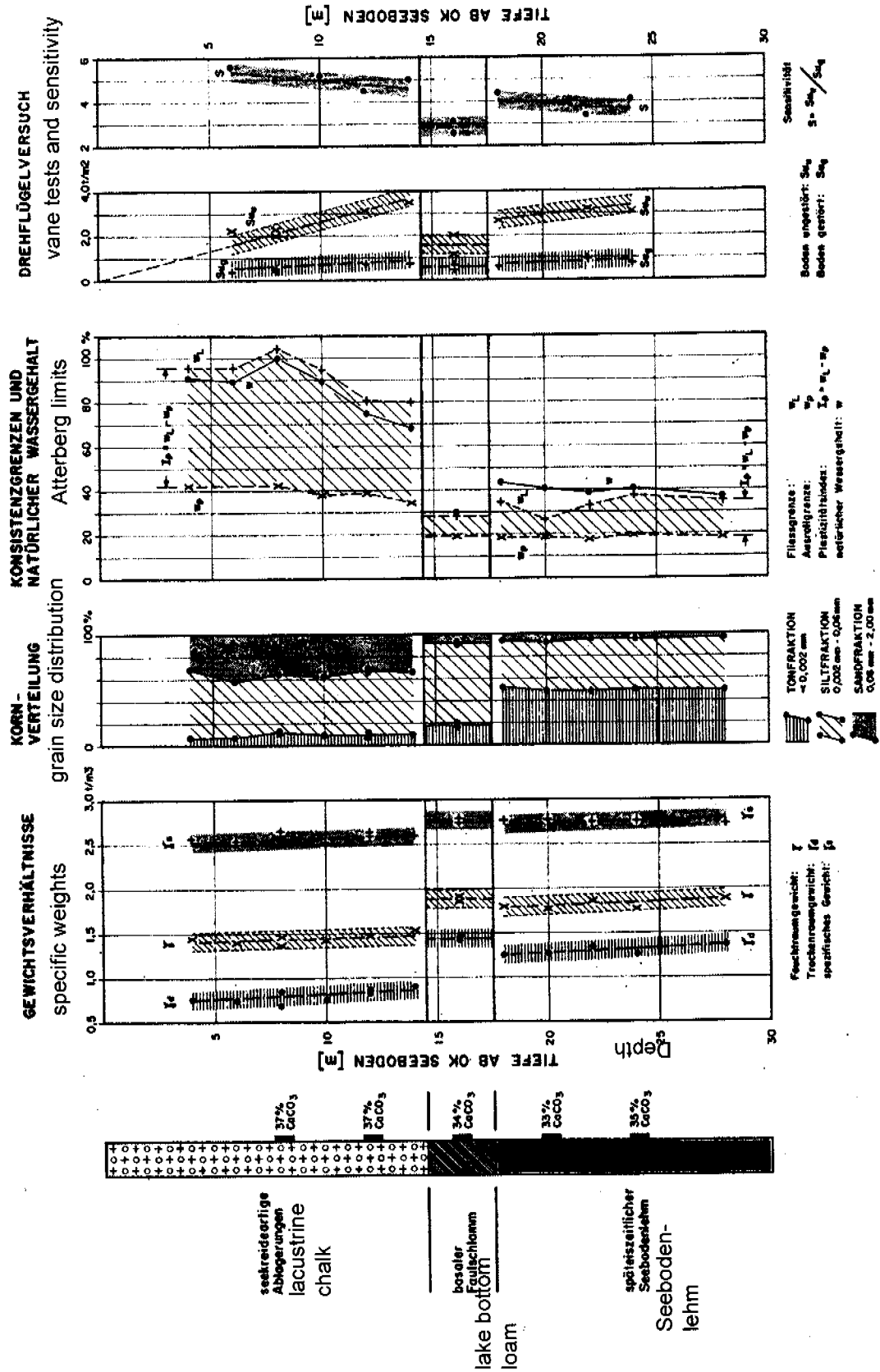


Figure 2-2: Deposits in the lakebed off Richterswil, canton Zürich, Switzerland (Gyger et al., 1976), (translation of key terms can be found in List of Symbols).

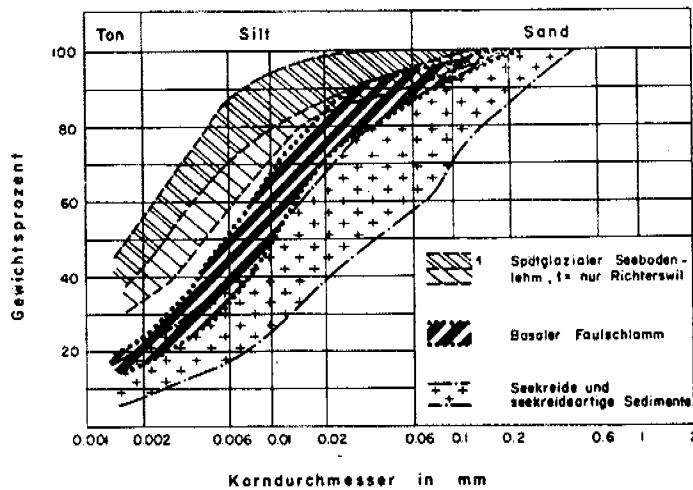


Figure 2-3: Characteristic range of grain size distribution (Korndurchmesser) for the glacio-lacustrine deposits in lake Zürich (Gyger et al., 1976)

Scherzinger (1991) studied the properties of soft lacustrine clay from Constance, a city in the south-west of Germany, by means of triaxial and oedometer tests. The city of Constance lies on the shores of Lake Constance, on the border with Switzerland. On the opposite site of the border lies the city of Kreuzlingen, where the "Swiss" Seebodenlehm samples studied in the present thesis have been extracted. The soft clays studied by Scherzinger belong to the same geological formation as the Kreuzlingen clay. Typical average values of state and index properties are $w = 27$ and 42% , $w_L = 28$ and 42% , $I_p = 14$ and 23% , clay fraction = 28 and 57% for the two extraction sites. The main results of Scherzinger's research are listed below:

- the coefficient of earth pressure at rest K_0 measured in triaxial tests was 0.54 to 0.66 , with a mean value of 0.61 .
- the compression index C_c , the swelling index C_s and the consolidation coefficient c_v correlate well with the liquid limit w_L , and $C_c/C_s \approx 1.5$.
- two limit states could be detected in undrained triaxial compression tests on one-dimensionally consolidated specimens. The first limit state corresponded to the maximum deviator stress q , the second to the maximum effective stress ratio σ'_1/σ'_3 . In tests on isotropically consolidated specimens, the two limit states coincided, showing that these tests are not suitable to describe the stress-strain behaviour of one-dimensionally consolidated soils.
- The measured undrained shear strength s_{uE} and the angle of shearing resistance ϕ'_E in extension tests were smaller than the equivalent values for compression tests. Therefore the undrained shear strength s_{uE} selected for design must be reduced if the soil is loaded in extension, e.g. in the toe region of a retaining wall and s_u has been measured in compression as s_{uC} .

- the ratio of the secondary compression coefficient to the normal compression line coefficient C_{α}/C_c was determined to be 0.02 to 0.03.
- triaxial tests with different loading rates showed that the stress-strain behaviour is strain rate dependent.

For the soft clays investigated by Scherzinger, the active earth pressure is reached behind a rigid propped wall after some initial movement of the wall. The so called relaxation earth pressure is the earth pressure that appears, after full dissipation of excess pore water pressure, due to relaxation and creep processes behind the fixed propped wall. Scherzinger found out that the active earth pressure and the relaxation earth pressure are only 5 to 10% smaller than the earth pressure at rest. To mobilise these earth pressures, a vertical compression strain of up to 1.5% is needed. Scherzinger states therefore that retaining walls in these soft clays should be designed for the earth pressure at rest.

The study of soil mechanics was born with investigations into landslides occurring in the marine clays of Norway and Sweden (Leroueil et al., 1990). According to Bjerrum (1954) and Larsson (1981), these marine clays are characterised by low plasticity indices, low overconsolidation ratios of the order of 1.0-1.5, extremely high liquidity indices, and as a result of leaching, very high compressibility and a not very marked structure. However the studies of these soils have been mostly carried out with small-diameter sampling tubes which can lead to a disturbance of their structure. Brousseau (1983) confirms, using special sampling devices, that in fact these clays possess a structure, which affects the peak strength and the stiffness of the clay.

Sample disturbance has a great influence on the test results on soft laminated clays, especially on one-dimensional compression tests, and the choice of an adequate sampling device is very important. Long (2003) shows clearly with the comparison of void ratio - stress curves from oedometer tests on Athlone laminated clay extracted using different sampler types, that it is possible to determine the vertical yield stress with some degree of confidence for a block specimen, while specimens taken with a variety of other samplers give very poor results (Figure 2-4). Long compares these data by normalising them according to the procedure proposed by Burland (1990), pointing out, however, that Burland's work concentrated on homogeneous clays and thus should be treated with caution when extrapolated to laminated clays. Burland (1990) found that for normally consolidated clays, whose natural state lies on or close to the Intrinsic Compression Line ICL, the oedometer compression curves are parallel to this line. This is the case for the Athlone clay and suggests that the clay has an oriented fabric due to rapid deposition from a dense suspension. Furthermore, the testing suggests that the soil does not have a well developed structure. The research on Athlone laminated clays showed that the sample disturbance due to the sampling method, caused both the small strain stiffness and the undrained shear strength to increase and induced a strong tendency for dilatant behaviour in undrained triaxial tests.

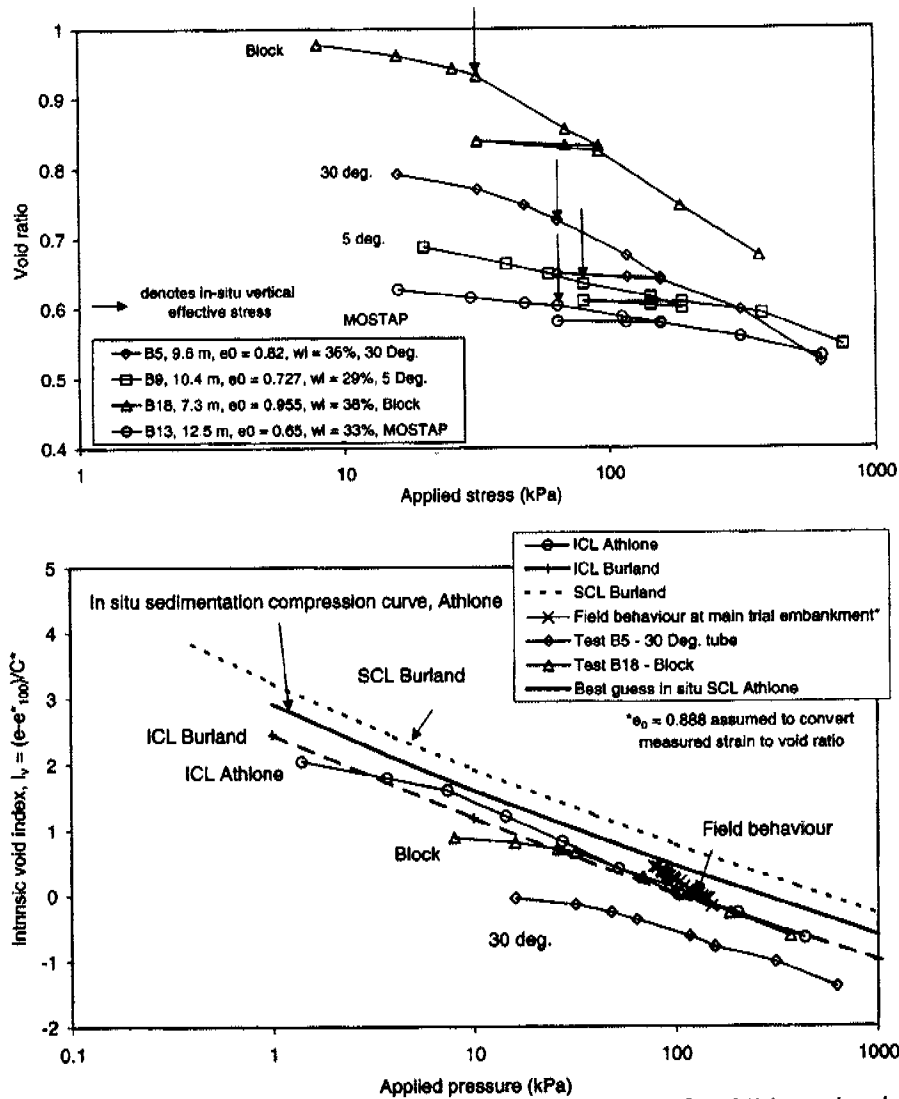


Figure 2-4: Comparison of oedometer compression curves for Athlone laminated clay (Long, 2003): in void ratio-mean effective stress plane (above), in normalised plane intrinsic void index I_v - mean effective stress (below). [SCL = sedimentation compression curve, ICL = intrinsic compression curve, e^*_{100} and C^* = intrinsic constant of compression (Burland, 1990)].

The compression response of a soil to the increase in effective stresses is strongly influenced by the natural structure of the soil. Following Burland (1990) and Leroueil and Vaughan (1990), the effects of soil structure may be highlighted by comparing the mechanical behaviour of natural and remoulded soil. Thus the difference in compressibility between undisturbed and remoulded states varies considerably in different clays, and its magnitude can be taken as a measure of the structural effect (Diaz-Rodriguez, 2003). Typical void ratio - effective stress relationships for undisturbed, remoulded and resedimented Mexico City clay are shown in Figure 2-5 after Mesri et al. (1975). The vertical yield stress is well defined for the undisturbed sample, while the remoulded curve is rounded. Ageing of the remoulded clay brings the consolidation curves closer to that of the undisturbed state, and all curves approach the resedimentation line for very high stresses, where the influence of structure is apparently eliminated.

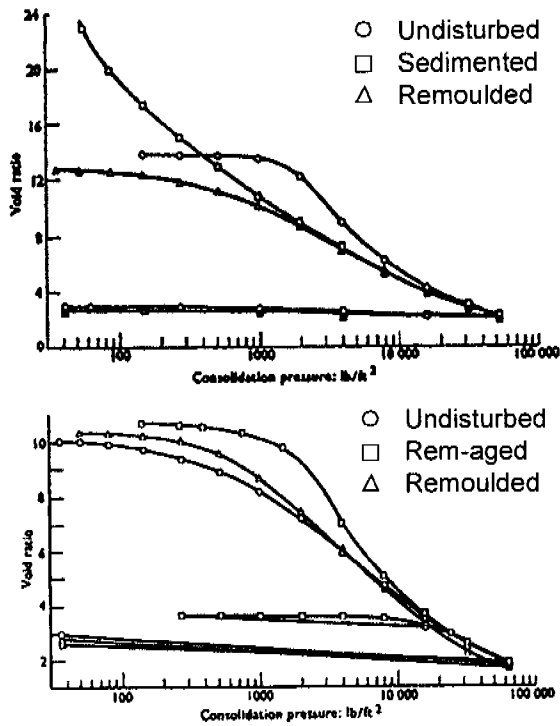


Figure 2-5: One dimensional consolidation curves showing influence of remoulding and ageing on Mexico City soil (Mesri et al., 1975)

Oedometer compression curves on Fucino clayey soil show a well defined vertical yield stress, confirming that sampling has not significantly altered the soil structure (Soccodato, 2003). In this case however, the undisturbed stress states are close to the Sedimentation Compression Line (Burland, 1990) and tend to become parallel to the ICL after yield (Figure 2-6). The compression curves of the undisturbed and of the remoulded Fucino soil remain separated, despite the high values of applied stress, thus indicating that the structure of the remoulded material and the damaged structure of the natural soil are different.

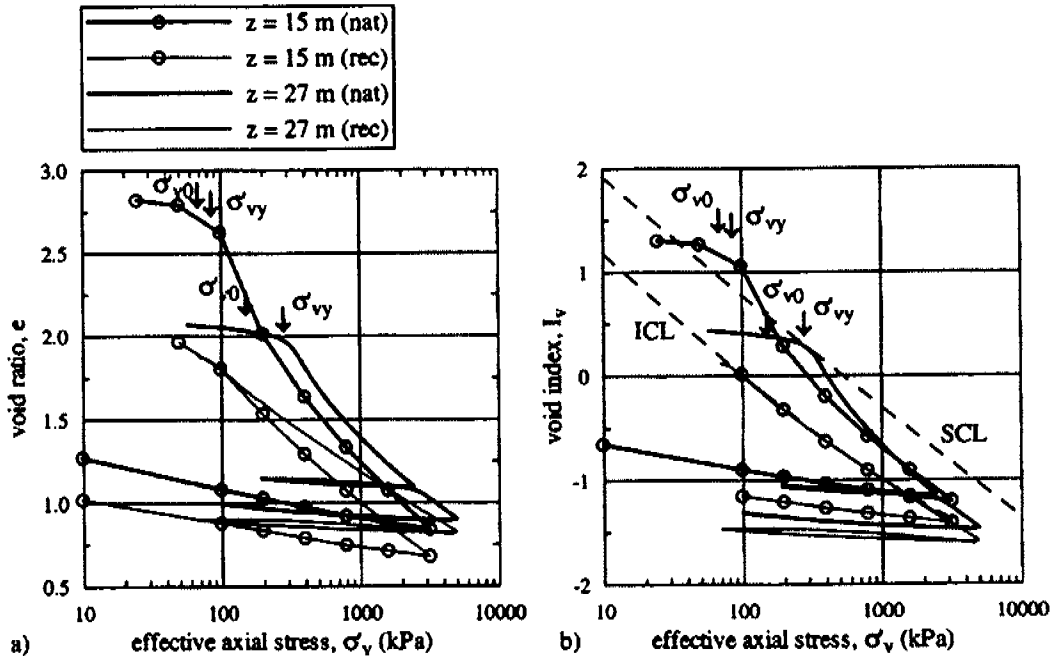


Figure 2-6: One dimensional compression curves on Fucino clay, represented in: a) standard $e-\sigma'_v$ plot; and b) normalised $I_v-\sigma'_v$ plot (Soccodato, 2003).

Cummings et al. (2003) report tests on a deep clay deposit at Swann's Bridge, Limavady in Northern Ireland, which was deposited in a fresh-water proglacial lake. The lower zone of this deposit (from 28 to 54 m depth) is heavily laminated, with many thin alternating layers of silt and clay. The compression

results of tests on specimens from the lower zone suggest that destructuring occurred during extrusion and unloading in the laboratory, despite careful sampling although there was no visual evidence from the tube samples that disturbance had occurred. Cummings et al. consider mechanisms of plastic softening during unloading as a possible explanation for the destructured behaviour of the lower zone of the deposit.

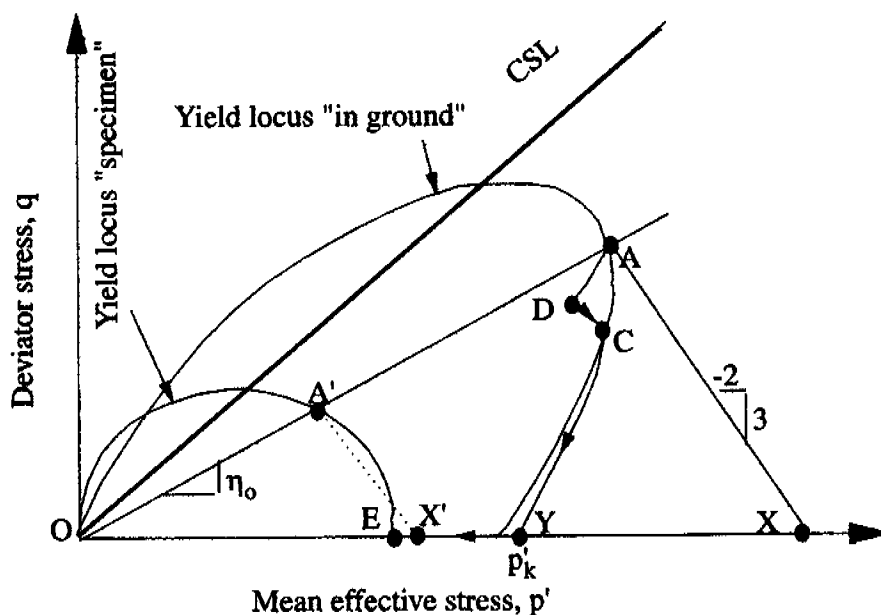


Figure 2-7: Stress path during sampling for the Lower Limavady clay (Cummings et al., 2003)

Figure 2-7 shows the stress path followed by a sample of the Lower Limavady Clay from deposition (point A) to unloading caused by geological processes (point D, erosion or melting of ice cover). Unloading the sample in the laboratory in preparation for trimming inevitably generates high negative pore water pressure and an isotropic effective stress p'_k immediately after the removal of the in situ stresses by extrusion from the tube (point Y in Figure 2-7) (Cummings et al., 2003). Cummings assumed perfect sampling, which implies that the process is undrained and that there is no change in the volume or total mass of the sample and in the overall moisture content of the sample. However a considerable change in the distribution of the water between the silt and clay layers can take place. The clay layers will absorb the water from the silt layers and thus experience a significant reduction in effective stresses (point E in Figure 2-7). This may lead to plastic softening along the isotropic $q=0$ axis, associated with a reduction in the size of the yield locus and with a lower vertical yield stress X' for the laboratory specimen compared with X for the in situ material. Particular care is therefore needed when reviewing laboratory results from deposits of soft stratified clay. Bjerrum (1973) already reported this mechanism of swelling of soft clays due to redistribution of water in the sampling tubes, which causes disturbance to the samples. Stress relief caused likewise cavitation in the silt laminae of the laminated facies of the Bothkennar clay, resulting in a possible swelling of the clay laminae and additional destructuring (Hight et al., 1992). Bjerrum recommended to reconsolidate the sample to the same stresses it carried in the field,

to restore the in-situ conditions. During Cummings' isotropically consolidated compression triaxial tests, however, the disturbance was not eliminated. The laminated structure of the soft soil can be the key issue to explain this behaviour: the silt laminae represent the preferential horizontal drainage layer leading to the side drains on the sample in the triaxial set up, and the differences in permeability of clay and silt laminae prevent a re-homogenisation within the triaxial specimen. In this case probably, the dimensions of the varving relative to the dimensions of the triaxial specimen assume great importance.

Finally, the results of a study on the influence of calcium carbonate content CaCO_3 on the physical characteristics and compressibility parameters of Pliocene lacustrine deposits carried out by Bozzano et al. (1999) will be reported briefly. Cementing agents, commonly silica, iron or aluminium oxides and calcium, magnesium or iron carbonates, highly affect the mechanical properties of soils. Average CaCO_3 content of these sediments was about 22% along a more than 100 m deep vertical profile. Bozzano et al. (1999) observed effects due to cementation by comparing natural and decalcified laboratory samples. Cementation induced an increase in the yield stress proportional to the degree of cementation, as quantified by the CaCO_3 content. The compressibility in the stress range lower than the yield stress decreases, as the carbonate stiffens the soil structure. Cementation also affects the shear modulus of the soil and the presence of bonds induce a brittle compressive behaviour. For the stress range above the yield stress, no relationship was observed between the compression index C_c and CaCO_3 content. Bozzano et al. (1999) conclude from these findings that the vertical yield stress for materials cemented by CaCO_3 corresponds to partial disruption of the structure.

2.1.2 Reconstituted material

Reconstituted soil is made by remoulding a natural soil to break down particle associations, destroy shear planes, eliminate large pores and produce a more homogeneous fabric at a macro scale. Cotecchia and Chandler (1997) showed, using electron microscopy, that reconstituted material still had a sedimentation structure, but that it was different from that of the natural material. They proposed that the differences in behaviour between the natural and reconstituted soil were primarily due to the nature, stability and strength of these different structures. Burland (1990) suggested that a reconstituted sample should be made from a natural sample, mixed with water to form a slurry, without drying the soil prior to mixing. The slurry should have a water content between the liquid limit w_L and $1.5w_L$. It is then consolidated, preferably under one-dimensional conditions. Ideally the water used for reconstitution should have a chemistry similar to that of the pore fluid. Burland referred to the parameters determined for a soil prepared in this manner as intrinsic, as these parameters were felt to be unique and inherent for a given soil type. Fearon and Coop (2000) analysed the effect of the work done in remoulding the soil on the behaviour of the reconstituted soil. They showed that soils that have been reconstituted using high- and low-energy methods may have different characteristics. In this case, the meaning of the term "intrinsic" as originally suggested by Burland (1990) may need to be reviewed as the intrinsic behaviour seems highly dependent on the preparation method.

2.2 Factors affecting the deformation behaviour

Preconsolidation pressure, defined as the maximum effective vertical stress to which a soil has been subjected, is one of the most important parameters required to assess the deformations of a clay deposit. Often this term is used to define the effective stress at which an undisturbed sample yields in an oedometer test, that is the stress at which the stiffness of the soils falls rapidly. Burland (1990) recommends use of the term vertical yield stress σ'_{vy} , to describe the critical stress at which the structural resistance of a clayey soil breaks down and where the subsequent compression curve is initially steeper than the standard virgin line. Because the strain rate of the test plays an important role (among other factors) in the laboratory testing of soft clays in the determination of soil parameters, the term "preconsolidation pressure" should be reserved for situations in which the magnitude of such a critical stress can be established by geological means (Burland, 1990). The preconsolidation or yield stress determines therefore the change of a soil's state from overconsolidated to normally consolidated: for an idealised elasto-plastic soil this means that during compression above the yield stress, in the normally consolidated region, the strains will have irrecoverable plastic character as well as a much smaller component of elastic recoverable strains, whereas during reloading of an overconsolidated soil the strains are purely of an elastic nature. The soil behaves however not as an idealised elasto-plastic material, and the passage between elastic and plastic region is not as clearly defined as with a yield stress or locus. The elastic strains inside the yield locus are not linear and depend from the stress and the strain path. Results of triaxial tests to investigate the stress-strain behaviour of a clayey soil for small strain and for stress states inside the yield locus demonstrates that the strains are inelastic except for a very small interval of loading at the start of test (Richardson, 1988, Stallebrass, 1990 and Atkinson et al., 1990).

Bjerrum (1973) recommends that the load steps in a staged oedometer should be as short as one hour before the preconsolidation pressure has been reached, as the time required for 90% consolidation is very short. In the normally consolidated region, the consolidation time increases and load steps should be as long as one day. The passage of a soil's state from stresses below the preconsolidation pressure to stresses above it, means therefore an important change in consolidation rate and stiffness. Länsivaara (1999) gives, based on the work done by Bjerrum (1973), a good description of the effects of stress, time and structure on the stress-void ratio relationship for clays from their deposition to their actual state (Figure 2-8).

A young normally consolidated clay can be represented by point A in Figure 2-8 on the virgin compression line, while ageing will decrease the void ratio without any change in effective stress to point B. For this aged clay the vertical yield stress will be detected at point C on the virgin compression line a-a. Another young normally consolidated clay is represented by point A* in Figure 2-8 on the virgin compression line, with ageing decreasing its void ratio to point B*. An additional decrease in effective overburden pressure or fluctuations of the ground water level, overconsolidate this clay to point O*. For this aged overconsolidated clay the vertical yield stress will be detected at point C*. Both clays show thus a higher yield stress (C respectively C*) than the actual in situ overburden pressure (B respectively O*). However the yield stress of natural clays is not always

a result of just stress and time history, but, as several experimental studies have shown, undisturbed samples can show higher void ratios for a given stress than samples sedimented in the laboratory (Mesri et al., 1975, Burland, 1990).

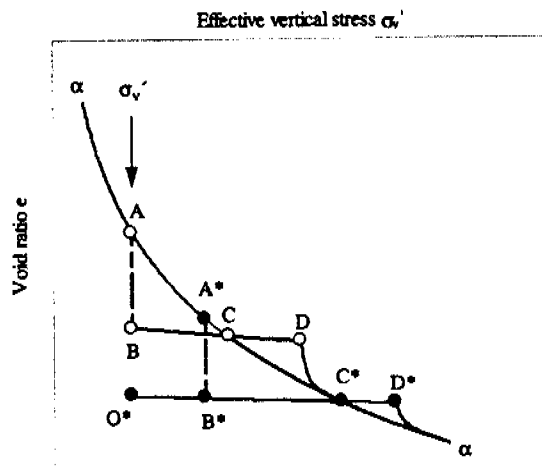


Figure 2-8: *The effects of stress, time and structure history on the stress void ratio relationship of clays, as reported by Länsivaara (1999).*

The yield surface can be regarded as a generalised yield stress; the preconsolidation pressure (vertical yield stress) observed in an oedometer test corresponds to just one point on this yield surface. The yield locus in the triaxial or q - p' stress plane is just a particular section through the current yield surface of the soil with one particular history (Muir Wood, 1990). The yield surface is not unique for a given preconsolidation pressure, but depends on testing rate or test duration (Tavenas and Leroueil, 1980; Graham et al., 1983b). Diaz-Rodriguez et al. (1992) presented the yield surfaces from different natural clays according to their friction angles, and Länsivaara reports their results, supplemented with data from Wong and Mitchell (1975), Larsson (1981), Hight et al. (1992) and Länsivaara (1995 a) (Figure 2-9). It can be concluded from Figure 2-9 that the yield curves of natural clays normalized by their yield stress and grouped according to their friction angle, are very similar, more or less elliptical in shape and centered along the K_0 -line reflecting the anisotropic stress conditions during deposition. The K_0 -line corresponds to a K_0 value evaluated from the Jaky (1944) equation $K_0 = 1 - \sin \phi'$.

It is difficult to translate the results of laboratory tests to in situ conditions, as the stress path in laboratory tests seldom corresponds to the in situ stress path, due, for instance, to construction work. The traditional approach to evaluate the in situ stress path in a clayey soil is to consider a construction process as undrained. However considering that the stress state of most clayey soil lies inside the yield surface (Point B, B* or O* in Figure 2-8) and therefore the coefficient of consolidation is considerably higher than in the normally consolidated region, it can be concluded that the degree of consolidation of the deposits has a great influence on the stress path followed in situ (Länsivaara, 1999). Leroueil and Tavenas (1986) supported this on studies of the behaviour of 45 embankments during construction. In Figure 2-10, the stress path for a one dimensional test and for most typical cases under an embankment are sketched (after Länsivaara, 1999).

Thus the yield stress can be higher than expected and lies at points D or D* above the virgin compression line. Leroueil and Vaughan (1990) used the term "structuration" for this additional hardening of the clay. If a structured clay is caused to yield, points D and D* in Figure 2-8, then large strains are likely to occur as the void ratio decreases towards the virgin compression line when the structure of the clay is destroyed.

The yield surface can be regarded as a generalised yield stress; the preconsolidation pressure (vertical yield stress) observed in an oedometer test corresponds to just one point on this yield surface. The yield locus in the triaxial or q - p' stress plane is just a particular section through the current yield surface of the soil with one particular history (Muir Wood, 1990). The yield surface is not unique for a given preconsolidation pressure, but depends on testing rate or test duration (Tavenas and Leroueil, 1980; Graham et al., 1983b). Diaz-Rodriguez et al. (1992) presented the yield surfaces from different natural clays according to their friction angles, and Länsivaara reports their results, supplemented with data from Wong and Mitchell (1975), Larsson (1981), Hight et al. (1992) and Länsivaara (1995 a) (Figure 2-9). It can be concluded from Figure 2-9 that the yield curves of natural clays normalized by their yield stress and grouped according to their friction angle, are very similar, more or less elliptical in shape and centered along the K_0 -line reflecting the anisotropic stress conditions during deposition. The K_0 -line corresponds to a K_0 value evaluated from the Jaky (1944) equation $K_0 = 1 - \sin \phi'$.

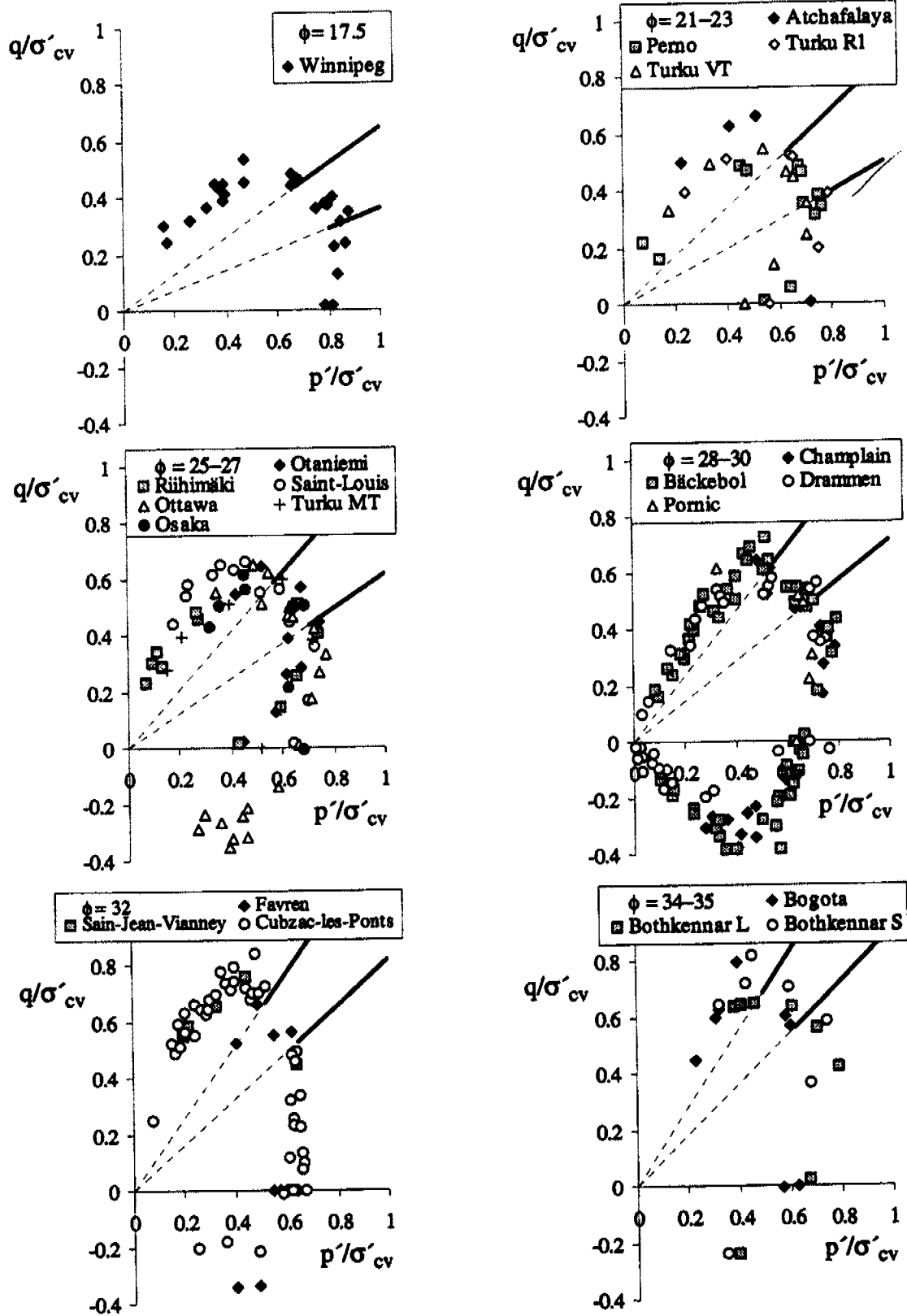


Figure 2-9: Yield curves of natural clays grouped according to their friction angles (ϕ' in degrees) as reported by Lämsivaara (1999).

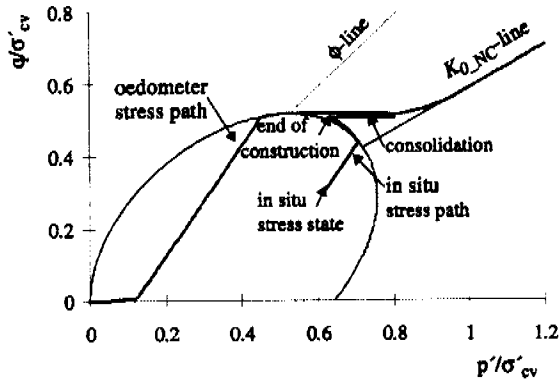


Figure 2-10: Possible differences in the effective stress paths between laboratory and in situ K_0 loading, after Länsivaara (1999)

The differences in yield stress and behaviour after yield can be considerable. Leroueil and Tavenas (1986) concluded that yield occurred in most cases between the K_0 -line and the ϕ' -line followed by a significant increase in excess pore pressure.

The effect of time and strain rate on the compressibility of clays has been recognized by several authors, Crawford (1964), Sällfors (1975), Janbu et al. (1981), Graham et al. (1983) and Leroueil et al. (1985). In general, the faster the loading rate, the higher are the effective stresses for a given strain. The strain rate in an incremental loading oedometer lies between $1 \cdot 10^{-8} \text{s}^{-1}$ and $1 \cdot 10^{-7} \text{s}^{-1}$ after 24 hours load increment for low and highly compressible clays respectively. The strain rates used in a continuous loading oedometer test are between $1 \cdot 10^{-8}$ and $1 \cdot 10^{-5} \text{s}^{-1}$.

An important consequence is therefore that the yield stress obtained in laboratory tests is test dependent. However, Leroueil et al. (1985) showed that a unique stress-strain-strain rate relationship exists for natural clays. For tests with constant strain rate, this implies that if two tests are performed with strain rates $\dot{\epsilon}_1$ and $\dot{\epsilon}_2$ showing preconsolidation pressures σ'_{cv1} and σ'_{cv2} , the effective stress σ'_{v1} and σ'_{v2} are such that (Länsivaara, 1999):

$$\frac{\sigma'_{v1}}{\sigma'_{cv1}} = \frac{\sigma'_{v2}}{\sigma'_{cv2}} \Leftrightarrow \frac{\sigma'_{v1}}{\sigma'_{v2}} = \frac{\sigma'_{cv1}}{\sigma'_{cv2}} \quad [2-1]$$

Leroueil et al. (1985) described this relationship with two curves determined by oedometer tests, one giving the normalized effective stress-strain relationship (Figure 2-11), and the other the variation of the preconsolidation pressure with strain rate (Figure 2-12). Equivalent tests for typical Finnish clays from Länsivaara (1995b) are also reported in Figure 2-12 and show very similar results.

Following Länsivaara (1995b), Equation 2-2 describes the relationship obtained with different strain rates, between yield stress and effective stresses at a given strain:

$$\frac{\sigma'_{v1}}{\sigma'_{v2}} = \frac{\sigma'_{cv1}}{\sigma'_{cv2}} = \left(\frac{\dot{\epsilon}_1}{\dot{\epsilon}_2} \right)^B \quad [2-2]$$

Länsivaara obtained a value of $B = 0.073$ for typical Finnish clays and of $B = 0.056$ for Champlain sea clays, showing that the strain rate effects for the Canadian clays are slightly smaller than those for the Finnish clays.

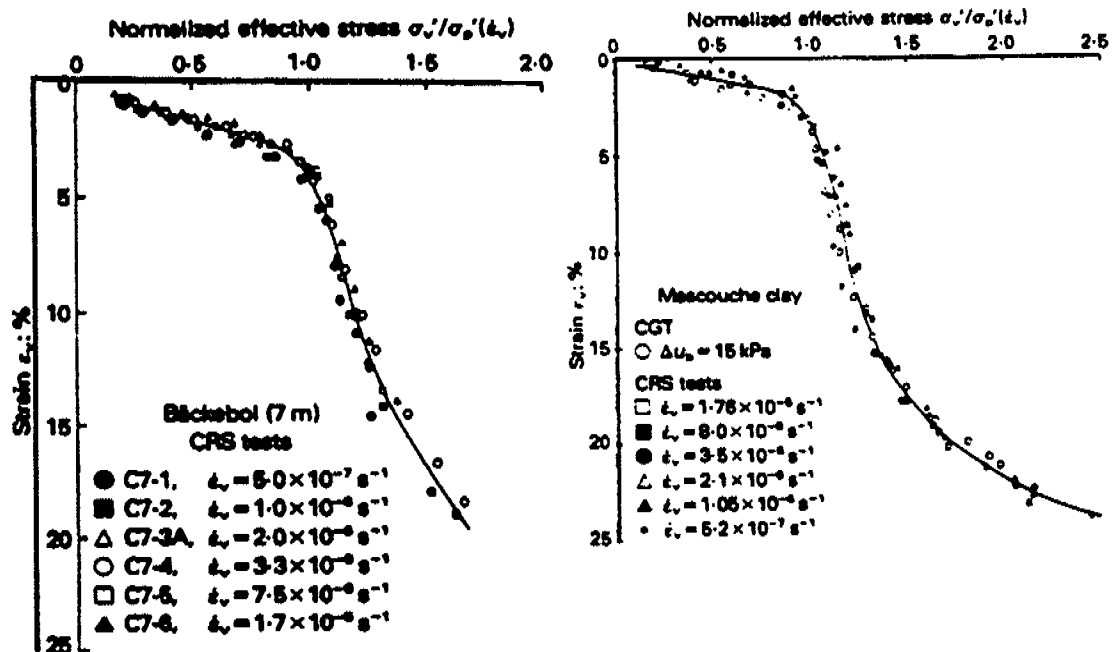


Figure 2-11: Normalized effective stress-strain curves for Bäckebol clay (Sällfors, 1975) and Mascouche clay from oedometer tests, from Leroueil et al. (1985). [CRS: constant rate of strain, CG: controlled gradient]

Mesri and Godlewski (1977) developed the C_α/C_c concept for the analysis of secondary settlement, where C_α is the secondary compression index and C_c the compression index (Mesri and Castro, 1987). This is based on the observation that the magnitude and behaviour of C_α with time is directly related to the magnitude and behaviour of C_c with consolidation pressure. For a variety of natural soils, including silts, clays and peats, they reported values of C_α/C_c in the range of 0.02-0.1. For a majority of inorganic soft clays, the value of C_α/C_c is approximately equal to 0.04 +/- 0.01 (Mesri and Castro, 1987). Mesri and Godlewski (1977) stated that the value of C_α/C_c together with the end-of-primary (EOP) e - $\log \sigma'_v$ curve completely defines the secondary behaviour of a given soil. With the actual knowledge of the strain rate dependence of the consolidation properties of clays, it can be stated that the value of C_α/C_c together with the unique stress-strain-strain rate relationship completely defines the compression behaviour of a given clayey soil.

The relationship given in Equation 2-1 implies that the creep properties are directly related to the primary deformation properties as well. This is illustrated in Figure 2-13 by means of fictitious stress-strain curves (after Länsivaara, 1999). The four curves represent two different strain rates for two clays with the same yield stress and a stiffness linearly increasing with stress in the normally consolidated domain. The viscous strain separating the two different strain rates is a direct function of C_c , so that with soil A having a C_c value twice as big as soil B, this viscous strain will be twice as big for soil A. Furthermore, the viscous strain is constant in the normally consolidated domain for the case of linearly stress dependent moduli. The parameter B from Equation 2-2 correlates with the ratio C_α/C_c as follows (Länsivaara, 1999):

$$B = \frac{C_\alpha}{C_c} \quad [2-3]$$

Equation 2-3 makes it possible to determine creep parameters from Continuous Loading (CL) oedometer tests and inversely to use data on the relationship between creep and primary deformation properties to evaluate rate effects.

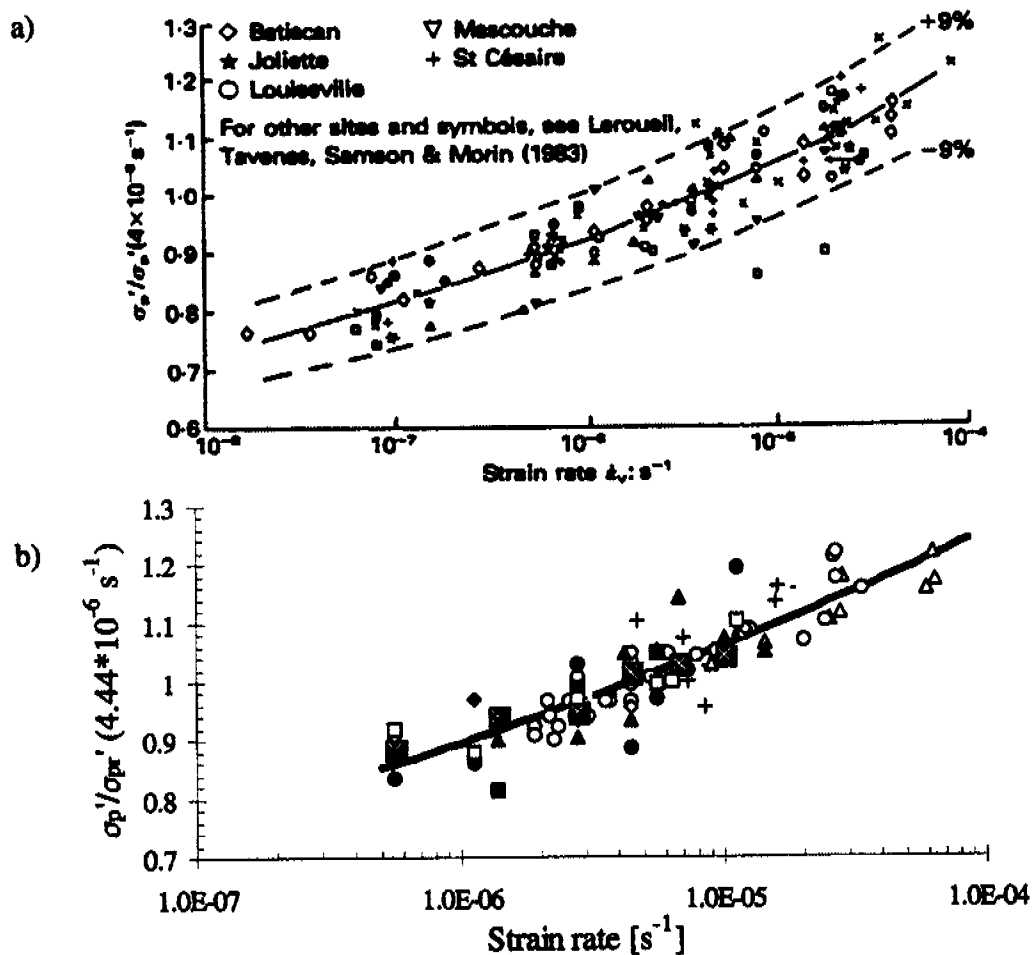


Figure 2-12: Normalized preconsolidation pressure - strain rate relationship for a) Champlain sea clay (Leroueil et al., 1983 and 1985) and for b) Finnish clays (Lämsivaara, 1995b), both after Lämsivaara (1999). [$\sigma'_p (4 \times 10^{-4} \text{ s}^{-1})$ = reference preconsolidation pressure σ'_p measured in a test carried out with strain rate $4 \times 10^{-4} \text{ s}^{-1}$]

The influence of the drainage length (distance to the nearest drainage boundary) on the compressibility of a clay has been studied by Berre and Iversen (1972). They varied the height of the specimen in multiple stage loading tests and measured the pore pressures at the base. They concluded that the value of yield stress is higher, the longer the effective stress has been kept constant, and the more rapidly the effective stress increases during further loading. Elements of the soil sample at a short distance from the drainage boundary will follow a different stress-strain curve and will show a higher yield stress than elements at a long distance.

The effect of rate of loading can be generalized to the entire yield surface as discussed for example by Graham et al. (1983). In the triaxial test, the behaviour is not unique after failure since localized shear zones may develop. The value of the friction angle is usually not considered to be affected by strain rate dependence, whereas the undrained shear strength is influenced by the strain rate.

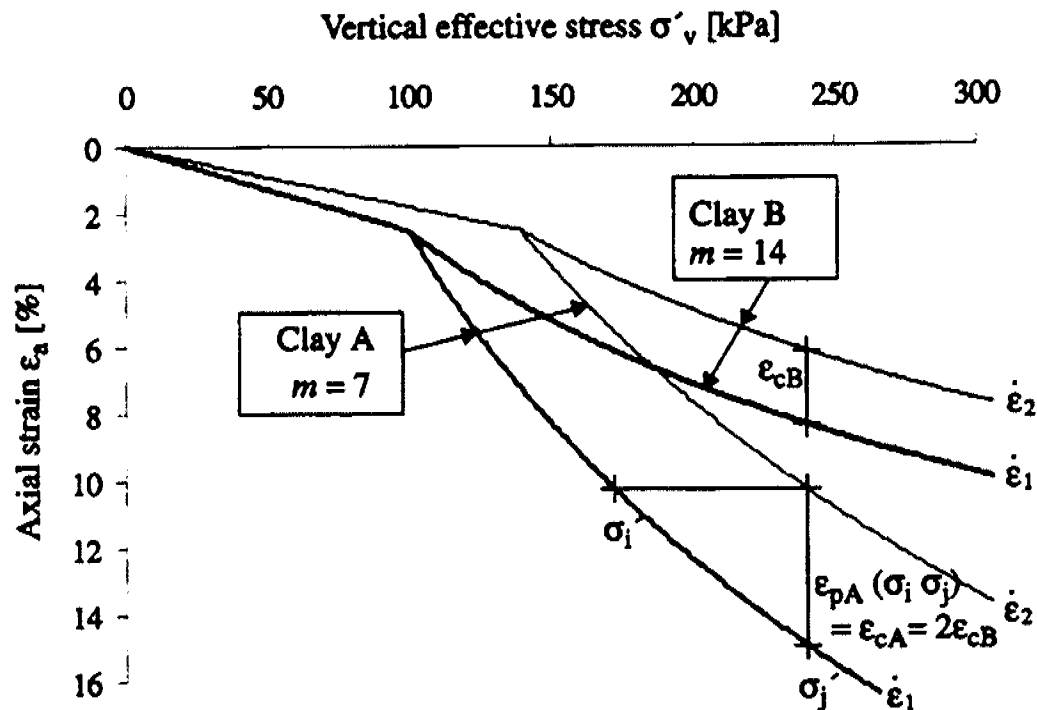


Figure 2-13: The dependence of the viscous strain of the primary deformation properties assuming that Equation 2-1 is valid (after Länsivaara, 1999) ($m = \text{modulus number} = 1/C_\psi$).

Another effect on the results of laboratory tests is sample disturbance. Sample disturbance results in a shrinkage of the yield surface and a reduction in mean effective stresses in the sample. Hight et al. (1992) concluded that there is a hierarchy of yield surfaces associated with different methods of extraction which cause different levels of destructuration. Furthermore sample disturbance changes the shape of the yield surface so that effects are more pronounced in triaxial compression than extension. Sample disturbance is more severe on some soils than in other, probably because the number and nature of inter-particle bonds vary for different soils (Länsivaara, 1999).

Clayton et al. (1992) tested high quality samples of Bothkennar clay to assess the reduction in strength and stiffness caused by sampling and laboratory reconsolidation procedures. The imposed undrained shear strain cycle due to extraction and reconsolidation causes an important loss in mean effective stress, and a loss of structure, even in very high quality samples. By means of appropriate reconsolidation procedures, the mean effective stress can be recovered, but stiffness cannot be fully recovered (Clayton et al., 1992). Furthermore, reconsolidation procedures risk taking the specimen beyond the in-situ yield surface, in which case significant destructuring will take place.

In addition to extraction and reconsolidation, preparation procedures can also cause sample disturbance. Atkinson et al. (1992) compared four different preparation methods for triaxial specimens of Bothkennar clay obtained using the Laval sampler. The results showed that the method of preparation had a significant influence on the strength and stiffness measured. Samples of Bothkennar clay prepared by wire saw trimming had the highest deviatoric stress and the highest stiffness at small strain, indicating that for this soil, wire saw trimming causes the least disturbance. Lacasse et al. (2002) illustrated clearly by comparison of triaxial test results on similar samples extracted with block and tube samplers, that a 54mm tube sample had a completely different behaviour to that of a block sample, the first was contractant and the second was dilatant. The change in volume during consolidation was 7 times higher in the tube sample than in the block sample, which showed a higher peak shear stress. Lacasse (1998) concluded that the more realistic determination of the yield stress will improve characterisation of the soil and that the higher peak strength and shear moduli determined from high quality samples will result in higher safety of engineering structures (because of reduced uncertainty of soil characteristics) and in reduced cost of the structure (because of higher resistance).

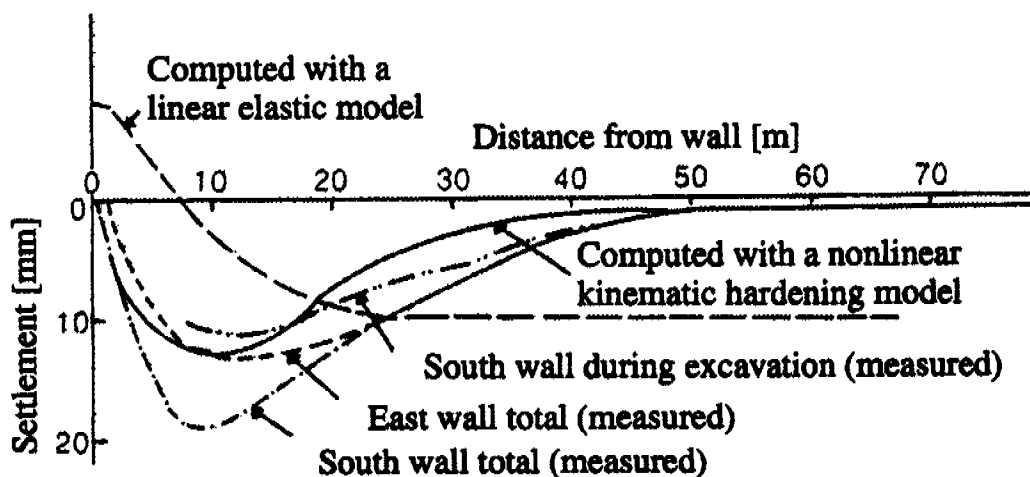


Figure 2-14: Measured and computed settlements near the excavation of the New Palace Yard car park (Simpson et al., 1979).

The onset of plastic strain development does not necessarily coincide with the gross yield surface identified by authors such as Graham et al (1993). The example of the New Palace Yard car park (Simpson et al., 1979) showed that the behaviour of soil is not elastic inside the yield surface and plastic irrecoverable strains occur from very small strains, leading to the conclusion that stiffness is not constant inside the yield surface, but decreases with increasing strain. The assumption of linear elasticity for the numerical modelling of the New Palace Yard car park led to a deformation pattern that was completely different from that experienced following excavation (Figure 2-14) and showed the importance of high stiffness at very small strain. Jardine et al. (1986) analysed the influence of non-linear stiffness on the soil-structure interaction on the basis of different boundary value problems. Figure 2-15 shows the variation of the apparent Young's modulus E_u , interpreted using linear elasticity from the results of the

numerical analysis, with load factor defined as the ratio of load to peak load. The comparison between the analyses reveals that the apparent elastic moduli is dependent upon boundary condition and load level.

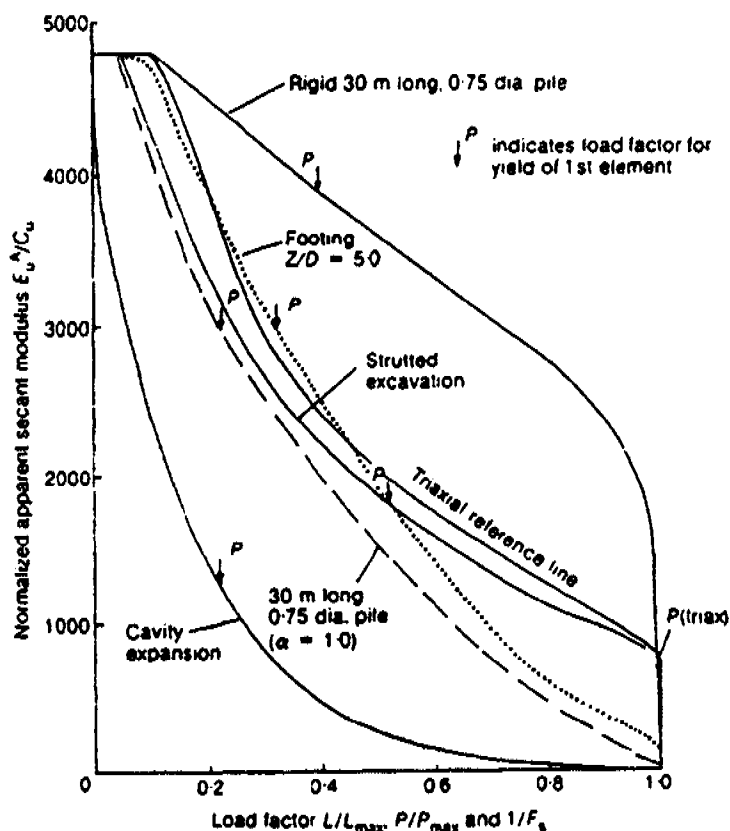


Figure 2-15: Normalized apparent secant modulus versus load factor for various boundary value problems, analysed with a non-linear model (Jardine et al., 1986)

Triaxial stress path tests on reconstituted samples of London clay were carried out by Richardson (1988) and Stallebrass (1990) to investigate the stress-strain behaviour of soil in the small strain range and for stress states inside the boundary surface (Figure 2-16). The state boundary surface represents a boundary to all possible states in q - p' - v space. All triaxial specimens were consolidated to point A, and then followed different stress paths to reach point O. In Figure 2-16 b the tangential stiffness of the final path OX is given. The highest stiffness was found for a full stress reversal DOX and the softer response for path BOX which continues in the same stress path direction passing through O. The results are shown also in Figure 2-17 (Atkinson et al. (1991)), where the stress path DOX corresponds to $\theta = 180^\circ$ and the stress path BOX to $\theta = 0^\circ$. The recent stress history is described in Figure 2-17 with the angle θ , which is the angle sustained by the stress path common to all specimens OX to reach the stress point for the shearing test and the recent stress path different for each tests (DO respectively BO). This results demonstrate that soil stiffness is markedly non-linear throughout the range of loading and that the strains are inelastic except for a very small interval of loading at the start of test (O in Figure 2-17). The soil yields at Y in Figure 2-17 and then the stiffness decreases rapidly. At some point H, the stiffness is then independent of the recent stress history. Thus the stress-strain response of an overconsolidated clay depends both on its current state and on the loading history followed to reach that state, in particular the relative directions of the current and previous loading paths.

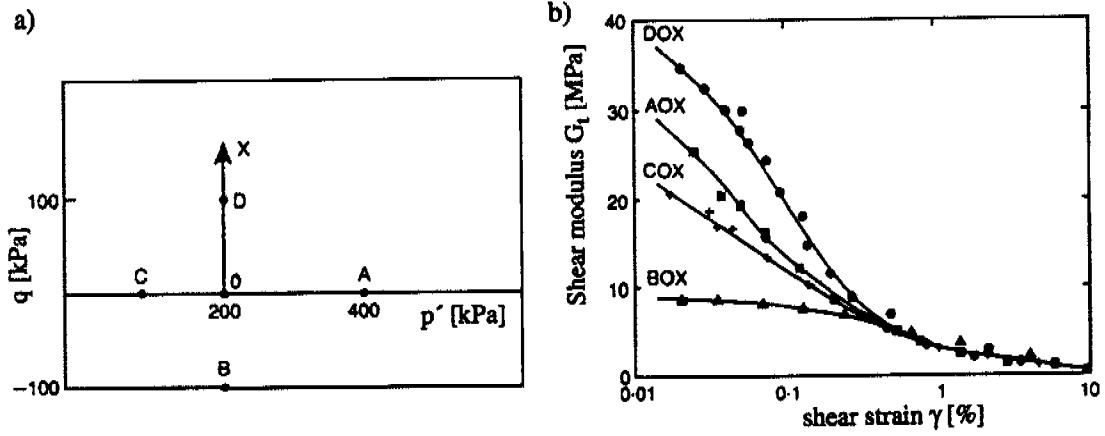


Figure 2-16: Results of triaxial stress path tests obtained by Richardson (1988) a) stress paths, b) tangential stiffness for path OX.

Janbu (1985) describes further an increase in shear modulus after undrained creep. In seven multi-stage tests, a monotonic undrained compression shear test was interrupted by a creep stage of 16 hours, after which the clay specimens were sheared to failure under undrained conditions. These tests showed that it is possible to recover stiffness in monotonic loading continuing in the same stress path direction, if the sample is allowed to creep for enough time (Janbu, 1985).

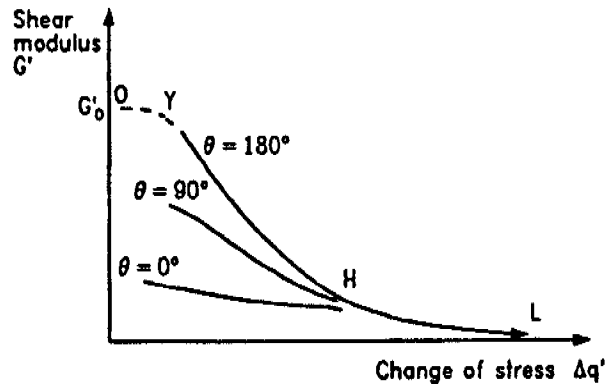


Figure 2-17: Typical variation of stiffness with stress change observed in laboratory tests (Atkinson and Stallebrass, 1991)

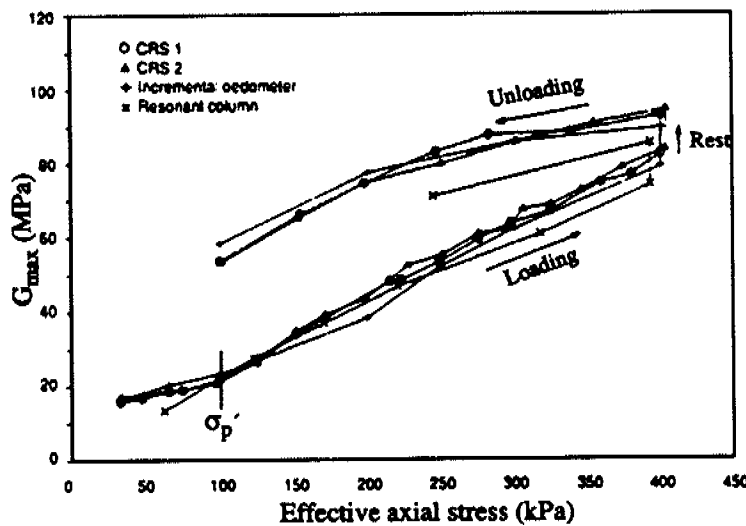


Figure 2-18: The effect of stress, preconsolidation pressure and time on the value of shear stiffness G_{max} (Drammen clay after Dyvik and Olsen (1989)).

In general the stiffness of soil increases with increasing mean effective stress. In Figure 2-18, the values of small strain shear modulus G_{max} from oedometer and resonant column tests on Drammen clay are shown (Dyvik and Olsen, 1989). The small strain stiffness increases almost linearly with stress for Drammen plastic clay in the normally consolidated range and increases also due to secondary effects when the effective axial stress is maintained constant before unloading. The influence of effective mean stress, void ratio and overconsolidation ratio can be related to their effects on the number of particle contact and on the stresses acting on these contact points. Hardin and Black (1978) suggested Equation 2-4, to be used for clays having void ratios e between 0.4 and 1.2:

$$G_{max} = \frac{A \cdot OCR^k}{F(e)} \cdot p_a^{1-n} \cdot p'^n \quad [2-4]$$

where $F(e) = 0.3 + 0.7e^2$, $A = 625$ (Hardin, 1978), p_a = the atmospheric pressure (100 kPa) and G_{max} in kPa. They reported values of k between 0 and 0.5 increasing with increasing plasticity index. n is a constant and $n \neq 1$ so that the equation contains a quantity that satisfies the dimensions of the equation (p_a^{1-n}). This equation is based on an empirical equation for the shear modulus of soils, given by Hardin and Black (1969), and determined from wave propagation velocities and from small amplitude cyclic simple shear test.

Houlsby and Wroth (1991) described a method for expressing the shear modulus of a clay as a power function of the applied pressure and of the yield stress. Since the undrained shear strength s_u is often expressed in a similar way, the rigidity index G/s_u can be expressed as a power function of the overconsolidation ratio (Equation 2-5):

$$\left(\frac{G}{s_u}\right) = \left(\frac{G}{s_u}\right)_{NC} \cdot OCR^{n-\Lambda} \quad [2-5]$$

where $\Lambda = \frac{\lambda - \kappa}{\lambda}$ and $0 \leq n \leq 1$. Houlsby and Wroth (1991) state that this approach can be used for definitions of G at different percentages of strain, although the absolute values of the moduli defined in alternative ways (G_{max} or G_{50}) will differ widely.

Larsson and Mulabdic (1991) related the maximum shear modulus to the plasticity properties (w_L in%) and the undrained shear strength (s_u in kPa) of soils. They suggested Equation 2-6 for low plasticity clays, where G_{max} is in kPa.

$$G_{max} = 504 \cdot s_u / w_L \quad [2-6]$$

Kagawa (1992) considered the main factors affecting the small strain behaviour of normally consolidated clays to be yield stress σ'_{vy} [kPa], current void ratio e [-] and plasticity index I_P [%] (Equation 2-7):

$$G_{max} = \frac{358 - 3.8 \cdot I_P}{0.4 + 0.7 \cdot e} \cdot \sigma'_{vy} \quad [\text{kPa}] \quad [2-7]$$

A change of stress dependency of the shear modulus of soft clays is expected when the yield stress is exceeded, because their void ratio decreases after yield with a faster rate than for stiff clays. For a structured clay, there should always be a change in behaviour when exceeding the yield stress. If this is not the case in laboratory tests, then the sample has possibly been disturbed (Lämsivaara, 1999).

The modulus reduction curve gives the reduction of the modulus with strain. A small range exists, bounded by an elastic threshold strain, in which the soil behaviour remains mainly elastic and reversible and the shear modulus G_{max} remains constant (Carubba and Maugeri, 1991). Atkinson and Sallfors (1991) and Burghignoli et al. (1991) give a value of $5 \cdot 10^{-5}$ for the threshold strain of clays, Lo Presti (1991) suggests a value of $1 \cdot 10^{-5}$ for sand, Tatsuoka and Kohata (1995) propose a value of $1 \cdot 10^{-5}$ for hard soils and soft rocks. The reduction curve can be described by a hyperbolic relationship after Kondner (1963). In terms of shear stress τ and shear strain γ this relationship is represented by Equation 2-8:

$$\tau = \frac{\gamma}{a + b \cdot \gamma} \quad \text{with } a \text{ and } b \text{ as constants.} \quad [2-8]$$

For the secant shear modulus, Equation 2-8 gives:

$$G_s = \frac{\Delta\tau}{\Delta\gamma} = \frac{1}{a + b \cdot \gamma} \quad [2-9]$$

And the tangential shear modulus is obtained by differentiating Equation 2-8:

$$G_t = \frac{d\tau}{d\gamma} = \frac{a}{(a + b \cdot \gamma)^2} \quad [2-10]$$

Both parameters a and b have a physical meaning: a is the inverse of G_{max} and $1/b$ is the maximum shear stress increase $\Delta\tau$ to failure along the loading path. Rearranging Equation 2-8, it can be seen that the hyperbola describes a straight line in a γ/τ - γ plot (Equation 2-11):

$$\frac{\gamma}{\tau} = a + b \cdot \gamma \quad [2-11]$$

Representing the hyperbola as in Figure 2-19, a is the intercept on the y axis and b is the slope of the line.

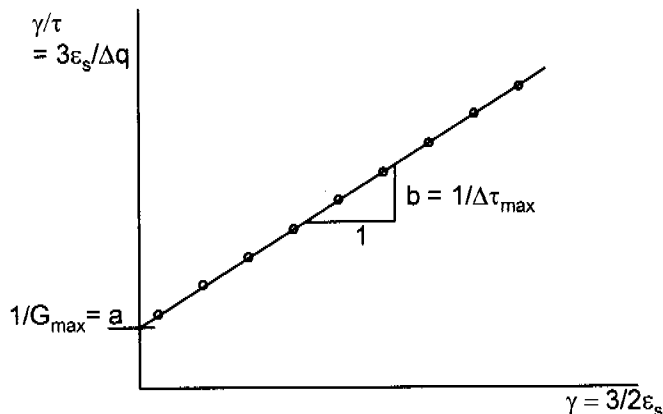


Figure 2-19: Determination of the parameter a and b from the Kondner hyperbolic stress-strain relationship.

Lacasse (1995) showed the effect of time to failure on the secant shear modulus G_{50} , where G_{50} is defined as the secant modulus by shear stress level of 50% of the shear strength. Lacasse observed that behavioural differences occur from the very start of the tests, with considerably higher shear modulus at shorter times to failure. This indicates that time influences the small strain domain as well as the response at large strains.

Stokoe et al. (1995) showed that the influence of frequency on G_{\max} is very small for clays, averaging 15% as frequency changes from 0.1 to 100 Hz. In contrast, the effect of frequency is important for the damping ratio at small strain D_{\min} , which increases about 100% over the frequency range 0.5 to 100 Hz.

2.3 Soil models

Muir Wood (1990) defines the assumptions that are needed to describe the soil behaviour within an analytical framework. These assumptions pertain to four aspects of the elastic-plastic response of soil:

- to the way in which deformations inside the yield surface are to be described: a description of the stiffness parameters and their change with strain is needed.
- to the boundary or boundaries in a general stress space that define a change in deformation mode.
- to the mode of plastic deformation that occurs when the soil is yielding: a plastic potential is needed to specify the relative magnitudes of the various components of plastic strain increment.
- to the way in which the absolute magnitude of the plastic deformation is linked with the changing size (and perhaps shape and inclination) of the yield locus: a hardening rule is needed describing the expansion of the yield locus (hardening of the soil).

Additionally, an assumption about the conditions under which failure occurs has to be made.

If the yield surfaces and the plastic potential surfaces for a soil are identical, then the material is said to obey the postulate of normality, because then the plastic strain increment vectors are in the direction of the outward normal, not only to the plastic potential but also to the yield surface (Muir Wood, 1990). The normality rule postulates that the plastic strain increment vectors should be normal to the yield surface irrespective of the stress increment vector at yield (Graham et al., 1983b). In Figure 2-20a, the plastic strain increment vectors for Winnipeg clay, reported by Graham et al. (1983a), are plotted at the appropriate yield points in the normalised stress plane $p'/\sigma'_{vc} - q/\sigma'_{vc}$ with local axes for the plastic strain increment vectors parallel to the stress axes. The plastic strain increment vectors show minor deviations from the normality postulate. Although the individual and the mean deviation from normality were small (ca. 1°), Graham et al. (1983) rejected the assumption of the normality rule, as the results showed evidence of systematic variation of the direction of the deviation. The deviation from normality was clockwise to the right of the critical state line CSL, whereas it was counter-clockwise to the left of the CSL. The results presented by Wong and Mitchell (1975), show likewise that the normality condition does not

apply for Champlain Sea clay (Figure 2-20b). Lämsivaara (1999) notes from the data by Wong and Mitchell (1975) that the deviation of the plastic strain increment vector from normality is always towards the direction of the stress increment vector and that this deviation is larger, the more the direction of the stress increment vector deviates from normality to the yield surface. Graham et al. (1983b) made no attempt to measure how the plastic strain increment vector changes with the direction of the stress increment vector at a single point of the yield surface. This was attempted by Newson (1995) and the results show that the direction of the plastic strain increment vectors is not unique for a yield point, but depends on the approach path to that yield point (Figure 2-21).

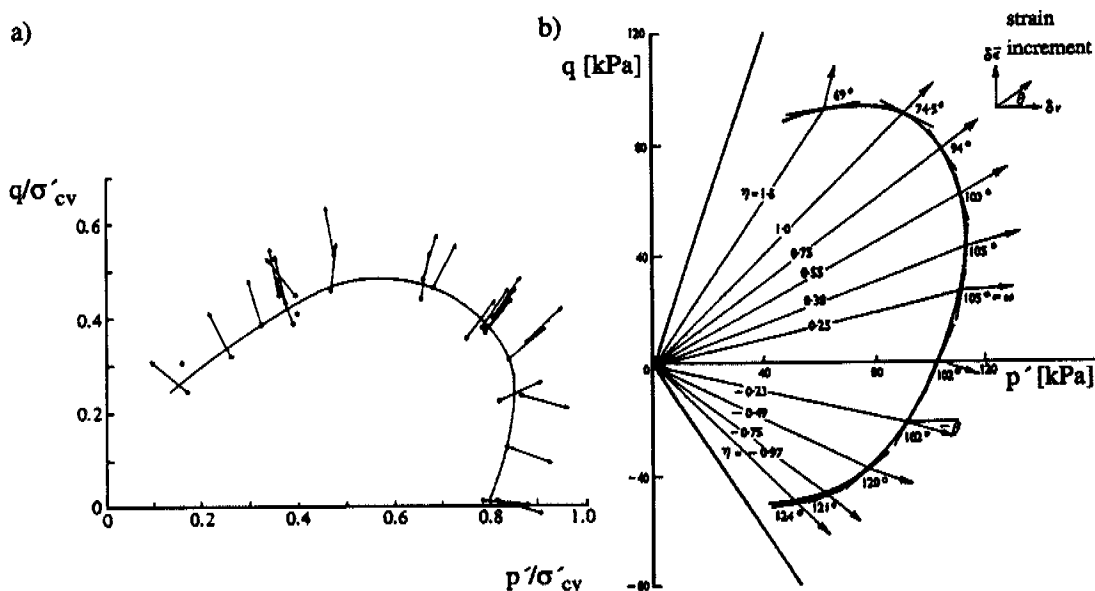


Figure 2-20: Yield data of a) Winnipeg clay by Graham et al. (1983b) and b) Champlain Sea clay by Wong and Mitchell (1975).

Leroueil et al. (1979) investigated the effect of destructuration on Saint Alban clay by consolidating the individual specimens to effective stresses in excess of their preconsolidation pressure. To produce different types of destructuration, the specimens were subjected to different stress ratios σ'_3/σ'_1 . Results showed that the upper part of the yield curves for the destructured specimens have the same shape as for the intact clay, whereas in the region near to the isotropic axes, the destructured clays yield at stresses in excess of those observed for the intact clay. The difference is greatest along the isotropic $p'=0$ axis and even larger for the specimens destructured with higher stress ratio σ'_3/σ'_1 . This indicated that the clay structure has become less anisotropic through destructuration and that for stress paths deviating more from the natural consolidation path, a larger re-orientation of the yield curve can be expected.

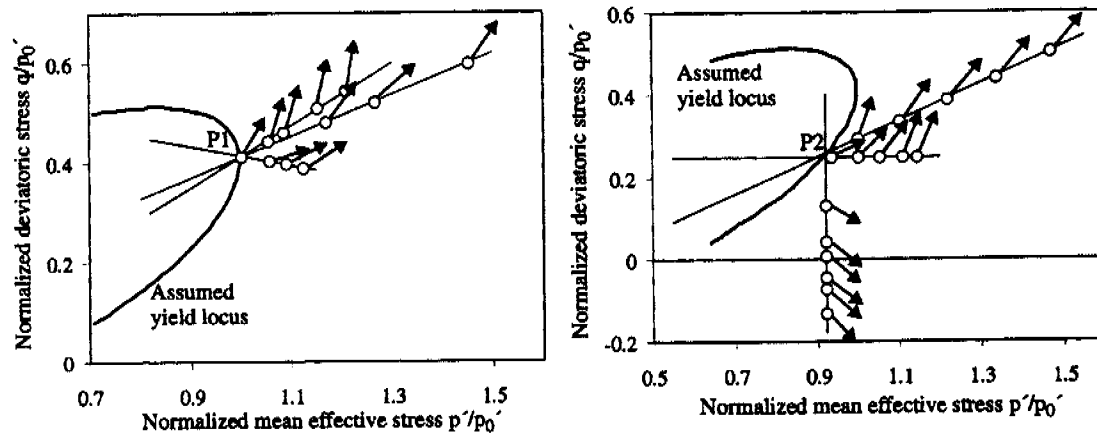


Figure 2-21: The non-uniqueness of plastic strain increment vectors for two yield points P1 and P2 (Newson, 1992).

In recent years therefore, many constitutive models have been proposed to take into account the effects of fabric anisotropy and structure. Anisotropy is a function of the fabric of the soil and leads to different strengths and stiffnesses, dependent upon the major principal stress direction and form of stress path. The anisotropic response of a soil is linked to the anisotropic stress history of one-dimensional consolidation in situ, which has left the soil particles with certain preferred orientation and results in inclined yield loci (Muir Wood, 1990), as confirmed by those shown in Figure 2-20 and Figure 2-21. Muir Wood reports data from Lewin (1973), which show that the initial anisotropy of a sample is virtually eliminated (but not completely) after an isotropic consolidation path to a mean effective stress five times the initial mean effective stress. The hardening of the soil (the expansion and rotation of the yield locus) follows preferentially the direction of the stress path, and previous anisotropy is changed if the soil is loaded far enough.

Anisotropic elasto-plastic soil models involve an inclined yield curve and a rotational hardening law. The inclination of the yield curve changes during plastic straining as the fabric anisotropy develops or is erased. Thus the rotational hardening law relates the change in inclination of the yield surface to plastic strain increments and current stress state (Wheeler et al., 2003b). Many of the models relate the plastic strain-induced change in anisotropy entirely to plastic volumetric strain (for instance Banerjee and Yousif (1986), Dafalias (1987), Davies and Newson (1993), Whittle and Kavvas (1994)). However, both plastic shear strains and plastic volumetric strains contribute to the evolution of anisotropy as they change the arrangement of particles and particles contacts. The anisotropic elasto-plastic model with rotational hardening (SCLAY1) was developed with the aim of capturing the main features of the yielding behaviour of soft clays, including explicit dependence of the yield surface inclination on both plastic volumetric and plastic shear strains, whilst remaining sufficiently simple (Wheeler et al., 2003a, Wheeler, 1997, Näätänen et al., 1999, Wheeler et al., 2003b and Wiltafsky (2003)).

S-CLAY1 is an extension of the critical state models, with anisotropy of plastic behaviour represented through an inclined ellipsoidal yield surface and a rotational component of hardening to model the development or erasure of fabric

anisotropy during plastic straining. The S-CLAY1 model assumes isotropic elastic behaviour and an associated flow rule. In triaxial q - p' stress space, the yield curve has the form of a sheared ellipse and is defined in stress space by the parameters M , the value of the stress ratio $\eta=q/p'$ at critical state, p'_m , the current size of the yield curve and α , the current orientation of the yield curve (Figure 2-22). The scalar parameter α is a measure of the plastic anisotropy of the soil. With $\alpha=0$, the soil behaviour is isotropic and the yield curve corresponds to the Modified Cam Clay yield curve.

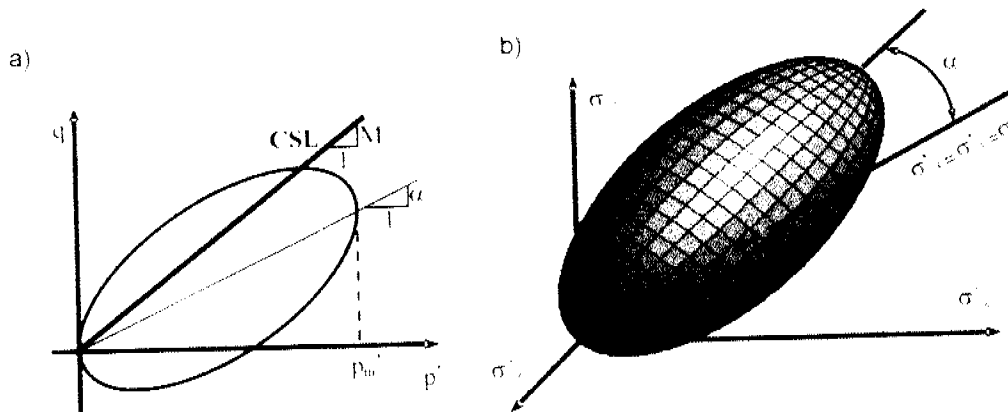


Figure 2-22: S-Clay1 yield surface a) in triaxial stress space and b) in 3D stress space (Wheeler et al., 2003a).

S-CLAY1 is based on two hardening laws, one describing the change in size of the yield surface with increments of plastic volumetric strain, the other describing the change in orientation of the yield surface with both plastic shear strain and plastic volumetric strain (in common with the model of Pestana and Whittle (1999)). Compared to Modified Cam Clay, two additional parameters relating to the rotational hardening law (β , μ) are needed and the state of the soil is defined by the initial values of size (p'_m) and of inclination (α) of the in situ yield surface. Näätänen et al. (1999) and Wheeler et al. (2003b) presented procedures for the determination of the values of the soil constants μ and β . Wheeler et al. (2003 a and b) give a detailed description of the constitutive equations and recommendations for determining parameters. The suitability of the S-CLAY1 model has been demonstrated with simulations of tests on reconstituted samples of POKO clay (Koskinen et al., 2002b) and of three other Finnish clays (Otaniemi, Murro and Vanttila, not yet published, from Wheeler et al., 2003a). Each simulated triaxial test involved two loading stages at two different values of stress ratio η , covering a wide range of η values. However simulations of tests on natural samples of Finnish clays were less successful, because it was difficult to match to plastic volumetric strain in all test stages (Wheeler et al., 2003a). This was attributed to the influence of destructuration, which progresses at different rates in test stages performed at different stress ratios η (Wheeler et al., 2003a, 2003b and 1999).

Gens and Nova (1993) presented a general framework for incorporating bonding and destructuration within elasto-plastic constitutive models. They introduced an intrinsic yield surface to represent the size of the yield surface for the unbonded state. The bonding effect is measured through the difference in size

between the yield surface and the intrinsic yield surface. Various other models have followed which differ in the precise form of destructuration law applied and in the form of the reference model used for the unbonded material.

The model S-CLAY1S is a further development of S-CLAY1, incorporating the effects of bonding and destructuration. An intrinsic yield surface is added in S-CLAY1S, which represents the unbonded soil, at the same void ratio and with equivalent fabric. The intrinsic yield surface has the same shape and orientation as the natural yield surface, but is smaller in size (Figure 2-23) (Wheeler et al., 2003a). A parameter x defines the current state of bonding and relates the size of the intrinsic yield surface to the size of the natural yield surface. S-CLAY1S incorporates three hardening laws: the rotational hardening law of S-CLAY1, a hardening law, which relates the change in size of the intrinsic yield surface to plastic volumetric strains, and a destructuration law, which describes the degradation of bonding during plastic straining. As for the rotational hardening law, the destructuration law incorporates explicit dependence on both plastic shear and plastic volumetric strains. Koskinen et al. (2002a), Zentar et al. (2002) and Wheeler et al. (2003a) offer more detailed descriptions of constitutive equations and determination of parameters.

The suitability of S-CLAY1 has been tested for Finnish clays (plasticity index I_p in the range of 37 to 82% and sensitivity S_t between 7 and 94) and an extensive series of multi-phase triaxial stress path tests have been simulated (Näätänen and Lojander 2000). The suitability of S-CLAY1 for a less sensitive, siltier clay such as Seebodenlehm ($I_p = 20\%$, $S_t = 4$) is of great interest. Messerklinger et al. (2003) compared therefore the mineralogical and mechanical properties of Finnish and Swiss post-glacial lacustrine clays to establish a basis for investigations into whether these models can also be adopted for normally consolidated Swiss lacustrine clays. Some of the effects of the different mineralogical compositions resulting from various deposition environments will be indirectly considered by the mechanically based determination of the soil parameters of the models.

For states inside the state boundary surface, the assumption of isotropic elasticity is not satisfactory, especially for some stress paths involving significant unloading (e.g. excavations), although for normally consolidated clays even small increases of stresses are likely to cause yielding and predominantly plastic straining. No attempt has been made to incorporate elastic anisotropy or to model non-linearity of pre-yield stiffness into the soil model S-CLAY1, and this is justified "by the fact that, for many practical problems involving soft clays, the primary requirement for accurate numerical analysis is likely to be successful modelling of the onset of large plastic strains and the subsequent pattern of plastic

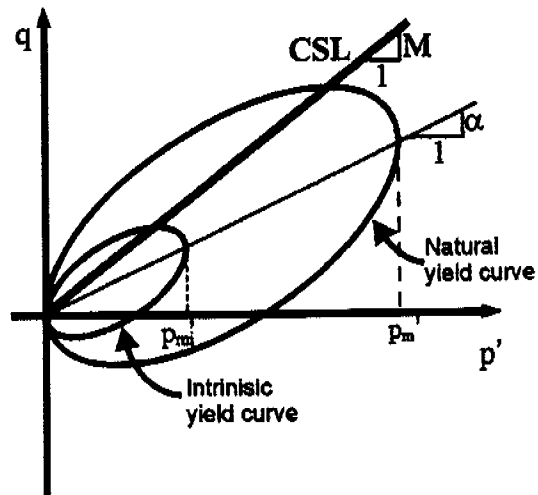


Figure 2-23: S-Clay1S yield surfaces in triaxial stress spaces (Wheeler et al., 2003 a).

straining" (cited from Wheeler et al., 2003b). This is certainly true for many boundary value problems for which most soil elements undergo loading, whether this is in compression, isotropically or in extension. However, for boundary value problems involving unloading, such as for excavations, this aspect become more important.

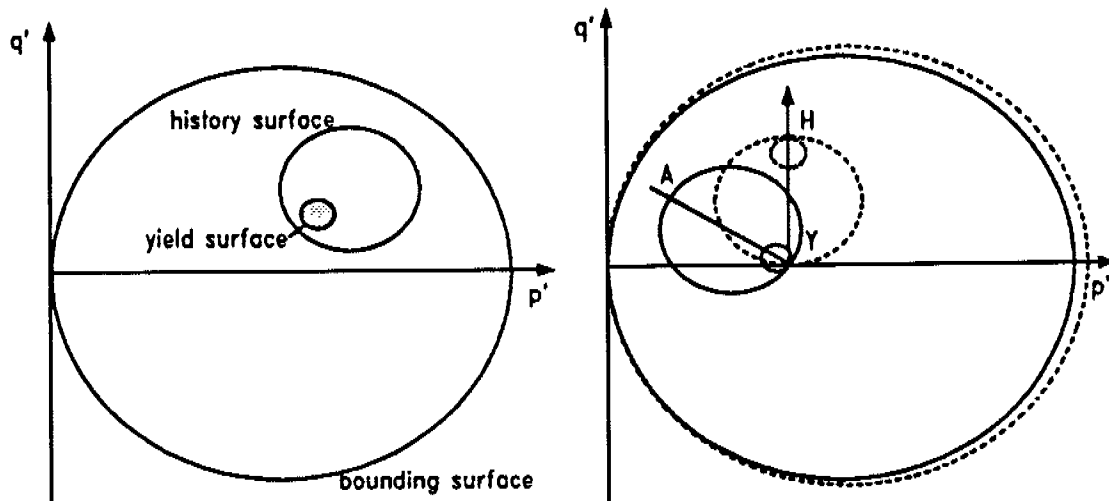


Figure 2-24: a) Basic features of the 3-SKH model, b) Kinematics of the yield and history surfaces following a rotation of the stress path (Atkinson and Stallebrass, 1991).

For overconsolidated clays, many authors have developed variable modulus models to incorporate non-linear stiffness in finite element analyses (Mröz et al, 1979, Simpson et al, 1979 and Simpson, 1992, Jardine et al., 1986, among others). Incorporating kinematic yield surfaces within a conventional state boundary surface is a straightforward method of representing the memory of recent loading history. Al Tabbaa (1987) recognized the benefit of kinematic yield surfaces and developed a "bubble" model using a single surface within the Modified Cam Clay state boundary surface. The three-surface kinematic hardening model 3-SKH is an extension of this model and was formulated to simulate the behaviour of clays in overconsolidated stress states and during early stages of loading (Stallebrass, 1990, Atkinson et al., 1990, Atkinson and Stallebrass, 1991, Stallebrass and Taylor, 1997). The stress-strain response of overconsolidated soils is initially dependent on the recent stress history, and this effect gradually decreases as loading continues. The two kinematic surfaces inside the bounding surface are required to describe the yield point Y (Figure 2-17) and the end of the memory of recent stress history at H (Figure 2-17). The 3-SKH model makes use of the framework of Critical State Soil Mechanics, and the boundary surface and the two kinematic surfaces within it, show the shape of the Modified Cam Clay boundary surface (Figure 2-24a). This implies that the soil behaviour described by this model is mostly isotropic, although there is limited anisotropy if the centre of the two kinematic surfaces have been shifted off the p' axis by the previous stress history. The kinematic surfaces can translate inside the boundary surface as they are dragged around by the current stress path (Figure 2-24b) (Atkinson and Stallebrass, 1991). The 3SKH model assumes associated flow on all surfaces and a hardening law, which extends the standard Modified Cam Clay hardening rule linking the expansion or contraction of all three surfaces to

changes in volumetric strain (Stallebrass and Taylor, 1997). The model requires three additional parameters to Modified Cam Clay: T and S link the size of the three surfaces and Ψ is the exponent in the hardening modulus. T and S can be inferred from multi-stage triaxial tests with different stress histories, whereas Ψ is the only parameter which has to be defined through parametric studies.

2.4 Summary from the literature review

A range of literature has been presented in this chapter and this deals with the geological deposition, composition and mechanical behaviour of soft lacustrine clays. A short description of the recent work on constitutive modelling, developed to describe the behaviour of soft soils, has been given in Section 2.3.

The Swiss lacustrine clays studied by Rey (1976), Gyger et al. (1994) and Scherzinger (1991) were extracted from a wide area of the Swiss Mittelland ranging from Zürich to the Constance in the North-East and show similar ranges of their state, index properties and grain size distribution. Compared to other natural lacustrine clays, the Swiss Seebodenlehm shows low natural water content (30 - 40%) and relatively low plasticity index (15 to 30%), when compared with the clay particle content (30 - 60%), which lies instead in a more typical range.

The sedimentological process during the formation of the varved clays determines the type of varving in the clay deposits: distal facies in post glacial lakes show a fine silt clay layering, with a clear anisotropy of mechanical and permeability characteristics. Chaotic layering of the laminae is characteristic of the deposition on the side boundaries of the sedimentation area. This is very important as the natural structure of a soil strongly influences its response to loading: for instance the yield stress for a structured soil can be higher than expected and lie above the virgin compression line. The structure of a soil consists of the fabric of the soil particles (spatial arrangement and contact points) and in the bonding at the contact points between particles. The fabric of the soil due to deposition can thus be anisotropic and influence the soil behaviour under load.

The determination of soil parameters by laboratory testing encounters a significant challenge as sample disturbance will always affect the results to some degree. In addition to extraction and reconsolidation procedures, preparation of the sample prior to testing can also affect the soil's structure. Sample disturbance results mainly in a shrinkage of the yield surface and in a reduction of mean effective stresses in the sample. Long (2003) however showed that sample disturbance caused both the small strain stiffness and the undrained shear strength to increase. Furthermore, varved clays show the tendency for considerable changes in the distribution of the water content between clay and silt layers and this can cause disturbance as well.

The main factors affecting the behaviour of soft clays are, besides the structure, time (load duration), loading rate, degree of overconsolidation and stress path history of the soil. In general, the faster the loading rate, the higher are the effective stresses for a given strain, therefore laboratory tests results are strain rate dependent. Leroueil et al. (1983 and 1985) and Lämsivaara (1995b) showed that a unique stress-strain-strain rate relationship exists for the natural clays investigated by the authors. This enables the results from different laboratory and in situ tests to be compared.

During creep, the void ratio of the soil decreases under constant stress and the soil will show a higher yield stress than the actual in situ overburden pressure. It has been shown that creep properties are directly related to the primary deformation properties of a soil. The influence of the drainage length on the compressibility of a clay involves both effects of creep and strain rate, as for a soil element at a short distance from the drainage boundary, the effective stress will increase faster during loading and act longer than for an element in the middle of the sample.

The recent stress history has a great influence on the soil's behaviour during loading as the stress-strain response of an overconsolidated clay depends both on its current state and on the loading history followed to reach that state, in particular the relative directions of the current and previous loading paths. It was demonstrated by several authors that soil stiffness is markedly non-linear throughout the range of loading and that the strains are elasto-plastic except for a very small interval of loading at the start of test. Until now, the non-linearity of stiffness has been investigated mainly on sands and on highly overconsolidated clays. It is interesting now to determine the small strain stiffness of soft varved lacustrine clays by means of laboratory and in situ tests.

The anisotropic stress history of one-dimensional consolidation of most soils, including lacustrine clays, results in an inclined yield surface in stress space. Tri-axial tests have shown that an anisotropic stress path changes the inclination of the yield curve, if the loading along this stress path is carried out far enough over the previous yield stress. The assumption of an associated flow rule simplifies the model necessary to describe the soil's behaviour, but it has been shown that this assumption is not always supported by test results. In effect, it has been shown that the direction of the plastic strain increment vectors is not unique for a yield point but depends on the stress path followed to approach this point.

Many constitutive models have been developed in recent years to consider anisotropy and rotational hardening of the yield surface of soils. The model SCLAY1 has been described in more detail in Section 2.3, as it is supported by a comprehensive set of experimental data on varved soft clays and it has the advantage to remain relatively simple. This is a pre-requisite for a model to be used with success in design. The suitability of S-CLAY1 has been tested for Finnish clays and is now of great interest for a less sensitive, siltier clay such as Seebodenlehm.

Seite Leer /
Blank leaf

Testing Material: Seebodenlehm

3.1 Site description

The locations of Kreuzlingen and Birmensdorf are shown on the map of Switzerland in Figure 3-1. Both sites lie in the highly populated Mittelland, the flat region that is located between the Jura mountains to the north and the Alps to the south. The Mittelland occupies 30% of the surface area of Switzerland and hosts the major population centres and transportation arteries. At both sites, new link roads have been constructed in the late 90's to extend or complete motorway junctions.

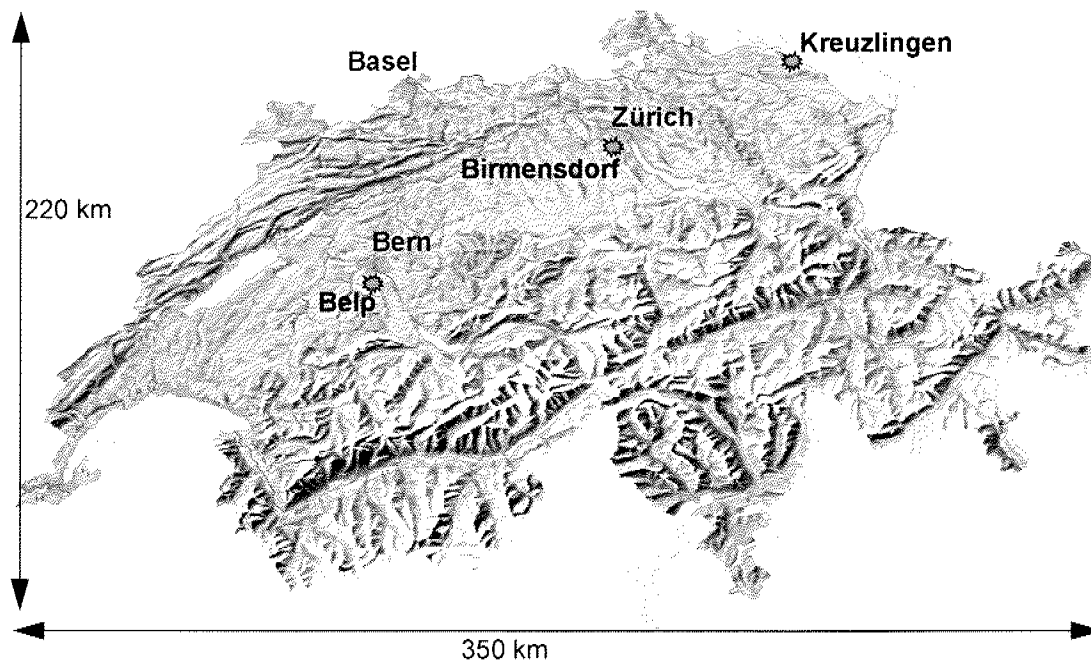


Figure 3-1: Location of the test sites in Switzerland.

3.1.1 Kreuzlingen

In Kreuzlingen, a project has extended the N7 motorway by 4km to join the German transportation network across the North-West end of Lake Constance, and included the construction of local link roads that cross the existing railway lines in Kreuzlingen. This had to be achieved without disturbing the daily national and international train service. The construction of a skewed underpass at Konstanzerstrasse began in 1998 and ended in 2000. In the early stages of construction, the Institute of Geotechnical Engineering had the possibility to perform in situ tests and to drill a borehole to study the layering and to extract undisturbed samples of Seebodenlehm (Giudici and Springman, 1998 a and b). A sketch of the site is given in Figure 3-2.

The total length of the link road is 211m, with ramps sloping down over 140m to a depth of 8.5m under the railway lines. The central tunnel section was built in a 37m long closed box, using top down construction to minimise disturbance to the train service. The approach sections (up to 70m on either side of the closed box) required a single prop between the parallel walls, whereas two props were installed in the central deeper section. Equivalent vertical static railway loads of 50kPa and road loads of 15kPa had to be designed for.

To restrict wall deformation, steel sheet piles were not used when the excavation was deeper than 6m, instead the walls were formed using 1m diameter reinforced secant piles, keyed into the underlying moraine. The topsoil was excavated either to place props or to allow the top slab to be constructed to act as the top prop. The remaining material was removed underneath in short sections, so that the base slab could be concreted as quickly as possible, and to allow access over the weak clay to the next section to be excavated (A. Keller AG, 1997).

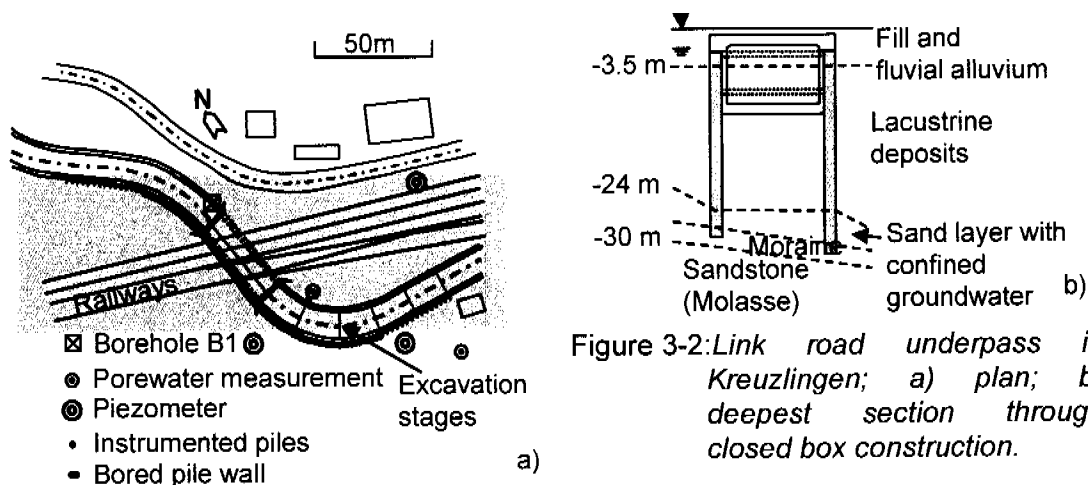


Figure 3-2: Link road underpass in Kreuzlingen; a) plan; b) deepest section through closed box construction.

A short term undrained shear strength of $s_u = 20\text{kPa}$ had been assumed for the design, while for the determination of the long term effective shear strength, values of $\phi' = 22^\circ$ for the effective friction angle and of $c' = 4\text{kPa}$ for the cohesion had been selected.

The ground water level was found at between 0.1 to 2.4m below ground level, with artesian pressures of up to 0.6m above ground level in the underlying silts, sands and moraine (depth >24 m). To prevent hydraulic uplift from occurring in the excavated area, dewatering was carried out in the lower layers of the higher permeability materials, to reduce the groundwater head by between 11 and 20m (Büchi + Müller, 1996).

Undisturbed samples were taken in February 1998 from a borehole drilled at the site (B1 in Figure 3-2). Samples from this site are labelled as Kreuz1. The samples were extracted using triple cored drill technique with thin walled sampling tubes. The tubes have an internal diameter of 66 mm and a length of 860 mm. The cutting edge of the tubes is designed with a reduction in inner diameter to 65 mm to minimise soil disturbance.

In March 2000, another road underpass under the railway line was constructed 1 km NW from Konstanzerstrasse. Undisturbed samples were also extracted from a freshly excavated area at 6.4 m depth using the same type of thin walled sampling tubes as in the borehole, but of shorter lengths (400 mm). In this case, the tubes were pushed carefully into the soil by hand. In the following work, samples from this site will be denoted as Kreuz2.

3.1.2 Reconstituted Kreuzlingen clay

A parallel testing programme was carried out on reconstituted samples of Kreuzlingen clay. To erase the structure and stress history of the clay, the natural soil was reconstituted at a liquidity index I_L of 3.0. The calculations for the consolidation of the slurry to obtain a final height of 200 mm under a total pressure of 60 kPa were based on average values of soil parameters obtained from previous oedometer testing of the natural samples. The final pressure of 60 kPa was chosen in order to have similar vertical effective stress conditions in the sample as those at a depth of 6.4 m.

The slurry was prepared from 32 kg of Kreuzlingen clay with an average natural water content w of 35% with the addition of 6.5 kg ground dry material. 21.5 litres of water were added to the mixture to obtain the calculated liquidity. This mixture was left for 3 days in a closed container and mixed so that the material was fully saturated with water. Subsequently, the slurry was mixed again under vacuum for 3 days, and then poured into a metallic cylinder of 400 mm diameter, with an initial height of 330 mm and initial water content w of 75%. The consolidation took place one dimensionally under a mechanical loading frame. The drainage at the top and bottom of the sample was guaranteed by sandwiching a geotextile filter between a filter paper and 10 mm of quartz sand. The press was instrumented with a load cell and a displacement transducer for surface settlement. Three transducers for pore water pressure measurement were inserted into the sample at different heights. The final total pressure of 60 kPa was reached in 5 incremental loading steps (2.8, 10, 20, 40 and 60 kPa). Each increment was left until dissipation of excess pore water pressures was almost completed (ca. 95%), i.e. 6.9, 6.0, 6.2, 15.0 and 14.7 days respectively per increment. After consolidation, the sample was extracted from the cylinder. 8

sample cores and 7 block samples were taken for testing in triaxial and oedometer tests. The sample cores were waxed and stored. The block samples were set in plastic bags under a light vacuum and stored.

Great care was taken to establish the distribution of water content, particle size and mineralogical content (Plötze, personal communication 2001) as a function of the height and position of the sample in the cylinder. Results showed that the reconstituted material (in the following work labelled as rec), was very homogeneous and had equivalent index properties to the natural Kreuzlingen clay (Chapter 3.4.2). The composition and grain size distribution were slightly changed through the reconstitution with water (Chapter 3.4.1), but the effect on the results of the mechanical tests was thought to be minor. As expected, the reconstituted clay showed a lower undrained shear strength $s_u = 10$ kPa (from fall cone tests) and lower sensitivity $S_t = 2.1$. These values are respectively 1/3 and 1/2 the values of the natural material and indicate the presence of a young clay with no structure. In the following sections, the representative index, state and composition values for the reconstituted clay will be shown with the natural clay values in the corresponding tables.

3.1.3 Birmensdorf

The intersection of three national highways on the plain between Wettswil and Bonstetten has been planned for more than 25 years before construction. This intersection connects the highway A4 from Lucerne to the by pass around Zurich, to the north-west through the Aeschertunnel and to the south-west through the Uetlibergtunnel, and represents one of the last parts of the circular highway bypass of the economic capital of Switzerland.

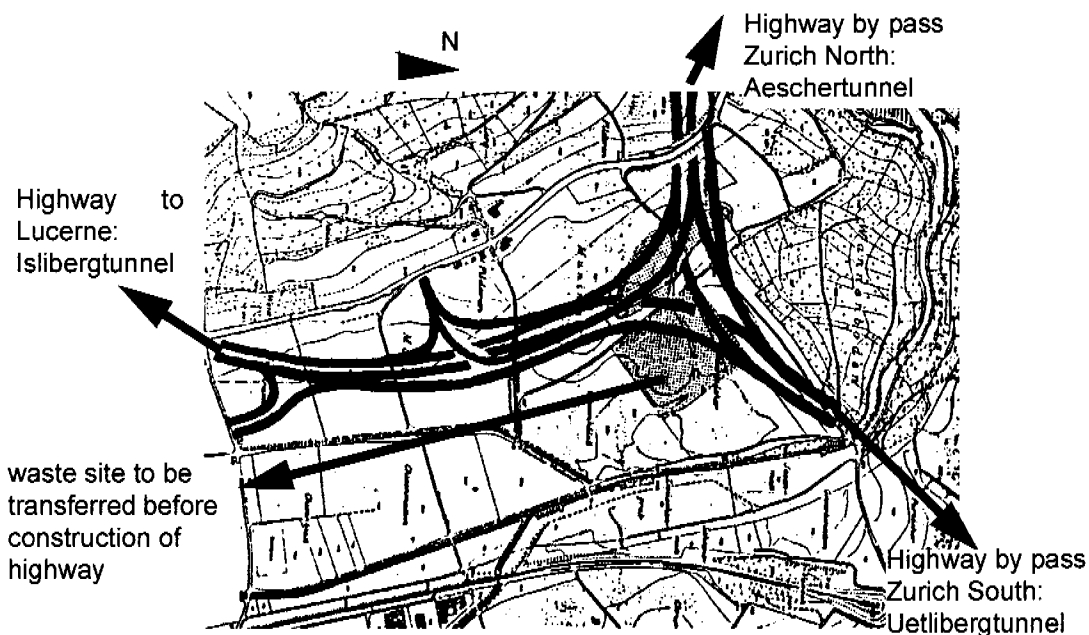


Figure 3-3: Layout plan of the highway intersections in Birmensdorf.

The highway "triangle" has been projected to run on the glacio-lacustrine plain created by the retreat of the Reuss glacier during the last ice-age. The site is characterised by Seebodenlehm deposits up to 45 m depth in the middle, which fade out towards the sides of the valley, and which is limited to the north-west by the end moraine deposited during the last ice-age. The highway intersection was planned with embankments and trenches, respectively up to 15 m high and 5m in depth.

The bearing capacity of the soft clay deposit and the development of total and differential settlements formed the central design problems that had to be dealt with. To define the geotechnical characteristics of the deposits, many boreholes were drilled, in situ vane tests were carried out, and laboratory characterisation tests were performed. A field test was carried out between December 1994 to March 1996 on three trial embankments, with and without sand drains. The embankments were instrumented to measure settlement, lateral displacement and pore water pressures during and after construction. Back calculation of these measurements gave values for the one dimensional stiffness modulus M_E and for the vertical and horizontal permeability k of the deposits. The results showed that the sand drains had virtually no effect on the rate of settlement. This was explained by the formation of a sealing layer of clay around the drains (a smear zone) during their installation in the soft deposit (Geotechnisches Institut, 1996). Preloading of the soft deposits was designed to limit the settlement of the final embankments. Construction began in 1996 with the preloading embankments and is still underway.

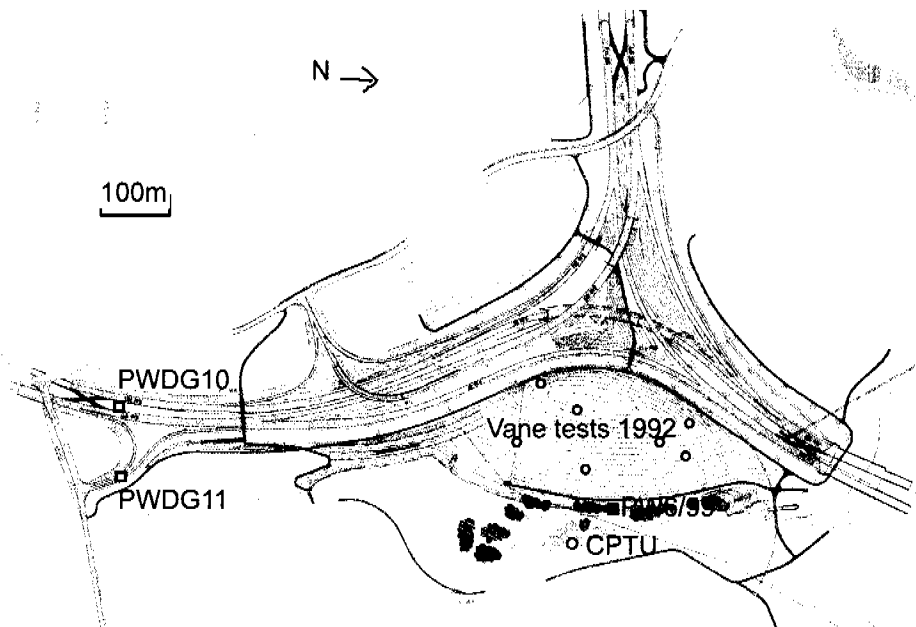


Figure 3-4: Sketch of the highway intersection with position of the boreholes and piezocone test site CPTU.

As in Kreuzlingen, two separate groundwater levels characterise the hydrogeological situation in this zone. The upper groundwater level is found at 0.5 to 1.5 m below ground level and is directly dependent upon the seasonal precipitation. The Seebodenlehm layer acts as a seal between the upper and the lower groundwater, which circulates in the underlying moraine. The lower groundwater

is supplied by seepage water from the surface moraine to the west and to the south of the valley, and therefore reacts slower to variations in precipitation than the surface groundwater. The lower groundwater can also show small artesian pressures, depending upon the thickness of the overlying Seebodenlehm layer (Geotechnisches Institut, 1994).

Undisturbed samples were taken from two boreholes (PWDG10 and PWDG11) in July 1998 (Figure 3-4), with thin walled sampling tubes and triple cored drilling techniques similar to those used in Kreuzlingen. In October 1999, another borehole (PW6/99) was drilled in the zone, where movements along a shear failure had been observed. The core of this borehole was taken to obtain disturbed samples of Birmensdorf clay (Fleischer, 2000), whereas two more undisturbed samples were taken at the assumed depth of shear failure. Samples from borehole PWDG 10 will be labelled Birm1, from borehole PWDG 11 Birm2 and from PW6/99 Birm3.

3.2 Stratigraphy

| Depth [m] | Log | USCS | Soil Description |
|-----------|-----|------|----------------------------------|
| 0.5 | | OL | top soil |
| 2.0 | | CL | medium clay, beige |
| 2.4 | | CL | medium clay, beige |
| 3.5 | | SM | medium clay, gray |
| | | | silty sand with stones |
| | | | lean clay / medium clay, gray |
| 15.2 | | SM | silt / fine sand |
| 22.0 | | CL | lean clay / medium clay |
| 24.2 | | CL | fine sand with gravel |
| 25.0 | | SW | fine sand |
| 26.0 | | SW | silt with stones |
| 27.5 | | ML | Moraine: clayey sand with gravel |
| 29.3 | | SC | Sandstone, soft |
| 31.0 | | | |

Figure 3-5: Borehole log at B1 in Kreuzlingen.

The soil profiles determined from the borehole cores are shown in Figure 3-5 for Kreuzlingen B1 and in Figure 3-6 for Birmensdorf PWGD10, PWGD11 and PW6/99.

The Seebodenlehm deposit begins in Kreuzlingen at a depth of 3.5 m below the ground surface and has a thickness of 11.7 m at this point. Interestingly, Seebodenlehm is found again at 22.0 m depth after a fine silt, sand layer of ca. 7 m thickness. Moraine underlies the second clayey silty deposit at a depth of 27.5 m, after some layers of fine sand and gravel, and the sandstone rockbed is encountered at ca. 30 m under the ground surface.

When comparing the three borehole profiles at Birmensdorf, the different elevations of the ground surface at the different drilling points must be kept in mind. The surface ground elevation at PWDG10 is 530.15 masL, at PWGD11 it is 527.65 masL and at PW6/99 it is ca. 527.0 masL. The Seebodenlehm layer begins in Birmensdorf between 3 and 5 m below the ground surface and has very different thickness depending on the position in the valley. The greater depth is reached towards the middle of the valley, and in fact PWGD11 shows thicknesses of >35 m. At PW6/99, the drilling was stopped at 15 m depth, because the aim of the drilling was here to detect a possible shear zone in the soft clay originated by too fast loading at the surface. In PWGD 10, the underlying moraine begins to interleave with the Seebodenlehm already at 20 m depth and is detected definitively at 27.0 m depth. In PWGD11, a silty fine sand has been found at 36 m depth, after the lacustrine clay deposits. The drilling did not reach the moraine and ended at 46 m depth below ground surface.

3 Testing Material: Seebodenlehm

| Depth [m] | Log | USCS | Soil Description | Depth [m] | Log | Depth [m] | Log | USCS | Soil Description |
|-----------|--|-------|--|-----------|--|-----------|--|--------|-----------------------------------|
| 0.5 | [Symbol: top soil] | GC-GO | top soil, | 1.0 | [Symbol: top soil] | 0.7 | [Symbol: top soil] | GC-GO | top soil |
| 0.8 | | GO | gravel | | | | | SM | silty sand with gravel |
| 2.0 | [Symbol: sand with fine gravel] | SP | sand with fine gravel | 1.8 | [Symbol: sand with fine gravel] | 2.2 | [Symbol: sand with fine gravel] | SM-SO | silty fine sand with organic mat. |
| 2.4 | | | | 2.3 | | | | | |
| 3.2 | | | | 2.5 | | | | | |
| 3.6 | | | | 3.6 | | | | | |
| 4.4 | [Symbol: clayey silt with fine sand layers, stiff] | ML | clayey silt with fine sand layers, stiff | 4.0 | [Symbol: clayey silt with fine sand layers, stiff] | 3.5 | [Symbol: clayey silt with fine sand layers, stiff] | CL | medium clay, gray |
| 5.2 | | | | 5.0 | | | | | |
| | [Symbol: medium clay gray, varved] | CL | medium clay gray, varved | | [Symbol: medium clay gray, varved] | 15.0 | [Symbol: medium clay gray, varved] | PW6/99 | |
| 17.2 | | | | | | | | | |
| | | | | | | | | | |
| | | | | | | | | | |
| | | | | | | | | | |
| | | | | | | | | | |
| | | | | | | | | | |
| | | | | | | | | | |
| | | | | | | | | | |
| | | | | | | | | | |
| | | | | 19.0 | | | | | |
| 20.4 | [Symbol: medium clay gray, varved, sporadic with gravel] | | medium clay gray, varved, sporadic with gravel | | [Symbol: medium clay gray, varved, sporadic with gravel] | | [Symbol: medium clay gray, varved, sporadic with gravel] | | |
| 21.1 | | | | | | | | | |
| | | | | | | | | | |

Figure 3-6: Borehole logs PWGD10, PWGD11 and PW6/99 at Birmensdorf (after Geotechnisches Institut, 1994-1999). Depth of samples see Chapter 5.

3.3 Engineering geology

“Seebodenlehme” are lacustrine soils deposited in glacial lakes during the retreat of the last Pleistocene ice sheet over the “Mittelland” about 15000 years ago (Figure 3-7, Würm ice-age).

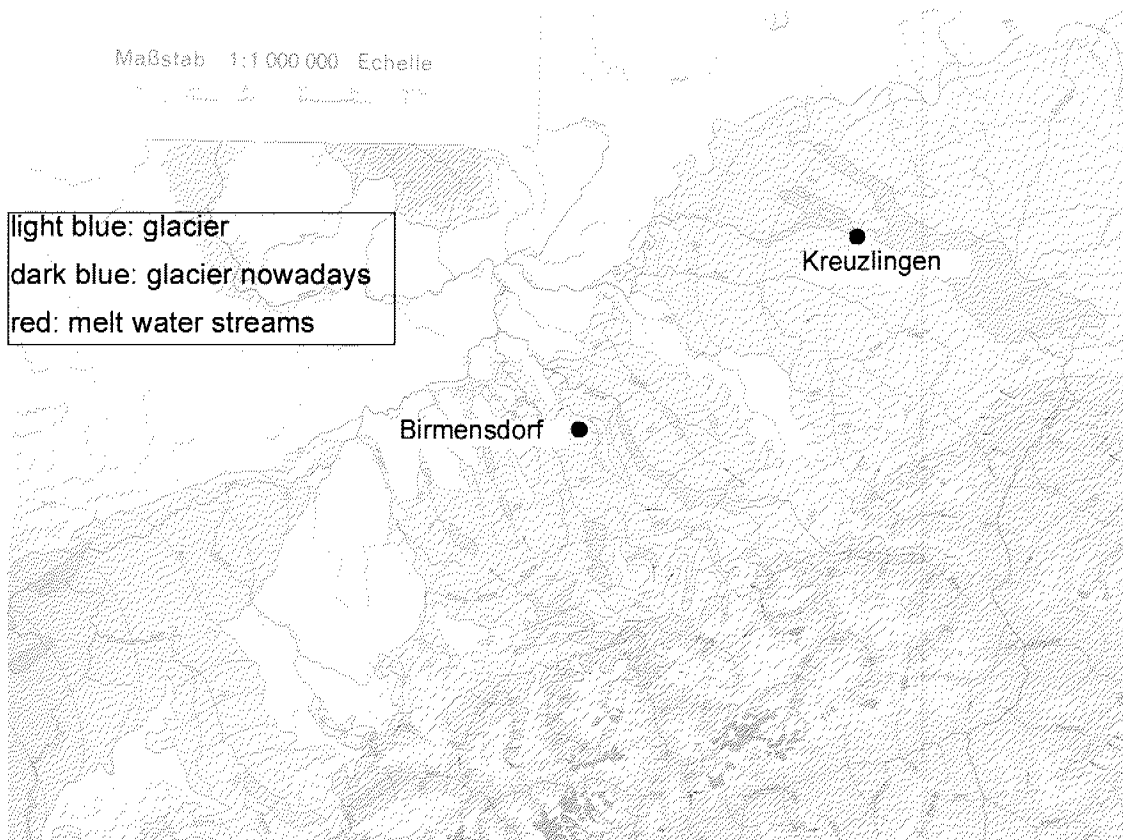


Figure 3-7: Ice sheet over the Swiss Mittelland during the Würm ice-age (Geotechnische Karte der Schweiz, 1:1000000). Contours show ice surface as masl.

The primary source materials for Seebodenlehme were the sandstone bedrock (Molasse) built during the alpine folding in the Tertiary (30 to 1.5 million years ago) and the crystalline basement of the Alps (gneiss and granite). Deposits were carried into the many lakes by melt water streams formed during the retreat of the Würm ice sheet of the Rhein, Reuss and Linth glaciers. In Figure 3-8 the end moraines left by the glaciers in the region of Birmensdorf and Kreuzlingen are visible from the geological charts. Glacial rivers with fast flowing streams formed gravels and coarse grained sand deposits (Schottern) in the river valleys. Fine sands, silts and clays were carried further out into the lakes. During the summer months, the active water conditions in the lake kept the finer clay particles in suspension and only silts and fine sands deposited on the lake bottom. During the winter months however, the calmer water conditions allowed the finer clay particles to settle down to the lakebed (Chapter 2.1). Thus the layering of the Seebodenlehm deposits is controlled by the seasonal water conditions in the lake. Variations occur due to annual changes in sediment discharge and climate conditions but also due to the proximity to the glacier. Each couplet of a silt-sand layer and a clay layer constitutes one varve. In other varved soils, this seasonal pattern is much more visible than in Swiss lacustrine deposits (DeGroot and Lutenegro, 2003, Long, 2003). Moreover between deposits from Kreuzlingen

and Birmensdorf, differences in the varving pattern are clearly visible (Figure 3-9). Seebodenlehme typically rest on top of a layer of coarse grained glacial till (moraine) that covers the underlying sandstone (Molasse) bedrock. The thickness of the Seebodenlehm deposits varies considerably due to different bedrock elevations and variations in post deposition erosion. Kreuzlingen lies at the extreme North-East edge of the Mittelland (Figures 3-1 and 3-7). The site is characterised by a soft clay deposit 10-20 m thick, which has settled out in a very flat region at the edge of lake Constance. Birmensdorf is located in the middle of the Mittelland (Figures 3-1 and 3-7), 10 km SW from Zürich. The landscape is more confined than in Kreuzlingen and the soft clay deposit settled during the retreat of the glacier along a wide valley. The soft clay deposit changes in thickness from 45 m in the middle rising to 5 m on the edge of the valley, where it is interleaved with the underlying moraine.

After drainage of the glacier lakes, the Seebodenlehme were exposed to climate changes, erosion and ground water level fluctuations. It is clear from CPTU data (Chapter 4) that the upper few metres of the deposits have undergone changes due to weathering. This crust extends to about 5 to 6 metres under the surface. The remaining deposits are usually normally consolidated.

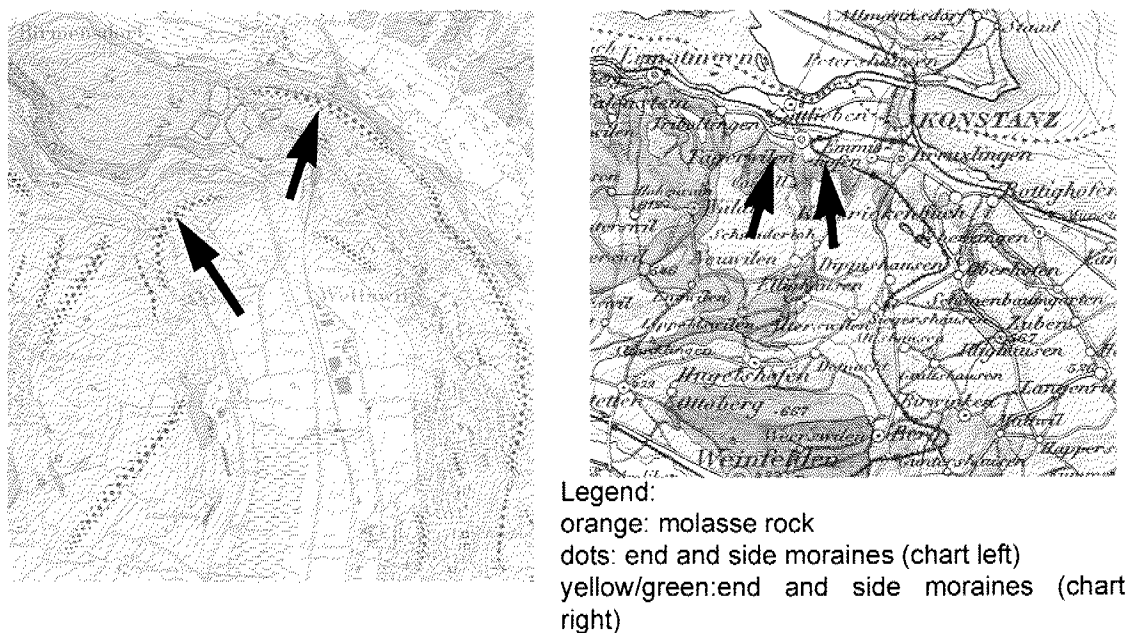


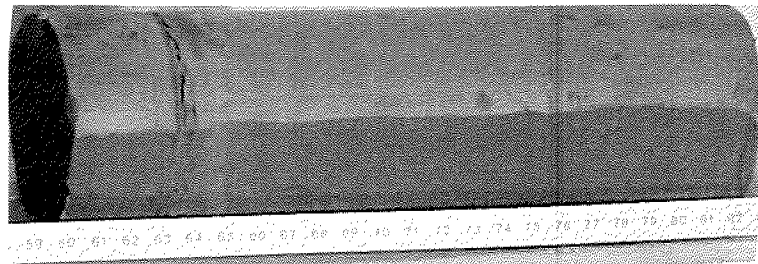
Figure 3-8: Geology charts: left at Birmensdorf (*Geologischer Atlas der Schweiz*, 1:25000); right at Kreuzlingen (*Geologische Generalkarte der Schweiz*, 1:200000).

Nominally undisturbed samples of both Kreuzlingen and Birmensdorf deposits have been taken from various depths with a piston sampler of 65 mm diameter and 800 mm length (Huder and Groebli, 1959). The Swiss Seebodenlehme are generally gray in colour, the lighter shaded material being silt layers and the darker shaded being the material clay layers (Figure 3-9, colour differences between the pictures are due to lighting). The varving pattern is more pronounced in Birmensdorf Seebodenlehm, where the varve thickness is few milli-

metres to ca. 2 cm. The thicker silt layers show cracks, which are probably due to the pull out force during sampling and also to some desiccation, which takes place faster in the silt layers.

Some disturbance occurred due to sampling and is visible in the distortion of the varves (Figure 3-9). However, the trimmed triaxial specimen in Figure 3-9d shows that the silt layers in the middle of the sample are still horizontal and have been taken to be nominally undisturbed. Some samples of Birmensdorf Seebodenlehm show a significant distortion of the normally horizontal varves, that cannot be attributed to sampling disturbance (Figure 5-31). In these cases, the varves that lie between two intact horizontal varves, are inclined up to 60° and show a wavy pattern. DeGroot and Lutenegro (2003) found distorted varving also in block samples of Connecticut Valley Varved Clay, and attributed it to lake-bed stability failures of the surface sediments during deposition (syndepositional distortion). In Birmensdorf, the distorted zones occur on the side of the valley where the deposit is less thick and probably where more wave agitation and active water conditions governed the deposition.

a) Kreuzlingen Seebodenlehm sample.



Birmensdorf Seebodenlehm: b) and c) are undisturbed samples, d) is a triaxial specimen trimmed from an undisturbed sample.

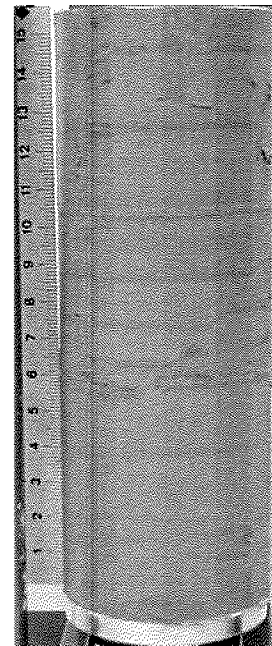
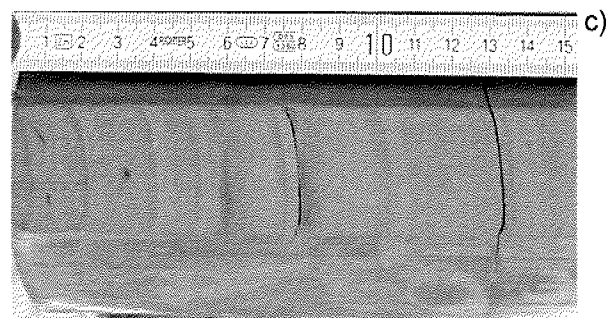
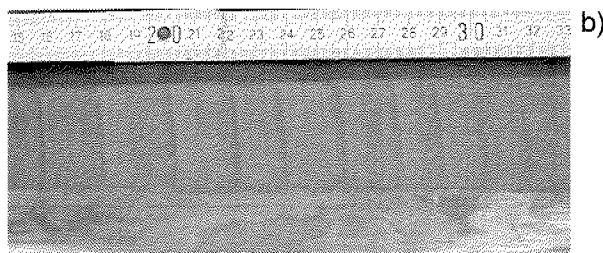


Figure 3-9: Picture of Seebodenlehm samples showing a clear varving pattern for Birmensdorf and a more homogeneous material for Kreuzlingen

The groundwater table typically occurs in the upper 2m below ground surface in both Kreuzlingen and Birmensdorf, and varies by as much as approximately 1m throughout the year, coinciding with changes in seasonal precipitation. Two separate ground water tables exist in Kreuzlingen: the upper one in the fill layer over the Seebodenlehme, as free groundwater varying about 1m during the year. The lower one is located in the sand layer under the Seebodenlehme and it shows an artesian head of about 2m.

3.4 Composition, state and index properties

3.4.1 Composition

Methods

The grain size distribution was determined with the laser light scattering apparatus MICROTRAC FRA (Leeds & Northrup). The instrument measures the particle size of suspended particles in the range 700 to 0.2 μm . The separation of the clay size fraction $< 2 \mu\text{m}$ is carried out by gravitational sedimentation out of a suspension, according to Stokes law and using the Andreasen pipette. In this case, the carbonates must be removed first to prevent flocculation. The grain size distribution was determined also by sedimentation analysis.

The mineralogical composition was determined from X-ray diffraction (XRD) with the Rietveld analysis. XRD measurements were made using a Bragg-Brentano diffractometer (Philips PW 1820 CuK α with automatic divergence slit, graphite monochromator and sample spinner) in the range of 1.5 to 65°2 θ with a step width of 0.03°2 θ and a counting time of 4 s. Mineralogy of the samples is determined firstly on randomly oriented powder specimens. The amount attributed to the different phases is determined from peak areas and by Rietveld analysis (Rietveld program BGMN®/AutoQuan). The second sample preparation produces specimens with oriented material from the clay fraction. This technique enhances basal reflections from clay minerals thereby facilitating their identification. Oriented samples were treated with ethylene glycol to identify characteristic swelling (e.g. smectites and mixed layer clay minerals).

The cation exchange capacity (CEC) of the bulk material was determined using the complexes of copper (II) ion (Meier and Kahr 1999). The CEC value gives information about the molecular bound water at the exchangeable cations in the interlayer of the clay minerals.

The water uptake was determined using the Enslin-Neff technique (Demberg 1991). The apparatus consists of a glass set of a sample container with filter, a connecting tube and a calibrated tube of 2 ml for the volume measurement. The apparatus is first completely filled with water. Then one gram of sample material (powder) is placed on the filter plate. The rate of volumetric adsorption of water is timed until there is no further change. The water uptake number gives the amount of water which can be stored by the clay. The maximum value is the sum of the inner crystalline adsorbed water and the capillary interaggregate water (from Plötze et al., 2003).

Electron microscopic investigations of the microstructural morphology were made on fresh broken pieces of air dried samples with a Scanning Electron Microscope LEO1530 (Carl Zeiss).

The analysis described in this section were carried out at the laboratory for clay mineralogy of the Institute for Geotechnical Engineering by Dr. M. Plötze and the staff of the Institute.

Results

The samples have a particle size distribution between 0.2 and 125 μm . The clay fraction amounts to ca. 40% for both sources, which is less than in Finnish Otaniemi clay (Messerklinger et al., 2003) or in Connecticut varved clay (DeGroot and Lutenecker, 2003). From sedimentation analysis, the grain size distribution curves of the three clays look very similar to each other (Figure 3-10). The distribution curve for grain sizes smaller than 100 μm indicate better the size of clay minerals and clay clumps contained in the soil. Kreuzlingen shows a predominant maximum at about 10 μm and a secondary peak at 1 μm . Birmensdorf in contrast shows a finer grain size distribution, where the dominant particle size is 1 μm with a much smaller, secondary peak at 25 μm .

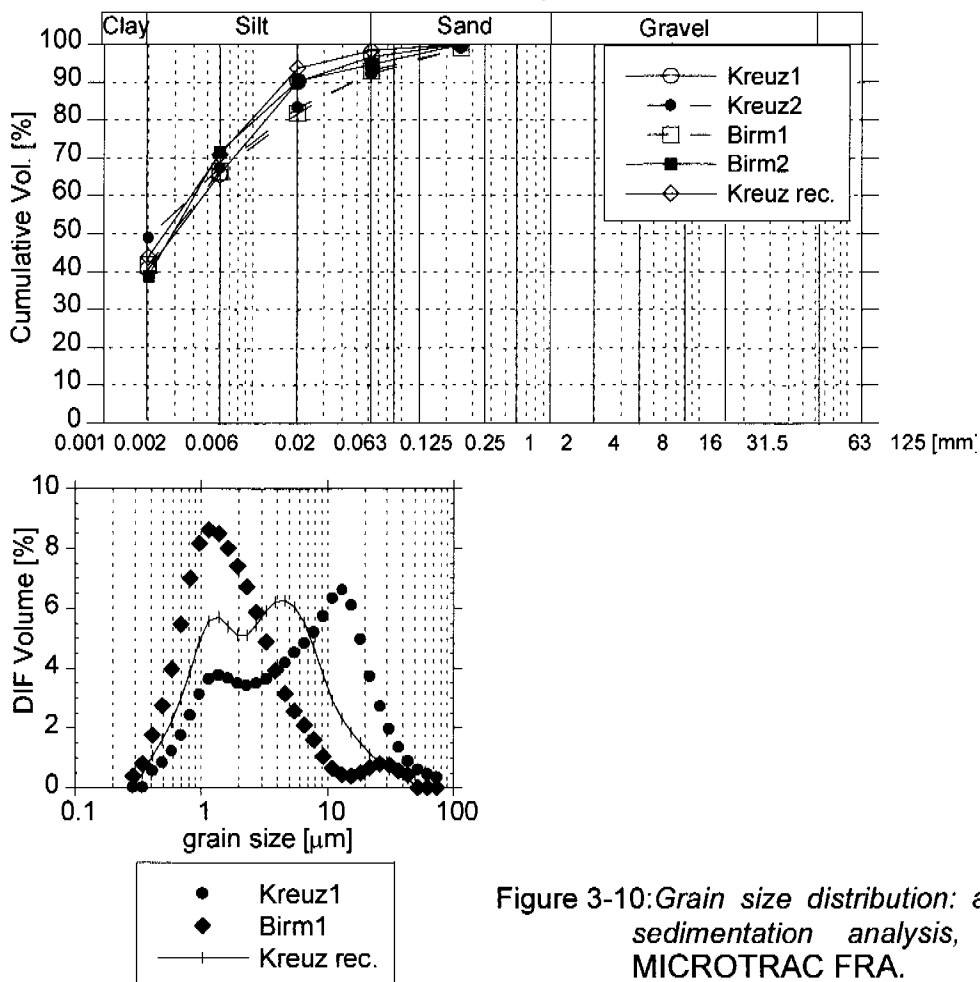


Figure 3-10: Grain size distribution: above by sedimentation analysis, left by MICROTRAC FRA.

The reconstituted Kreuzlingen clay is finer than the original material, having two peaks at 1 and 5 μm . The mechanical remoulding to a slurry and the chemical dissolution of gypsum aggregates by the added water has the effect of breaking clay clumps, that maybe present in the original clayey soil. This induces a finer grain size distribution particularly in the range $< 0.06 \text{ mm}$.

For Kreuzlingen Seebodenlehm, separate grain size distributions and water contents have been determined on individual clay and silt layers. Individual clay layers have a clay fraction of ca. 40% and individual silt layers of ca. 25%.

The investigated clays were found to be illitic (about 25%) with high carbonate content ($> 35\%$, mainly calcite). Lower quartz content and a higher amount of clay minerals, in particular of swellable mixed layer clay minerals, were determined for the Birmensdorf clay (Table 3-1 and Table 3-2, Plötze et al., 2003). The composition of the reconstituted clay is identical to that of the original soil. A gypsum content was non detectable, which means that it was lower than 0.5% by weight.

| Site | carbonate | | quartz | feldspar | clay minerals | | |
|-------------|------------------------------|-----------------------------|------------------------------|-------------------------|--------------------|----------------------------|----------------------|
| | calcite | dolomite | | | chlorite | illite | mixed layer |
| Kreuzlingen | 29.2 \pm 1 (24-32) | 7.4 \pm 0.6 (5-19) | 22.5 \pm 0.9 (15-32) | 8.3 \pm 1.8 (4-11) | 5 \pm 1 (4-7) | 23 \pm 3 (17-29) | 4 \pm 2 (2-8) |
| Kreuz. rec | 31.6 \pm 0.9 | 6.0 \pm 0.6 | 21.7 \pm 0.7 | 8.3 \pm 1.8 | 5 \pm 1 | 24 \pm 3 | 2 \pm 1 |
| Birmensdorf | 27.6 \pm 1.4 (23-31) | 10.7 \pm 0.8 (8-15) | 12.2 \pm 0.8 (10-16) | 6.3 \pm 1.7 (4-9) | 8 \pm 1 (6-9) | 22 \pm 4.0 (19-27) | 13 \pm 4 (7-20) |

average values \pm deviation, and range in% by weight, second line, in brackets.

Table 3-1: Mineralogical composition of the bulk material (Plötze et al., 2003).

| Site | quartz | feldspar | clay minerals | | |
|-------------|-------------------------|-------------------------|------------------------|-----------------------|------------------------|
| | | | chlorite | illite | mixed layer |
| Kreuzlingen | 8.5 \pm 0.9 (5-11) | 7.4 \pm 1.5 (4-11) | 16 \pm 5 (5-20) | 30 \pm 5 (22-37) | 30 \pm 8 (20-45) |
| Birmensdorf | 8.1 \pm 0.9 (6-9) | 7.0 \pm 1.3 (4-11) | 11 \pm 2.0 (5-25) | 29 \pm 5 (22-35) | 41 \pm 10 (35-50) |

average values \pm deviation, (range) in wt%

Table 3-2: Mineralogical composition of the decarbonised fraction $< 2 \mu\text{m}$ (Plötze et al., 2003).

Finnish clays (Messerklinger et al., 2003) and the North American Connecticut clay (DeGroot and Lutenegeger, 2003) have a much lower carbonate content than the Swiss Seebodenlehme (carbonate totalled nd and <4% respectively). Fucino clay from Italy (Soccodato, 2003) and Athlone laminated clay from Ireland (Long, 2003) have a much more similar mineralogical composition to the Swiss Seebodenlehme (for instance carbonate totalled around 30% and 25% respectively). The sensitivity is a good indicator of cementation and structure, and although the Swiss Seebodenlehm has a carbonate content of more than 30%, the sensitivity S_t measured with the fall cone tests (Table 3-5) is very low compared with the values of the eastern Canada marine clays studied by Leroueil (1985). The high carbonate content of Seebodenlehm does not result in an open-plan structure but results in the formations of distinct clumps (Figure 3-15b), which acts as bigger silt particles. The clumps influence the behaviour of the Seebodenlehm, which acts despite the high carbonate content as an uncemented soil with low sensitivity.

The results in Table 3-3 show that the Birmensdorf clay, with the higher clay content, has a higher CEC value and can bind more water chemically (inner crystalline). All water additional to the maximum inner crystalline water is stored in intra-aggregate voids as capillary water. The capillary water uptake is faster than the inner crystalline water uptake. Mechanical vibration of the sample after adsorption causes a lowering of the porosity in the intra-aggregate region where the capillary bound water is stored. This leads to a decreasing Enslin-Neff value, which is finally near the liquid limit w_L determined with the Casagrande cup device (Plötze et al., 2003).

| Site | CEC | Water uptake | Enslin-Neff | |
|-------------|----------|--------------|-------------|-----------------|
| | meq/100g | mg/g | Time [s] | vibrated [mg/g] |
| Kreuzlingen | 9.2 | 0.564 | 300 | 0.345 |
| Birmensdorf | 19.1 | 0.649 | 800 | 0.513 |

Table 3-3: Cation exchange and water uptake capacity, average values (Plötze et al., 2003).

An ion chromatography analysis was performed on samples of pore water (Table 3-4) collected from undisturbed samples during consolidation tests. The main difference was the higher anion content in the Birmensdorf clay (Cl^- , NO_3^- , PO_4^- , Table 3-4), which can be explained by the mainly agricultural activity in Birmensdorf and the consequent use of fertilisers (Plötze, personal communication 2001). The analysis of the pore water ions indicates that the addition of water for reconstituting has dissolved the small amount of gypsum ($CaSO_4 \cdot 2H_2O$, calcium sulphate), resulting in higher Ca^{2+} , Mg^{2+} and SO_4^{2-} content. Free calcium ions in the pore water can then exchange the sodium ions Na^+ in the internal clay mineral layers, which explains the higher Na^+ content of the reconstituted soil. Residual shear resistance of Na^+ clay minerals is lower when compared to Ca^{2+} clay minerals, and this could influence the shear resistance of the reconstituted Kreuzlingen clay. However, considering the very low gypsum content and the consequently low free ions content, this influence is marginal (Plötze, personal communication 2003).

| Site | Na ⁺ | NH ₄ ⁺ | K ⁺ | Mg ²⁺ | Ca ²⁺ | F ⁻ | Cl ⁻ | NO ₃ ⁻ | PO ₄ ³⁻ | SO ₄ ²⁻ |
|-------------|-----------------|------------------------------|----------------|------------------|------------------|----------------|-----------------|------------------------------|-------------------------------|-------------------------------|
| ppm | | | | | | | | | | |
| Kreuzlingen | 52.3 | 2.4 | 50.5 | 52 | 78 | 4.8 | 6 | nd | nd | 298.5 |
| Kreuz rec. | 89.9 | nd | 11.2 | 180.4 | 318.2 | 1.2 | 12.5 | nd | nd | 1528 |
| Birmensdorf | 50.1 | 2 | 29.5 | 34.9 | 61.2 | 5 | 222.3 | 72.2 | 58 | 212.9 |

Table 3-4: Pore water chemistry (nd = not detected)

3.4.2 State and index properties

State and index properties such as water content and the Atterberg limits for a varved clay depend on what relative portions of the silt and clay layers are in the test specimen. Most of the data presented here are based on bulk properties, but some individual layer properties are also presented. Inevitably, some portion of the scatter in the bulk properties will be due to the varying amounts of silt and clay in the individual specimen. This influences the correlations between the index properties and the mechanical properties as well. For consistency, samples for bulk water content and other index properties should be collected using vertical cuts along tube samples to test several layers at once. This may not always have been the case for all the data presented here.

In Table 3-5, typical average values of state and index properties are given for the two clays, whereas Figure 3-11 and Figure 3-12 shows the soil profiles of the state and index properties. The density of the solids is uniform throughout

| Site | CF <2 μ m | w | w _L | w _P | I _P | I _L | Hm | ρ_s | S | e ₀ |
|------------|--------------------------|-------|----------------|----------------|----------------|----------------|------|---------------------|---------|----------------|
| | [%] | [%] | [%] | [%] | [%] | [%] | [%] | [t/m ³] | [-] | [-] |
| Kreuz | 44.0 | 30-36 | 30-46 | 17-19 | 15-30 | 0.83 | <0.5 | 2.75 | 3.8-4.3 | 1.0 |
| Kreuz rec. | 43.0 | 35.6 | 39.5 | 17.3 | 22.2 | 0.82 | <0.5 | 2.76 | 2.1 | 0.98 |
| Birm | 48.0 | 35-50 | 42-76 | 16-27 | 26-56 | 0.75 | <0.5 | 2.74 | 2.6-3.7 | 1.0 |
| CF | Clay fraction <2 μ m | | | | | | | | | |
| Hm | Organic Content | | | | | | | | | |

Table 3-5: Typical average values of state and index properties.

the deposits with $\rho_s = 2.75 \text{ t/m}^3$ for the Kreuzlingen clay and 2.74 t/m^3 in Birmensdorf samples. No difference in ρ_s was found for the individual silt and clay layers. The sensitivity of the Seebodenlehme detected with the fall cone tests is low, with values of about 4 for Kreuzlingen and of about 3 for Birmensdorf. These values are general lower than those for the Finnish clays. As already stated in Chapter 3.1.2, the state and index properties of the reconstituted Kreuzlingen clay is comparable to the original material.

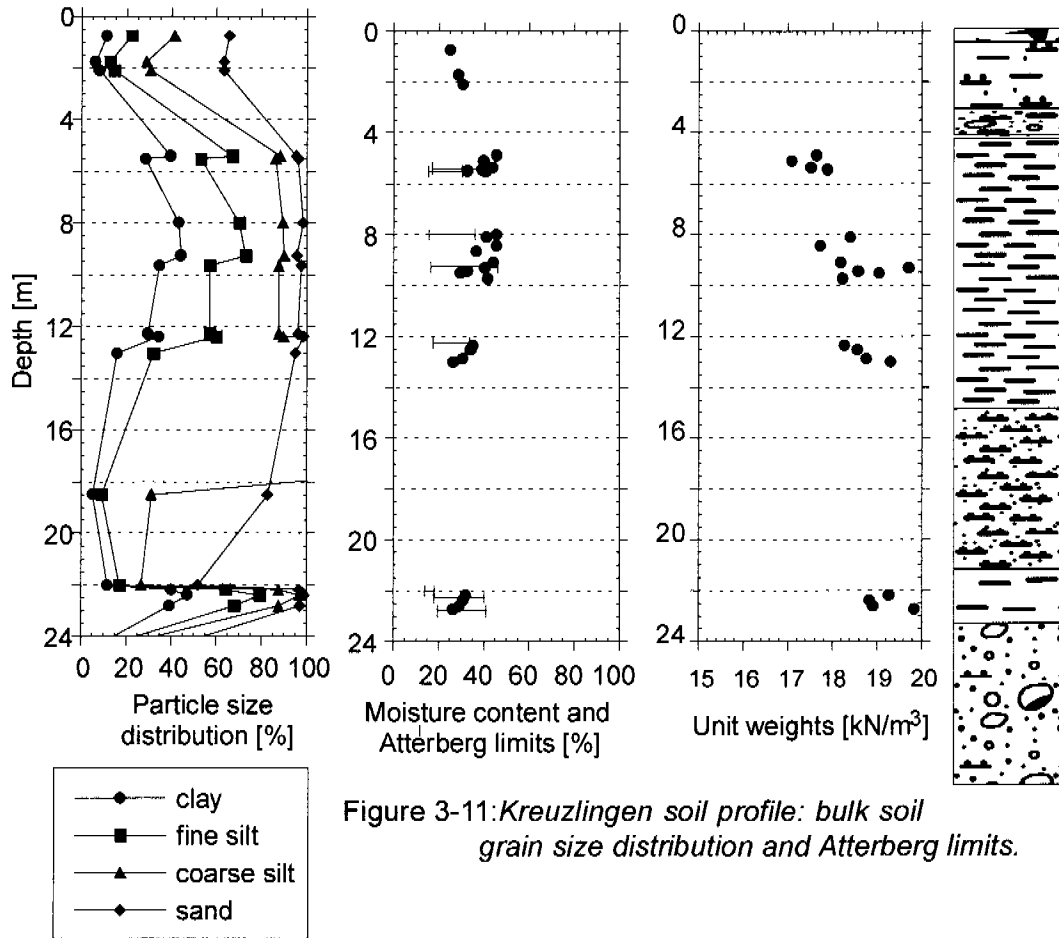


Figure 3-11: Kreuzlingen soil profile: bulk soil grain size distribution and Atterberg limits.

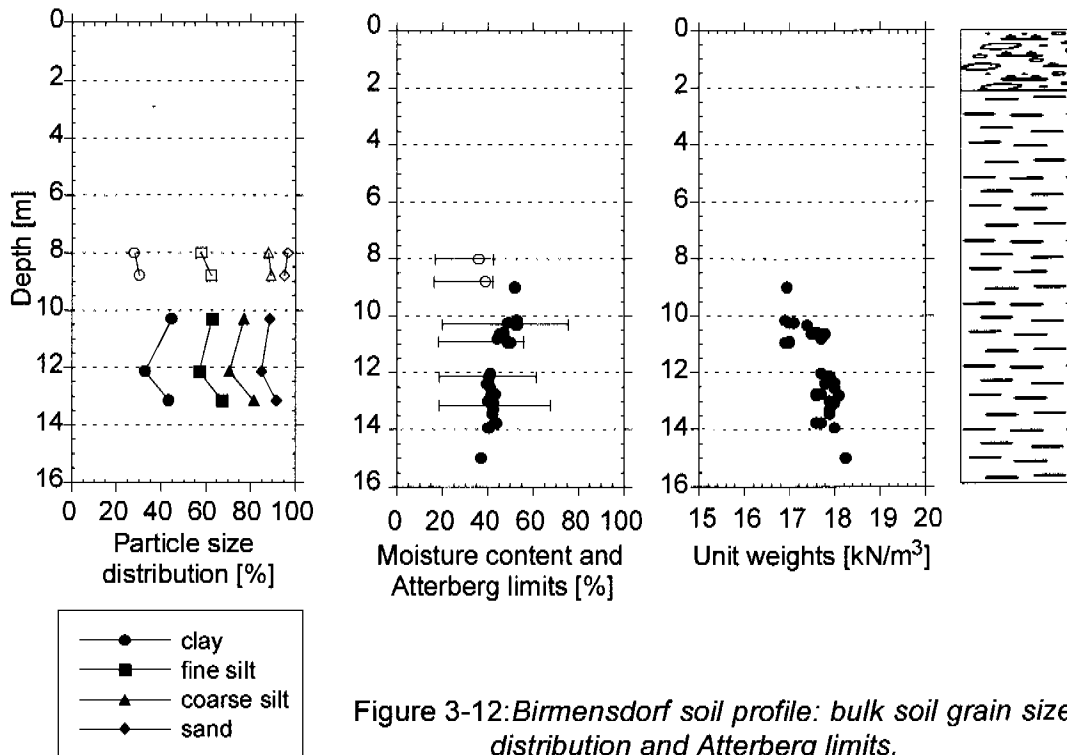


Figure 3-12: Birmensdorf soil profile: bulk soil grain size distribution and Atterberg limits.

Within a varve, the water content typically is a minimum value at the bottom of the varve and gradually increases with increasing height as the soil becomes finer grained and more plastic. It is known that it abruptly changes back to the minimum coinciding with the transition from winter to summer deposition mode (DeGroot & Lutenegger, 2003). For Connecticut Valley varved clay, the natural water content varies as much as 40% within a varve (DeGroot and Lutenegger, 2003). In the Swiss Seebodenlehm, the difference in water content between silt and clay layers reaches maximum values of 14%.

Birmensdorf clay shows a higher Plasticity Index and in situ natural water content ($I_P = 26-56\%$, $w = 35-50\%$, $I_L = 0.75$), whereas the Liquidity Index is marginally higher for Kreuzlingen ($I_P = 15-30\%$, $w = 30-36\%$, $I_L = 0.83$), whose consistency in situ is thus less stiff. The values of I_P depend upon the amount of the clay fraction as well as the clay mineral content. The higher amount of the clay size fraction of the Birmensdorf clay in particular, with the higher content of (swellable) clay minerals concentrated therein, is reflected in the values of CEC and water uptake capacity. The Birmensdorf clay has a higher CEC value and can bind chemically more inner crystalline water (Plötze et al., 2003).

The Unified Soil Classification System (USCS) gives the bulk soils classification of CM for Kreuzlingen (Figure 3-13), and CM / CH for Birmensdorf. Compared to Finnish clays, the plasticity of the Swiss Seebodenlehme is low when compared to the clay fraction content. An explanation for the low plasticity of the Swiss clays could be the high Calcite content. Calcite tends to cement the clay minerals together, for example in the form of peds, and these combined clay minerals may react like granular materials such as silts (Messerklinger et al., 2003). Connecticut Valley varved clay has likewise a clay fraction which averages 45%, and a Plasticity Index I_P as low as 20% (DeGroot and Lutenegger, 2003). In this case however, the total carbonate content is very low (3%).

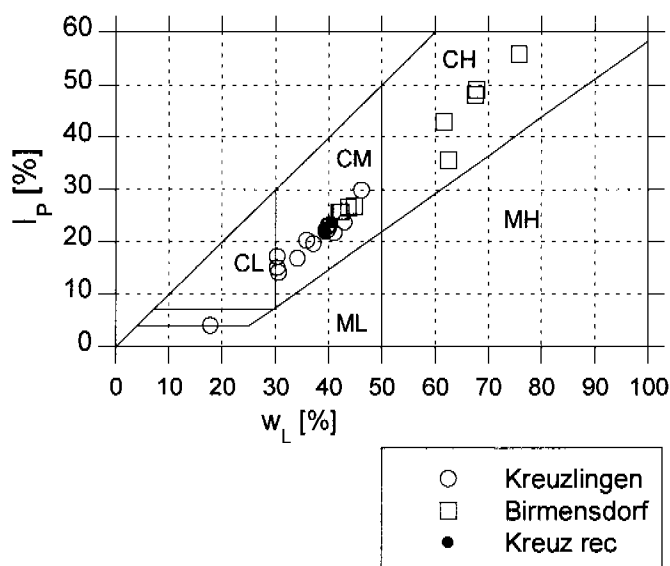


Figure 3-13: Plasticity chart after USCS.

The higher chemical water uptake capacity of Birmensdorf Seebodenlehm is also visible from the Activity Index I_A (Figure 3-13) (Skempton, 1953).

$$I_A = \frac{I_P [\%]}{CF < 2\mu m [\%]} \quad [3-1]$$

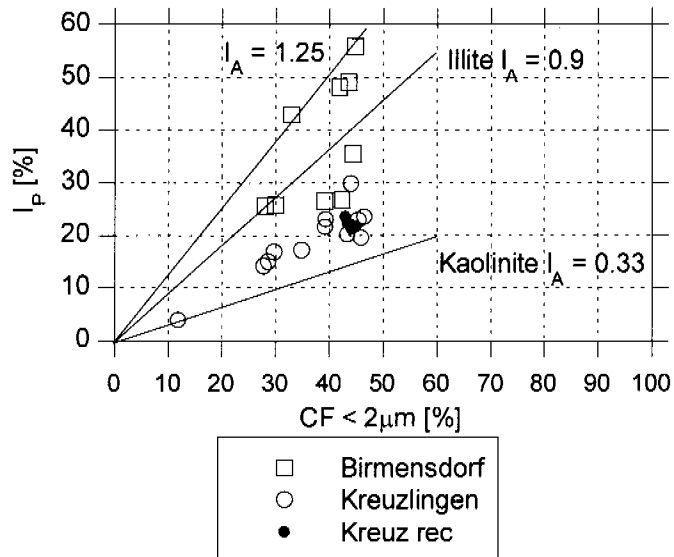


Figure 3-14: Activity chart.

Inactive soils have values of I_A smaller than 0.75 and very active soils have values greater than 1.25 (Skempton, 1953). As a reference, the Illite clay mineral has an Activity Index of 0.9 and Kaolinite of 0.33. Birmensdorf clay can bind more water and is therefore more active than Kreuzlingen clay.

3.4.3 Structure

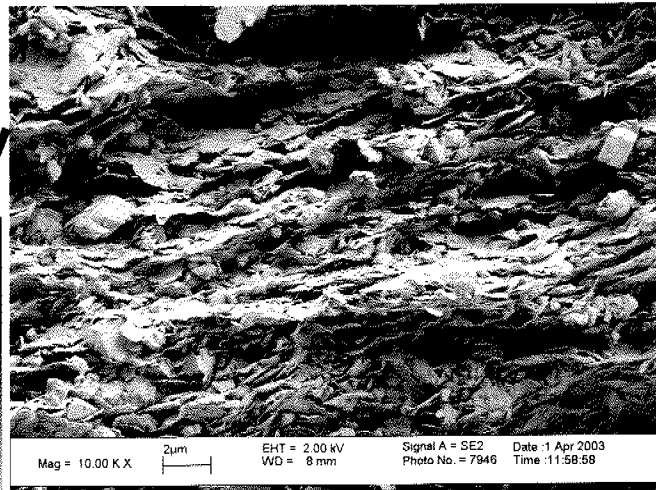
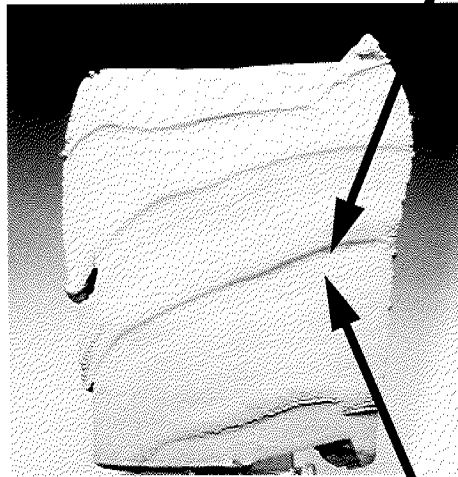
Birmensdorf Seebodenlehm has a distinct macro fabric with alternating silt and clay layers, whereas Kreuzlingen is more homogeneous, showing rather a coloured layering, as described in Section 3.3. Although these clays are more or less varved, their appearance in situ, for instance in an excavation, is homogeneous. The influence of the varving depends upon scale factors, which makes the laboratory testing of these soils difficult.

The specimen of Birmensdorf Seebodenlehm in Figure 3-15 sheared sooner than expected during a stress path aimed to impose conditions of zero radial strain due to the following reasons: (1) inhomogeneous excess pore water pressure distribution in the sample and (2) the presence of inclined varving. The dark layers are clay-rich layers which have developed as shear planes. This is confirmed by the SEM pictures. The upper one shows mobilisation of a residual shear surface in the clay platelets which are mainly parallel to each other, whereas the lower picture shows clumps of siltier clay (Plötze et al., 2003).

Drained direct shear tests on soft soils and pure clay minerals show that residual shear strength is primarily dependent on mineral composition and not related to the plasticity or grain-size characteristics (Kenney 1967). Even clay mineral contents below 20% can cause a strongly decreasing friction angle with shear strain. The swellable clay minerals have the highest influence. Pure illite had a residual friction angle of about 25° and Ca-montmorillonite of about 10° (Müller-Vonmoos and Løken, 1989). The value for mixed layers (illite-montmorillonite) lies in between. Considering these and the higher content of swellable clay minerals, we should expect a lower friction angle for the Birmensdorf clay. However, this was not confirmed by the laboratory tests. The explanation lies in the bedding formation and microstructure of the clay, in terms of the sample size,

shape and orientation, which affects the values of deviator stress mobilised throughout a triaxial stress path test, and from which a friction angle maybe deduced. The thin parallel layers of clay and silt lie mainly perpendicular to the major principal stress direction in the triaxial tests. This leads to an averaging of the mobilised shear properties. In the case of inclined layers, the measured shear strength drops dramatically.

a) clay-rich layer: residual shear surface in the clay platelets mainly parallel to each other.



b) clumps of siltier clay.

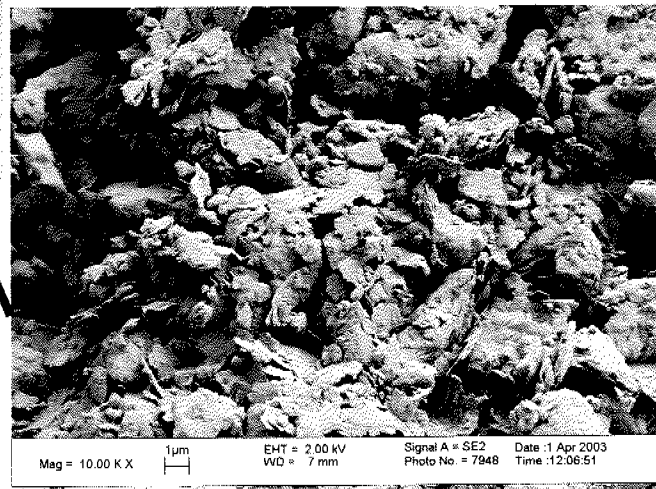


Figure 3-15: SEM pictures of layers in varved clay body from Birmensdorf after triaxial testing (Plötze et al., 2003)

In situ testing

4.1 In situ testing programme

In situ tests were carried out on both the Kreuzlingen and Birmensdorf sites. The research programme in Kreuzlingen was designed to deliver more detailed information about the stratigraphy and properties (e.g. strength, stiffness, permeability) of the soils found on site. A by-product of this research should be to develop greater confidence in the piezocone testing (cone penetration testing with pore pressure measurement at the tip, CPTU) as a site investigation tool within Switzerland. The CPTU can often be used economically in partnership with other in situ testing methods or laboratory tests, to establish a database of in situ soil strength as a function of depth, and to evaluate spot values of permeability, which can be then used for design of future construction projects.

In consequence, the testing programme for the Kreuzlingen test site included:

1. A CPTU at B1 to 25m depth (Figure 3-2), with measurement of cone resistance q_c , side friction f_s , and pore pressure behind the tip u_{bt} , with excess pore pressure dissipation tests carried out to steady state in situ conditions at specific depths (Giudici and Springman, 1998 a and b).
2. An adjacent borehole to 31m depth, drilled using triple cored techniques.
3. Associated undisturbed sampling, to deliver a set of 65mm diameter Kreuzlingen clay cores for testing in laboratory triaxial apparatus and oedometers (Chapter 5).
4. Tomographic geophysical seismic testing to deliver soil profile and small strain elastic stiffness in the various key soil layers (Chapter 2.3) (Maurer et al., 1998).

Results from the first three programme items were presented in Springman et al., 1999.

The Birmensdorf site was spread out over a larger area than in Kreuzlingen and when the CPTU was planned, construction of the preload embankments had already begun. So the locations of the various boreholes and the CPTU sites lie within the perimeter of ca. 1 km from each other (Figure 4-1). Two CPTU's were carried out at a distance of 1 m from each other to check the reproducibility of the measurement.

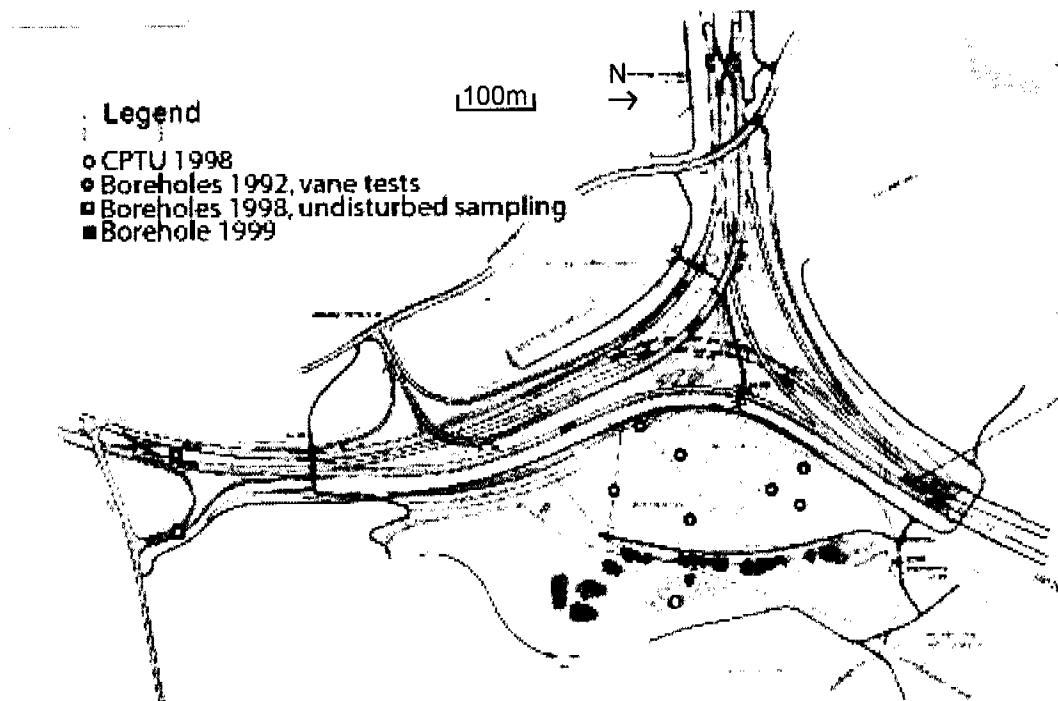


Figure 4-1: Position of the boreholes and CPTU sites in Birmensdorf.

Various boreholes logs with corresponding borehole vane tests were available from the Bureau of Underground Construction of the Canton of Zürich to correlate with the CPTU results and the laboratory tests. The CPTU's were carried out in Birmensdorf to complete the test series in the same way as in Kreuzlingen, but there was no seismic tomographic experiment. The main goal of the CPTU was to evaluate the correlation between undrained shear strength and effective overburden pressure as well as the relationship between strength parameter determined in situ from correlations and from triaxial compression tests. Furthermore, the clay characteristics could be compared.

A detailed description of the sites and of the soil geology and stratigraphy is given in Chapter 3.

4.2 Cone penetration testing

4.2.1 Introduction

Amann and Heil (1995) have discussed the growing use of cone penetration (CPT) or piezocone (CPTU) testing to characterise typical fine grained or soft clayey or peaty deposits in Switzerland (Figure 4-2) and to determine an undrained shear strength profile. These fine grained deposits are primarily found in the Mittelland between the Alps and Jura mountains, which occupies 30% of the

surface area of Switzerland and hosts the majority of the transportation arteries. The soils in these areas may be characterised most effectively using CPTs or CPTUs.

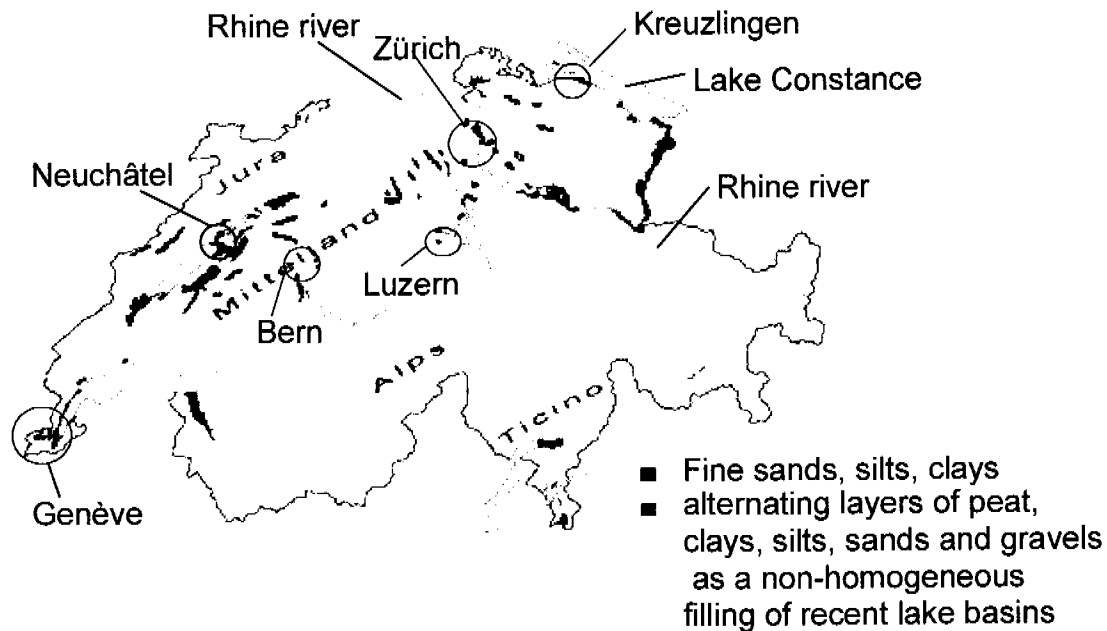


Figure 4-2: Occurrence of fine grained and soft clayey and peaty deposits in Switzerland (Amann & Heil, 1995)

Case histories relating to transportation projects are described (e.g. Steiner et al., 1992; Steiner and Togliani, 1998), in which the CPT or CPTU was one of a suite of in situ and laboratory tests used to characterise glacial soils of variable soil type and stress history, and to derive appropriate properties for design. Some uncertainty still remains over the choice of a design value for the undrained shear strength. The complementary nature of field and laboratory testing leads to correlations, which may then be applied, based on past experience. Pore pressure measurement from the CPTU was found to be extremely valuable in determining the hydraulic response to cone penetration, as well as the boundaries between clayey and sandy-silty soil layers to within a few decimetres.

Heil et al. (1997) and Amann et al. (1992) report results of specific cone penetration, associated field vane and triaxial testing programmes on the Kreuzlingen clay related to another part of the highway project described here. These have revealed that the undrained shear strength s_u increases linearly with depth for the normally consolidated deposits encountered (Figure 4-3), and that Critical State Soil Mechanics theory may be used to characterise the failure state on the Critical State Line (CSL) in undrained triaxial compression.

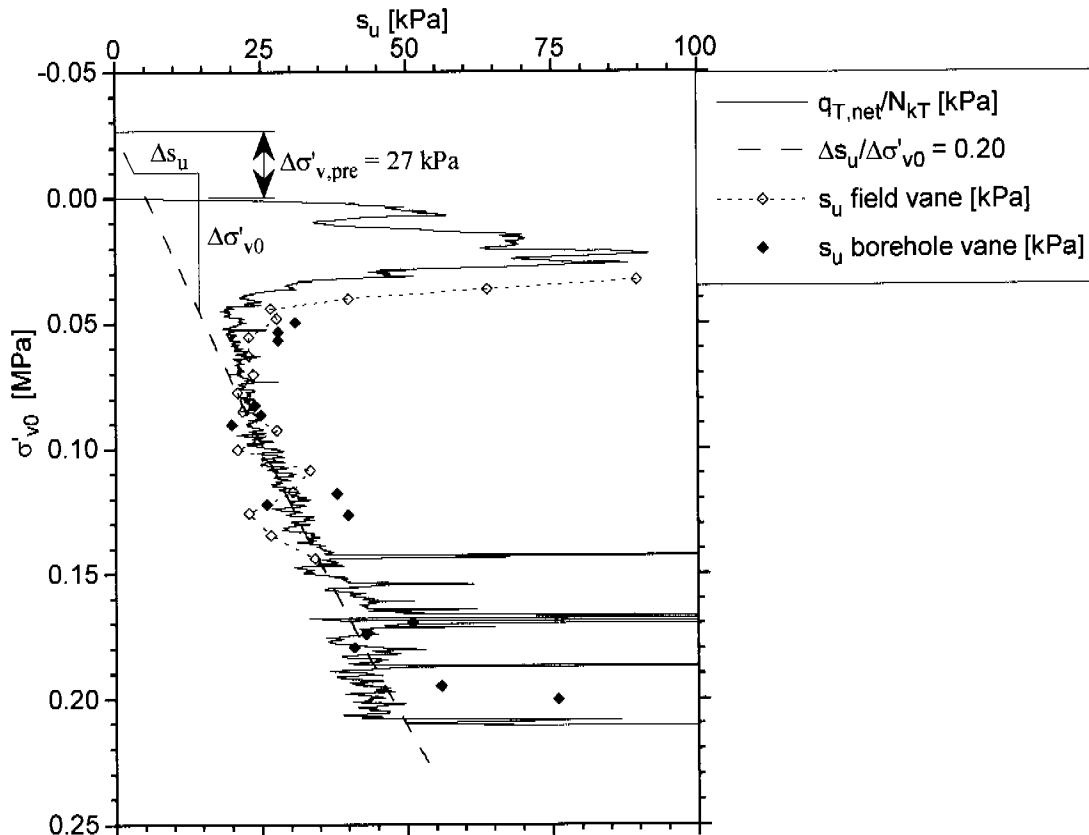


Figure 4-3: Correlation between the undrained shear strength s_u and the effective overburden pressure σ'_{v0} for the Kreuzlingen Seebodenlehm from Heil et al., 1997.

4.2.2 Interpretation procedures

The cone penetration testing was carried out using a piezocone from the Institute for Geotechnical Engineering, which was manufactured by van den Berg, with a data acquisition system developed in house. The cone has a cross sectional area of 10 cm^2 and a cone angle of 60° . The ceramic filter stone used for the measurement of the pore pressure behind the tip, u_{bt} , is located between 2 and 6 mm behind the shoulder: the location of this is important when evaluating the excess pore pressure induced during penetration Δu (Baligh and Levadoux, 1980). The rate of penetration was 2 cm/s, and readings were taken every 0.05 seconds.

Readings of the cone resistance, q_c , were corrected for the pore pressure, u_{bt} , acting at the joint between the cone tip and friction sleeve, to obtain the total pressure acting on the cone tip, q_T :

$$q_T = q_c - u_{b0} \cdot (1 - a) \quad [4-1]$$

The net area ratio, a , is 0.76 for this cone. Eliminating the contribution of the total overburden pressure, σ_{v0} , to the cone resistance gives the net cone resistance, $q_{T,net}$, where

$$q_{T,net} = q_T - \sigma_{v0} \quad [4-2]$$

The net cone resistance is used with the local friction, f_s , to calculate the normalised friction ratio:

$$R_{fT} = f_s / q_{T,net} \quad [4-3]$$

and the normalised cone resistance in terms of effective overburden pressure σ'_{v0} :

$$n_{qT} = q_{T,net} / \sigma'_{v0} \quad [4-4]$$

and the pore pressure ratio:

$$B_q = (u_{bt} - u_0) / q_{T,net} = \Delta u / q_{T,net} \quad [4-5]$$

where u_0 is the initial in situ steady state pore pressure and Δu is the excess pore pressure developed during penetration. R_{fT} , n_{qT} and B_q in turn are used for the determination of the soil type and stratification (Robertson, 1990).

A value of undrained strength s_u may also be obtained from CPTU data based on use of a cone factor N_{KT} , whereby:

$$s_u = \frac{q_{T,net}}{N_{KT}} \quad [4-6]$$

Yu and Mitchell (1998) summarise the current state of the art regarding analysis of cone resistance and hence the determination of N_{KT} . They discuss the various theoretical and analytical methods, which rely on bearing capacity, cavity expansion, steady state (strain path) approach or finite element analysis. Values derived for N_{KT} are dependent on the roughness of the cone and also the stiffness index of the soil, i.e. shear stiffness normalised by s_u , and were found to vary from 10 to 17.5, all for rough cones.

4.2.3 Results

Kreuzlingen

The CPTU data are given in Figure 4-4 a to d for f_s , q_T , R_{fT} and B_q and show clearly that there are two clayey layers between 4 to 13m and 22 to 24m. The total cone resistance increases linearly, almost passing through zero, with relatively low values of q_T and f_s , and with R_{fT} oscillating about 1%. This was presumed to be the weak normally consolidated Kreuzlingen clay. From 13 - 22m, the minimum values of q_T more or less followed the linear trend established between 4 and 13 m, however the peaks in q_T implied that the clay layers were interspersed with layers of silts and sands.

Consideration of the pore pressure ratio (Figure 4-4 d) confirmed the above interpretation of the stratigraphy. B_q reached values up to 0.8 between 4 - 13m and 22 - 24m, indicating quite sensitive behaviour and an OCR of less than 1.5 (Lacasse and Lunne, 1982). In between these clay layers, a highly variable deposit is found, which is essentially free draining and probably granular within the middle 5m from 15 - 20m. Cone resistance is quite variable and increases up to 25MPa at peak, with correspondingly lower values of R_{fT} and B_q . In the 2m

transition zones above and below this granular layer (13 - 15m, 20 - 22m), the fluctuations in B_q offer a sensitive indicator of the presence of thin layers of clay interleaving between the silts and sands.

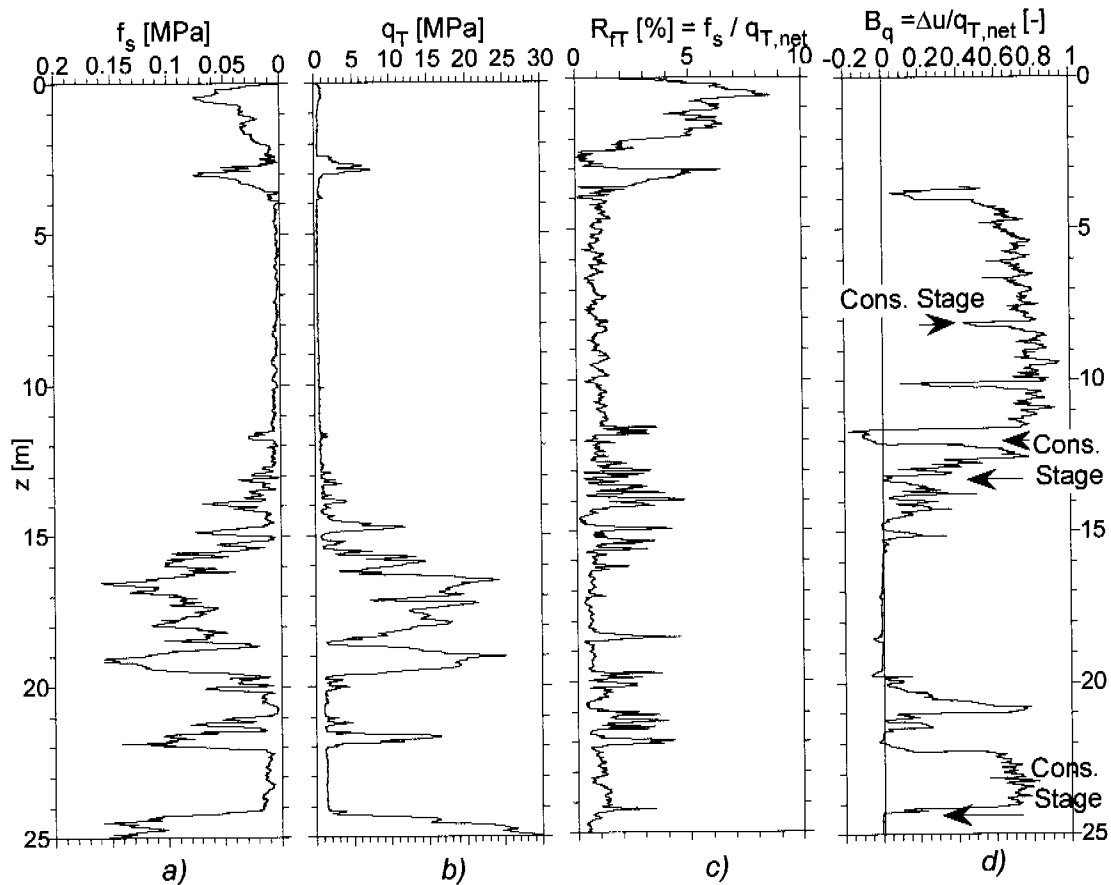


Figure 4-4: CPTU at B1 in Kreuzlingen: a) shaft friction f_s ; b) total pressure on tip q_T ; c) normalized friction ratio R_{TT} ; d) pore pressure ratio B_q .

The linearity of the total cone resistance in Figure 4-4 shows the homogeneity of the clay layer, but the small peaks in normalised friction ratio and pore pressure ratio indicate fine layers of more permeable and less plastic material. The thickness of these layers from the CPTU is in the order of few centimetres and their spacing ca. 0.2m. The varve thickness of Kreuzlingen Seebodenlehm varies as observed in undisturbed samples extruded in laboratory, between few millimetres and ca. 5 cm. So it would seem that the resolution of the data from the 10 cm² cone is not fine enough to detect these relatively thin and closely spaced layers. The experiments of Hird et al. (2003) demonstrate the feasibility of using miniature piezocones to detect individual permeable layers as thin as 2 mm in normally consolidated clay deposits, provided their vertical spacing is at least two cone diameters and a sufficiently fast data recording rate is used. The use of such a miniature cone in a deposit of Seebodenlehm could probably deliver a much more detailed data set about the varying in situ, especially the spacing, and improve the quality of characterisation achieved from the site investigation.

Charts based on Robertson (1990) of n_{qT} against R_{FT} (Figure 4-5 a) and of n_{qT} against B_q (Figure 4-5 b) allow characterisation of the deposits and depict more or less one main grouping with all results plotting together, showing sensitive clays and silts for these two depths.

In situ consolidation tests were carried out at several depths as indicated in Figure 4-4d. The complete saturation of the porous stone is a fundamental requisite for the determination of consolidation parameters from CPTU consolidation tests (Jamiolkowski, 2003). If this prerequisite is not accomplished, then the dissipation curve is irregular, and upon restart of penetration the response of the pore pressure transducer will be slow. In Figure 4-4, it is visible that the silty sand layer between 15 and 20 m has desaturated the porous stone with high suction pressures, and that the pore pressure response after 20m depth is delayed. Two procedures can be used to evaluate the in situ permeability, one based on the strain path method combined with FE analysis (Levadoux and Baligh, 1980, Baligh, 1985), the other based on cavity expansion theory (Torstensson, 1979). In the present work, the in situ permeability was determined on the basis of the cavity expansion theory (Torstensson, 1979) and a coefficient of compressibility obtained from oedometer tests at equivalent depth. The in situ permeability was of the order of 10^{-8} m/s (radial drainage).

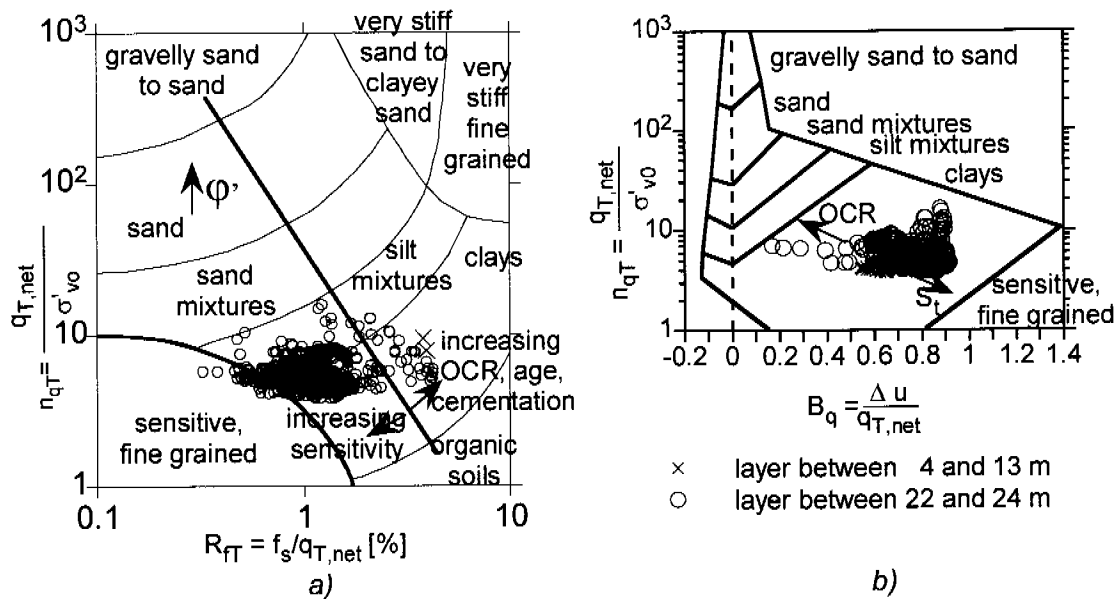


Figure 4-5: CPTU characterisation charts for B1 (Kreuzlingen) based on Robertson (1990).

Heil et al. (1997) had correlated field vane and borehole vane test data, with cone data for Kreuzlingen clay to give an N_{KT} of 17, which is higher than might be expected based on the recommendations of Yu and Mitchell (1998), although a sensitivity of 3 - 5 may be partially responsible for this. This value was used initially to determine the profile of the undrained shear strength against effective overburden stress for this project (Figure 4-6). An equation relating the variation of s_u with σ'_{v0} in these normally consolidated layers was then found to be:

$$s_u = 0.23 \cdot (\sigma'_{v0} + 15) \text{ [kPa]} \quad [4-7]$$

Although the $s_u - \sigma'_{v0}$ line should pass through zero for a normally consolidated clay, the resulting undrained shear strength s_u of 3.45 kPa is considerably small and can represent a certain influence of the crust at the surface. The line was set as a best fit to the mean values of the CPTU curve in the clay layers and constraining it through the origin would have resulted in an increase of $0.25 \cdot \sigma'_{v0}$.

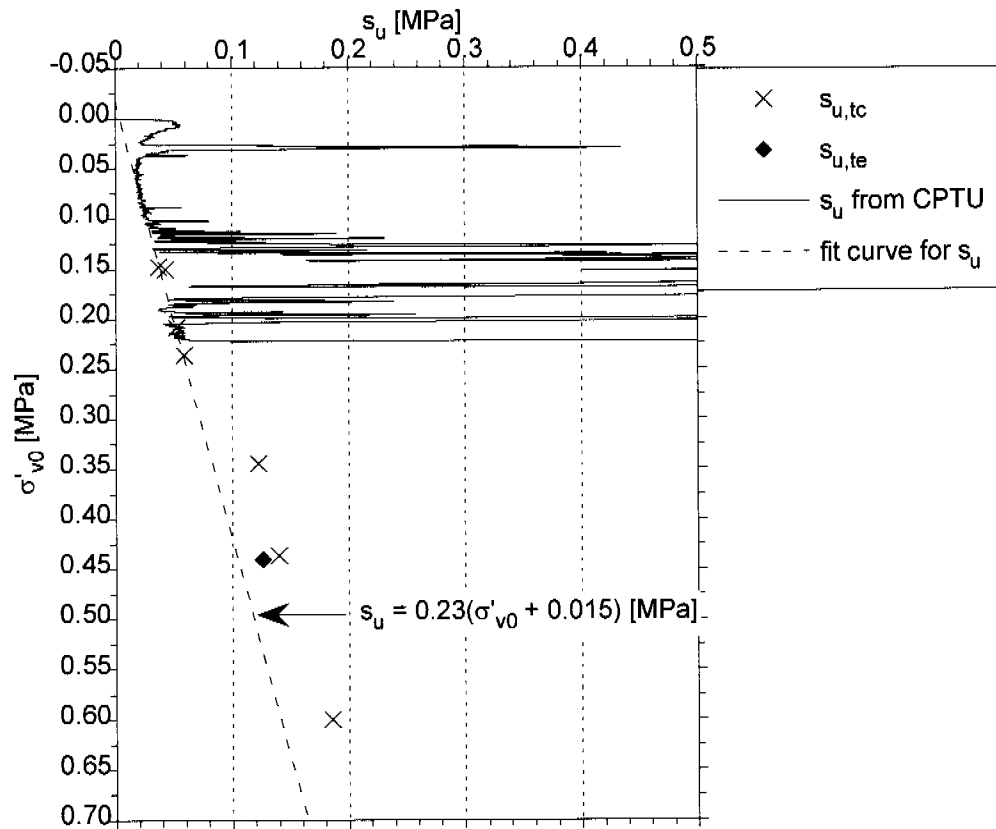


Figure 4-6: Undrained shear strength profile with effective overburden pressure from CPTU at B1

The undrained shear strength s_u determined from triaxial tests on undisturbed specimen of Kreuzlingen clay (discussed in more detail in Chapter 5) are also shown in Figure 4-6. The $s_{u,tc}$ refers to the isotropically consolidated undrained compression tests CIUC, whereas $s_{u,te}$ refers to the isotropically consolidated undrained extension tests CIUE and the values of σ'_{v0} for the triaxial results correspond to the consolidation stress during the test. It is apparent from Figure 4-6 that the correlation of the CPTU with the triaxial tests is valid for the upper part of the plot, until $\sigma'_{v0} > 0.25$ MPa. If this characteristic line (Equation 4-7) is extended to higher values of σ'_{v0} and compared with the data from the triaxial tests, it is however, apparent that Equation 4-7 gives lower values of the undrained shear strength. The value of 0.25 MPa for the effective vertical stress corresponds to a depth of ca. 25-30 m, which is probably within the typical scope of most geotechnical projects for which a prediction of undrained shear strength is needed. At higher stresses and depths the prediction of s_u based on $N_{KT} = 17$ could represent a lower bound and safer design. Lacasse et al. (2002) predicted lower cone factors for Norwegian clays, using high quality block samples as a reference. Lower cone factors results in higher s_u values and lower cost, and if

the reference tests are realistic, then the uncertainty is also reduced and safety guaranteed. The choice of the cone factor for the Swiss clays will be discussed further in Chapter 6.

Birmensdorf

Two CPTU measurements were carried out in Birmensdorf at 1m distance from each other. Results are given in Figure 4-7 a to d for f_s , q_T , R_{ff} and B_q with a full line for the first and with a dashed line for the second measurement. From ground level downwards, the results show a dry sandy crust to 0.5m depth and a light overconsolidated clayey layer to 4.3m. Both sets of measurements show a very consistent normally consolidated clay layer between 4.3 and 11.5m. q_T and f_s increase linearly, after almost passing through zero, with a constant value of B_q of either 0.65 or 0.8 in this normally consolidated clay layer. From 11.5m to 17.5m, the minimum values of q_T more or less follow the linear trend, however the peaks in q_T imply that the clay layers are again interspersed with layers of silts and sands. The low values of pore pressure ratio B_q (Figure 4-7d) confirm the presence of more permeable layers.

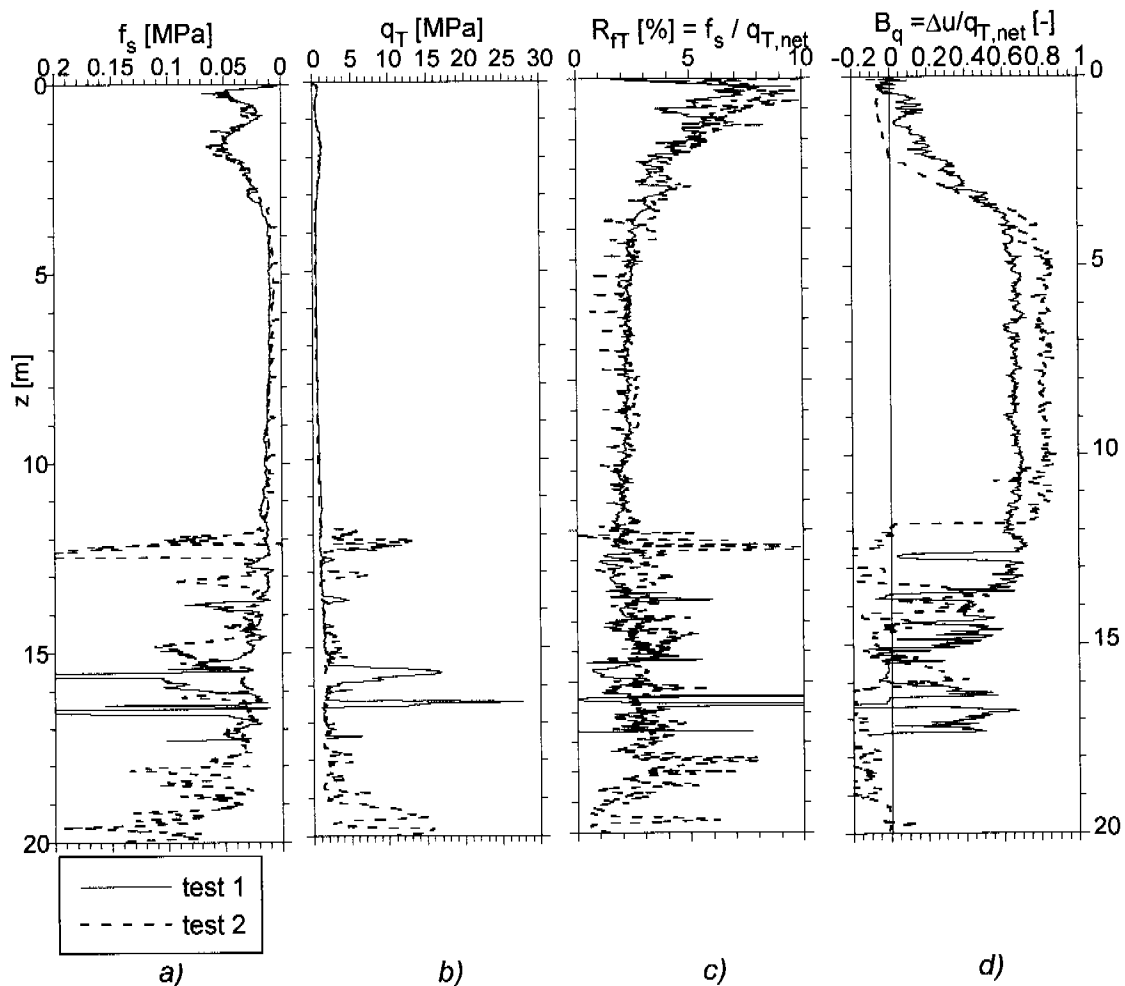


Figure 4-7: CPTUs in Birmensdorf: a) shaft friction f_s ; b) total pressure on tip q_T ; c) normalized friction ratio R_{ff} ; d) pore pressure ratio B_q .

In measurement 2 (dashed in Figure 4-7 a to d), two thicker sand layers can be picked out from 11.95 to 12.5m and from 14.7 to 15.5m. The moraine is reached below 19m depth, with gravelly sand and clayey sandy silt layers and some boulders, when both measurements were stopped because the cone tip resistance was too high for continued penetration. The pore water measurement of CPTU 2 is valid up to 12m depth, afterwards the filter stone may have been desaturated by the negative pressures in the sand layer, which clearly indicate a tendency of this layer to dilate during shearing.

Even if the two CPTUs were carried out only 1m apart from each other, the results below 11.5m are very different. The transition zone between the normally consolidated Seebodenlehm and the moraine is blurred and the sand layers are not always continuous over a large area but interleave with the lowest deposits of the clay. This implicates that the consolidation behaviour of the Seebodenlehm is influenced by radial drainage in this sand lenses.

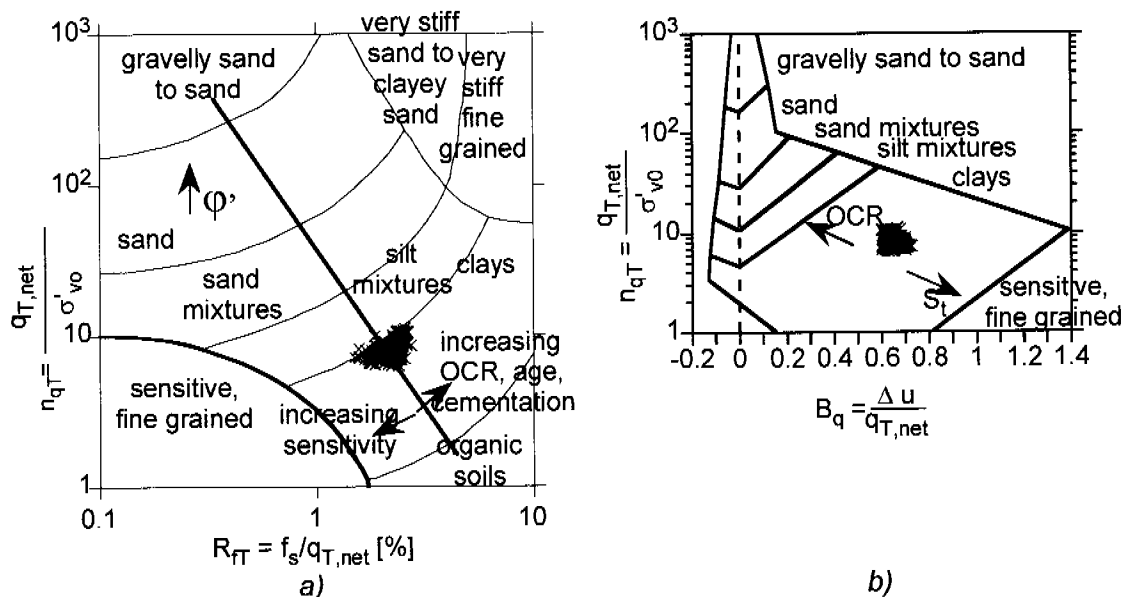


Figure 4-8: CPTU characterisation charts for depth 4.3m to 11.5m based on Robertson (1990) from results of the first CPTU measurement in Birmensdorf.

Charts based on Robertson (1990) of n_{qT} against R_{TT} (Figure 4-8 a) and of n_{qT} against B_q (Figure 4-8 b) depict a very homogeneous group of normally consolidated clays or silty clays for the layer between 4.3 and 11.5m from Birmensdorf. A comparison with Figure 4-5 a and b from Kreuzlingen shows higher homogeneity, lower sensitivity and a much lower proportion of silts for the Birmensdorfer Seebodenlehm, which is confirmed by the classification and mineralogical tests (Chapter 2; Plötze et al., 2003; Messerklinger et al., 2003).

In situ consolidation tests were carried out at 13.8 m and 19.78 m depth respectively in the first and second CPTU tests. Using cavity expansion theory (Torstensson, 1979) and a coefficient of compressibility obtained from oedometer tests at equivalent depth, an in situ permeability on the order of $9 \cdot 10^{-8}$ m/s was obtained (radial drainage). This value is nearly one order of magnitude

higher than in Kreuzlingen and can be explained by the more pronounced bedding of fine silt layers in the Birmensdorfer clay, which is also indicated by the higher frequency of the peaks and troughs in the B_q plot from Figure 4-7d.

Panduri (2000) correlated the borehole vane test data from 1992 with the CPTU data for Birmensdorf clay in his diploma thesis, and obtained an N_{KT} of 17, similar to Kreuzlingen. This value was then used to determine the strength profile for this site (Figure 4-9).

The linear equation relating the lower bound variation of s_u with σ'_{v0} from the CPTU data in these normally consolidated layers was then found to be (Panduri, 2000):

$$s_u = 0.285 \cdot (\sigma'_{v0} + 2) \text{ [kPa]} \quad [4-8]$$

The undrained shear strength of the Birmensdorf Seebodenlehm increases with depth or effective overburden pressure more than for Kreuzlingen Seebodenlehm, but the preconsolidation at the surface, indicated by the intercept of 2, is smaller than in Kreuzlingen.

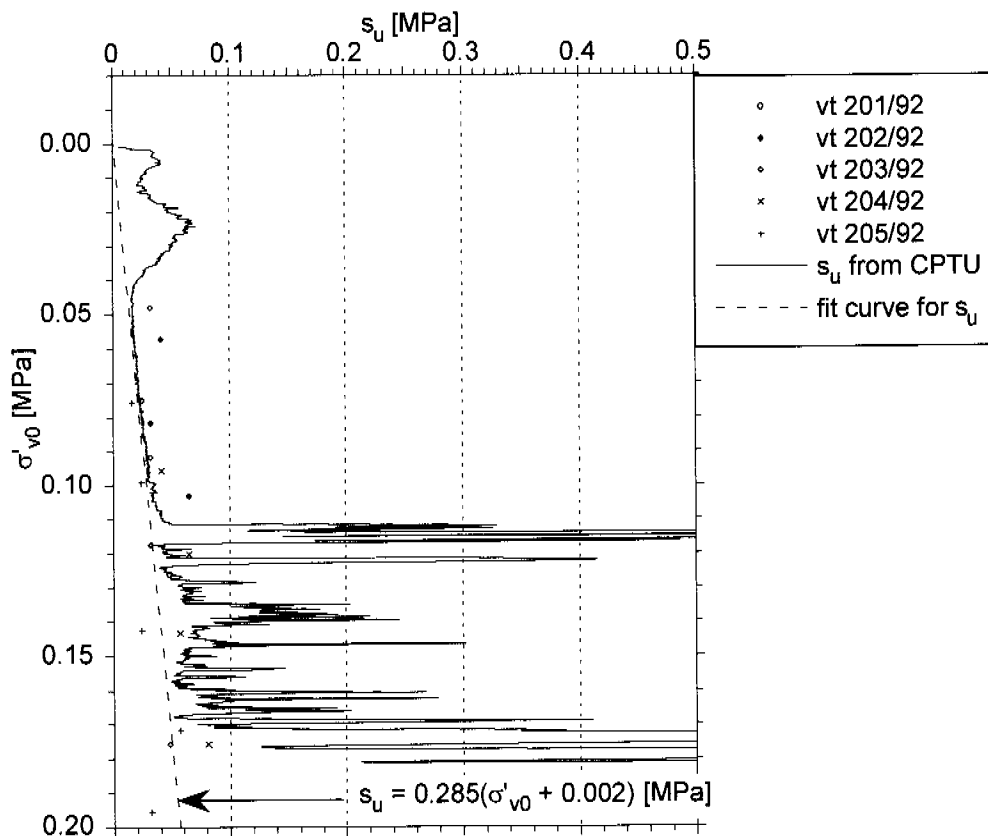


Figure 4-9: Undrained shear strength profile with effective overburden pressure from CPTU1 in Birmensdorf (Panduri, 2000).

4.3 Seismic tomography

4.3.1 Introduction

Geotechnical methods, e.g. triaxial testing of undisturbed borehole samples, allow laboratory determination of the static elastic moduli but the results suffer from large inaccuracies in the small-strain domain unless local strain transducers are used. On the other hand, results from seismic measurements (dynamic moduli) are representative for larger subsurface volumes and can provide average small-strain stiffness values. In this case however the values have to be determined indirectly via measurements of travel-times of seismic body waves and an assumed density distribution in the soil. Evidently, combined application of geotechnical and geophysical techniques seems to offer a reasonable approach to obtain reliable results (Maurer et al., 2000).

4.3.2 Transmission experiment

A stratigraphic profile of the key soil layers, as well as small strain estimates of the elastic parameters, were obtained from a seismic surface-to-borehole transmission experiment, carried out by the Institute of Geophysics IG (Maurer et al., 1998). Seismic energy was excited at the surface along a 40 m long profile that extended from the collar of borehole B1 to the north (Figure 4-10 a). The experiment was carried out late at night till early in the morning to minimise environmental noise (Figure 4-10 b). Seismic waves were recorded with a 3-component seismometer clamped to the borehole wall at various depths. Shot and receiver spacing were both 1 m. The seismic source consisted of 3 solid steel plates welded together to give a structure with a triangular cross-section (Figure 4-11). Spikes attached to the base plate ensured good coupling to the ground. Hammer blows on the left and right plates can be represented by force vectors. Addition of the two vectors yields a vertical point source and seismic records dominated by P-wave energy, whereas subtraction of the vectors simulates a horizontal force and seismic records dominated by S-wave energy.

Prior to the picking of the P- and S-wave onsets, a component rotation was performed by the IG team. As indicated in Figure 4-11, the new coordinate system is oriented such that one component is perpendicular to the incident P-wave fronts (normal component) and one component is perpendicular to the shot profile (transverse component). Effects of the component rotation are illustrated in Figure 4-12. The signals from the left and the right hammer blow on the normal component (Figure 4-12a) should be almost identical (supposing that the hammer blows were identical), which is indeed the case. Addition of the two normal components (Figure 4-12c) improved the signal-to-noise-ratio, and the first-arriving P-wave could be identified clearly.

The transverse components (Figure 4-12 c) exhibit a polarity reversal for the wave-trains between 75 and 100 ms. Such a reversal identifies this seismic phase as an SH-wave, which is expected to be polarized perpendicular to the profile line (e.g. Aki and Richards, 1980). Note that later phases at about 100 ms are polarized in the profile-borehole plane, and show no polarity reversal and thus most likely represent Rayleigh waves (Aki and Richards, 1980). Subtraction of the "left" and "right" transverse components (Figure 4-12 d) reveals unambigu-

ously the first arriving SH-wave train, which could be hardly identified on the original traces. The picked P- and S- waves onset were inverted for P- and S-wave velocity-depth functions, which were parameterised as a stack of 15 layers with fixed thickness.

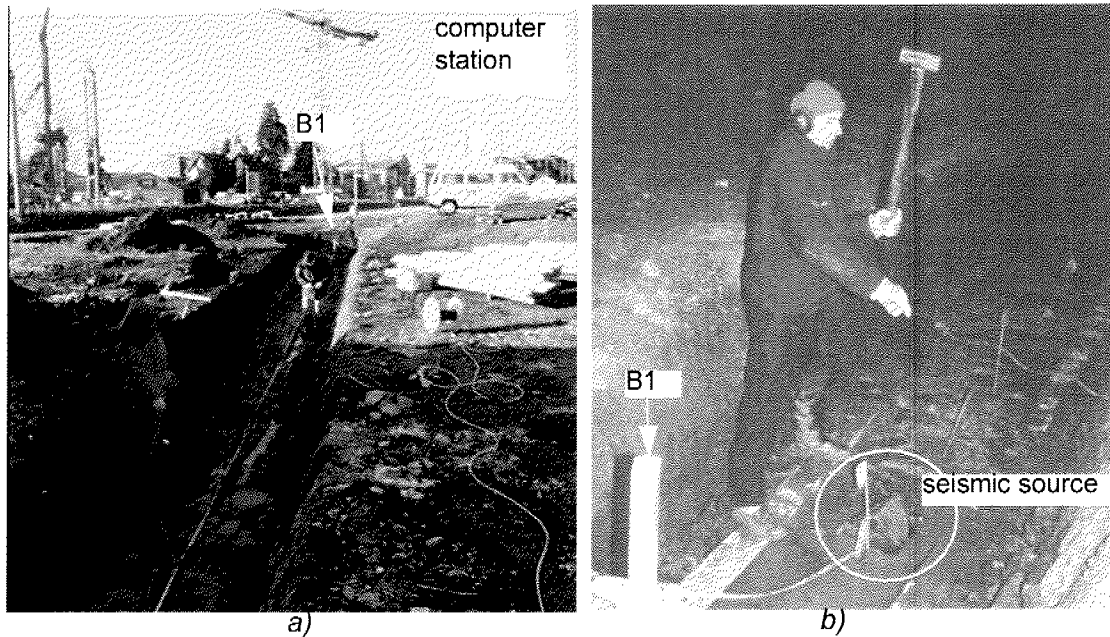


Figure 4-10: a) Preparation for the seismic experiment, b) Seismic source in place, in preparation for the hammer blow.

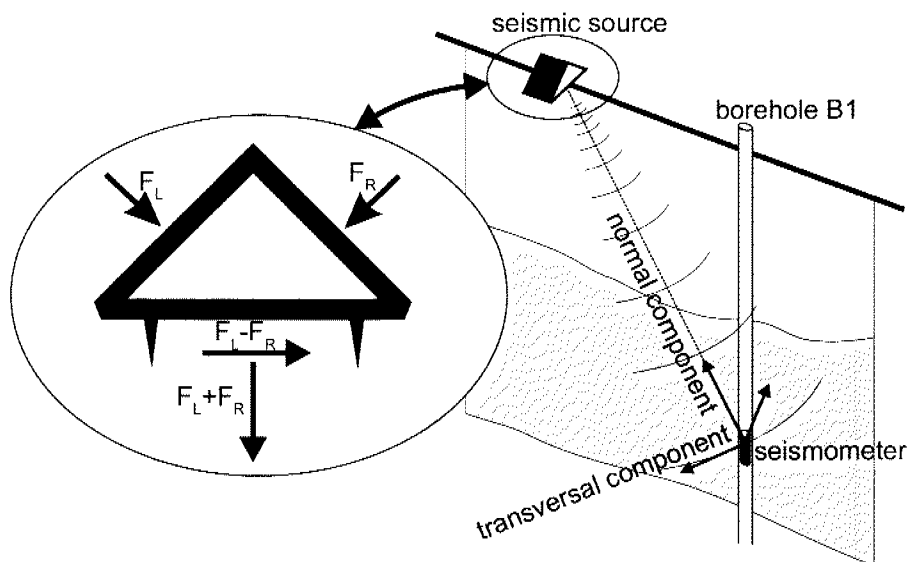


Figure 4-11: Schematic overview of the seismic transmission experiment. The expanded view shows the source, the force directions of the hammer blows (F_L and F_R) and the resulting force vectors for added and subtracted signals (Maurer et al., 1998).

4.3.3 Results

A total of 962 P- and 397 S-wave onsets were picked from the recorded seismograms. They were inverted for P- and S-wave velocity-depth functions, which were parameterised as a stack of 15 layers with fixed thickness (Maurer et al., 1998). Figure 4-13 a to e shows the results of the experiment.

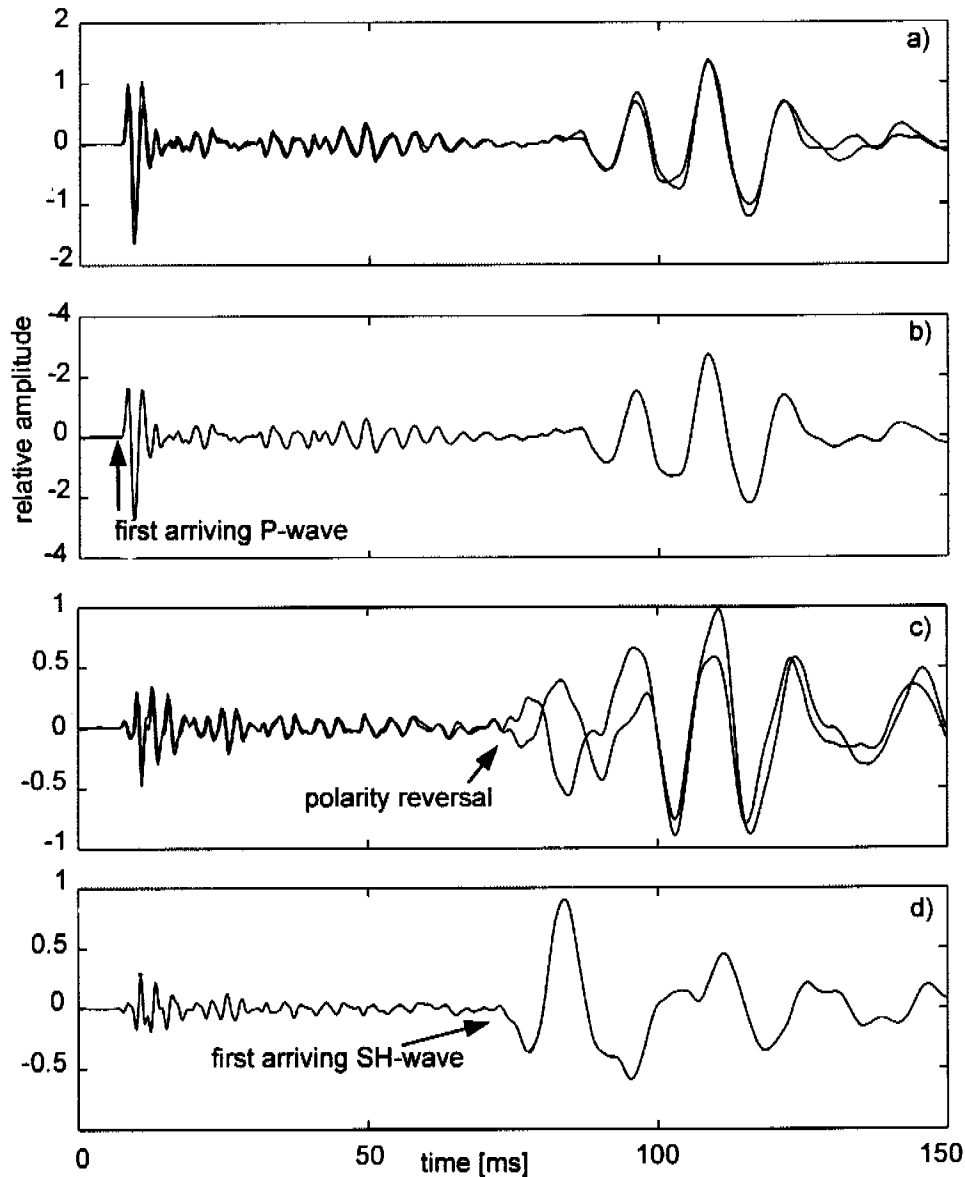


Figure 4-12: Seismographs recorded with a source at 10 m distance and 4 m depth. a) normal-component seismographs from the left and the right hammer blows, b) addition of the normal components, c) equivalent transverse-component seismographs, d) subtraction of the transverse components (Maurer et al., 1998).

Near-surface P-wave velocities (Figure 4-13 a) are about 1200 m/s. At a depth of 4 m the velocity increases to 1500 m/s, then gradually to 1700 m/s at 28 m depth. S-wave velocities (Figure 4-13 b) are approximately 150 m/s within the uppermost 8 m, and lie in the range of 250 - 300 m/s below 15 m depth. Very high Poisson's ratios of 0.480-0.495 and extremely low shear modulus values

G_{\max} of 45-150 MPa (Figure 4-13 c and d) were derived from the velocity-depth-functions, based on an assumed bulk unit weight of 18.0 kN/m^3 , as obtained from the borehole samples.

Stratigraphy determined from the seismic measurements (Figure 4-13 e) correlate up to a depth of 15m with the data from the CPTU and the borehole log. The uppermost 15 m are deduced to consist mainly of normally consolidated lacustrine clays. These sediments are expected to exhibit low shear modulus G values. Between 15 and 22 m, coarser material is expected, as indicated by the profiles in Figure 4-13. These units manifest themselves with increased G values. Between 22 and 25 m the lacustrine clay units reappear in the CPTU profiles (Figure 4-4). The resolution of the seismic data is insufficient to identify this rather thin clay layer unambiguously, although the shear modulus values determined from the seismic measurements seem to decrease at about 24m depth. The moraine, which should exhibit increasing shear modulus, was identified from the inspection of the borehole log at B1 and from the CPTU results at about 25 m depth. The seismic measurement however shows decreasing values of G from 24m to 30m, indicating decreasing resolution at the base of the borehole.

The comparison between the shear modulus obtained from the seismic tomography, and the shear modulus obtained by monotonic and dynamic loading in the triaxial apparatus will be discussed in Chapter 6.

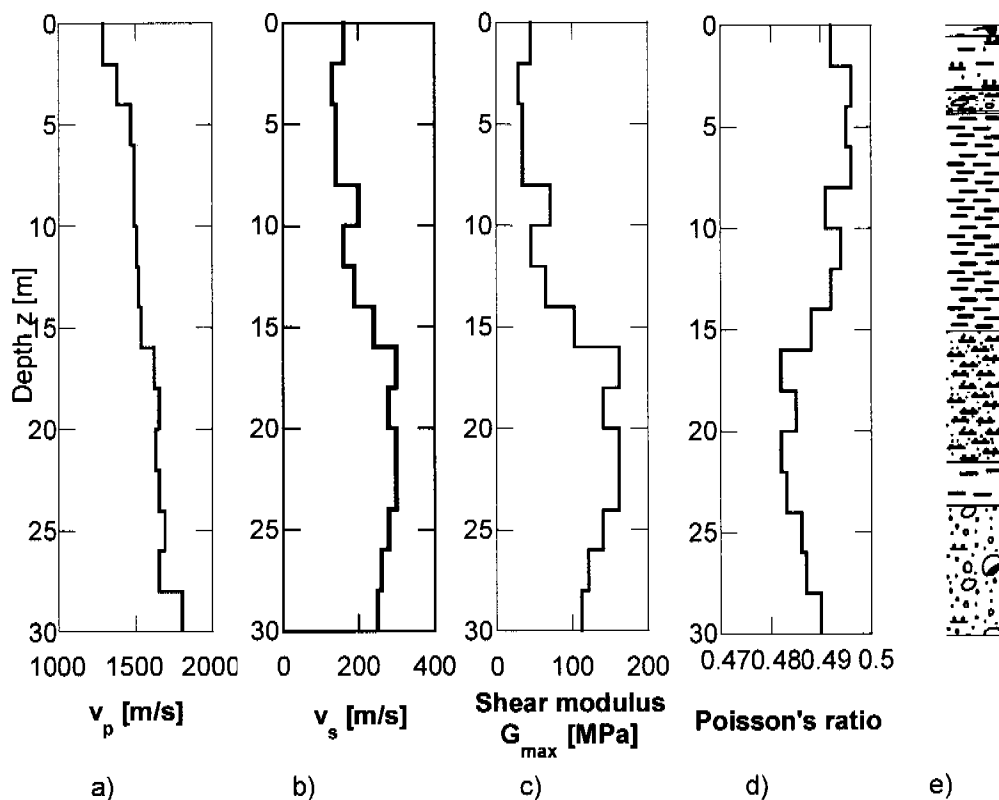


Figure 4-13: Wave velocity-depth functions and elastic parameters from seismic experiment, stratigraphy from borehole log at B1 in Kreuzlingen (Chapter 3.2) (Maurer et al., 1998).

Seite Leer /
Blank leaf

Laboratory testing

5.1 Triaxial stress path tests

5.1.1 Testing equipment

The first series of triaxial tests on Seebodenlehm was performed in 1998 in a standard apparatus, which is described in Fleischer (2000) and Panduri (2000). The second series of triaxial tests was performed in the triaxial apparatus designed and constructed at the Institute for Geotechnical Engineering in 1999/2000. This new equipment is capable of performing fully automated stress and strain controlled tests and will therefore be described in detail in this chapter.

The predecessor of this triaxial apparatus was designed for triaxial tests on snow (Bartelt and von Moos, 2000; von Moos, 2002; von Moos et al., 2003). The original design was then adapted to suit tests on soft soils as well as on frozen soils (Arenson, 2002). The air controlled cell pressure acting on the snow triaxial sample was replaced by a standard system using water as cell fluid. In contrast to the frozen soil triaxial apparatus, volumetric deformations in the sample are measured by a separate system, which can also control the back pressure in the sample. The adaptation of the prototype apparatus for snow and frozen soils to the use as a common soil testing apparatus (Arenson et al., to be published) took quite a long time and several test runs for equipment development and calibration and for solving the “teething” problems of the apparatus and for solving problems due to the procedure of installation of soft clay specimens in the cell. The results of these developments are summarised in following sections which describe the final mechanical and software set up inclusive of the bender elements testing device, which the author has additionally implemented in the apparatus. Also the testing procedures including the sample preparation, the testing programme adaptations and the interpretation procedures (Chapter 5.1.2) are results of the development time spent on the apparatus, which took about 1 year .

The triaxial apparatus was placed in a temperature controlled room, whose temperature was fixed at 18° C +/- 1°C.

Mechanical set up

Sketches of the triaxial apparatus are given in Figure 5-1 and Figure 5-2. In the following text, the numbers in brackets refer to these figures.

The device is computer controlled, with software developed at the Institute for Geotechnical Engineering, based on National Instrument's control and data acquisition software Lab View, Version 5.1. Three Phytron ZSH 57/2.200.4.2 (type DCX-AT200) stepper motors control axial force and displacement (2, middle), back pressure and pore volume change (2, left) and cell pressure and cell volume change (2, right). The stepper motors use an additional gear box, with a reduction gear ratio of 16, to regulate the advancement of the lead screw (3). The shaft coupling (4) between the gear box and the screw reduces stresses in the system. The lead screw, which has a 1 mm pitch, moves the loading frame (5) downwards or upwards by rotation in a satellite roller nut. With this combination of reduction gear ratio and pitch of the satellite roller screw, the motor needs 6400 steps to run 1 mm (400 steps per rotation), which corresponds to $0.15 \mu\text{m}$ per step.

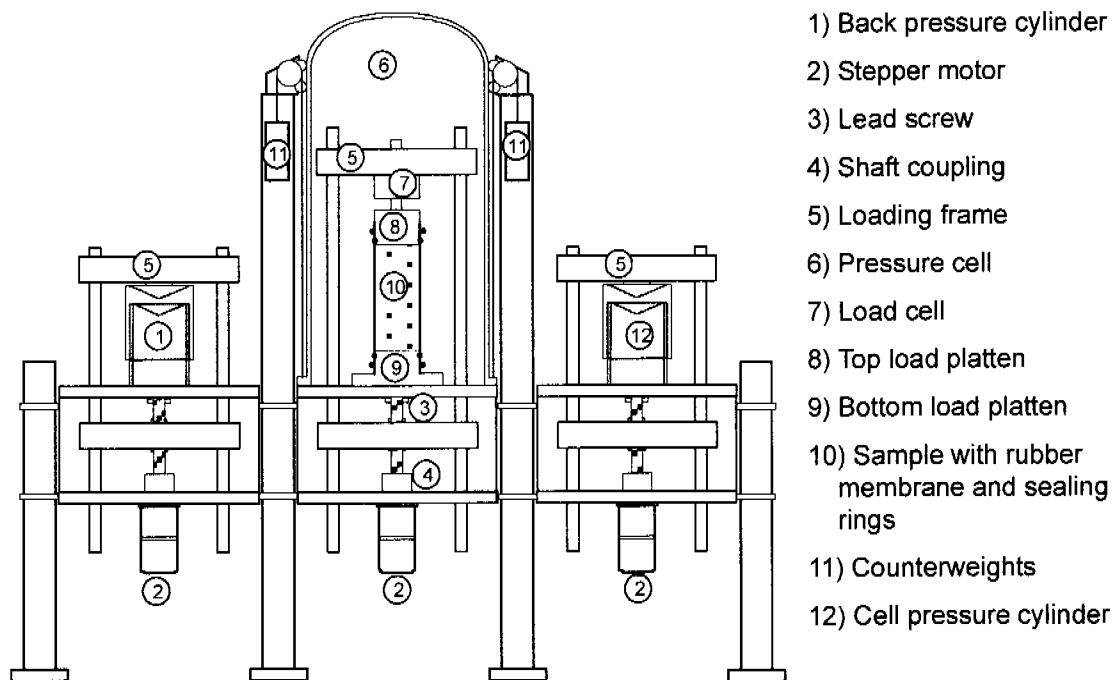


Figure 5-1: Triaxial test apparatus: mechanical set up

The tie bars of the loading frame (5) for the axial force system pass through the base plate of the pressure cell (6) through an air-tight interface. The load cell (7) is fixed to the upper cross beam of the loading frame, i.e. the friction between tie bars and base plate does not affect the axial force readings of the load cell. However, the cell pressure that acts on the area, on which the load cell is mounted to the frame, is guided out of the cell and therefore compensation is necessary. The following correction value to the axial force readings back pressure was determined for this device:

$$- 0.3276 \text{ N/kPa}_{\text{cell pressure}}$$

This device has been constructed with top and bottom load plattens for a specimen diameter of 54.6 mm. The top load platten (8) is connected beneath the load cell with the displacement transducer (16) mounted on a bracket fixed in-between them. The compliance of the top and bottom load platten can slightly affect the measurement of the displacement transducer. However, the stiffness of soft clay is considerably lower than the stiffness of steel, therefore this influence was not considered. Bedding at the end of the sample is also known to reduce the vertical stiffness derived from this measurement of displacement (Atkinson and Salfors, 1991). The bottom load platten (9) is fixed to the base plate of the cell. Drainage from the top and bottom plattens is assured by brass filters of 0.8 mm diameter and by PVC pore water tubes, which lead through the base plate of the cell into two pore pressure transducers (13/14) and forward to the back pressure cylinder (1). In the middle of the plattens, piezoceramic elements (enel.hydro) are installed. The rest of the platten surface in contact with the specimen is smooth. The pore water pipes, between sample and back pressure cylinder, do not need to be removed and hence stay saturated during mounting of the sample. All stepper motors can be controlled manually with a joystick for the placement of the sample. A special mount (Figure 5-3) is used first to hold the sample centrally in the correct position, while the top platten is driven downwards to make contact with the sample, and then to secure the membrane with O-rings for correct sealing of the sample.

The cell is closed and filled with deaired water from a barrel using a pump. The filling process has to be carried out slowly and carefully, to avoid air in the cell. Counterweights (11) are placed within the legs of the apparatus in order to assist the opening and closing of the 20 kg pressure cell without shocks or vibrations for the sample. The pressure cell is sealed to the base plate with a pre-stained O-ring and screwed down to the base plate with 12 M14 screws, allowing a cell pressure of up to 1 MPa.

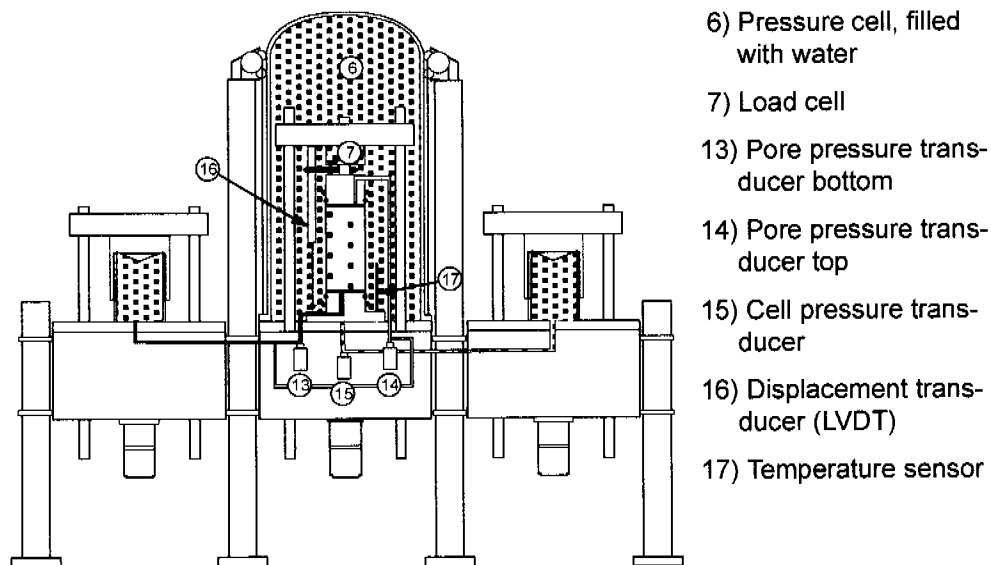


Figure 5-2: Triaxial test apparatus: test control set up.

A conical piston has been used for the volume measurement devices within the cell pressure and the back pressure cylinders (12 and 1). The piston has an inverted cone at its upper face with a channel at the base, which leads to the cell or pore water system respectively. The top is the counterpart to the inverted-cone. The cylindrical shell around the piston is sealed to the piston cap by an O-ring and to the piston by two O-rings, which are set into rills in the metal host. If the system is not completely saturated, air bubbles will flow up the sides of the cones where the de-airing opening is mounted. In this manner just water will flow downwards to the cell or pore water system. One step of the stepping motor corresponds to a volume change of 1.227 mm^3 (this corresponds to $4 \cdot 10^{-4}\%$ of the total volume for a specimen of 2500 mm^2 base area and 120 mm height). PVC tubes connect the cylinders to the cell or pore water system with the pressure transducers under the base of the cell (13/14/15). The pore water system is split before the transducers into two tubes, respectively for the top and bottom drainage. Pore water pressure can thus be measured separately for the top and bottom drainage. Both drainage tubes can be reconnected by means of valves in order to put a constant back pressure on the sample.

Cell volume is measured in the same manner as within the back pressure cylinder and is used to control and detect unexpected events such leakages, that leads to emptying of the cell pressure cylinder. A correction of the cell volume has to be considered when moving the loading frame within the cell. This correction is a function of the diameter of the frame support rods. For the system used herein, the cell volume changes exactly 1.4 cm^3 per millimetre axial displacement.

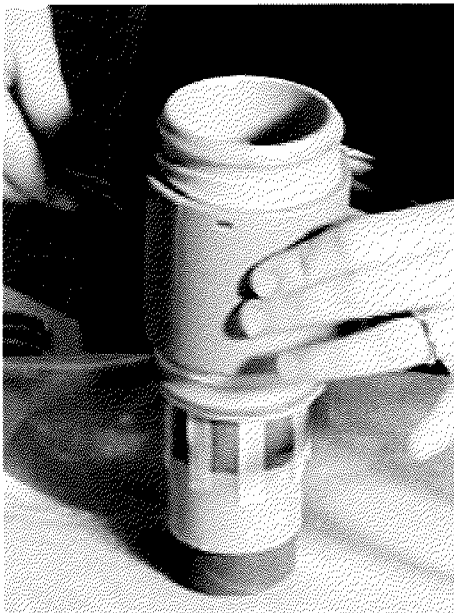
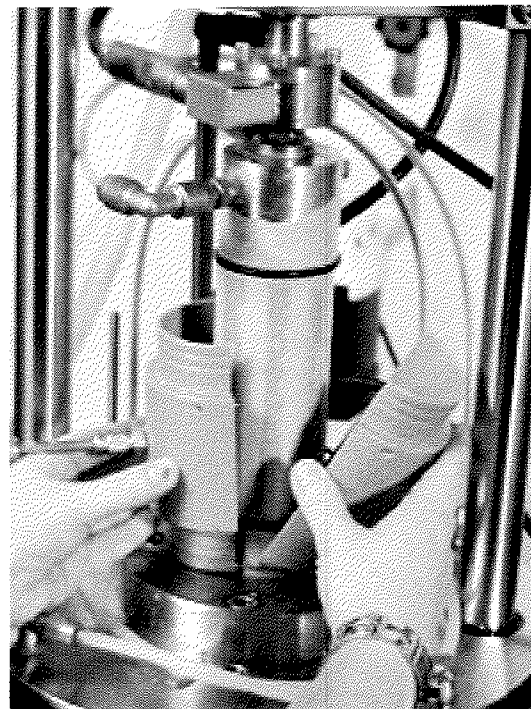


Figure 5-3: *Mount for the correct positioning of the sample*



Two temperature sensors measure the cell water temperature close to the sample and the room temperature. These data are logged and stored in the computer with all other sensor data.

Electronic set up

Each transducer signal is amplified in a junction box. A 16 bit AD board with 8 channels digitizes the signals prior to storage in the computer. The stepper motors are controlled by a motion controller and a motor interface, which has a switch that limits the maximum allowed load and displacement of the stepper motors. A manual control device, in the form of a joystick, is connected to the motor interface, in order to control manually the position of the stepper motors during installation of the specimen. An emergency stop button enables the test to be stopped manually.

Software set up

Different control modes are possible for each control unit (cell pressure, back pressure and axial force):

- *Panel Mode*: The control of the unit is possible with the joystick.
- *Move Velocity Mode*: The displacement rate in mm/s can be specified.

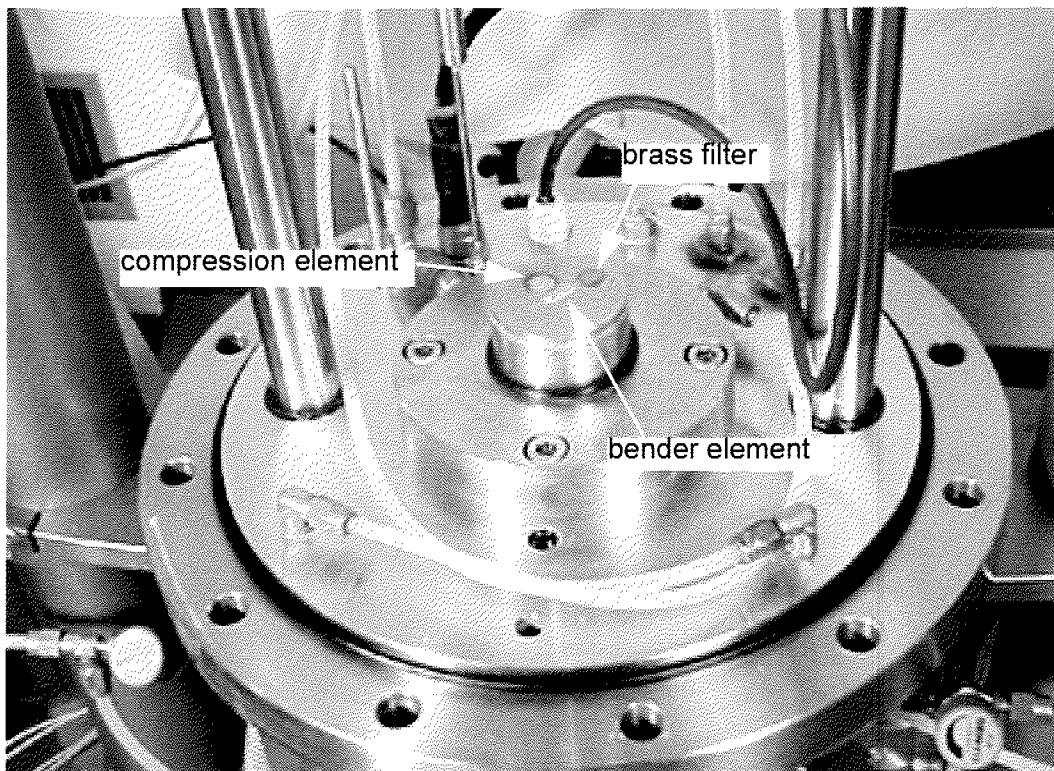


Figure 5-4: Cell base and bottom platten with piezoceramic elements.

- *Move Position Mode*: The displacement rate in mm/s and a relative or absolute position of the piston can be specified. This mode corresponds to a classical strain controlled shear test.
- *Regulating Mode*: A stress or force ramp can be defined by giving a rate in kPa/s or in N/s and the maximum stress in kPa or the maximum load in kN. This is the standard mode used to regulate back

pressure in the sample and to hold it constant during the test or to regulate the cell pressure during an shear test.

- *(X · Q + Y) Mode:* This mode can be chosen just for the cell pressure unit. To run stress path tests with a defined stress ratio $\eta = q/(p')$, the axial force and cell pressure ramps need to be coupled. In this mode, the cell pressure will depend on the measured deviatoric force Q, by means of a percentage factor X and of a constant Y in kPa. The factors X and Y can be calculated easily by knowing η and the back pressure in the test. In this way, if the axial force is controlled by a force ramp in N/s up to a maximum value in kN in Regulating Mode, the cell pressure will follow also a pressure ramp corresponding to the chosen η ratio. This mode was used in the present work to run drained stress path tests. Although Q was used as the direct control quantity for the inclination η of the stress path, the influence of change in specimen's area during the drained consolidation stages did not appear to be significant. Goal η values and post-test calculated η values varied typically by 0.01 and by 0.05 at an absolute maximum.
- *K₀ mode:* This mode can be chosen just for the cell pressure unit. The software compares the change in pore water volume measured by the pore water cylinder with the theoretical volume change in case of no lateral straining $\Delta V = A \cdot \Delta h$. Then it adjusts the cell pressure so that these two volumes are equal. In a K₀ test, back pressure and axial force have to be controlled in Regulating Mode.

The software controls the progression of the test with a PID-control device (Proportional, Integral, Differential). It is possible for the user to specify the regulating parameters, which control how the system corrects errors between nominal and actual value of the considered measurement. The controlling parameters are as follows:

- *The proportional parameter*, which, when multiplied by the error (nominal - actual) in digits, results in the rate at which the stepper motor attempts to eliminate the error (the bigger the error, the faster the rate).
- *The integral parameter*, which, when multiplied by the time integral of the error results also in a rate of correction so that the error will not increase with time.
- *The differential parameter*, which, when multiplied by the time differential of the error results in a rate of correction so that the instantaneous error is not too large.
- *The deadband*, which is the minimum accepted nominal error minus the actual errors in digits.
- *The integral limit*, which limits the results of the integral parameter to increase the stability of the control system.

During a test, the software is able to display the measured data in a value table or on different graphs. Both table and graphics are updated on-line with the same frequency as the storage rate. It is possible to view up to four graphics at the same time. The graphics can be specified by the user to suit their needs. In addition to the measured values, variables can be defined, which are then calculated from measured data and geometrical data, such as those based on the sample dimensions at the start of the tests. The calculated values can be evaluated also in the on-line graphics and will be stored together with the measured data. The software stores measured and calculated values with a minimum rate of 5 sec. The user can specify the sampling rate for each test stage during the test.

Table 5-1 and Table 5-2 give an overview of the technical details of the various measurements:

| transducer | range calibration | accuracy | resolution | temperature range | sensor |
|------------------|-----------------------|---------------------|------------|-------------------|---------------|
| displacement | 100 mm 10 mm/V | ± 0.1% of end value | 0.003 mm | -20 – 85°C | HBM WA100 |
| load cell | 5 kN 1 kN/V | ± 0.1% of end value | 0.2 N | -10 – 70°C | HBM U2B |
| PWP top | 1 MPa 200 kPa/V | ± 0.1% of end value | 0.03 kPa | -15 – 85°C | SENSTEC 8267 |
| PWP bottom | 1 MPa 200 kPa/V | ± 0.1% of end value | 0.03 kPa | -15 – 85°C | SENSTEC 8267 |
| cell pressure | 1 MPa 200 kPa/V | ± 0.1% of end value | 0.03 kPa | -15 – 85°C | SENSTEC 8267 |
| cell temperature | -45 – 100°C 10°C/V | < 0.1°C | 0.003°C | | PHILIPS PT100 |

Table 5-1: *Triaxial test apparatus: instrumentation.*

| transducer | range calibration | resolution | velocity | movement rate | pressure or force |
|----------------------------|--|-----------------------------------|-----------------------|-----------------------|-------------------|
| cell volume | 720 cm ³ 1.227 mm ³ / step | 0.02 cm ³ < 0.5 kPa | 0.00001 – 10 kPa/s | 0.0024 – 2.1 mm/s | 0.5 – 1000 kPa |
| axial force | 92 mm 0.15625 µm/ step | < 0.003 kN | 0.00001 – 100 N/s | 0.05 mm/d – 1 mm/s | 0.005 – 5 kN |
| PW volume back pressure | 720 cm ³ 1.227 mm ³ / step | 0.02 cm ³ < 0.5 kPa | 0.00001 – 10 kPa/s | 0.0024 – 2.1 mm/s | 0.5 – 1000 kPa |

Table 5-2: *Details of the stepper motors, type DCX-AT200.*

The transducers have been calibrated at the beginning of the test series by adjusting their signal output to the values given in Tables 5-1 and 5-2. The zero drift of the transducers' output over time has been checked before each test and the signal has been adjusted. Finally the temperature effect on the signals from the transducers is minimised by controlling the room temperature to $\pm 1^\circ\text{C}$.

Bender element test

The initial or maximum shear modulus of a soil G_{max} is an important parameter for a variety of geotechnical design applications. This modulus is normally associated with shear strain levels of about 0.001% and below (Carubba and Maugeri, 1991, Atkinson and Salfors, 1991, Burghignoli et al., 1991, Lo Presti, 1991 and Tatsuoka and Kohata, 1995). In bender element tests, the maximum shear strain was estimated by Dyvik and Madshus (1985) to be less than 0.001% so that the shear modulus determined is taken as G_{max} and is relevant for very small strains. The dynamic measurement of G_{max} using bender elements can be done at any stage of the triaxial test without interfering with the particular test.

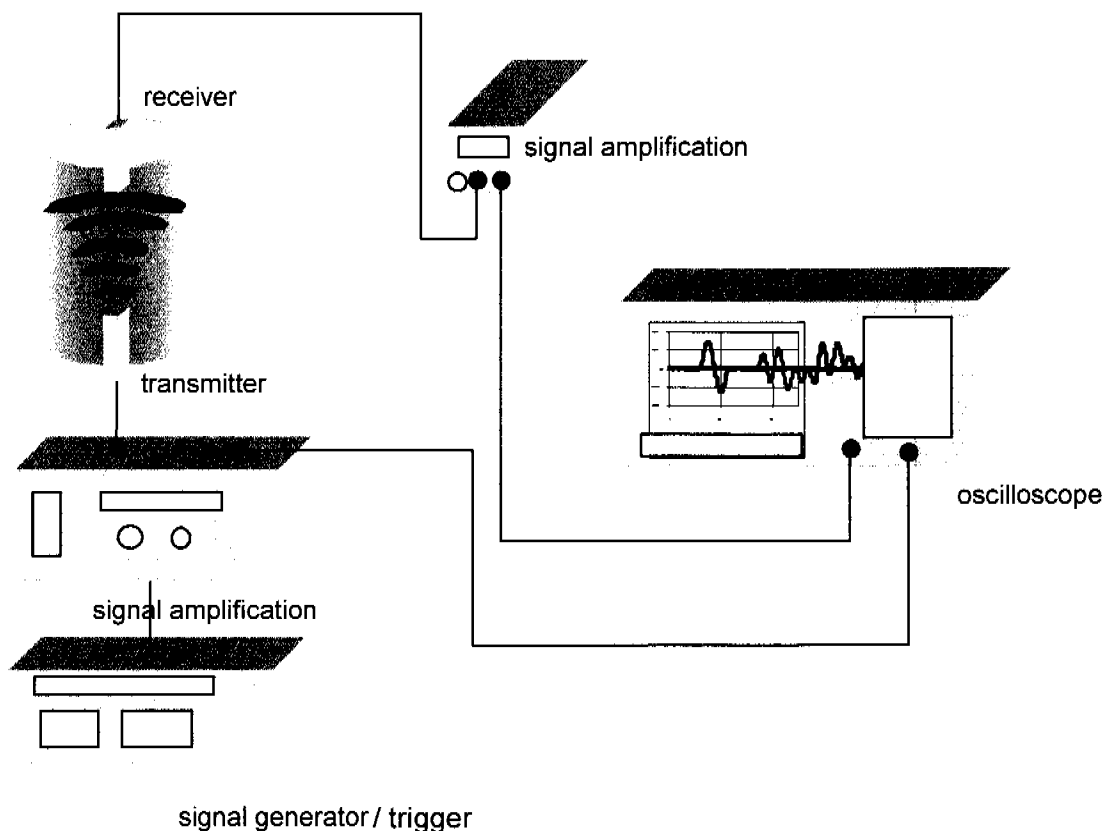


Figure 5-5: Schematic set up of bender test equipment

The piezoceramic bender element is an electro-mechanical transducer which is capable of converting mechanical energy (movement) either to or from electrical energy. The transmitter element is mounted in the pedestal and the receiver element in the top cap (Figure 5-4). The bender elements were mounted and sealed

in the top and bottom cap of the triaxial apparatus (by the enel.Hydro company, Bergamo, Italy). The signal amplification unit is also a product of the enel.Hydro company.

During a G_{max} test, the travel time of the dynamic shear waves from transmitter to receiver is measured with a digital oscilloscope (Lecroy 9310) (Figure 5-5).

G_{max} is related to the shear wave velocity v_s in an homogeneous, isotropic elastic medium by:

$$G_{max} = \rho \cdot v_s^2 = (\rho \cdot (l^2/t^2)) \quad [5-1]$$

where ρ is the density of the soil at the time of measurement, l the effective travel length (not the same as the initial or actual length of the specimen L_0 or L respectively) and t the travel time. The shear wave bender elements protrude 2 mm into each end of the soil specimen. Different methods have been used to determine the effective travel distance between the bender elements (Viggiani and Atkinson, 1995, Mohsin and Airey, 2003). There is good evidence that the effective travel length is the distance between the tip of the transducers and not the actual height of the specimen. When using bender elements the correct alignment and polarity is very important. By placing the bender elements in contact, the correct polarity can be checked and time lag of the electronic equipment determined (Dyvik and Madshus, 1985, Mohsin and Airey, 2003). The observations made during this study indicate that the time lag was very small. Tests with specimens of different geometry and dimensions indicate that the wave reflection from the sample boundaries is of great importance for conventional triaxial sample geometries, and that a significant near field effect can be observed (Blewett et al., 2000, Mohsin and Airey, 2003). Therefore it is important that the separation between the transmitter and the receiver is sufficient to place the transmitter in the far field (Theron et al., 2003). This implies a spacing of more than one wave length between the transmitter and the receiver (for instance if the wave needs 300 ms to travel from transmitter to receiver, than its frequency should be equal to minimum 5 kHz).

The principle behind the bender element test is very simple, but unfortunately detection of the time delay is not straightforward and significant errors can arise (Viggiani and Atkinson, 1995). Errors in the initial length of the specimen L_0 and in the measurement of the change of length ΔL induce uncertainty in density of the specimen and travel length of the shear waves. The instant of the transmission of the wave is clearly defined by the triggering oscilloscope, whereas the specification of its arrival time depends on the waveform used, on the interpretation procedure and on the disturbance due to other waves, which also travel in the soil specimen (Viggiani and Atkinson, 1995) (Figure 5-6). For instance, Salinero et al. (1986) show that the first deflection of the signal may not correspond to the arrival of the shear wave but to the arrival of the so-called near-field component, that travels with the velocity of a compression wave (Brignoli and Gotti, 1992; Mancuso and Vinale, 1988).

This has resulted in different researchers using a range of methods to obtain the "correct" travel time (Jovicic et al., 1996, Mohsin & Airey, 2003). Viggiani and Atkinson (1995) have suggested the use of frequency domain analysis to deter-

mine the phase angle indirectly. Blewett et al. (1999) used phase-sensitive detection techniques to determine it directly. Jovicic et al. (1996) recommended using the first arrival of the shear wave. This method requires however great care to reduce the system noise, a sine wave pulse is recommended and the pulse frequency must be adjusted to minimise the near field effects. During this study, this simple interpretation procedure was used, determining the arrival of the shear wave by the point of the first sharp inversion (Figure 5-7).

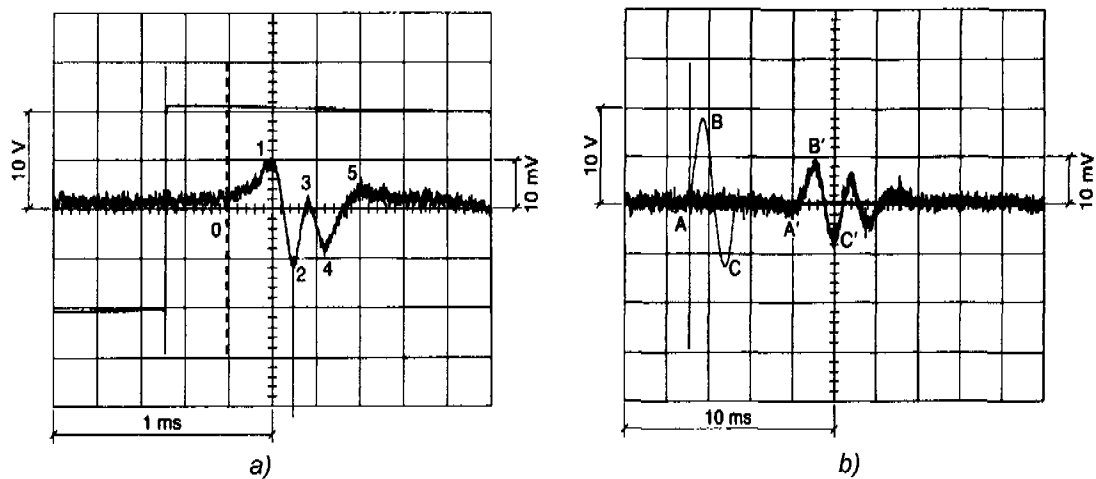


Figure 5-6: Typical oscilloscope signals from a bender element test a) with a square pulse excitation and b) with a sine pulse excitation (Viggiani and Atkinson, 1995)

According to Viggiani and Atkinson (1995), this analysis would overestimate G_{max} by about 14%, taking the true travel time as the time defined by numerical analyses of the waveforms. This error lies in the same order of magnitude as the combined errors due to travel distance and density. On the basis of the error propagation law of systematic errors, the potential relative error in G_{max} is given by:

$$\frac{\Delta G_{max}}{G_{max}} = \frac{\Delta \rho}{\rho} + \frac{2 \cdot \Delta l}{l} + \frac{2 \cdot \Delta t}{t} \quad [5-2]$$

So the potential worst case scenario is an error in G_{max} of the order of magnitude of 30%. However Mohsin and Airey (2003) show with bender element tests on sand in the triaxial apparatus, that there is an optimum frequency, below which the first arrival method gives an accurate travel time. This frequency is stress dependent, and as the effective confining pressure increases from 20 kPa to 100 kPa to 1000 kPa, the optimum frequency increases from 8 kHz to 13 kHz to 15 kHz. In the present study, the first arrival times of three sine wave pulses with frequency 5, 10 and 20 kHz respectively, have been compared always to determine the correct arrival time. For the stresses used in this tests, these frequencies were in the optimum range and the time detected with the first arrival method is thought to be reliable. Recently, sine wave pulses have been shown to give more reliable time measurement than square wave pulses. Blewett et al. (2000) pointed out that this is primarily because they reduce the frequency com-

ponents and thus minimise any frequency dependence on wave velocity. It is also visible from Figure 5-7 that the first arrival of the sine wave is easier to detect than that of the square wave.

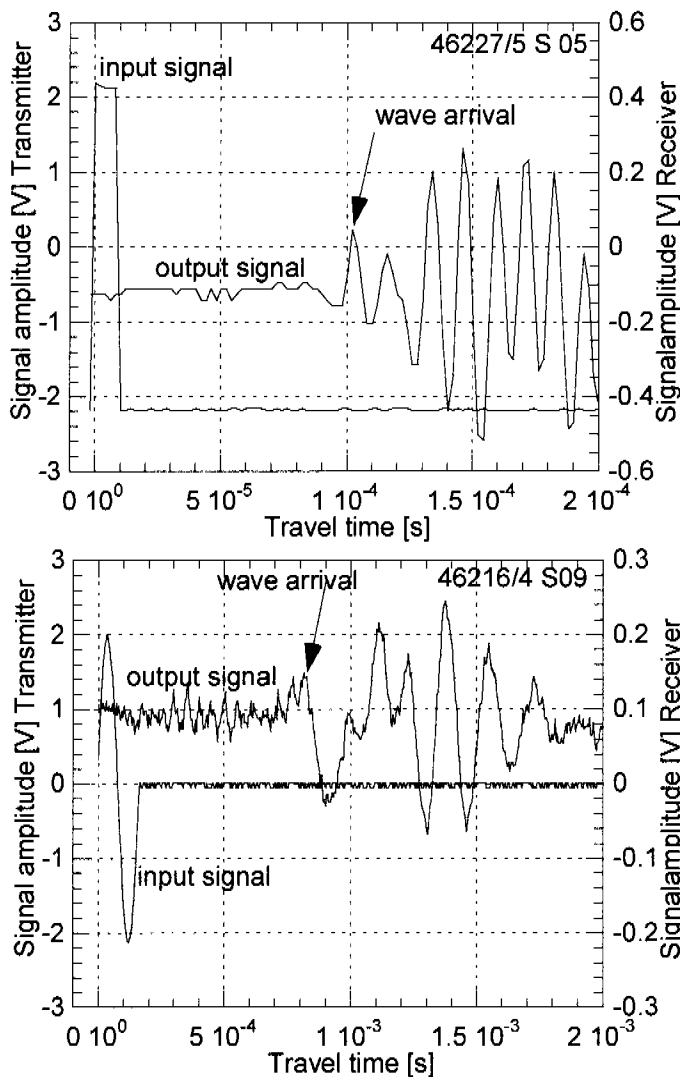


Figure 5-7: Two oscilloscope signals from a bender element test with a square pulse excitation (above) and with a sine pulse excitation (below), for Kreuzlingen clay samples.

A compression element is also shown in Figure 5-4. This is a piezoceramic transducer, which produces compression waves instead of shear waves. The compression wave velocity in an homogeneous, isotropic elastic medium is given by (Mavko et al., 1998):

$$v_P = \sqrt{\frac{K + (4/3) \cdot G}{\rho}} \quad [5-3]$$

which consequently means that the bulk modulus K can be extracted from measurement of density and the two wave velocities v_S and v_P (Equation 5-4):

$$K = \rho \cdot \left(v_P^2 - \frac{4}{3} \cdot v_S^2 \right) \quad [5-4]$$

However in the specific case of time-harmonic waves propagating in the axial direction along a circular cylindrical rod, radial, circumferential and axial components of displacement have to be taken into account. Longitudinal waves

are axially symmetric and have displacement components in axial and radial direction. The phase velocity of the longitudinal mode depends on the geometry of the medium and on the wave length (Mavko et al. 1998) and tends towards

- the bar velocity v_E , if the transmitter source is big in comparison to the soil medium. Then the compression waves are related to E (Equation 5-5):

$$E = \rho \cdot v_E^2 \approx \rho \cdot v_P^2 \quad [5-5]$$

- the Rayleigh wave velocity, if the transmitter source is small in comparison to the soil medium and the wave length is small enough. This is the case for a triaxial specimen. Then the compression waves are related to M (Equation 5-6), where M is the P wave modulus, defined as the ratio of axial stress to axial strain in a uniaxial strain state (i.e. the one-dimensional modulus M_E):

$$M = \rho \cdot v_E^2 \approx \rho \cdot v_P^2 \quad [5-6]$$

The compression element test has been performed in just three triaxial tests on sample 46216. The average value of the P wave modulus was 5000 MPa, which is comparable to results from the oedometer tests. However it was clear that the measured compression wave velocity was near the value of the velocity measured in water of 1483 m/s.

If we wish to predict the effective elastic moduli of a mixture of grains and pores theoretically, we generally need to specify:

- the volume fractions of the various phases
- the elastic moduli of the various phases
- the geometric details of how the phases are arranged relative to each other

If we specify only volume fractions and constituent moduli, only a prediction of upper and lower bounds in dependence of the relative volume fractions of the constituent can be delivered. The best bounds, defined as giving the narrowest possible range without specifying anything about the geometries of the constituents, are the Hashin-Shtrikman bounds (Mavko et al. 1998), which in a general form to be applied to more than two phases, can be written as follows for the bulk modulus K :

$$K^{HSmax} = \Lambda \cdot (G_{max,i}), K^{HSmin} = \Lambda \cdot (G_{min,i}) \quad [5-7]$$

where

$$\Lambda(G_x) = \left\langle \frac{1}{K_i + \frac{4}{3} \cdot G_x} \right\rangle^{-1} - \frac{4}{3} \cdot G_x \quad [5-8]$$

with i distinguishing the different phases of the mixture and $G_{max,i}/G_{min,i}$ being the maximum and minimum shear stiffness values among the values of the single phases.

For the shear modulus G , the Hashin-Shtrikman bounds are (Mavko et al. 1998):

$$G^{HSmax} = \Gamma(\zeta(K_{max,i}, G_{max,i})), \quad G^{HS(min)} = \Gamma(\zeta(K_{min,i}, G_{min,i})) \quad [5-9]$$

where

$$\zeta(K, G) = \frac{G}{6} \cdot \left(\frac{9 \cdot K + 8 \cdot G}{K + 2 \cdot G} \right) \quad [5-10]$$

and

$$\Gamma(x) = \left\langle \frac{1}{G_i + x} \right\rangle - x \quad [5-11]$$

The brackets $\langle \dots \rangle$ indicate an average over the medium, which is the same as an average over the constituents weighted by their volume fractions.

The bounds for the stiffness moduli K and G described by Equations 5-7 to 5-11 can be used to compute the upper and lower bounds of stiffnesses for the clays from Kreuzlingen and Birmensdorf as a mixture of mineral phases and fluids (mineral composition see Table 3-1, water content see Table 3-5). These bounds can be then compared to the measured values from the bender element tests (Chapter 6). The Hashin-Shtrikman bounds are valid under the boundary condition that each constituent and the soil mixture behave as isotropic linear elastic materials. The separation between upper and lower bounds depends on how different the constituents are. For a mixture of solids, the bounds are quite often similar, as the moduli of common minerals are usually within a factor of two of each other. When however the constituents are quite different (minerals and pore fluid), the bounds become quite separate and their predictive value will be partly lost.

5.1.2 Testing procedures

Sample preparation

The majority of the samples were taken with a thin walled sampler of 65 mm diameter and 200 or 800 mm length, from boreholes drilled using triple coring techniques. The samples were waxed and stored in a temperature controlled room until they were required for testing. Then the samples were carefully extruded from the sampler (Figure 5-8) and a thin slice of soil was cut from the side (Figure 5-9). This enabled the varving of the soil to be inspected, in order to decide where to cut the triaxial specimen to be tested.

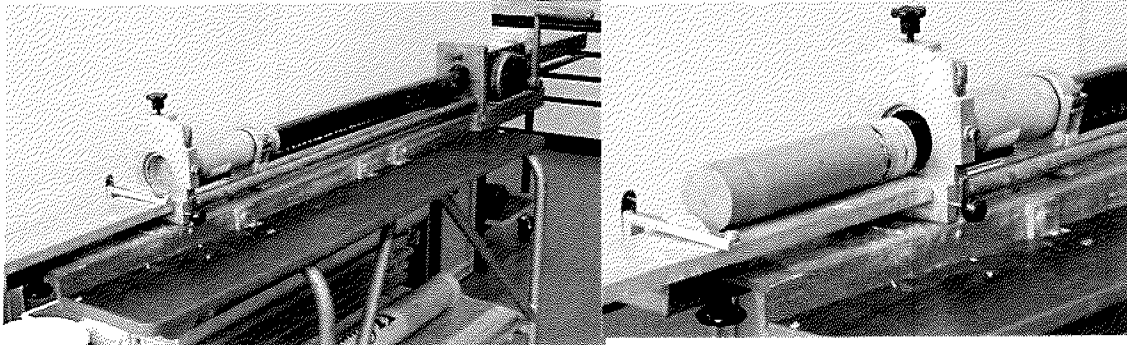


Figure 5-8: *Extrusion of test sample*

Three triaxial and five oedometer specimens, as well as material for classification tests, could be extracted from a 800 mm sampler. The specimens not used at once were placed in plastic bags and sealed with a light vacuum (Figure 5-9). They were then stored again in a temperature controlled room with high relative humidity.

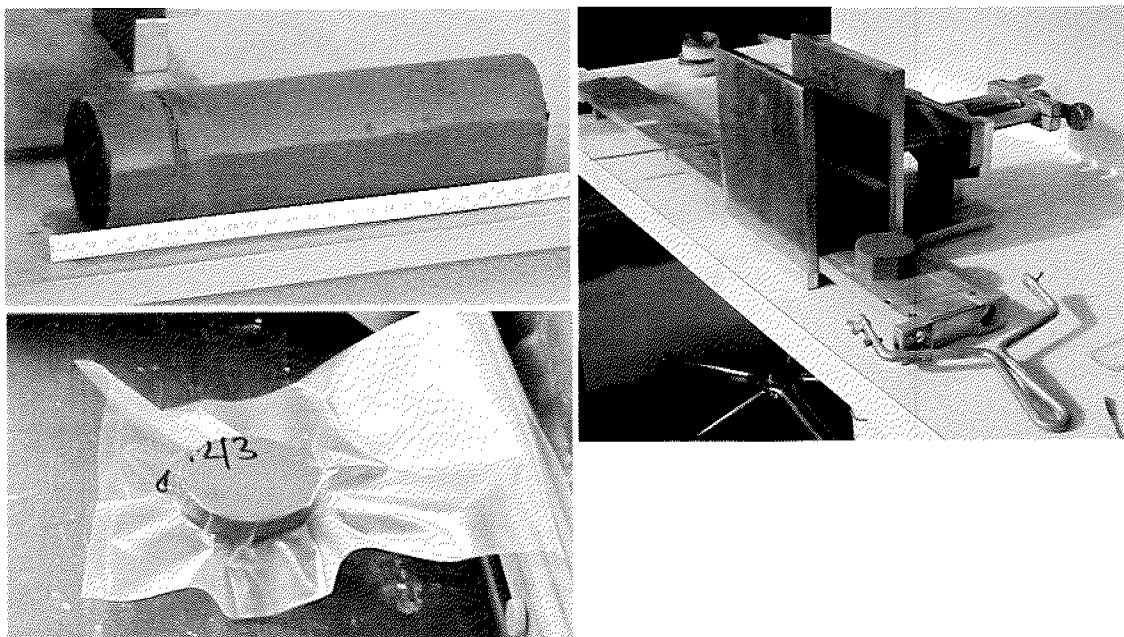


Figure 5-9: *Extruded sample, cut and sealed specimen*

The triaxial specimens were trimmed to a diameter of 56.4 mm and cut to a length of minimum 120 mm using a cheese wire saw (Figure 5-10).

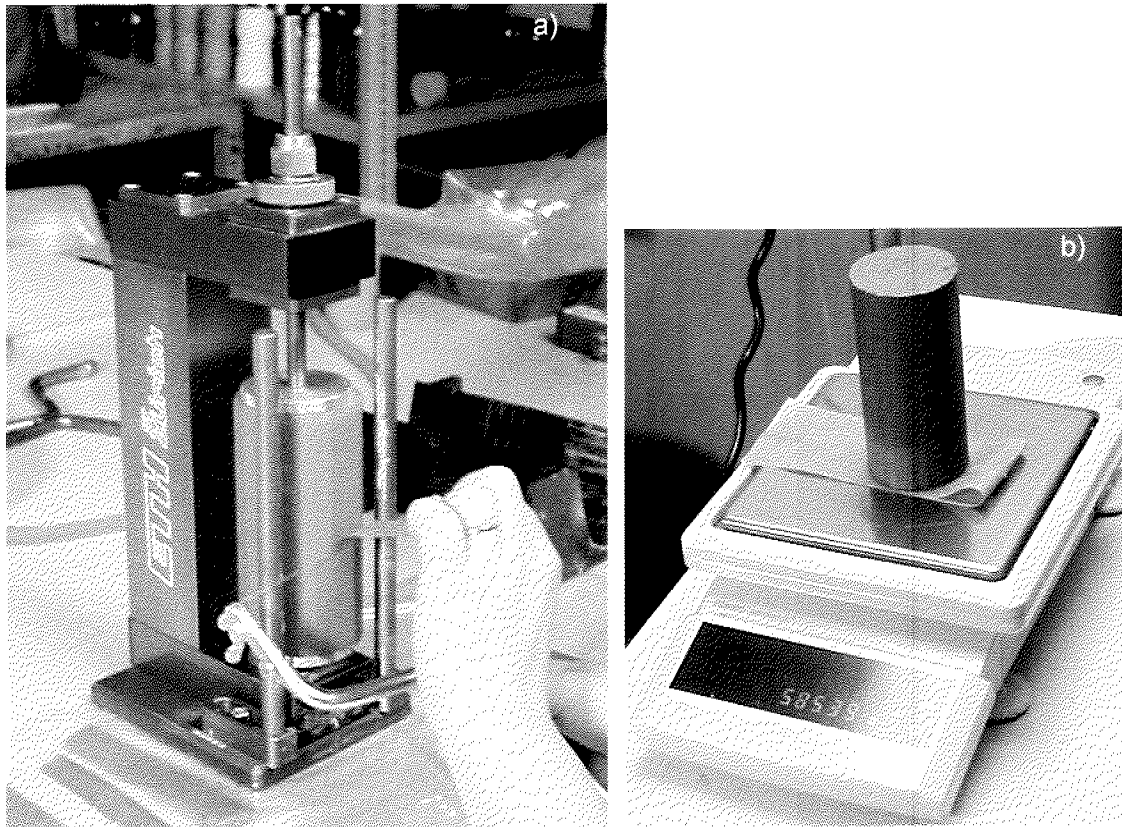


Figure 5-10: a) *Trimming the triaxial specimen*; b) *weighing the triaxial specimen*

To avoid alignment errors due to non-conformity of the specimen (Scholey et al., 1995), the specimen had to be trimmed carefully and cut to have coplanar top and bottom faces and to be vertical. This procedure was sometimes difficult, as the clay was very soft and tended to deform very easily, although it was achievable. This concern applied all the more for the reconstituted samples. The specimen was then carefully measured in length, diameter and weight. The material remaining from the trimmings was used to measure the actual water content of the specimen and sometimes for classification tests.

To allow radial drainage, eight 10 mm wide filter bands, previously soaked in deaired water, were placed along the sides of the specimen (Figure 5-11). To safeguard the drainage tubes against blockage, two round filter papers were placed on the top and bottom faces. The side filters were cut and overlapped the top and bottom filters by a few millimetres to avoid interruption of the water flow to the drainage tubes. Finally, a thin rubber membrane (0.3 mm thick) was placed around the specimen using the special mount (Figure 5-3) and the sample was placed on the base of the triaxial cell. The top platten was moved to seat on the specimen, causing a small force of ca. 10 N to act to fix the specimen in place. The rubber membrane could then be placed on the top and bottom caps and sealed with O-rings.

The cell was closed and filled with deaired water and the test set up could be finalised before beginning the consolidation phase of the stress path test.

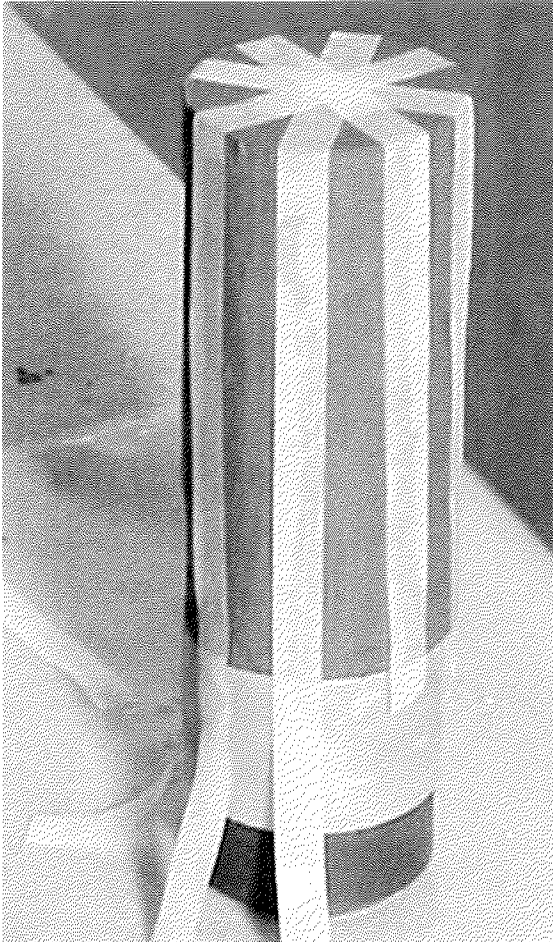


Figure 5-11: *Drainage bands along sides of the sample*

Testing programme

Seebodenlehm deposits are widespread in the Swiss Mittelland (see Chapter 3) and in the past years, experience has been gained from practical projects about the shearing resistance of this soil. However, a lot of questions remain about the deformation behaviour of the clay at yielding (e.g. under embankments) and inside the yield surface (relevant to unloading paths related to excavations). Therefore the main interests of the present study were the yielding characteristics and the small strain level behaviour of this particular soft clay. Furthermore, the pronounced varving of Birmensdorf clay imposed the question about the anisotropic characteristics of this soft clay and their influence on resistance, deformation behaviour and on excess pore water pressure development.

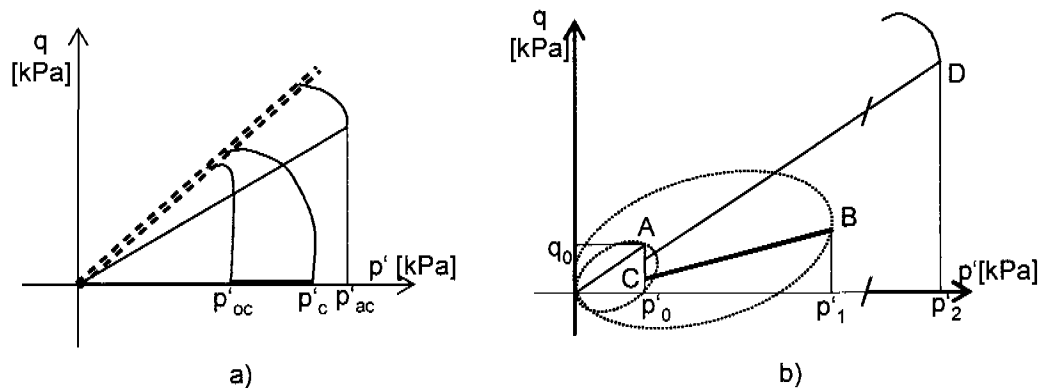


Figure 5-12: *Principal illustration of the triaxial testing programme a) test series 1, b) test series 2 (not scaled).*

A first series of tests consisted of isotropic and anisotropic consolidated undrained triaxial compression tests (CIUC and CAUC). One isotropic consolidated undrained triaxial extension test (CIUE) was also carried out on Kreuzlingen clay. This series was performed on a standard triaxial apparatus (Fleischer, 2000; Panduri, 2000). All specimens were either isotropically or anisotropically consolidated to between 1.5 and 2.5 times the estimate of the in situ effective vertical stress (p'_c or p'_{ac} in Figure 5-12 a), so that a truly isotropic state was reached prior to shearing (Houlsby & Sharma, 1999, Heil, 2001). Back pressure of between 200 and 400 kPa was applied to ensure full saturation of the system. After consolidation, the cell pressure was held constant, and axial stress was either increased (CIUC) or decreased (CIUE) under strain control at a rate of 0.00055 mm/s until failure was reached. Three additional tests on Birmensdorf clay were unloaded to a mean effective stress p'_{oc} , to overconsolidation ratios of 3.0, 2.0 and 1.5 before shearing (Fleischer, 2000). This series included 23 tests, including the tests performed by Panduri (2000) and Fleischer (2000) (Figure 5-12 a and Tables 5-4 and 5-5).

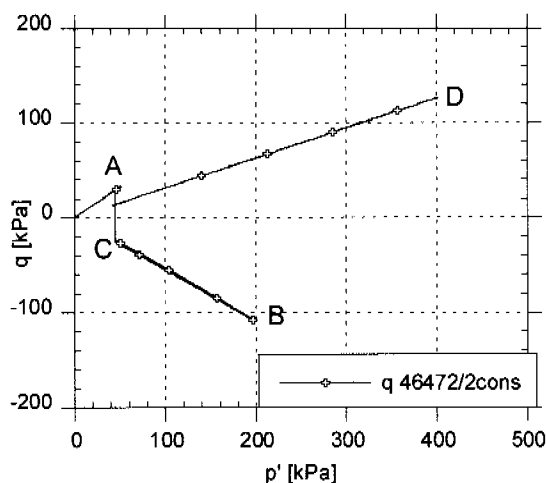


Figure 5-13: *Example of TSPT of series 2.*

The second series of tests included 15 triaxial stress path tests (TSPT) and these were performed on the device described in Chapter 5.1.1. This test series involved the determination of the initial yield surface and of the rotational hardening of the clay when submitted to a new stress history (Figure 5-12 b). During these tests, the small strain stiffness was measured by means of bender elements mounted in the top and bottom platten (Figure 5-4). Each test began with a first loading stage to the estimate of the in situ effective stress state (p'_0 and q_0) followed by a loading stage at a constant value of $\eta = \eta_1$ to a mean effective

stress p_1' , 2 times the initial in situ stress p_0' . The η value is the ratio between deviator stress q and the mean effective stress p' i.e. $\eta=q/p'$. After unloading with an unchanged value of η_1 , a second loading stage with a new constant value of $\eta=\eta_2$ raised the mean effective stress p' to up to 2 times the previous maximum stress to a value p_2' . The loading rate for the mean effective stress \dot{p}' was set at 1.5 kPa/h for loading and at 2 kPa/h for unloading. This was found to be slow enough to permit dissipation of excess pore water pressure and to ensure a reasonable test duration, which already requires 5 weeks for the stages described.

A preliminary test on a sample of 60 mm height, drained from the bottom and with excess pore water pressure measurement at the top, was carried out to model half of a 120 mm high sample drained from both top and bottom (Table 5-3). The pore water pressure response to different strain rates was tested at different mean effective stress p' , and inevitably the consolidation of the specimen had an influence on this response, as the permeability k will decrease with increasing consolidation stress. However, the results indicated that excess pore water pressure of between 7 and 15 kPa can be generated for a loading rate of 1.5 kPa/h, in a stress range that corresponded to that applied in the tests. There-

| stress increment $\Delta p'$ [kPa] | loading rate \dot{p}' [kPa/h] | measured excess pore water pressures [kPa] |
|---------------------------------------|------------------------------------|--|
| 10 - 50 | 0.45 | 0.2 |
| 50 - 100 | 0.8 | 2.5 |
| 100 - 400 | 2 | 12 |
| 400 - 800 | 4 | 141 |

Table 5-3: Excess pore water pressure development with loading rate

fore, to minimise errors in effective stresses and to equilibrate effective stresses, an interval of ca. 24 hours was given to the specimen before any change in stress path direction. During consolidation along these stress paths, a back pressure of 50 kPa was applied to the sample, which was far smaller than in series 1. Most of the samples used in test series 2 were taken from a depth of about 6 m and were subjected to in situ pore water pressures not exceeding 60 kPa. The choice of a low back pressure aimed to find a balance between obtaining a good saturation of the system and minimising the differences between testing and in situ state. Because the system in the new triaxial apparatus was easier to saturate, the B-values were still about 0.95 -0.98. After the last stage of drained stress path loading, an undrained shear stage followed, where axial stress was either increased (compression) or decreased (extension) under strain control at a rate of $3.7 \cdot 10^{-4}$ mm/s until failure was reached (two thirds of the rate used in test series 1). The lower strain rate was chosen to minimise excess pore water pressure.

Tables 5-4, 5-5 and 5-6 give an overview of the tests from series 1 and 2 (for site notation and description see Chapter 3).

| test No | clay | | | | | test type | p' _c [kPa] | BP [kPa] |
|---------|--|-----------|-------|------------------------|----------------------|-----------|-----------------------|----------|
| | site | depth [m] | state | p ₀ ' [kPa] | q ₀ [kPa] | | | |
| 46215/1 | Kreuz1 | 4.87 | u | 43.1 | 27.8 | CIUC | 150 | 250 |
| 46218/5 | Kreuz1 | 8.34 | u | 63.7 | 41.1 | CIUC | 230 | 200 |
| 46219/1 | Kreuz1 | 9.10 | u | 68.2 | 44.0 | CIUC | 200 | 200 |
| 46219/4 | Kreuz1 | 9.37 | u | 69.8 | 45.0 | CIUC | 150 | 250 |
| 46222/2 | Kreuz1 | 12.27 | u | 87.1 | 56.2 | CIUC | 280 | 220 |
| 46222/9 | Kreuz1 | 12.91 | u | 90.9 | 58.6 | CIUC | 360 | 250 |
| 46226/3 | Kreuz1 | 22.09 | u | 152.6 | 98.41 | CIUC | 450 | 300 |
| 46226/6 | Kreuz1 | 22.35 | u | 154.2 | 99.41 | CIUC | 600 | 300 |
| 46226/8 | Kreuz1 | 22.55 | u | 155.3 | 100.2 | CIUE | 450 | 300 |
| BP | back pressure | | | | | | | |
| CIUC | isotropically consolidated undrained compression triaxial test | | | | | | | |
| CIUE | sotropically consolidated undrained extension triaxial test | | | | | | | |
| u | undisturbed sample | | | | | | | |

Table 5-4: Overview of test series 1, part 1: tests on Kreuzlingen clay.

Interpretation procedures

Notation for stresses and strains

The interpretation of strains and stresses from laboratory tests were made using natural strains (Richardson, 1988) and Cauchy stresses. The notation used for the analysis of the data is the following (for triaxial compression):

σ' effective stress = $(\sigma - u)$, where σ is the total stress and u the pore water pressure

$\sigma_1 = \sigma_a$ axial stress defined as = N/A where N is the axial force and A the true area of the cross section. A correction for the area A is needed to consider the change in shape of the specimen during test, see chapter *correction to the data*.

$\sigma_3 = \sigma_2 = \sigma_r$ radial stresses equal in all horizontal directions for axi-symmetry

p' mean effective stress = $\frac{\sigma'_1 + 2 \cdot \sigma'_3}{3}$

$q = q'$ deviatoric stress = $(\sigma_1 - \sigma_3)$

τ_{\max} shear stress = $\frac{q_f}{2} = s_u$

| test No | clay | | | | test type | p'_c / p'_{ac} [kPa] | BP [kPa] | |
|---------|--------------------|-----------|-------|--------------|-----------|------------------------|----------|-------------|
| | site | depth [m] | state | p_0' [kPa] | | | | q_0 [kPa] |
| 46294/1 | Birm2 ^a | 8.0 | u | 53.6 | 35.0 | CIUC | 400 | 200 |
| 46294/5 | Birm2 ^a | 8.18 | u | 54.6 | 35.6 | CIUC | 300 | 200 |
| 46294/7 | Birm2 ^a | 8.52 | u | 56.5 | 36.9 | CIUC | 150 | 200 |
| 46294/8 | Birm2 ^a | 8.66 | u | 52.2 | 37.4 | CIUC | 400 | 200 |
| 46417/0 | Birm3 ^b | 10.1 | dc | 65.3 | 42.6 | CIUC | 330 | 200 |
| 46418/0 | Birm3 ^b | 10.35 | dc | 66.7 | 43.5 | CIUC | 400 | 200 |
| 46421/1 | Birm3 ^b | 12.1 | dc | 76.4 | 49.9 | CIUC | 200 | 200 |
| 46425/2 | Birm3 ^b | 13.45 | dc | 83.9 | 54.8 | CIUC | 400 | 200 |
| 46419/1 | Birm3 ^b | 10.8 | dc | 69.2 | 45.2 | CAUC | 200 | 200 |
| 46421/2 | Birm3 ^b | 12.3 | dc | 77.5 | 50.6 | CAUC | 300 | 200 |
| 46422/0 | Birm3 ^b | 12.5 | dc | 78.6 | 51.4 | CAUC | 400 | 200 |
| 46423/0 | Birm3 ^b | 12.8 | dc | 80.3 | 52.5 | OC3.0 | 200 | 200 |
| 46424/0 | Birm3 ^b | 13.0 | dc | 81.4 | 53.2 | OC1.5 | 400 | 200 |
| 46426/1 | Birm3 ^b | 13.7 | dc | 85.3 | 55.7 | OC2 | 300 | 200 |

BP back pressure
 CIUC isotropically consolidated undrained compression triaxial test
 CAUC anisotropically consolidated undrained compression triaxial test
 OC overconsolidation ratio
 u undisturbed sample
 dc drilled core sample (dc)

Table 5-5: Overview of test series 1, part 2: tests on Birmensdorf clay. a) Panduri (2000), b) Fleischer (2000).

$s_u = \tau_f$ undrained shear strength = $\frac{q_f}{2}$, with q_f at critical state

ε_a axial strain = $\frac{\Delta L}{L_0}$, where ΔL is the change of length of the specimen and L_0 the initial length. In the undrained shear tests, the axial strains were calculated with the dimensions of the specimen after consolidation as reference length L_{s0} .

ε_v volumetric strain = $\frac{\Delta V}{V_0}$, where ΔV is the change of volume of the specimen, as measured from the back pressure cylinder, and V_0 the initial volume. The volume of the specimen after consolidation is referenced as V_{s0} .

| test No | clay | | | | test type | η_1 / η_2 | BP [kPa] | |
|--------------------|---------------------------------------|-----------|-------|--------------|-----------|--------------------|-------------|-------------|
| | site | depth [m] | state | p_0' [kPa] | | | | q_0 [kPa] |
| 46216/1 | Kreuz1 | 5.9 | u | 48.9 | 32.9 | TSPT | 0.75 / 0.3 | 50 |
| 46216/2 | Kreuz1 | 6.1 | u | 49.9 | 33.5 | TSPT | 0.75 / 0.5 | 50 |
| 46216/3 | Kreuz1 | 6.2 | u | 50.6 | 34.1 | TSPT | 0.75 / -0.3 | 50 |
| 46471/1 | Kreuz2 | 6.4 | u | 45.5 | 29.3 | TSPT | -0.3 / 0 | 50 |
| 46472/2 | Kreuz2 | 6.4 | u | 45.5 | 29.3 | TSPT | -0.5 / 0.3 | 50 |
| 46473/2 | Kreuz2 | 6.4 | u | 45.5 | 29.3 | TSPT | 0 / -0.2 | 50 |
| 46474/1 | Kreuz2 | 6.4 | u | 45.5 | 29.3 | TSPT | -0.3 / 0 | 50 |
| 46475/1 | Kreuz2 | 6.4 | u | 45.5 | 29.3 | TSPT | -0.5 / 0.3 | 50 |
| 46297/2 | Birm2 | 11.15 | u | 95.3 | 62.2 | TSPT | 0.3 / 0 | 50 |
| 46297/3 | Birm2 | 11.35 | u | 96.3 | 62.9 | TSPT | 0.3 / 0.5 | 50 |
| 46496/56 | Rec | - | u | 39.4 | 30.9 | TSPT | -0.5 / 0.3 | 50 |
| 46496/57 | Rec | - | u | 39.4 | 30.9 | TSPT | -0.3 / 0 | 50 |
| 46496/58 | Rec | - | u | 39.4 | 30.9 | η_{k_0} creep | - | 50 |
| 46496/510 | Rec | - | u | 39.4 | 30.9 | η_{k_0} creep | - | 50 |
| BP | back pressure | | | | | | | |
| TSPT | triaxial stress path test | | | | | | | |
| u | undisturbed sample | | | | | | | |
| η_{k_0} creep | K_0 consolidation, then creep stage | | | | | | | |

Table 5-6: Overview of test series 2.

ε_a and ε_v are strains that relate the total displacement accumulated to the initial sample dimensions (L_0 and V_0 respectively). The use of this strain definition can lead to large errors in derived strain quantities e.g. radial strain or true shear strain, when deformations become large. In order that results remain consistent, natural strains were used (Richardson, 1988). The relationship between strains ε and natural strains ε_n is:

$$\varepsilon_n = -\ln(1 - \varepsilon) \quad [5-12]$$

$$\varepsilon_{r,n} \quad \text{natural radial strain} = \frac{\varepsilon_{v,n} - \varepsilon_{a,n}}{2}$$

$$\varepsilon_{s,n} \quad \text{natural true shear strain} = \left(\varepsilon_{a,n} - \frac{\varepsilon_{v,n}}{3} \right)$$

$$\gamma \quad \text{engineers' shear strain} = \frac{3}{2} \cdot \varepsilon_{s,n} \quad (\text{Atkinson \& Bransby, 1978})$$

Stiffnesses

Shear and bulk modulus were chosen as the main stiffness parameters and are defined as

$$G = \frac{\Delta q}{3 \cdot \Delta \varepsilon_{s,n}}$$

$$K = \frac{\Delta p'}{\Delta \varepsilon_{v,n}}$$

During the drained consolidation stages, the tangential moduli were determined by a sliding regression: a straight line was fitted to 100 measured data pairs of the stress-strain diagram and the gradient of this regression line was set as the stiffness in the middle of the data interval. The interval was then moved to the next data pair. With this method, stiffnesses cannot be calculated for the first and last 50 stress-strain data pairs. An "axial stiffness" E_a and a "radial stiffness" modulus E_r were also used to identify the yield points during the drained stress path stages and are defined as:

$$E_a = \frac{\Delta \sigma'_a}{\Delta \varepsilon_{a,n}}$$

$$E_r = \frac{\Delta \sigma'_r}{\Delta \varepsilon_{r,n}}$$

Soil behaviour is non-linear, starting from very small strains (typical threshold strain of clays $5 \cdot 10^{-5}$, Atkinson and Sallfors (1991) and Burghignoli et al. (1991)). A main goal of the triaxial investigation was to determine the initial stiffness and its reduction under load during the undrained shear stages. In this case, if the tangential stiffness G is approximated with the sliding regression, the important information about stiffness in the small strain region is lost. For the undrained shear stages therefore, the tangential stiffness was calculated with discrete differences between two data pairs as follows:

$$G_{tan} = \frac{(q_i - q_{i-1})}{(\varepsilon_{s,n(i)} - \varepsilon_{s,n(i-1)}) \cdot 3} \quad [5-13]$$

The Kondner hyperbola (Chap. 2) together with the dynamic shear modulus G_{max} from the bender tests were used to model the modulus reduction curve in the very small strain region.

Yielding

One of the main goals of the triaxial investigation was the determination of the yield surfaces of these soft clays. The yield locus in the triaxial or $p':q$ stress plane is just a particular section through the current yield surface of the soil with one particular history (Muir Wood, 1990). The yield surface can be regarded as a generalised preconsolidation pressure; the preconsolidation pressure observed

in an oedometer test corresponds to just one point on this yield surface. The yield surface is not unique for a given preconsolidation pressure, but depends on testing rate or test duration (Tavenas and Leroueil, 1980, Graham et al., 1983a).

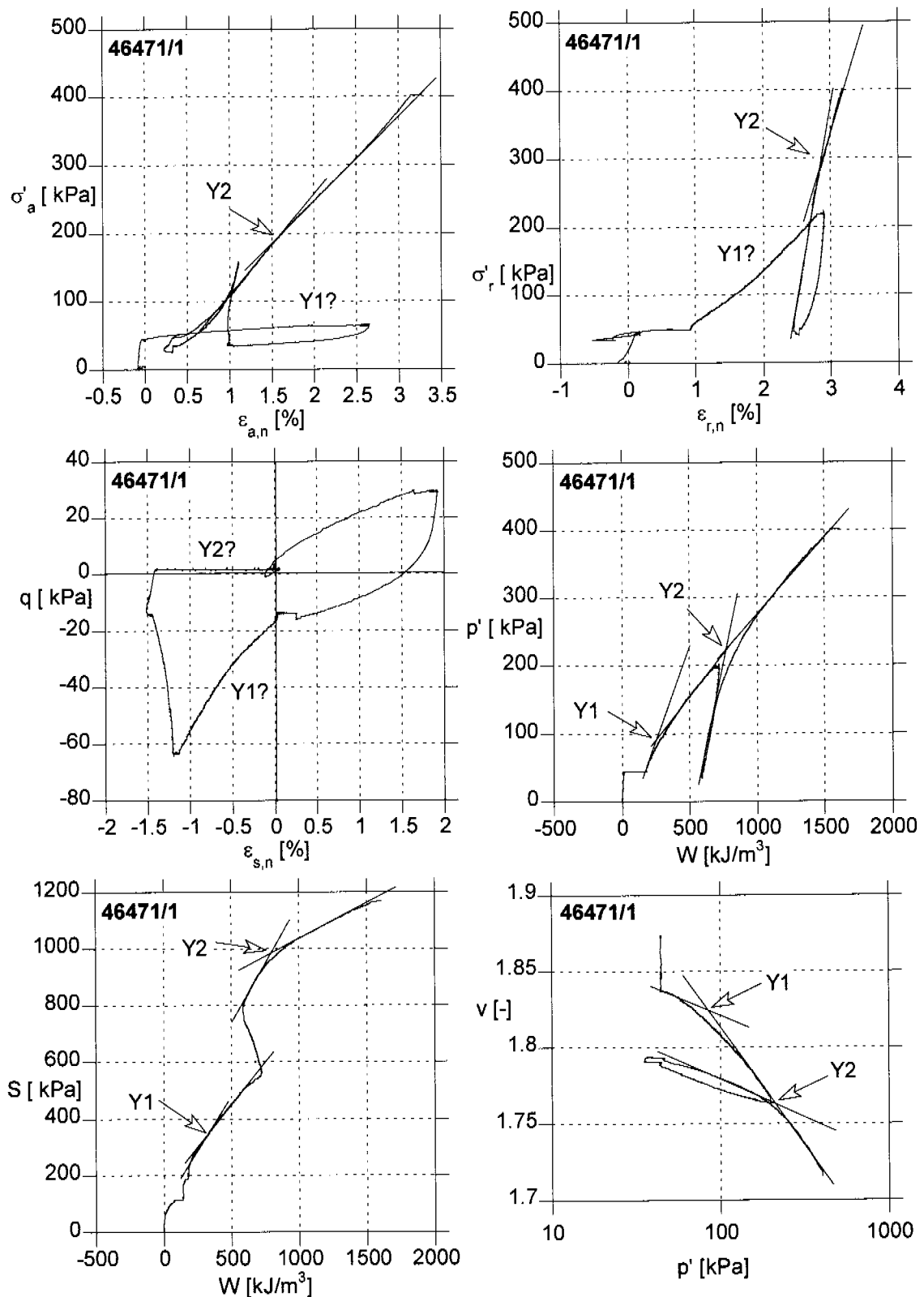


Figure 5-14: Various stress-strain and work input plots used to determine the yield stress during test 46471/1.

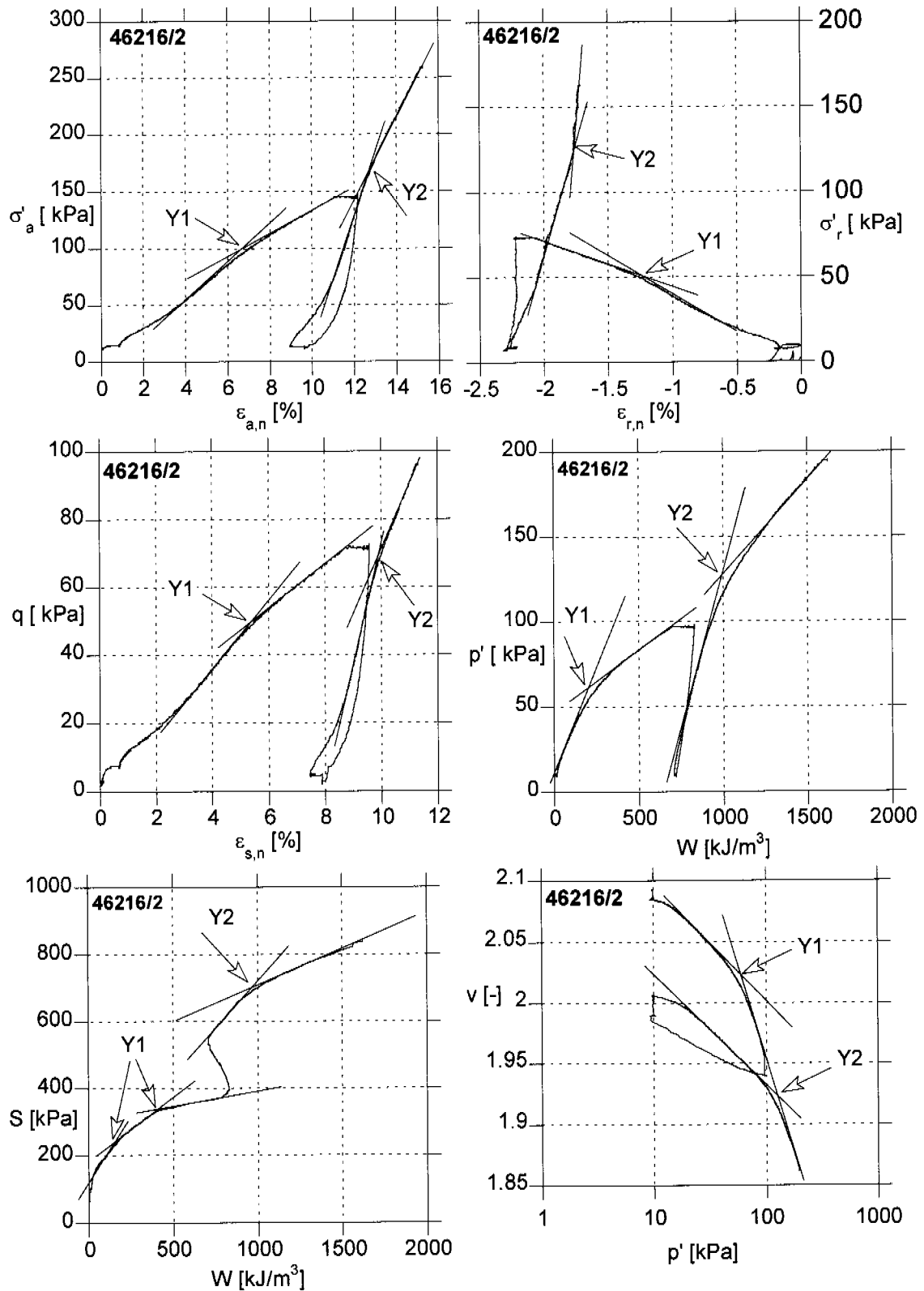


Figure 5-15: Various stress-strain and work input plots used to determine the yield stress during test 46216/2.

Since different loading paths generate different modes of deformation or straining, different strain variables may provide a more sensitive indication of the occurrence of yield on a particular stress path (Muir Wood, 1990). A yield point can be identified as a sharp bend in a stress-strain curve, where the stiffness changes markedly. Appropriate stress-strain curves are $\varepsilon_{a,n}-\sigma'_a$, $\varepsilon_{r,n}-\sigma'_r$, $\varepsilon_{s,n}-q$, $\varepsilon_{v,n}-p'$, $\ln p'-v$. In addition to the stress-strain curves, the equivalent stiffness-stress or -strain curves can be used to detect the bend in the curves. For most of the tests, these plots were easier to interpret and gave a better agreement with the $\ln p'-v$ and the work input plots.

The energy W required to deform the specimen during a specific triaxial stress path is another useful quantity to aid detection of a yield point. The work per unit volume W is defined as:

$$W = \int (p' \cdot d\varepsilon_v + q \cdot d\varepsilon_s) \quad [5-14]$$

and this equation is valid whatever changes in strain may occur, since compression and distortion of the sample have both been incorporated (Muir Wood, 1990). The cumulative work input can be plotted against the stress variable p' or against the length s of the stress path, where:

$$\delta s = \sqrt{\delta p'^2 + \delta q^2} \quad [5-15]$$

s is a scalar quantity, which increases monotonically, whatever the direction of the stress path (Muir Wood, 1990). The additional plots used for identifying yielding for the triaxial tests were: $W-p'$ and $W-s$ (Figures 5-14 and 5-15).

The main effective stress - strain plots and work input plots used to identify the yield stress during consolidation are shown in Figures 5-14 and 5-15 for two typical tests 46471/1 ($\eta_1 = -0.3$, $\eta_2 = 0$) and 46216/2 ($\eta_1 = 0.75$, $\eta_2 = 0.5$), whereby the first sample was subsequently sheared to failure in undrained triaxial compression and the latter in undrained triaxial extension. The identification of yield for specimen 46471/1 was more difficult, as it was not possible to make a bilinear approximation of the curve in some of the plots. The stiffness - effective stress plots are not shown here, although they were mostly in agreement with the $\ln p'-v$ plot. It has to be noted that stiffnesses are calculated with a sliding regression in the consolidation stage and are therefore affected by inaccuracies depending on the number of data pairs considered by the sliding regression.

The stresses and energies at yield found from these plots were converted to the equivalent mean effective stress p' for comparison (Table 5-7). Discrepancies between the different values of p' obtained from these plots reached 30% in some cases. The $\varepsilon_{r,n}-\sigma'_r$ plot was not particularly reliable and showed very high discrepancies in comparison with the $\ln p'-v$ plot. The yield value identified from the $\ln p'-v$ plot was then used to define the yield surface in $p'-q$ space.

| Specimen Nr. | 46471/1 yield 1 | | 46471/1 yield 2 | | |
|--------------|---------------------------------|----------|-----------------|----------|-------|
| | Graph type | p' [kPa] | % | p' [kPa] | % |
| | lnp' - v | 88.8 | 100 | 222.3 | 100 |
| | $\varepsilon_{a,n} - \sigma'_a$ | 91.8 | +3.3 | 192.3 | -13.5 |
| | $\varepsilon_{r,n} - \sigma'_r$ | 75.8 | -14.7 | 256.9 | +15.6 |
| | $\varepsilon_{s,n} - q$ | ? | ? | ? | ? |
| | $\varepsilon_{v,n} - p'$ | ? | ? | 233.1 | +4.8 |
| | W - p' | 74.8 | -15.8 | 220.2 | -0.9 |
| | W - s | 64.3 | -27.6 | 221.3 | -0.4 |
| | E - σ'_a | 86.3 | -2.8 | 248.2 | +11.6 |
| | G - q | 69.2 | -22.1 | ? | ? |
| | K - p' | 63.8 | -28.2 | 208.2 | -6.31 |

Table 5-7: Determination of a yield point from different stress-strain plots for specimen 46471/1.

Corrections to the measured data

Corrections have to be applied to the measured data to take into account temperature effects on volume changes and deformation effects on the cross sectional area of the specimen. The effects of the rubber membrane and the side filter papers on the stresses has to be discussed too.

Temperature changes have a great influence on the cell volume measurement due to the large amount of water involved ($V_{w,c}$ about 52 litres), and less on the pore water volume measurement, where the maximum quantity of water in cylinder and tubes $V_{w,p}$ is 0.72 l. Cell volume measurement was used for general control purposes, whereas volumetric strains were calculated from the pore water volume changes. Calibration tests showed that the coefficient of volume change due to temperature δ is about $2 \cdot 10^{-4} \text{ K}^{-1}$ for this test equipment. The temperature of the cell water at the very beginning of the test was used as the reference temperature T_0 , and any changes in temperature T have an effect on the water volume V_w . The change in volume ΔV_T due to temperature effects is then:

$$\Delta V_T = V_w \cdot (T - T_0) \cdot \delta \quad [5-16]$$

The corrected volume change measurement is calculated from the measured volume change ΔV_m as follows:

$$\Delta V = \Delta V_m + \Delta V_T \quad [5-17]$$

The cross sectional area changes when the specimen deforms during consolidation and shearing. It is assumed that the specimen deforms as a right cylinder during consolidation, keeping its original shape. The corrected area A_c is calculated from the initial area A_0 as (Head, Vol.2, 1996):

$$A_c = A_0 \cdot \left[\frac{1 - \varepsilon_v}{1 - \varepsilon_a} \right] \quad [5-18]$$

During shearing, two types of deformation behaviour can be observed (Figure 5-16).

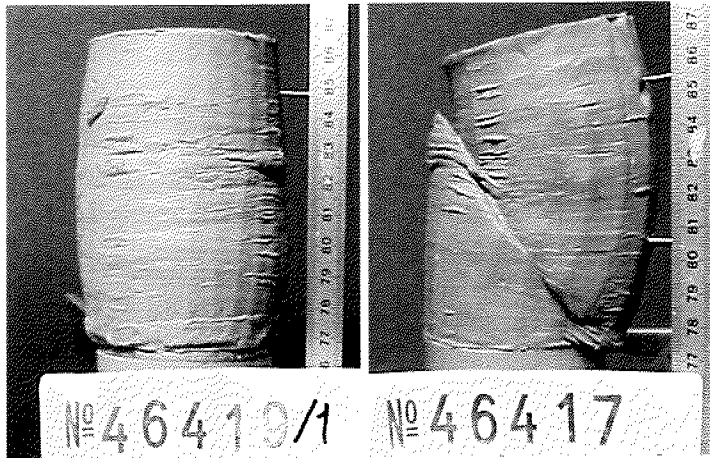


Figure 5-16: Deformation behaviour during undrained shear in Birmensdorf clay (Fleischer, 2000) a) ductile, barrelling b) brittle, slip plane.

Following so-called ductile behaviour in an undrained test, the specimen assumes the outline of a barrel and the volume lost in the length must appear as an increase of diameter. The friction at the unlubricated end plattens prevents the specimen from deforming uniformly, therefore the cross sectional area in the middle of the specimen is larger than in the end sections. It is assumed in this analysis that the deformation is equivalent to an idealised shape of uniform diameter but of the same volume as the barrel shape (see e f g h in Figure 5-17). The corrected area A_s is calculated from the initial area at beginning of the shearing test A_{s0} as (Head, Vol.3, 1985):

$$A_s = \frac{A_{s0}}{1 - \varepsilon_a} \quad [5-19]$$

There are however preferentially dilating or contracting zones, even if external evidence of localisation is not apparent. Desrues et al. (1996) presented a study of strain localisation in sand specimens tested in the triaxial apparatus, using computer tomography. Although strain localisation can occur in different localisation patterns depending on test conditions, they found a pattern similar for many of the tested specimens: this is a central cone with sets of planes in pairs, radially adjusted around the cone. The local void ratio evolution in the localisation zone indicates that a limit void ratio is reached in the shear zones and that the global void ratio has no physical meaning (Desrues et al., 1996).

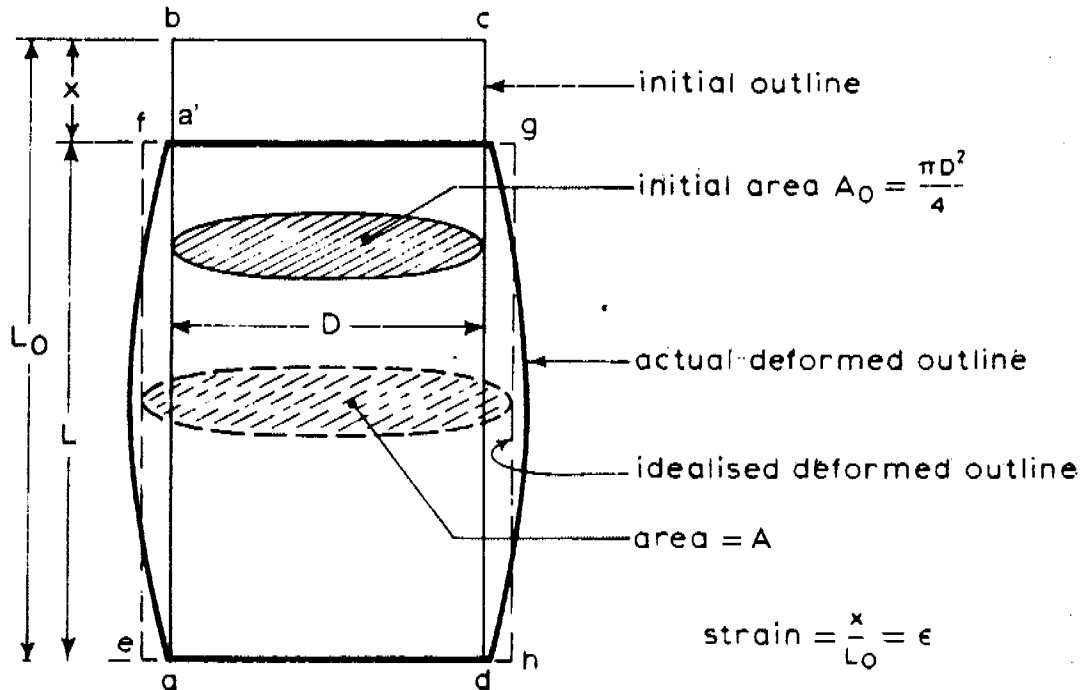


Figure 5-17: Barrelling deformation of undrained compression test specimen (Head, 1985).

In a so-called brittle failure, clear evidence of shear localisation can be seen as a plane of slip develops. When localisation occurs by slipping along a preferential shear surface, the effective plan area used for calculating axial stress decreases as movement takes place (Figure 5-18). The slip area factor f_s , by which the initial area A_{s0} must be divided to obtain the corrected area A_s , can be calculated as (Head, Vol.3, 1985):

$$f_s = \frac{\pi}{2 \cdot (\beta - (\sin \beta \cdot \cos \beta))} \quad [5-20]$$

The angle β (Figure 5-18c) can be calculated from:

$$\cos \beta = \epsilon_{a, \text{slip}} \cdot \frac{L_{\text{slip}}}{D_{\text{slip}}} \cdot \tan \theta \quad [5-21]$$

where $\epsilon_{a, \text{slip}}$ is the axial strain measured from the start of slip, L_{slip} and D_{slip} are the specimen length and diameter at the start of slip and θ the angle of the slip surface to the vertical. The slip mechanism does not usually start at zero strain, therefore the area A_{s0} must be calculated until slip occurs with Equation 5-18.

It is difficult to observe exactly when the start of slip occurs. Head (Vol.3, 1985) proposes an estimation based on the total vertical displacement due to slip ΔL_{slip} (Figure 5-18 d). If the displacement z along the slip surface at the end of the test is measured, then ΔL_{slip} is equal to $z \cos \theta$ (Figure 5-18) and subtracting this from the total recorded axial deformation gives the point at which slip started. The measurement of z is unreliable as the membrane prevents this idealised mechanism of slip (Figure 5-16) from forming. In this analysis, the start of

slip has been taken to coincide with the maximum axial force measured. In the present work, this procedure has been used for those specimens, which showed that the localised slip plane had developed before the peak deviator stress q_{peak} was reached, i.e. if the maximum axial force was reached before q_{peak} . In this case, the localisation has direct influence on the measured strength as it reduces the area of the specimen, whereas if the localised slip plane developed after peak deviator stress, then just post peak behaviour was affected.

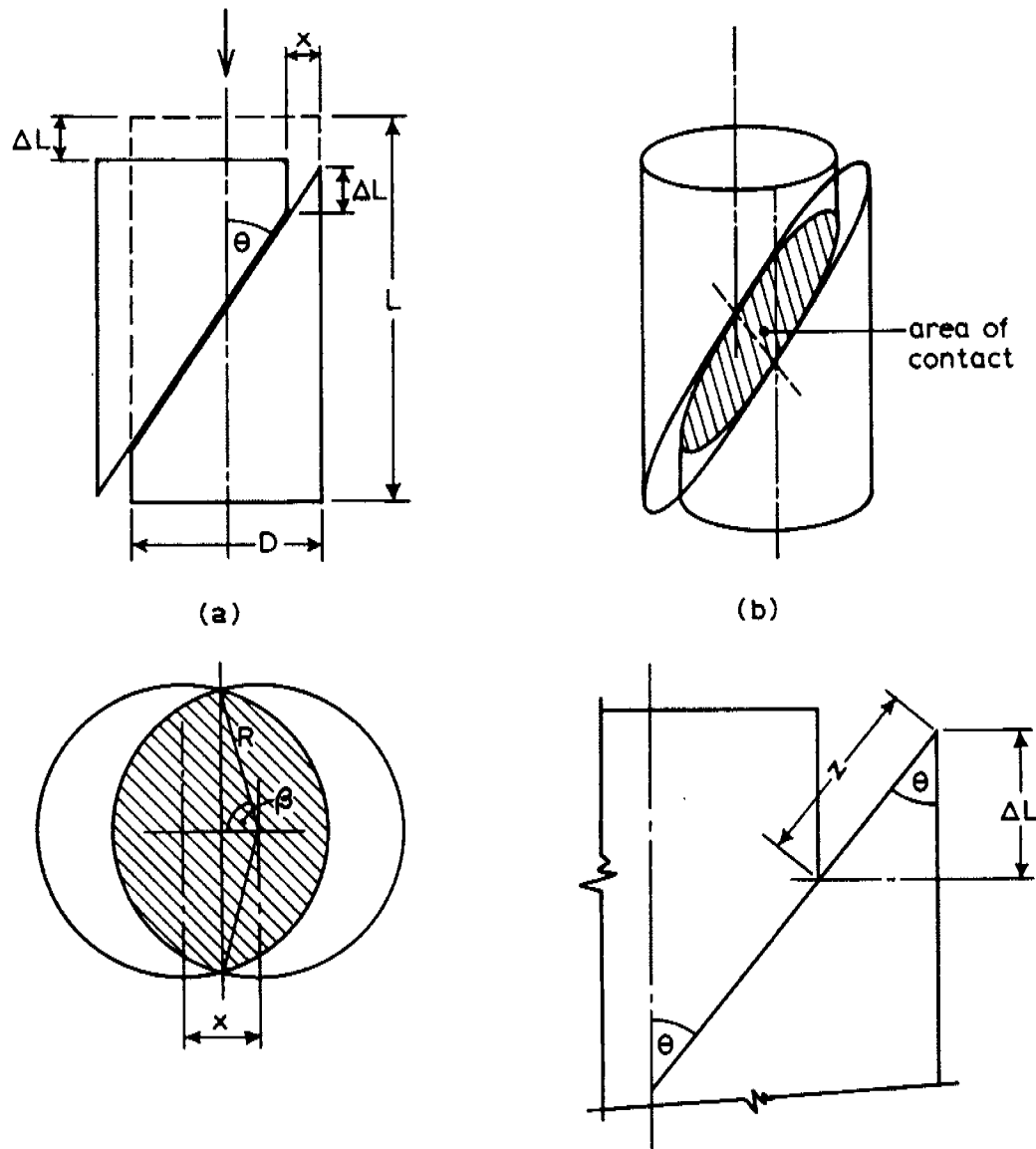


Figure 5-18: Area correction due to single plane slip (Head, 1985): a) mechanism of slip, b) area of contact between the two portions of the sample, c) projected area of contact, d) displacement along slip surface related to vertical deformation.

In test series 1, 10 of 23 tests showed a localised shear plane, in 6 of these 10, the slip plane developed before q_{peak} and in the remaining 4 after q_{peak} (Chapter 3.1.3).

In test series 2, 8 of the 15 tests showed a single shear plane. Test 46216/3 showed a failure mechanism with double slip surfaces.

Finally, the influence of the rubber membrane and the side filter papers on the stresses applied to the sample or existing within it must be discussed. The restraining effect of the rubber membrane enclosing the triaxial specimen makes a small contribution to the resistance offered against compression. Head (1996) dealt with the membrane correction to the deviator stress at critical state for barrelling by means of a graph. For a specimen of 56.4 mm diameter and a rubber membrane of 0.3 mm thickness, a maximum membrane correction to the deviator stress of 2 kPa is obtained for an axial strain at failure of 20%. On the basis of this assumption the ratio of membrane correction to maximum deviator stress would exceed 5% just in two tests. A test was carried out to measure the membrane's extension modulus m as described by Bishop and Henkel (1962, from Head, 1996). On the basis of the measured m modulus, the membrane correction for this membrane would be equal to 20 kPa. This value is suspiciously high considering the values given in Head (1996). It is assumed in this analysis that the correction due to the restraining effect of the membrane is negligible (< 5% for axial strain at peak of 20%).

An additional correction to those of the membrane correction is usually applied to the measured deviator stress to allow for the restraint imposed by vertical filter paper side drains, when fitted. Spiral drains, as used by Gens (1992) were found to need no correction to the measured strength. The correction for a specimen diameter of 56.4 mm and side drains is described in Head (Vol. 3, 1985) and is about 6.6 kPa. No data exists to quantify this influence for the side drains set up used in this test series. In this case, an attempt has also been carried out to measure the tear-out stress of a strip of soaked filter paper in a uniaxial extension test (Head, Vol. 2, Section 13.7.4, 1996) and this averaged 1.5 MPa. This would lead to an extremely high correction value. However, after the consolidation stage, the filter paper side drains do not fit the specimen any more because of the large volumetric strains and they show a lot of folding. To restrain the specimen, the filter paper side drains must be loaded in extension, i.e. the deformation during shearing must be enough to stretch the side drains again before the maximum deviator stress is reached. This is not the case for these specimens within the given axial strain ranges, as it can be shown considering as example specimen 46227/5: the initial height h_0 of this specimen was 130.5 mm (ab in Figure 5-17) and the height h_c after consolidation was 124.2 mm (ef in Figure 5-17). This specimen sheared with a barrel form and the length of the deformed outline is equivalent to a segment of circle (aa' in Figure 5-17) and averaged 113.5 mm < 124.2 mm. The large volumetric strains during consolidation of a soft clay explain why the membrane and filter cannot restrain the specimen during shearing, as they are not loaded in extension.

Radial drainage can also cause non-uniformities in water content in samples subjected to undrained loading followed by one-step consolidation or subjected to rapid drained loading (Atkinson et al., 1985). Atkinson et al. (1985) tested loading rates in the range $\dot{p} = 4$ to 2650 [kPa/h] on clay and showed that for rates less than 10 kPa/h, the difference between the water content at the centre and the water content at the outer boundary averaged less than 0.4%. The loading rates chosen for test series 2 of 1.5-2 kPa/h are slow enough to prevent such non-uniformities, whereas in test series 1, the difference in water content between centre and outer boundary were subsequently predicted to have reached 1.5%.

5.1.3 Results

Kreuzlingen clay

The effective stress paths to failure in either triaxial compression or extension plotted in terms of deviator stress q and effective mean stress p' space, are given in Figure 5-19 and show reasonable consistency in shape and location of the critical state for both series 1 and 2. Critical state is reached by constant excess pore water pressure (Muir Wood, 1990), which corresponded in most specimens with peak deviator stress q_{peak} (Figure 5-20) and with maximum effective stress ratio σ'_1/σ'_3 . The locus of these stress states can be defined by a Critical State Line (CSL) with:

$$q = M \cdot p' \quad [5-22]$$

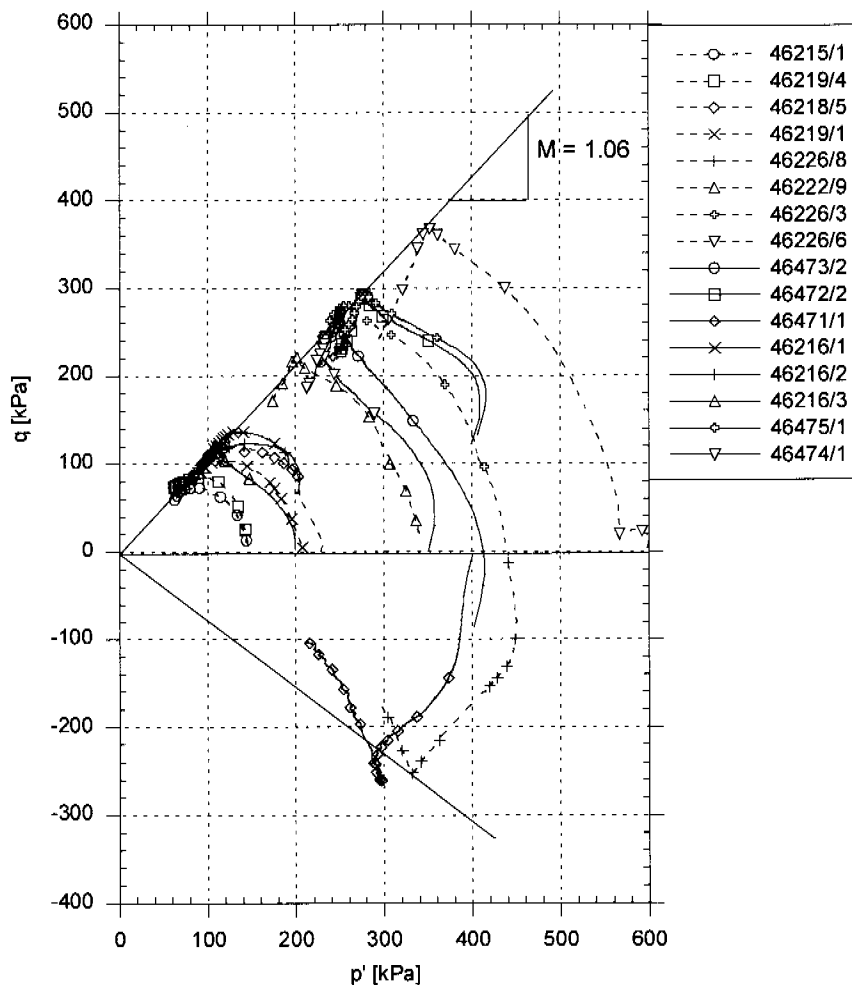


Figure 5-19: q - p' diagrams for Kreuzlingen clay: undrained shear stage to failure, series 1 (dashed line) and 2 (full line).

For compression tests, M is equal to 0.96 for series 1 and equal to 1.06 for series 2 (as drawn in Figure 5-19), both series having 8 tests each. M may also be described in terms of the angle of shearing resistance ϕ' :

$$\sin\phi' = \frac{3 \cdot M}{6 + M} \text{ in compression} \quad [5-23]$$

$$\sin\phi' = \frac{3 \cdot M}{6 - M} \text{ in extension} \quad [5-24]$$

which in triaxial compression for $M = 0.96$ gives 24.4° , and for $M = 1.06$ gives 26.8° . Typically, strength in compression exceeds that in direct shear, and both are higher than strength in extension. Wroth (1984) and Kulhawy (1993) suggest that the CIUC test is defined as the reference test against which the various values of undrained shear strength are compared. In this case, just two extension tests are available, which give a value of M equal to 0.8 ($\phi' = 27.5^\circ$) for series 1 and equal to 0.9 ($\phi' = 31.9^\circ$) for series 2. Heil (2001) published data on 6 triaxial extension tests on Kreuzlingen clay. He observed quite uniform behaviour, resulting in a very similar shape of the effective stress paths, that are comparable with the results presented here. The effective stresses have been calculated applying the mean cross-sectional sample area correction throughout the test. Shear banding and necking were observed at the end of the tests, which results in abrupt change of sample stiffness post-peak (Heil, 2001). Thus, for the post-peak stages of the tests, the stress paths given in Figure 5-19 are not reliable.

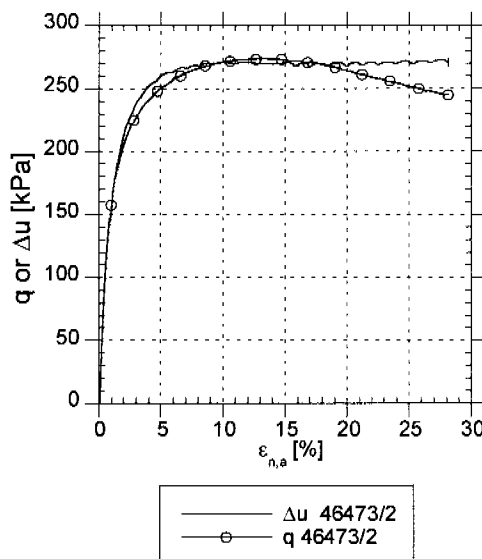


Figure 5-20: Excess pore water pressures and deviator stress development during shearing: typical test.

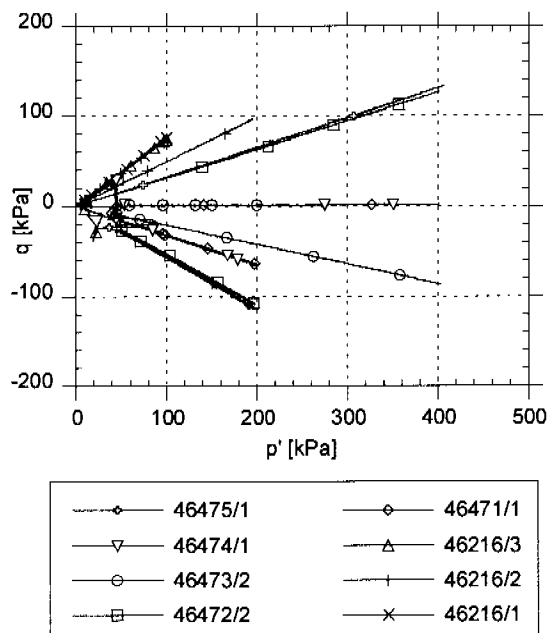


Figure 5-21: q - p' diagrams for Kreuzlingen clay: stress path controlled consolidation in series 2.

The Kreuzlingen clay has a relatively homogeneous structure and does not show large varving patterns. The development of deviator stress and excess pore water pressures are similar in all tests, showing the typical trend for a normally consolidated clay (Figure 5-20). The failure mode does not appear to influence the failure parameters determined for this clay (Figure 5-19).

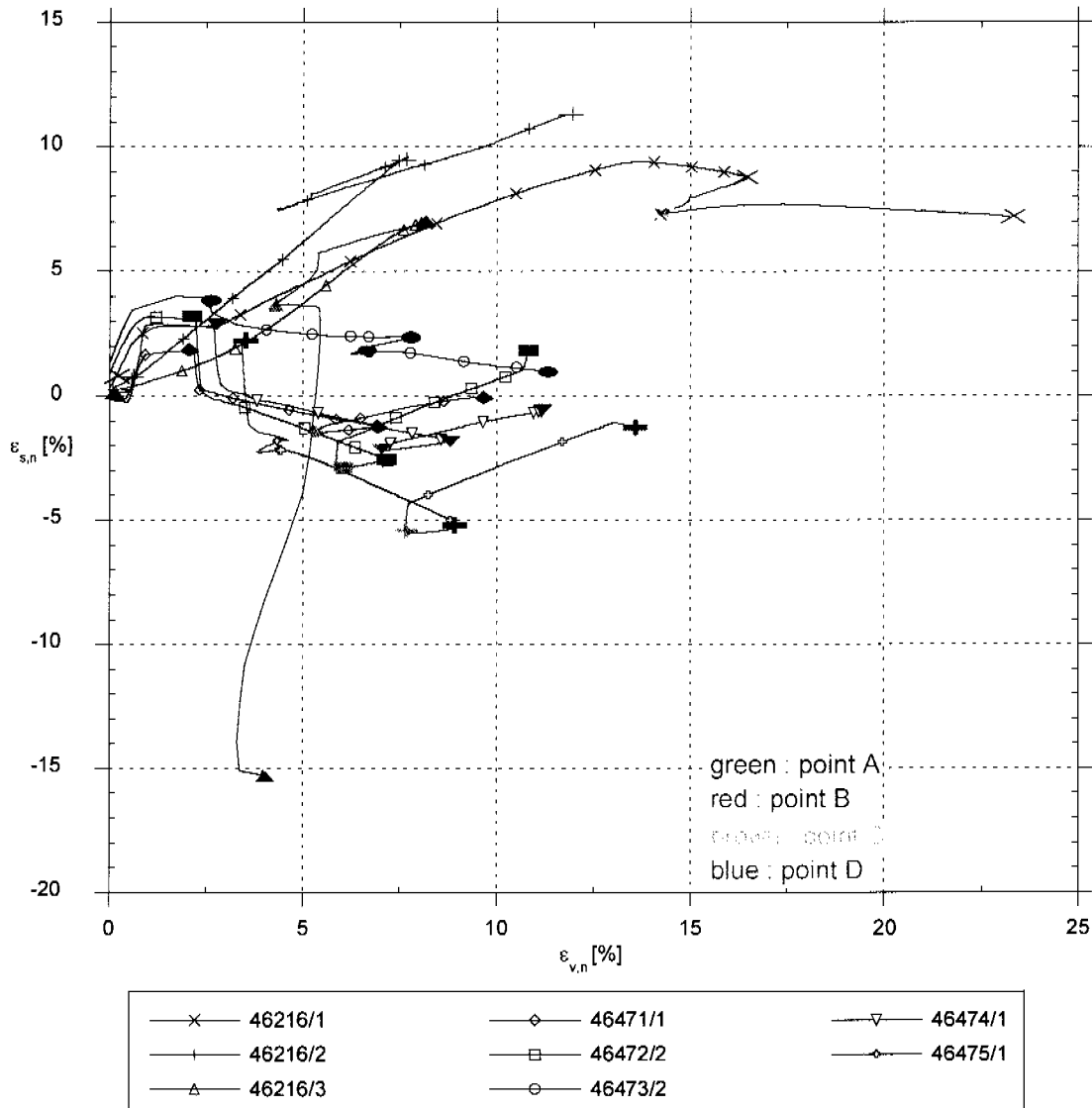


Figure 5-22: Strain paths $\varepsilon_{s,n} - \varepsilon_{v,n}$ for Kreuzlingen clay during stress controlled consolidation stages in series 2. Points A to B refer to stress reversal points as shown in Figure 5-12.

During a shear stage, the test is strain controlled, i.e. the measured stress path shows the (failure) behaviour of the soil tested. In contrast, the test is stress controlled during consolidation and the key charts that show soil behaviour are the measured strain path $\varepsilon_{s,n} - \varepsilon_{v,n}$ and the $\ln p' - v$ diagram. The strain path diagram shows the total strains experienced by the specimen during drained consolidation, which are composed of an elastic and a plastic component. To separate the two components, small unload-reload cycles have to be undertaken at various points during consolidation and this was not carried out in the present work.

The stress paths followed during consolidation for series 2 are given in Figure 5-21 and these may be referred back to Table 5-6 to determine the values of η_1 and η_2 . The corresponding strain paths are plotted in Figure 5-22. After installation, the specimens of sample 46216 had 24 hours to equilibrate at $p'=10$ kPa and $q=\eta_1 p'$, whereas the samples 46471 to 46475 were brought to the estimate

of the in situ stresses p_0' and q_0 . It can be seen, that the combinations of total shear and volumetric strain after this re-equilibration stage are different for each specimen, but fall in a small zone indicating that the installation of the specimen had a similar influence on the state of all specimens. All specimens, except 46216/2 and 46216/3, show volumetric creep. The largest shear strains developed during the first loading of the tests 46216/1 to 3, where $\eta_1 = 0.75$. This stress ratio lies between that at the K_0 condition η_{k0} and the stress ratio at critical state $\eta_{cs} = M = 1.06$, and constitutes a more critical loading path, because it takes the samples closer to the CSL than before. The second load path of test 46216/3 could not be accomplished because of problems with the controlling software, instead a one step isotropic consolidation was carried out. However the shear strength of this specimen is $M_{46216/3} = 1.08$, which is comparable with the average value of M from series 2.

The strain paths for tests following the same stress paths, correspond well in Figure 5-22. For instance, by comparing 46471/1 and 46474/1, both of which have $\eta_1 = 0.3$ and $\eta_2 = 0$, it appears that the inclination of the strain paths is the same along both of the η_1 and η_2 stress paths, whereas the absolute value of both of the shear and volumetric strains change at the end of consolidation by about 1%.

Table 5-8 reports the test results of series 2 in terms of shearing resistance (M and ϕ') and of compressibility parameters λ and κ . λ is the slope of the Normal Consolidation Line (NCL) in a v - $\ln p'$ graph, measured during first consolidation stage with η_1 . κ is the slope of the Unload-Reload Line (URL), measured by unloading on the first consolidation stage with inclination η_1 . The initial state of the specimens is defined by the initial void ratio e_0 and the initial water content w_0 with reference to the plasticity index I_p .

| Specimen Nr. | η | e_0 | w_0 % | I_p % | λ | κ | M | ϕ' ° |
|-----------------|--------|-------|------------|------------|-----------|----------|-----------|--------------|
| 46496/56 | -0.5 | 0.99 | 35.6 | 22.2 | 0.098 | 0.025 | 0.98 | 25.2 |
| 46496/57 | -0.3 | 1.0 | 34.9 | 22.2 | 0.12 | 0.016 | 1.04 | 26.4 |
| 46471/1 | -0.3 | 0.89 | 32.4 | 23.7 | 0.067 | 0.019 | 0.88(Ext) | 31.4(Ext.) |
| 46472/2 | -0.5 | 0.88 | 32.6 | 23.7 | 0.082 | 0.021 | 1.06 | 26.9 |
| 46473/2 | 0 | 0.91 | 33.9 | 23.7 | 0.088 | 0.024 | 1.04 | 26.6 |
| 46474/1 | -0.3 | 0.92 | 32.9 | 23.7 | 0.069 | 0.024 | 1.02 | 26.7 |
| 46475/1 | -0.5 | 0.91 | 33.8 | 23.7 | 0.077 | 0.035 | 1.06 | 26.9 |
| 46216/1 | 0.75 | 1.02 | 31.2 | 19.6 | 0.164 | 0.043 | 1.08 | 27.4 |
| 46216/2 | 0.75 | 1.1 | 38.8 | 19.6 | 0.134 | 0.039 | 1.09 | 27.5 |
| 46216/3 | 0.75 | 1.05 | 36.9 | 19.6 | 0.199 | 0.023 | 1.08 | 27.9 |

Table 5-8: Results of triaxial stress path tests, series 2.

Sample 46216 from 6 m depth shows higher λ and κ values than samples 46471 to 46475 from 6.5 m depth. Based on its lower I_p value, sample 46216 should be stiffer, and its slightly higher w_0 and e_0 values hardly explain such higher values of the compressibility parameters λ and κ . Figure 5-23 shows a consistent trend between the inclination of the stress path η and the λ values measured, which indicate that the higher η is, the higher is also λ . This is due to destructuration, which increases with η approaching the critical state value M (Koskinen et al., 2002a).

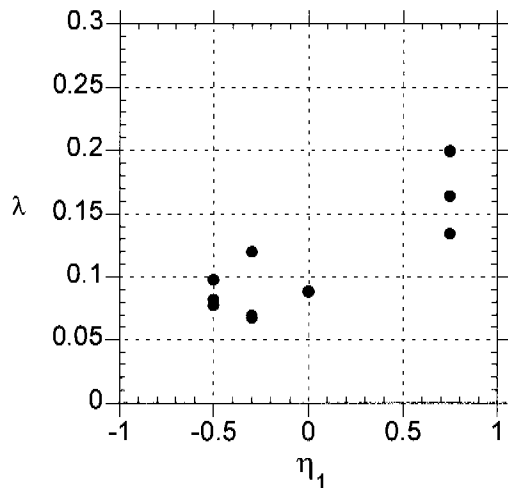


Figure 5-23: Trend between the λ values and the inclination η of the stress path during which λ was measured.

Reconstituted Kreuzlingen clay

Specimens 46496/58 and /510 were installed in the triaxial cell under the estimated effective stress state during the last stage of consolidation in the 400 mm diameter oedometer. A K_0 value of 0.549 was estimated from Jaky's (1944) formula $K_0 = 1 - \sin\phi'$ and used to estimate the horizontal stresses in the oedometer cell. Both specimens stayed under these stress conditions for two weeks, and were then sheared to failure. The effective stress paths to failure of specimens 46496/58 and /510 show the typical behaviour of lightly overconsolidated clay samples (Figure 5-24 a), which reach the actual yield surface and then bend off towards the Critical State Line, with reducing mean effective stress.

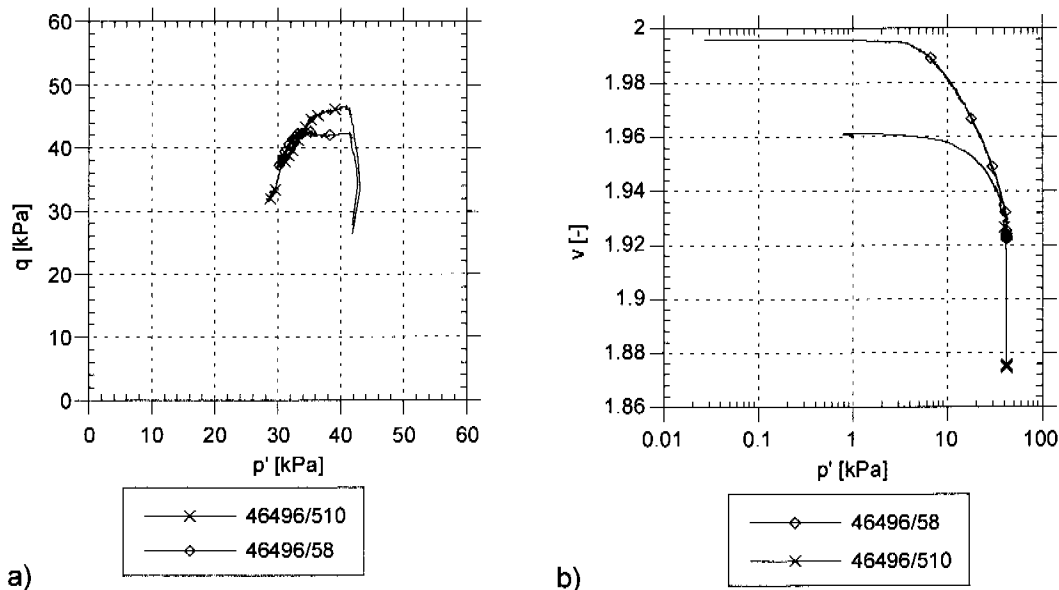


Figure 5-24: a) q - p' diagram for reconstituted Kreuzlingen clay: undrained shear stage to failure, b) v - $\ln p'$ diagram of the consolidation and creep stage.

Both tests showed a ductile failure mode with the sample forming a barrel shape. The critical state parameter M for these two specimens is equal to 1.25 ($\phi' = 31.1^\circ$), which is higher than for the natural samples and also for the other normally consolidated reconstituted samples. It can be seen from Figure 5-24 b that 46496/510 shows a much higher volumetric change during the creep stage than test 46496/58, with v decreasing from 1.92 until ca. 1.87.

Though tests 46496/56 and /57 have been subjected to the same stress path history as tests on natural samples, they show a completely different and quite unusual shearing behaviour (Figure 5-25 a and b). Specimen 46496/56 was subjected to a stress path with $\eta_1 = -0.5$ and $\eta_2 = 0.3$ and it was in a normally consolidated stress state with $p' = 418$ kPa and $q = 140$ kPa at beginning of the shearing stage. Specimen 46496/57 was subjected to a stress path with $\eta_1 = -0.3$ and $\eta_2 = 0$ and it was in a normally consolidated stress state with $p' = 406$ kPa and $q = 1$ kPa at beginning of the shearing stage.

Initially the stress paths are similar to those on natural samples, but then they show a strong tendency for strain hardening. After diminution of the mean effective stress p' due to peak excess pore pressures by axial strains of less than 3% and 1% respectively, the effective stress paths bend towards increasing p'

and q to reach peak strength at strains $\varepsilon_{a,n}$ of about 20%. The reconstituted samples show large strain softening post peak, but they appear ductile with peak deviator stress occurring at about 20% axial strain. However the strength parameter M agrees well with the results on natural samples, with values of 0.98 and 1.04 respectively (Figure 5-26 a and Figure 5-27 a). Both specimens show a failure mechanism with a localised slip surface. The natural Kreuzlingen clay could consolidate under self weight for a long period of time and the effect of this ageing can be detected in the lower void ratio (Bjerrum, 1973) when compared to the reconstituted Kreuzlingen clay (Figure 5-26 b and Figure 5-27 b).

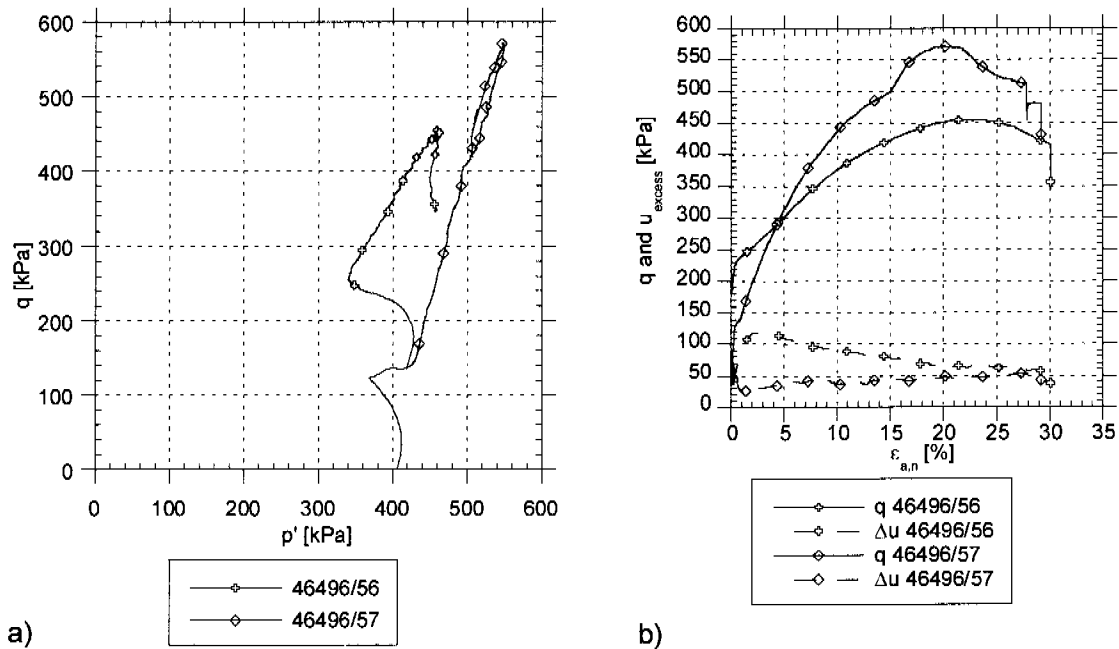


Figure 5-25: a) q - p' diagrams for reconstituted Kreuzlingen clay: undrained shear stage to failure, b) excess pore water pressures and deviator stress development during shearing.

Comparisons of the volumetric behaviour of the natural and reconstituted samples however, indicate that in spite of the differences in initial void ratio, the reconstituted clay reaches more or less the same void ratio condition at the end of consolidation. Values of $\Delta V/V_0$ and $\Delta e/e_0$ during consolidation are much higher for the reconstituted than the natural samples.

Long (2003) also observed similar behaviour on Athlone laminated clay during CAUC tests, when the specimen was of poor quality. The tests results suggests that the tube sampling process may have densified and destructured the Athlone laminated clay (Long, 2003). Lunne et al. (1997) and Hight et al. (1992) both present a similar conclusion and Long also reports tests on other soils, where similar behaviour has been observed (Karlsrud, 1995, Seierstad, 2000) and explains it through sample disturbance and densification. In the present case, greater compression of the reconstituted specimens took place during the stress path consolidation, when compared with the natural samples. The unusual shearing behaviour could be explained, according to the experience on Athlone laminated clay, with a densification of the specimen, which in this case is not due to sampling procedures but rather to consolidation. Küng (2003) tested

reconstituted samples of Birmensdorf clay in his diploma project. The samples, which were reconsolidated during a preliminary stage using a support until the specimen reached a certain stiffness, showed the same behaviour as the reconstituted Kreuzlingen clay described above, while the samples consolidated without the support showed the expected behaviour of a normally consolidated clay.

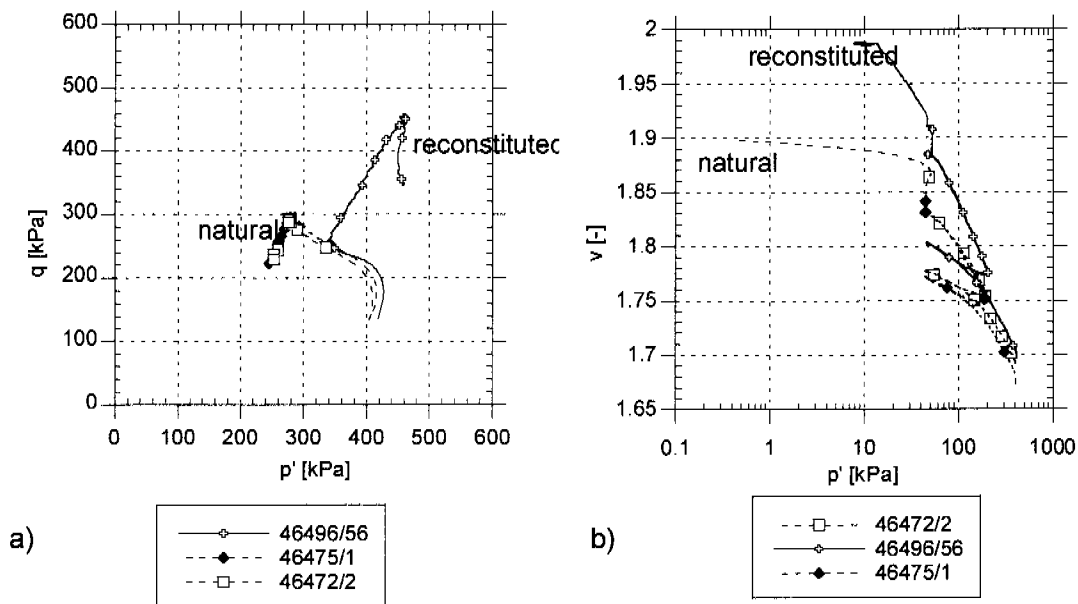


Figure 5-26: Comparison between natural and reconstituted Kreuzlingen clay: tests with same stress path history.

The slope λ of the Normal Consolidation Line (NCL) in $\ln p'$ - v space is steeper for the reconstituted samples, as expected for young clays, whereas the slopes κ of the unload-reload line (URL) are more or less identical for both materials for these equivalent stress cycles (Table 5-8).

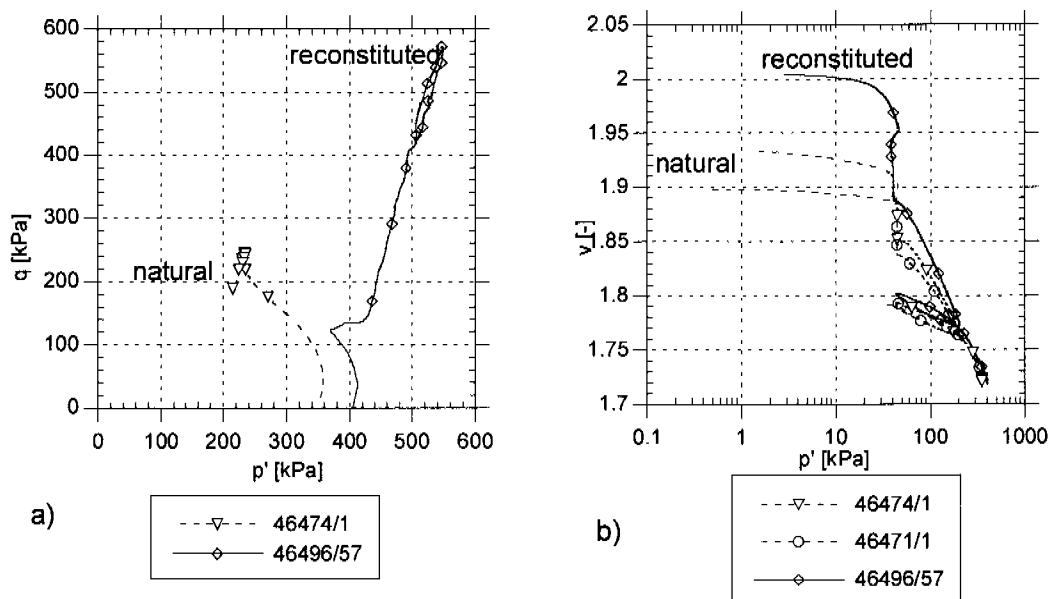


Figure 5-27: Comparison between natural and reconstituted Kreuzlingen clay: tests with same stress path history.

The total strain paths during consolidation are comparable for specimens of reconstituted and natural Kreuzlingen clay when subjected to the same stress path history (Figure 5-28). Specimen 46496/57 shows very high initial shear strains under in situ stresses, which perhaps reflects disturbance of the specimen. The rest of the strain path however, runs more or less parallel to those of the natural samples 46474/1 and 46471/1.

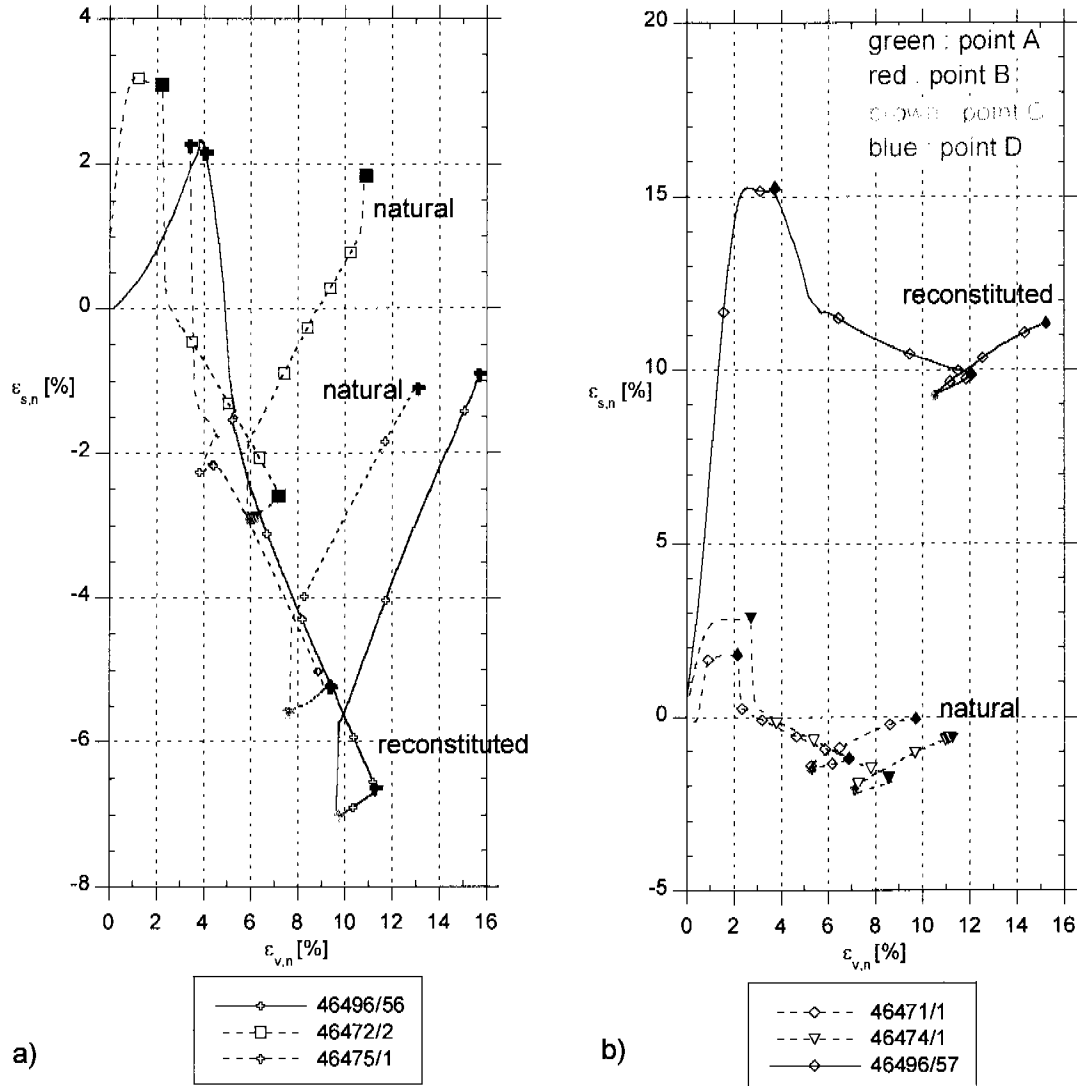


Figure 5-28: Comparison of the strain paths of reconstituted and natural Kreuzlingen clay during stress controlled consolidation stages on the same stress paths. Points A to B refer to stress reversal points as shown in Figure 5-12.

Birmensdorf clay

Various types of tests have been carried out on undisturbed samples and on drilling core samples of Birmensdorf clay. Some tests were carried out in the framework of two diploma projects co-supervised by the author (Panduri, 2000, Fleischer, 2000). Table 5-9 reports the test results on Birmensdorf clay in terms of shearing resistance (M and ϕ'). The values of λ and κ , the slopes of the Normal Consolidation Line (NCL) and the Unload-Reload Line (URL) respectively in $\ln p'-v$ space, are evaluated for the drained consolidation stages, and therefore they cannot be determined for tests from series 1. The initial state of the specimens is defined by the initial void ratio e_0 and the initial water content w_0 , with reference to the plasticity index I_p .

Observing the failure points in effective stress space of all tests from series 1 and 2, would allow a Critical State Line for compression be outlined, with M equal to 0.9 (Figure 5-29). Again, not enough extension tests are available to define a unique Critical State parameter in the negative quadrant of the q - p' stress space.

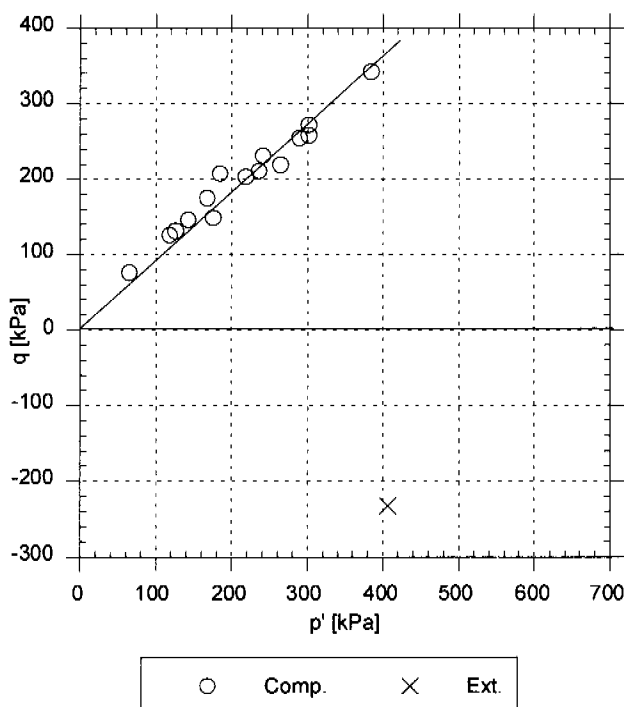


Figure 5-29: Failure points in effective stress space for Birmensdorf clay, series 1 and 2.

To differentiate between the test results however, the effective stress paths to failure should be discussed on the basis of the material used and of the test type. In Figure 5-30, the stress paths are given for undisturbed (u) samples and drilled core (dc) samples separately.

The undisturbed samples are similar in I_p but show great differences in initial void ratios e_0 and water contents w_0 (Table 5-9). Two groups are clearly visible, each having different failure parameters. Specimens 46294/1 and 46297/2 have M equal to 0.87, which is very low if compared also with results on Kreuzlingen clay, whereas specimens 46294/5, 17 and 18 show higher values of M (1.02 - 1.15).

Looking at the varving pattern of these five specimens (Figure 5-31), it can be observed that inclined silt layers in specimens 46297/2 and 46294/1 have favoured failure at a lower value of deviator stress q than expected from the Critical State Line. In the specimens 46294/8 and 46294/7, thick horizontal silt layers have also influenced failure resulting in higher shear resistance (M equal to 1.12 and 1.15 respectively). 46294/5 is the most homogeneous specimen and can be taken as the reference specimen to evaluate the shearing resistance of Birmensdorf clay from triaxial testing. The failure properties of the other specimens would have been more relevant in

direct and ring shear tests. In consequence, the M value of Birrnsdorf clay can be set equal to 1.02. It is evident from these results that the varving has a great influence on the results of triaxial tests, where their extent is important in terms of the dimensions and orientation of the specimen.

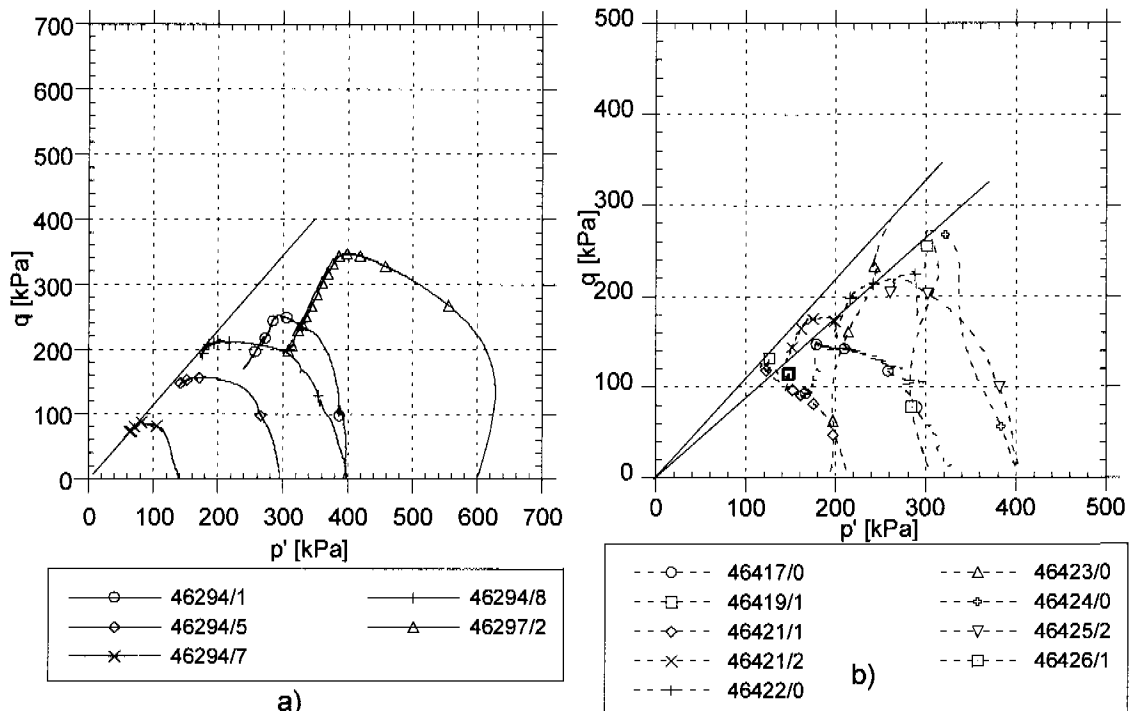


Figure 5-30: Stress paths in p' - q space: a) undisturbed samples (Panduri, 2000, and Giudici), b) drilled core samples (Fleischer, 2000).

In contrast to the undisturbed samples, the drilled core samples are characterized by very high water content and plasticity index. They do not show any trend in respect of the critical state parameter M in q - p' space. All but the two CAUC tests 46419/1 and 46421/2 result in values of M lower than unity.

An influence of the varving pattern could not be detected following tests on these drilled core samples, which were more homogeneous in the macro-appearance and did not present failure mechanisms dictated by the spatial arrangement of clay and silt layers. Even though the samples were reconsolidated at mean effective stresses higher than in situ, the disturbance due to the drilling may still have influenced the test results. The samples extracted from borehole number 3 all show higher I_p than the values from other samples.

The weighting of the test results shows that it is not valid to define a failure parameter on the base of failure points of several tests, when the structure of the material has such an influence on the test results. This raises two questions:

- how can the results on a small triaxial specimen be transferred into design calculations, where the dimensions of the object are orders of magnitude greater than the varving in the clay layer?
- on the other hand would it be possible for the spatial arrangement of clay and silt layers (perhaps with favourable inclination with respect to load) to have a similar influence on shear resistance under design

conditions as in tests 46297/2 and 46294/1, with a localisation of failure and smaller shear resistance parameter, such as a residual shear strength?

These questions will be discussed further in Chapters 6 and 7.

| Specimen Nr. | Soil state | Test type | e_0 | w_0 | I_p | λ | κ | M | ϕ' |
|-----------------|---------------|--------------|-------|-------|-------|-----------|----------|------|---------|
| | | | - | % | % | - | - | - | ° |
| 46294/1 | u | CIUC | 1.02 | 36.0 | 25.7 | - | - | 0.87 | 22.5 |
| 46294/5 | u | CIUC | 1.07 | 36.3 | 25.7 | - | - | 1.02 | 26.0 |
| 46294/7 | u | CIUC | 0.93 | 33.3 | 25.7 | - | - | 1.15 | 29.4 |
| 46294/8 | u | CIUC | 0.96 | 34.6 | 25.7 | - | - | 1.12 | 28.2 |
| 46421/1 | dc | CIUC | 1.82 | 40.7 | - | - | - | 1.07 | 27.1 |
| 46417/0 | dc | CIUC | 1.72 | 52.9 | - | - | - | 0.85 | 21.8 |
| 464218/0 | dc | CIUC | 1.78 | 52.9 | 55.8 | - | - | 0.89 | 22.8 |
| 46425/0 | dc | CIUC | 1.81 | 42.1 | 49.1 | - | - | 0.82 | 21.1 |
| 46419/1 | dc | CAUC | 1.80 | 44.0 | - | - | - | 1.05 | 26.5 |
| 46421/2 | dc | CAUC | 1.83 | 40.4 | 43.0 | - | - | 1.04 | 26.2 |
| 46422/0 | dc | CAUC | 1.83 | 41.3 | - | - | - | 0.93 | 23.7 |
| 46423/0 | dc | OC3.0 | 1.85 | 41.5 | - | - | - | 0.96 | 24.5 |
| 46424/0 | dc | OC1.5 | 1.83 | 42.3 | - | - | - | 0.9 | 23.1 |
| 46426/1 | dc | OC2.0 | 1.86 | 43.3 | - | - | - | 0.85 | 22.0 |
| 46297/2 | u | TSPT | 1.86 | 39.2 | 26.6 | 0.116 | 0.038 | 0.87 | 22.8 |
| 46297/3 | u | TSPT | 1.80 | 44.2 | 26.6 | 0.137 | 0.047 | -0.6 | 18.5 |

Table 5-9: Results of triaxial stress path tests on Birmensdorf clay, series 1 and 2.

Only two specimens of sample 46297 have been tested in triaxial stress path tests (Table 5-6). The specimens have been brought to the estimated in situ stresses and then loaded with η_1 equal to 0.3. After unloading on the same stress path, specimen 46297/3 followed a 2nd. loading path with η_2 equal to 0.5, and 46297/2 with η_2 equal to 0 (Figure 5-32). The strain paths of TSPT 46297/2 and /3 are shown in Figure 5-33 b. Specimen 46297/3 developed higher shear strains during reconsolidation at in situ stresses, and is possibly slightly disturbed. During the 2nd loading path with η_2 equal to 0, the strain path of specimen 46297/2 show zero shear strains, indicating that the assumption, that increments of solely mean effective stress cause only volumetric strains is valid for this sample.

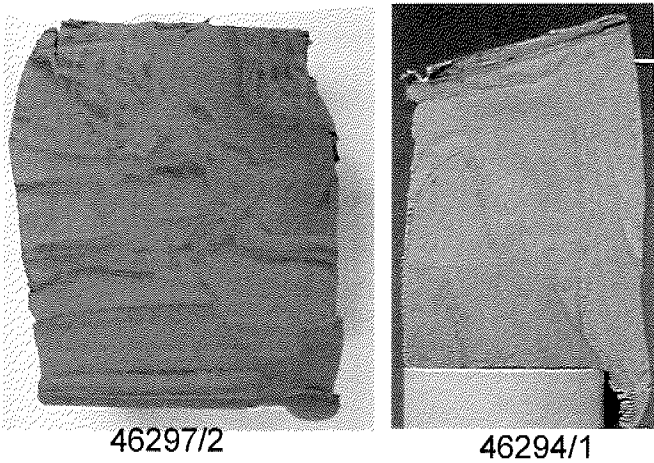


Figure 5-31: Pictures of sheared specimens of undisturbed Birmensdorf samples.

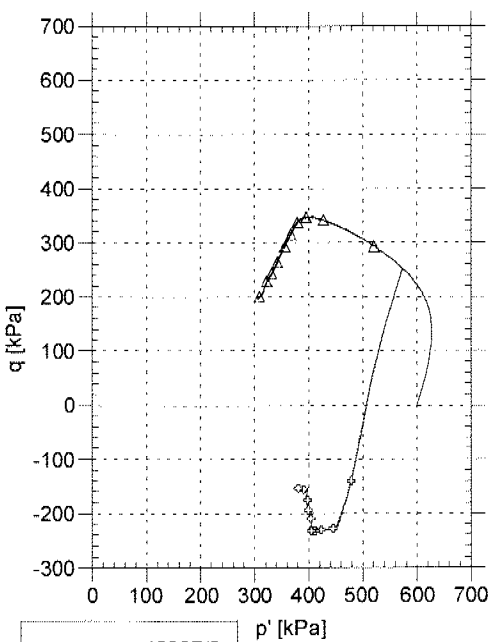
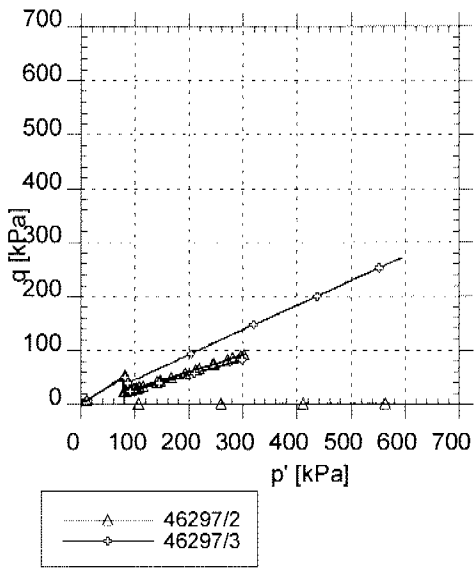
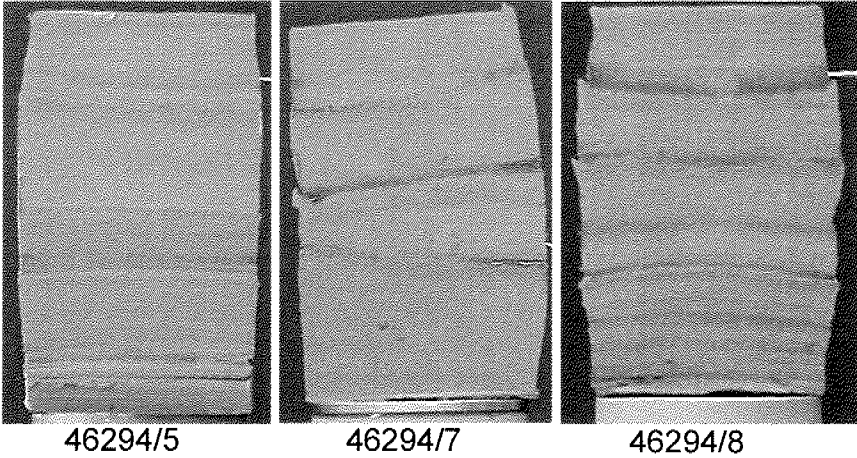


Figure 5-32: Stress paths during consolidation and shearing for specimens 46297/2 and 46297/3.

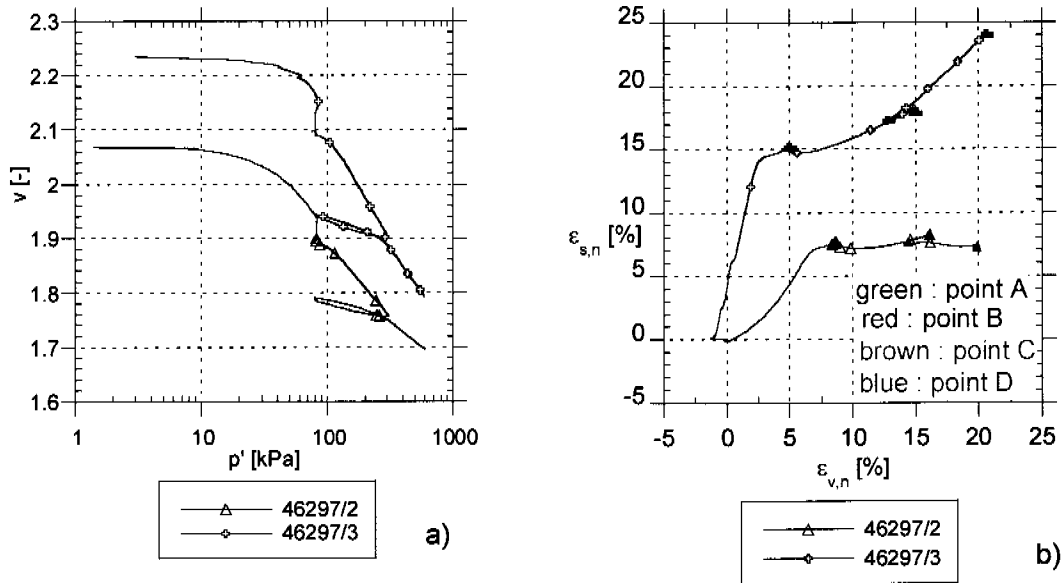


Figure 5-33: v - $\ln p'$ and strain path graphs for specimens 46297/2 and 46297/3 during stress controlled consolidation. Points A to B refer to stress reversal points as shown in Figure 5-12.

5.2 One-dimensional compression tests

5.2.1 Oedometer testing equipment

Two different continuous loading oedometers were used for this research and will be described briefly here (Figure 5-34).

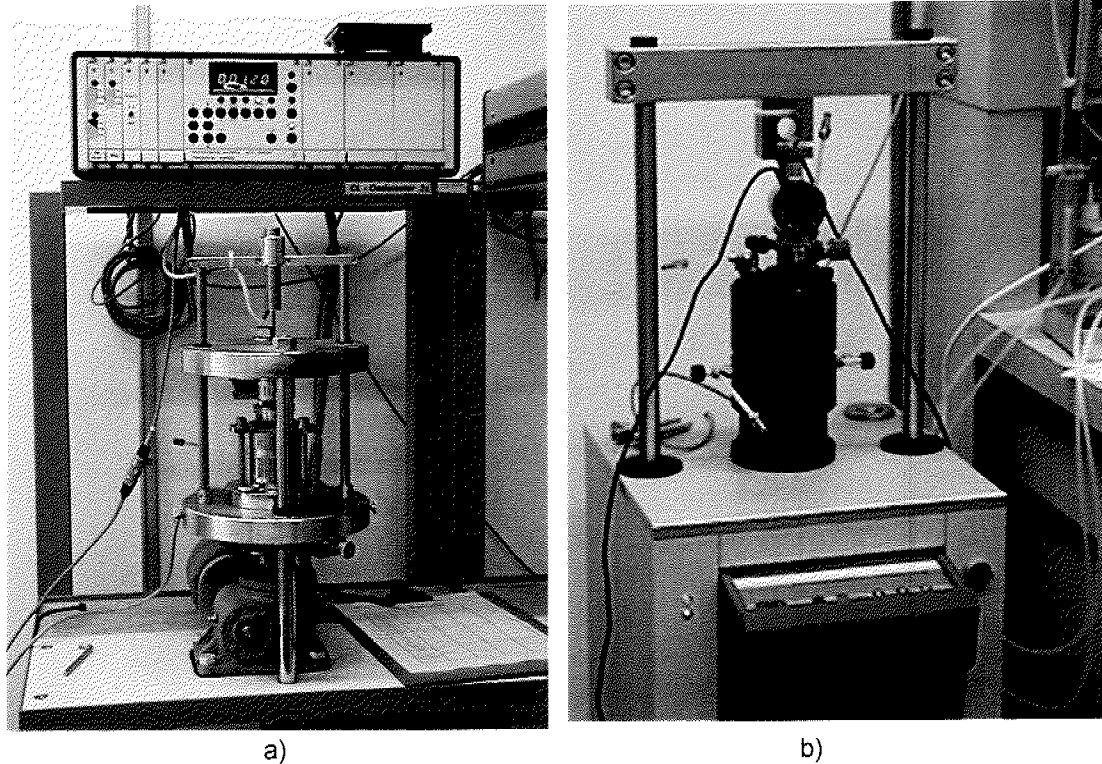


Figure 5-34: a) NGI oedometer device, b) Wille oedometer device

The NGI oedometers have a specimen diameter of 56.4 mm and a height of 20 mm. They are computer controlled by a program similar to that described for the triaxial apparatus, and allow constant rate of strain (CRS), constant rate of load (CRL), controlled gradient (CG) and creep tests to be carried out. The specimen is drained from the top and pore water pressures are measured at the bottom. To prevent the specimen from drying out due to drainage at the top during slow tests and creep tests, a sponge has been placed over the top platten and has been kept wet. The installation of the specimen in the cell and under the loading frame is relatively straightforward, although when the loading frame is not set exactly on the specimen, then some limited displacements and friction forces are measured.

The Wille oedometer has a specimen diameter of 50.0 mm and a variable height of 20 to 40 mm. It is computer controlled and allows CRS, CRL, CG and creep tests as well as unload-reload stages to be carried out. The lower and upper drainage filters are connected to an air-water-interface supplied by compressed air, which allows a back pressure to be set on the specimen. It is convenient to use a back pressure to prevent negative pore pressures during unload stages. When used, the back pressure was left constant on the specimen for 8 hours to ensure a constant distribution of pore water pressures, then the lower

drainage was closed. The installation of the specimen in the cell can cause some difficulties, and limited start displacements and loads are also possible with this device.

A comparison of the data obtained from both devices with similar natural samples (from the same sample core) showed that the results are comparable, but difficulties are encountered when start displacements and forces are present in either or both of the tests.

5.2.2 Testing procedures

Sample preparation

Three triaxial and five oedometer specimens could be extracted from a 800 mm sampler as well as material for classification tests. For the procedure used to extrude the samples and to store them, see Section 5.1.2.

The specimen was cut to a size of 2 cm without trimming the diameter. Then the oedometer ring, which has a smaller diameter, was pushed into the specimen, so that the soil material filled the ring without gaps between the sample and the sides of the ring. The oedometer ring had a cutting edge to minimise disturbance of the soil. The material remaining outside the ring was used for the determination of initial water content.

The cell was filled with deaired water and care was needed to avoid air bubbles appearing in the cell tube system. Then the oedometer ring containing the specimen was placed in the cell with filter papers and brass filters at the top and bottom.

The cell was closed and placed under the press and the transducers for excess pore water pressure, vertical displacement and vertical load were connected. An air-water interface was installed in the Wille oedometer to provide the specimen with back pressure.

Testing programme

The soft clays encountered in the Swiss Mittelland create difficulties for project engineers in defining the deformation and the consolidation properties for safe design. Many of the soft clays evaluated in recent years by means of laboratory tests showed high to very high sensitivities, from 7 up to more than 100 (Leroueil et al., 1985, Näätänen et al., 1999, Näätänen & Lojander, 2000), while the Swiss lacustrine clays tested to date have maximum sensitivities of 4-5. Cone penetration tests show that the cone resistance q_c of Seebodenlehm increases linearly with depth, which indicates that the clays are normally consolidated and therefore extremely compressible (Springman et al., 1999, Chapter 4). Natural clay behaviour is complex and there are important differences between soil conditions in situ and during a laboratory test, which should prevent test results being used directly for design, without the boundary conditions in the test being considered. During in situ primary consolidation, the main factors that could induce differences between laboratory and in situ behaviour are strain rate, temperature and structuring phenomena (Leroueil, 1996). The strain rate is typically between $5 \cdot 10^{-8}$ and $5 \cdot 10^{-6} \text{ s}^{-1}$ in oedometer tests and between $5 \cdot 10^{-12}$ and $1 \cdot 10^{-8} \text{ s}^{-1}$

under embankments. The representative parameters for the calculation of long-term settlements should be determined with these differences in mind (Leroueil, 1996).

The aim of the oedometer test investigation is a comprehensive comparison of permeability and compressibility properties for different Swiss clays under various compression test procedures.

The continuous loading (CL) oedometer tests were performed on Kreuzlingen and Birmensdorf clays with different boundary conditions and testing procedures. During the period leading up to submission of her Diploma thesis, Basler (2001) also tested Seebodenlehm from Belp, located again in the Swiss Mittelland near to Bern. Basler (2001) compares the response from Belp, Kreuzlingen and Birmensdorf clays. To analyse the influence of strain rate, the strain rate and the specimen height were varied in Constant Rate of Strain (CRS) tests, whereas the excess pore pressure at the base was changed in Controlled Gradient (CG) tests. To analyse the influence of structure, reconstituted samples of Kreuzlingen clay were also tested. Finally, some creep tests were performed to investigate the influence of ageing of these clays.

The CL-oedometer test series on undisturbed samples include 44 tests carried out by Basler (2001), 4 tests carried out by Panduri (2000) and 47 tests carried out within this research programme. The strain rates employed in this series were in the range of $1.8 \cdot 10^{-7} - 1 \cdot 10^{-5} \text{ s}^{-1}$. Table 5-10 gives an overview of this test series. Fleischer (2000) carried out 18 CL-Tests on Birmensdorf clay with 12 vertical and 6 horizontal specimens to evaluate the difference in vertical and horizontal permeability due to the structural anisotropy of the clay. In these tests, the strain rate was held constant at $3.7 \cdot 10^{-6} \text{ s}^{-1}$ (Table 5-11). Four incremental loading tests were performed as well, and used for comparison purposes with the CL-Oedometer test results.

| test No | clay | | test type | initial height [mm] | strain rate $\dot{\epsilon}$ s^{-1} | Δu_B [kPa] | σ_{cr}' [kPa] | t_{cr} [h] |
|----------|-------|-----------|-----------|---------------------|--|---------------------|----------------------|--------------|
| | site | depth [m] | | | | | | |
| 46292/1 | Birm2 | 8.01 | 77.0 | CRS | 20 | $1.8 \cdot 10^{-7}$ | - | - |
| 46292/2 | Birm2 | 8.09 | 77.6 | CRS | 20 | $1.8 \cdot 10^{-7}$ | - | - |
| 46292/3w | Birm2 | 8.18 | 78.3 | CRS | 20 | $3 \cdot 10^{-6}$ | - | - |
| 46292/4w | Birm2 | 8.27 | 79.0 | CRS | 20 | $3 \cdot 10^{-6}$ | - | - |
| 46292/3 | Birm2 | 8.34 | 79.6 | CRS | 20 | $3 \cdot 10^{-6}$ | - | - |
| 46292/4 | Birm2 | 8.42 | 80.3 | CRS | 20 | $3 \cdot 10^{-6}$ | - | - |
| 46292/5 | Birm2 | 8.49 | 80.8 | CRS | 20 | $6 \cdot 10^{-6}$ | - | - |
| 46292/5w | Birm2 | 8.55 | 81.3 | CRS | 20 | $6 \cdot 10^{-6}$ | - | - |
| 46292/6 | Birm2 | 8.62 | 81.9 | CRS | 20 | $6 \cdot 10^{-6}$ | - | - |
| 46292/7 | Birm2 | 8.69 | 82.4 | CRS | 20 | $1 \cdot 10^{-5}$ | - | - |

Table 5-10: Overview of CL-oedometer test series

| test No | clay | | σ_v' [kPa] | test type | initial height [mm] | strain rate $\dot{\epsilon}$ s ⁻¹ | ΔU_B [kPa] | σ_{cr}' [kPa] | t_{cr} [h] |
|-----------------------|--------|-----------|-------------------|-----------|---------------------|--|--------------------|----------------------|--------------|
| | site | depth [m] | | | | | | | |
| 46292/8 | Birm2 | 8.74 | 82.8 | CRS | 20 | 1*10 ⁻⁵ | - | - | - |
| 46292/9 | Birm2 | 8.78 | 83.1 | Creep | 20 | 3*10 ⁻⁶ | - | 368 | - |
| 46295/2 ^a | Birm2 | 8.22 | 78.7 | CRS | 20 | 1*10 ⁻⁵ | - | - | - |
| 46295/3 ^a | Birm2 | 8.26 | 79.0 | CRS | 20 | 1*10 ⁻⁵ | - | - | - |
| 46295/4 ^a | Birm2 | 8.29 | 79.2 | CRS | 20 | 1*10 ⁻⁵ | - | - | - |
| 46295/5 ^a | Birm2 | 8.12 | 77.9 | CRS | 20 | 6*10 ⁻⁶ | - | - | - |
| 46295/6 ^a | Birm2 | 8.15 | 78.1 | CRS | 40 | 3*10 ⁻⁶ | - | - | - |
| 46295/7 ^a | Birm2 | 8.19 | 78.4 | CRS | 20 | 6*10 ⁻⁶ | - | - | - |
| 46295/8 ^a | Birm2 | 8.02 | 77.1 | CRS | 40 | 1*10 ⁻⁵ | - | - | - |
| 46295/9 ^a | Birm2 | 8.07 | 77.5 | CRS | 20 | 3*10 ⁻⁶ | - | - | - |
| 46295/10 ^a | Birm2 | 8.08 | 77.5 | CRS | 20 | 3*10 ⁻⁶ | - | - | - |
| 46295/11 ^a | Birm2 | 8.34 | 79.6 | CRS | 40 | 1*10 ⁻⁵ | - | - | - |
| 46295/12 ^a | Birm2 | 8.55 | 81.3 | CG | 20 | - | 15 | - | - |
| 46295/13 ^a | Birm2 | 8.59 | 81.6 | CG | 20 | - | 30 | - | - |
| 46295/14 ^a | Birm2 | 8.38 | 79.9 | CRS | 40 | 3*10 ⁻⁶ | - | - | - |
| 46296/2 ^a | Birm2 | 5.55 | 57.3 | CRS | 20 | 3*10 ⁻⁶ | - | - | - |
| 46296/3 ^a | Birm2 | 5.58 | 57.5 | Creep | 20 | 3*10 ⁻⁶ | - | 180 | 49 |
| 46296/4 ^a | Birm2 | 5.11 | 53.8 | CRS | 20 | 1*10 ⁻⁵ | - | - | - |
| 46296/5 ^a | Birm2 | 5.15 | 54.1 | CRS | 20 | 6*10 ⁻⁶ | - | - | - |
| 46296/6 ^a | Birm2 | 5.32 | 55.5 | CRS | 40 | 3*10 ⁻⁶ | - | - | - |
| 46296/7 ^a | Birm2 | 5.17 | 54.3 | CRS | 20 | 6*10 ⁻⁶ | - | - | - |
| 46296/8 ^a | Birm2 | 5.51 | 57.0 | CRS | 40 | 6*10 ⁻⁶ | - | - | - |
| 46296/9 ^a | Birm2 | 5.41 | 56.2 | CG | 20 | - | 15 | - | - |
| 46296/10 ^a | Birm2 | 5.46 | 56.6 | CG | 20 | - | 30 | - | - |
| 46294/2 ^b | Birm2 | 8.18 | | CRS | 20 | 3.3*10 ⁻⁶ | - | - | - |
| 46294/3 ^b | Birm2 | 8.21 | | CRS | 20 | 3.3*10 ⁻⁶ | - | - | - |
| 46294/4 ^b | Birm2 | 8.25 | | CRS | 20 | 3.3*10 ⁻⁶ | - | - | - |
| 46294/6 ^b | Birm2 | 8.43 | | CRS | 20 | 3.3*10 ⁻⁶ | - | - | - |
| 46215/4 | Kreuz1 | 5.37 | 65.9 | CRS | 20 | 3.2*10 ⁻⁶ | - | - | - |
| 46215/6 | Kreuz1 | 5.45 | 66.6 | CRS | 20 | 1.7*10 ⁻⁶ | - | - | - |
| 46218/9 | Kreuz1 | 8.5 | 92.5 | CRS | 20 | 3.7*10 ⁻⁶ | - | - | - |
| 46219/3 | Kreuz1 | 9.32 | 99.5 | CRS | 20 | 3*10 ⁻⁶ | - | - | - |

Table 5-10: Overview of CL-oedometer test series

| test No | clay | | σ_v' [kPa] | test type | initial height [mm] | strain rate $\dot{\epsilon}$ s ⁻¹ | ΔU_B [kPa] | σ_{cr}' [kPa] | t_{cr} [h] |
|----------------------|--------|-----------|-------------------|-----------|---------------------|--|--------------------|----------------------|--------------|
| | site | depth [m] | | | | | | | |
| 46219/5 | Kreuz1 | 9.54 | 101 | CRS | 20 | $3.2 \cdot 10^{-6}$ | - | - | - |
| 46222/6 | Kreuz1 | 12.5 | 126 | CRS | 20 | $3 \cdot 10^{-6}$ | - | - | - |
| 46222/8 | Kreuz1 | 12.9 | 130 | CRS | 20 | $3 \cdot 10^{-6}$ | - | - | - |
| 46226/9 | Kreuz1 | 22.7 | 223 | CRS | 20 | $3.2 \cdot 10^{-6}$ | - | - | - |
| 46217/1 | Kreuz1 | 6.95 | 79.3 | CRS | 20 | $1.8 \cdot 10^{-7}$ | - | - | - |
| 46217/4 | Kreuz1 | 7.1 | 80.6 | CRS | 20 | $3 \cdot 10^{-6}$ | - | - | - |
| 46217/5 | Kreuz1 | 7.2 | 81.5 | CRS | 20 | $3 \cdot 10^{-6}$ | - | - | - |
| 46217/6 | Kreuz1 | 7.25 | 81.9 | CRS | 20 | $6 \cdot 10^{-6}$ | - | - | - |
| 46217/7 | Kreuz1 | 7.3 | 82.3 | CRS | 20 | $1 \cdot 10^{-5}$ | - | - | - |
| 46217/8 | Kreuz1 | 7.4 | 83.2 | CRS | 20 | $1 \cdot 10^{-5}$ | - | - | - |
| 46217/9 | Kreuz1 | 7.5 | 84.0 | Creep | 20 | $3 \cdot 10^{-6}$ | - | 360 | 628 |
| 46217/9w | Kreuz1 | 7.6 | 84.9 | Creep | 20 | $3 \cdot 10^{-6}$ | - | 476 | 336 |
| 46476/1 | Kreuz2 | 6.41 | 65.1 | CRS | 20 | $3 \cdot 10^{-6}$ | - | - | - |
| 46476/2 | Kreuz2 | 6.46 | 65.5 | CRS | 20 | $6 \cdot 10^{-6}$ | - | - | - |
| 46476/4 | Kreuz2 | 6.54 | 66.2 | CRS | 40 | $3 \cdot 10^{-6}$ | - | - | - |
| 46478/1 | Kreuz2 | 6.41 | 65.1 | CRS | 20 | $1.8 \cdot 10^{-7}$ | - | - | - |
| 46478/2 | Kreuz2 | 6.5 | 65.8 | CRS | 20 | $1.8 \cdot 10^{-7}$ | - | - | - |
| 46477/2 | Kreuz2 | 6.46 | 65.5 | CRS | 40 | $1 \cdot 10^{-5}$ | - | - | - |
| 46477/3 | Kreuz2 | 6.5 | 65.8 | Creep | 20 | $3 \cdot 10^{-6}$ | - | 355 | 109 |
| 46477/4 | Kreuz2 | 6.54 | 66.2 | CRS | 40 | $6 \cdot 10^{-6}$ | - | - | - |
| 46490/1 | Kreuz2 | 6.5 | 65.8 | CRS | 20 | $1.8 \cdot 10^{-7}$ | - | - | - |
| 46474/1 ^a | Kreuz2 | 6.4 | 65.0 | CRS | 20 | $1 \cdot 10^{-5}$ | - | - | - |
| 46474/2 ^a | Kreuz2 | 6.5 | 65.8 | CRS | 20 | $1 \cdot 10^{-5}$ | - | - | - |
| 46474/3 ^a | Kreuz2 | 6.6 | 66.7 | CRS | 20 | $6 \cdot 10^{-6}$ | - | - | - |
| 46475/1 ^a | Kreuz2 | 6.5 | 65.8 | CRS | 40 | $1 \cdot 10^{-5}$ | - | - | - |
| 46483/1 ^a | Kreuz2 | 6.4 | 65.0 | CRS | 40 | $6 \cdot 10^{-6}$ | - | - | - |
| 46483/2 ^a | Kreuz2 | 6.5 | 65.8 | CRS | 20 | $6 \cdot 10^{-6}$ | - | - | - |
| 46482/1 ^a | Kreuz2 | 6.4 | 65.0 | CG | 20 | - | 15 | - | - |
| 46482/2 ^a | Kreuz2 | 6.5 | 65.8 | CG | 20 | - | 30 | - | - |
| 46484/1 ^a | Kreuz2 | 6.4 | 65.0 | Creep | 20 | $3 \cdot 10^{-6}$ | - | 218 | 49 |
| 46484/2 ^a | Kreuz2 | 6.5 | 65.8 | CRS | 40 | $3 \cdot 10^{-6}$ | - | - | - |
| 46485/2 ^a | Kreuz2 | 6.5 | 65.8 | CRS | 40 | $3 \cdot 10^{-6}$ | - | - | - |

Table 5-10: Overview of CL-oedometer test series

| test No | clay | | σ_v' [kPa] | test type | initial height [mm] | strain rate $\dot{\epsilon}$ s ⁻¹ | ΔU_B [kPa] | σ_{cr}' [kPa] | t_{cr} [h] |
|----------------------|--------|-----------|-------------------|-----------|---------------------|--|--------------------|----------------------|--------------|
| | site | depth [m] | | | | | | | |
| 46488/1 ^a | Kreuz2 | 6.4 | 65.0 | CRS | 20 | 3*10 ⁻⁶ | - | - | - |
| 46488/2 ^a | Kreuz2 | 6.5 | 65.8 | CG | 20 | - | 15 | - | - |
| 46488/3 ^a | Kreuz2 | 6.56 | 66.4 | CG | 20 | - | 30 | - | - |
| 46600/1 ^a | Belp | 12 | 119 | CRS | 20 | 6*10 ⁻⁶ | - | - | - |
| 46600/2 ^a | Belp | 12 | 119 | CRS | 20 | 1*10 ⁻⁵ | - | - | - |
| 46600/3 ^a | Belp | 12 | 119 | CRS | 20 | 6*10 ⁻⁶ | - | - | - |
| 46600/4 ^a | Belp | 12 | 119 | CRS | 20 | 3*10 ⁻⁶ | - | - | - |
| 46600/5 ^a | Belp | 12 | 119 | CRS | 20 | 3*10 ⁻⁶ | - | - | - |
| 46496/511a1 | Rec | - | 60.0 | CRS | 20 | 1*10 ⁻⁵ | - | - | - |
| 46496/511a2 | Rec | - | 60.0 | CRS | 20 | 6*10 ⁻⁶ | - | - | - |
| 46496/511a3 | Rec | - | 60.0 | CRS | 20 | 3*10 ⁻⁶ | - | - | - |
| 46496/510a1 | Rec | - | 60.0 | CRS | 20 | 1*10 ⁻⁵ | - | - | - |
| 46496/510a2 | Rec | - | 60.0 | CRS | 20 | 1.8*10 ⁻⁷ | - | - | - |
| 46496/510a3 | Rec | - | 60.0 | CRS | 20 | 1.8*10 ⁻⁷ | - | - | - |
| 46496/510a4 | Rec | - | 60.0 | CRS | 20 | 8*10 ⁻⁷ | - | - | - |
| 46496/510b1 | Rec | - | 60.0 | CRS | 20 | 6*10 ⁻⁶ | - | - | - |
| 46496/510b2 | Rec | - | 60.0 | Creep | 20 | 3*10 ⁻⁶ | - | 1400 | 119 |
| 46496/562 | Rec | - | 60.0 | CRS | 20 | 1.8*10 ⁻⁷ | - | - | - |
| 46496/563 | Rec | - | 60.0 | CRS | 20 | 8*10 ⁻⁷ | - | - | - |
| 46496/571 | Rec | - | 60.0 | CRS | 20 | 6*10 ⁻⁶ | - | - | - |
| 46496/572 | Rec | - | 60.0 | Creep | 20 | 3*10 ⁻⁶ | - | 890 | 124 |
| 46496/581 | Rec | - | 60.0 | CRS | 20 | 3*10 ⁻⁶ | - | - | - |
| 46496/582 | Rec | - | 60.0 | CRS | 20 | 3*10 ⁻⁶ | - | - | - |
| 46496/511b1 | Rec | - | 60.0 | CRS | 40 | 3*10 ⁻⁶ | - | - | - |
| 46496/511b2 | Rec | - | 60.0 | CRS | 40 | 3*10 ⁻⁶ | - | - | - |
| 46496/511b3 | Rec | - | 60.0 | CRS | 40 | 6*10 ⁻⁶ | - | - | - |
| 46496/511b5 | Rec | - | 60.0 | CRS | 20 | 1*10 ⁻⁵ | - | - | - |

Table 5-10: Overview of CL-oedometer test series

a. Basler (2002)

b. Panduri (2000)

| test No | clay | | σ_v' [kPa] | test type | height [mm] | strain rate $\dot{\epsilon}$ s ⁻¹ | direction |
|-----------|-------|-----------|-------------------|-----------|-------------|--|------------|
| | site | depth [m] | | | | | |
| 46417/0.1 | Birm3 | 10.25 | | CRS | 20 | $3.7 \cdot 10^{-6}$ | vertical |
| 46417/0.2 | Birm3 | 10.25 | 94.9 | CRS | 20 | $3.7 \cdot 10^{-6}$ | vertical |
| 46426/2.1 | Birm3 | 13.85 | 123.7 | CRS | 20 | $3.7 \cdot 10^{-6}$ | vertical |
| 46418/1 | Birm3 | 10.60 | 97.7 | CRS | 20 | $3.7 \cdot 10^{-6}$ | vertical |
| 46419/0 | Birm3 | 10.65 | 98.1 | CRS | 20 | $3.7 \cdot 10^{-6}$ | vertical |
| 46419/1 | Birm3 | 10.65 | 98.1 | CRS | 20 | $3.7 \cdot 10^{-6}$ | vertical |
| 46421/2 | Birm3 | 12.40 | 112.1 | CRS | 20 | $3.7 \cdot 10^{-6}$ | vertical |
| 46420/0.1 | Birm3 | 10.95 | 100.5 | CRS | 20 | $3.7 \cdot 10^{-6}$ | horizontal |
| 46420/0.2 | Birm3 | 10.95 | 100.5 | CRS | 20 | $3.7 \cdot 10^{-6}$ | horizontal |
| 46426/2.2 | Birm3 | 13.95 | 124.5 | CRS | 20 | $3.7 \cdot 10^{-6}$ | horizontal |
| 46426/2.3 | Birm3 | 13.95 | 124.5 | CRS | 20 | $3.7 \cdot 10^{-6}$ | horizontal |
| 46422/0.1 | Birm3 | 12.75 | 114.9 | CRS | 20 | $3.7 \cdot 10^{-6}$ | horizontal |
| 46422/0.2 | Birm3 | 12.75 | 114.9 | CRS | 20 | $3.7 \cdot 10^{-6}$ | horizontal |
| 46421/0 | Birm3 | 12.03 | 109.14 | CRS | 20 | $3.7 \cdot 10^{-6}$ | vertical |
| 46426/1 | Birm3 | 13.75 | 122.9 | CRS | 20 | $3.7 \cdot 10^{-6}$ | vertical |
| 46425/1 | Birm3 | 13.30 | 119.3 | CRS | 20 | $3.7 \cdot 10^{-6}$ | vertical |
| 46423/0 | Birm3 | 12.80 | 115.3 | CRS | 20 | $3.7 \cdot 10^{-6}$ | vertical |
| 46424/0 | Birm3 | 13.0 | 116.9 | CRS | 20 | $3.7 \cdot 10^{-6}$ | vertical |

Table 5-11: Overview of CL-oedometer test series Fleischer (2000)

Interpretation procedures

CRS-Test

During a CRS test, the strain rate is held constant. This rate must be chosen to induce as low excess pore pressures as possible in the sample and will depend primarily upon the permeability and compressibility of the soil. Smith & Wahls (1970) offer an empirical relationship, which can be combined with previous experience to select suitable strain rates. The strain rates employed here were in the range of $1.8 \cdot 10^{-7} - 1 \cdot 10^{-5} \text{ s}^{-1}$.

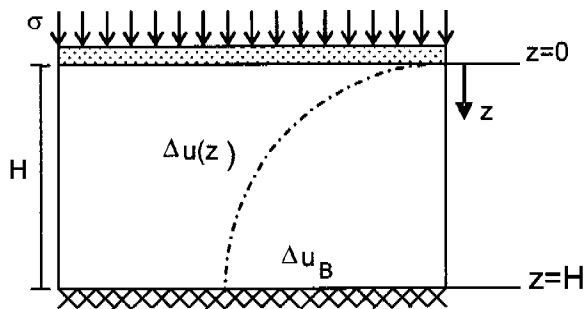


Figure 5-35: Boundary conditions for a CRS-Oedometer test.

A parabolic pattern of excess pore pressure develops in the specimen during a CRS test (Figure 5-35). This pattern is not constant as the excess pore pressure increases during the test until maximum load is reached. Considering the assumptions of Terzaghi's one dimensional consolidation theory to be valid, a derivation of the consolidation equation,

written in terms of void ratio e , is:

$$\frac{k}{\gamma_w} \cdot \frac{\partial^2 \Delta u}{\partial z^2} = \frac{1}{1+e} \cdot \frac{\partial e}{\partial t} \quad [5-25]$$

where k = permeability, γ_w = unit weight of water, u = excess pore pressure at a depth z of the specimen, e = void ratio.

Assuming that the void ratio e is constant over the thickness H of the specimen at any particular moment in time, Equation 5-25 can be rewritten in terms of strain rate $\dot{\epsilon}$ (Equation 5-26). The validity of this assumption depends upon the extent of the excess pore water pressure at the base, which affects the distribution of effective vertical stress in the sample. For the relatively thin samples commonly used, and for relatively slow strain rates, the assumption appears justifiable.

$$\frac{k}{\gamma_w} \cdot \frac{\partial^2 \Delta u}{\partial z^2} = -\dot{\epsilon} \quad [5-26]$$

The boundary conditions for this problem are:

$$\Delta u(z) = 0 \quad \text{for } z = 0$$

$$\frac{\partial \Delta u}{\partial z} = 0 \quad \text{for } z = H$$

The equation linking the excess pore pressure over the thickness z of the specimen (Figure 5-35) is then:

$$\Delta u(z) = \frac{1}{2} \cdot \frac{\gamma_w}{k} \cdot \dot{\varepsilon} \cdot \langle H^2 - (z-H)^2 \rangle \quad [5-27]$$

As Δu_B , the excess pore pressure at $z = H$, is measured, it is possible to calculate the permeability k :

$$k = \frac{1}{2} \cdot \frac{\gamma_w}{\Delta u_B} \cdot \dot{\varepsilon} \cdot H^2 \quad [5-28]$$

The mean excess pore pressure in the specimen, Δu_m , can be calculated from the integral of Δu from $z = 0$ to $z = H$, divided by H :

$$\Delta u_m = \frac{1}{3} \cdot \frac{\gamma_w}{k} \cdot \dot{\varepsilon} \cdot H^2 \quad [5-29]$$

The mean effective vertical stress σ'_m may be derived from Equation 5-29, where σ = total measured vertical stress:

$$\sigma'_m = \sigma - \frac{1}{3} \cdot \frac{\gamma_w}{k} \cdot \dot{\varepsilon} \cdot H^2 \quad [5-30]$$

Knowing k and the mean effective vertical stress σ'_m , it is possible to calculate the constrained modulus M_E and subsequently the coefficient of consolidation c_v . Having determined the void ratio versus effective stress relationship, it is possible to calculate the coefficient of compression C_c .

The CRS testing programme included tests with varying specimen heights of 20 mm and 40 mm, to investigate the influence of the length of the drainage path (Berre & Iversen, 1972).

CG-Test

If the rate of loading is too fast, the high excess pore pressure at the undrained face will give rise to errors due to a large hydraulic gradient and lead to significantly non-uniform effective stresses. The need to limit excess pore pressure leads to a class of continuous loading oedometer tests in which the measured excess pore pressure is used to control the rate of loading (Davison & Atkinson 1990).

The pore pressure difference between the drained and the undrained faces of the specimen is maintained constant, usually at either 15 or 30 kPa. The specimen is first loaded with a high rate of stress [2 kPa/min] to the chosen excess pore water pressure Δu_B , measured at the bottom of the specimen, so that the conditions at the beginning of the test are undrained. Then the bottom pressure is held constant during loading, which means that the compression rate depends on the consolidation and drainage conditions of the clay. The rate of compression cannot be chosen in advance, but different excess pore pressures set at the base automatically cause different rates of compression.

A parabolic pattern of excess pore pressure develops in the specimen under these boundary conditions, which varies from the excess pore pressure maintained at the bottom to zero at the top. This parabolic pattern remains constant during the test, except at the beginning, when the excess pore pressure is being built up, and at the end, when it is being dissipated (Lowe et al., 1969).

The strain rate of the test is an unknown here, but Equation 5-25 can be rewritten in terms of effective stress rate:

$$\frac{k \cdot \langle 1 + e_0 \rangle}{\gamma_w} \cdot \frac{\partial^2 \Delta u}{\partial z^2} = \frac{\langle 1 + e_0 \rangle}{M_E} \cdot \dot{\sigma} \quad [5-31]$$

During the test, the excess pore pressure at the base remains constant, therefore $(\partial u)/(\partial t) = 0$ and Equation 5-31 can be written in terms of total stress σ . The definition of the coefficient of consolidation c_v is:

$$c_v = \frac{k \cdot \langle 1 + e_0 \rangle}{a_v \cdot \gamma_w} = \frac{k \cdot M_E}{\gamma_w} \quad [5-32]$$

Substituting c_v to Equation 5-31 results in:

$$c_v \cdot \frac{\partial^2 \Delta u}{\partial z^2} = \dot{\sigma} \quad [5-33]$$

The boundary conditions for this problem are again:

$$\begin{aligned} \Delta u(z) &= 0 && \text{for } z = 0 \\ \Delta u(z) &= \Delta u_B \text{ and } \frac{\partial \Delta u}{\partial z} = 0 && \text{for } z = H \end{aligned}$$

The equation linking the excess pore pressure over the thickness z of the specimen is then:

$$\Delta u(z) = \Delta u_B \cdot \left(1 - \frac{(z-H)^2}{H^2} \right) \quad [5-34]$$

A simple formula for the direct computation of c_v in terms of stress rate can be obtained inserting the boundary conditions for $z = H$ in Equation 5-33 to give:

$$c_v = \dot{\sigma} \cdot \frac{H^2}{2 \cdot \Delta u_B} \quad [5-35]$$

Substituting Equation 5-32 into Equation 5-35 results in:

$$k = \frac{1}{2} \cdot \frac{\gamma_w}{\Delta u_B} \cdot \frac{\dot{\sigma}}{M_E} \cdot H^2 \quad [5-36]$$

which can be linked to Equation 5-28 under elastic and one-dimensional conditions by $\dot{\sigma} = M_E \cdot \dot{\epsilon}$.

Creep test

A creep stage under an effective vertical stress σ_v' in the range 100 - 1500 kPa followed a CRS loading in some tests. The creep stress was held constant for 2 to 26 days and then the CRS test was continued until end displacement was reached. The value of the secondary compression coefficient c_α can be calculated from the inclination of the creep curve in a semi-logarithmic void ratio to time (e-t) diagram.

5.2.3 Results

The initial void ratio e_0 fluctuated remarkably, even for specimens from the same sample, and the differences were in some cases significant (up to $\Delta e = 0.3$). Not only the natural variability of the specimens was responsible for these differences, some samples had almost certainly suffered some disturbance. Moreover, the vertical yield stress σ'_{vy} was difficult to determine in these samples. The vertical yield stress σ'_{vy} has been determined in the present study by the common method proposed by Casagrande, in contrast to the bilinear method used for the analysis of the triaxial test data.

Burland (1990) recommends using the term vertical yield stress σ'_{vy} , to describe the critical stress at which the structural resistance of a clayey soil breaks down and where the subsequent compression curve is initially steeper than the standard virgin line. Other authors use the term quasi-preconsolidation pressure σ'_p . Because in laboratory testing of soft clays, the strain rate of the test plays an important role in the determination of most parameters, the term "pre-consolidation pressure" should be reserved for situations in which the magnitude of such a critical stress can be established by geological means (Burland, 1990). The degree of sample disturbance can be estimated by plotting the void ratio e to mean effective vertical stress σ'_m curves together with the intrinsic compression line ICL for the clay studied (Burland, 1990). The ICL for Kreuzlingen clay can be estimated in two ways, from the correlation equations based on e_L (the void ratio at liquid limit w_L) presented in Burland (1990) and from the experimental results of the reconstituted clay preparation.

The reconstituted clay was prepared from a mixture of Kreuzlingen clay with a water content of $1.25w_L$. The one dimensional consolidation was carried out in a 400 mm diameter cylinder, and the maximum load was only 60 kPa. However the results show the beginning of the ICL for Kreuzlingen clay, and by using the equation of the ICL given by Burland (Equation 5-37), then the whole curve can be extrapolated and the intrinsic parameters C^*_c and e^*_{100} can be estimated (curve e_{ICL} in Figure 5-36):

$$e_{ICL} = I_v \cdot C^*_c + e^*_{100} \quad [5-37]$$

where I_v is the void index, defined as

$$I_v = \frac{e - e^*_{100}}{e^*_{100} - e^*_{1000}} = \frac{e - e^*_{100}}{C^*_c} \quad [5-38]$$

It is possible to use the empirical correlations proposed by Burland (1990) between e_L and the intrinsic constants of compression C^*_c and e^*_{100} to determine the ICL. Considering that the liquid limit w_L for Kreuzlingen clay shows a fluctuation between 30% and 46% (fluctuation of e_L between 0.83 and 1.27), the ICL has been determined for these two limits ($e_{ICL-wL30}$ and $e_{ICL-wL46}$ in Figure 5-36).

The experimentally extrapolated ICL does not fall between the two correlation curves $e_{ICL-wL30}$ and $e_{ICL-wL46}$, but cuts them both at respectively 20 and 350 kPa vertical effective stress. Specimens 46222/8 (nat) and 46496/511b5 (rec) can be regarded as disturbed also by comparing them with the curve e_{ICL} .

w_{L30} . Specimens 46488/1, 46217/5, 46217/4 (nat) and 46496/511a1 to 3 (rec) plot well over this curve, and also to the right of the experimentally extrapolated curve e_{ICL} . The data from the other specimens lie exactly in between the range given by $e_{ICL-wL30}$ and $e_{ICL-wL46}$. All natural samples were tube samples, whereas block samples (100x100x300 mm) were used for the reconstituted clay (46496/511a and 46496/511b). The quality of the block samples is not always better than the quality of the tube, for instance 46496/511b maybe highly disturbed, whereas the data from the tube sample 46496/581 plots in the middle of the range.

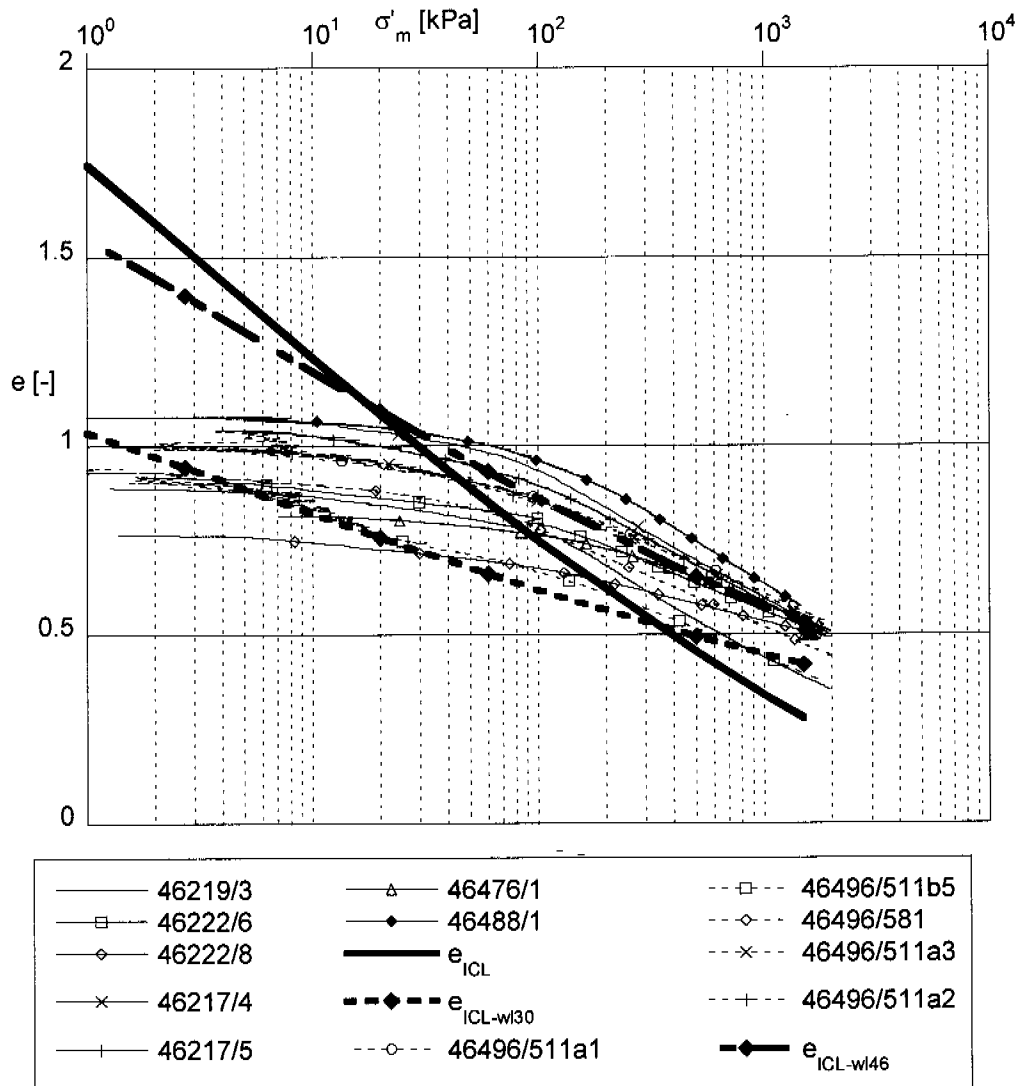


Figure 5-36: Correlations between ICL and CRS-oedometer results for Kreuzlingen clay. (bold: ICL lines; full lines: natural samples; dashed lines: reconstituted)

The empirical correlations (Burland, 1990) between e_L and the intrinsic constants of compression C_c^* and e_{100}^* have also been used to determine the ICL of Birmensdorf clay. The ICL has been determined for both limiting values of the liquid limit w_L for Birmensdorf clay ($e_{ICL-wL42}$ and $e_{ICL-wL76}$ in Figure 5-37). Messerklinger (2003, personal communication) also prepared reconstituted

samples from a mixture of Birmensdorf clay with a water content of $1.75w_L$. The results of this 400 mm diameter oedometer test are presented in Figure 5-37 (e_{ICL}), although this water content is slightly higher than recommended to deduce the ICL line experimentally. The value of the liquid limit of the clay used for this test was 55%, and it can be seen that the experimental ICL line plots well between the two limiting curves.

The results of the CRS oedometer tests are also presented in Figure 5-37. Most of the tests, except 46292/3 and 4, 46295/2 and 46292/7, plot to the right of the $e_{ICL-wL42}$. Specimen 46292/5w shows extremely high void ratios and plots above the experimentally determined ICL line e_{ICL} and the empirical $e_{ICL-wL76}$. However the vertical yield stress is not characterised by a sharp bend in the curve and the value of σ'_{vy} determined from this plot does not lie in the expected range (23.9 kPa for strain rate $6 \cdot 10^{-6} \text{ 1/s}$).

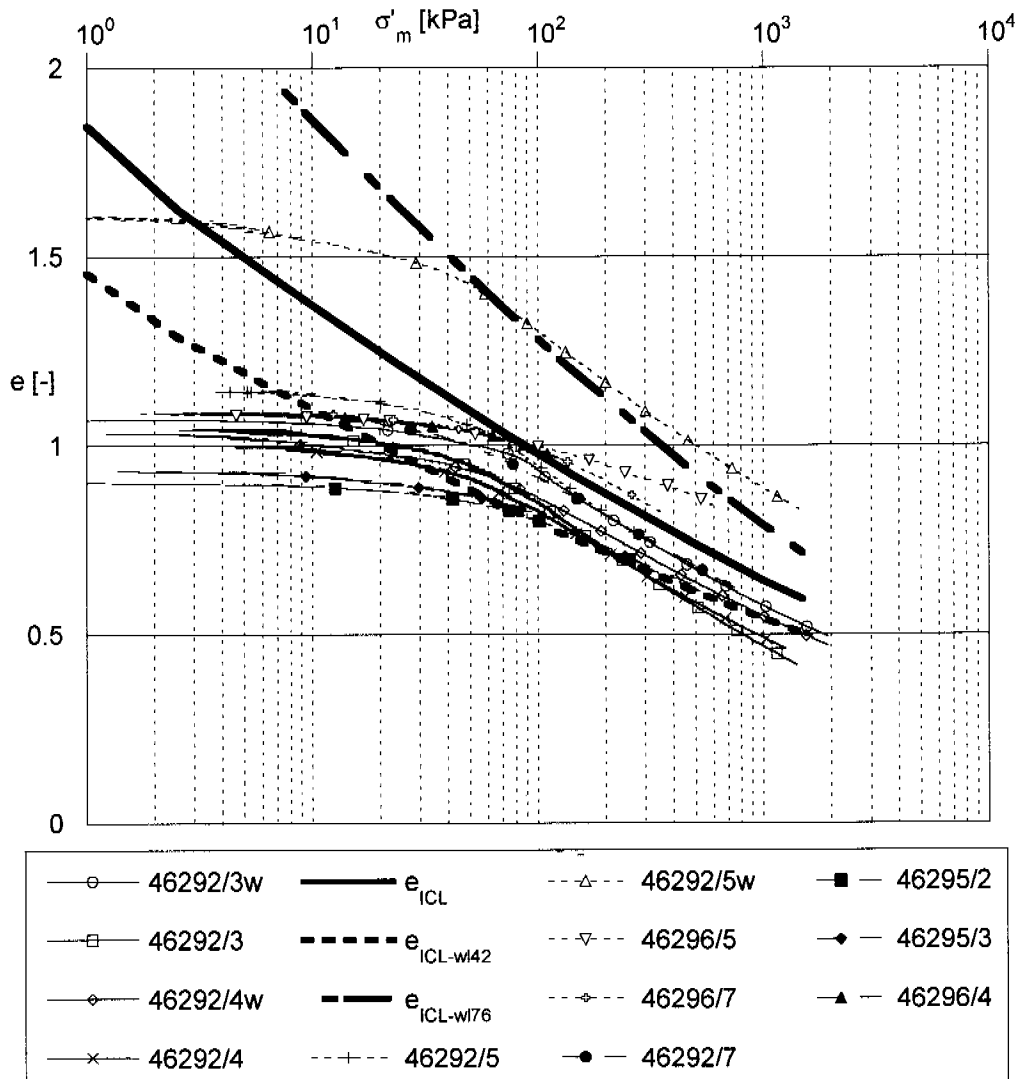


Figure 5-37: Correlations between ICL and CRS-oedometer results for Birmensdorf clay (Messerklinger, 2003, pers. comm.). (bold: ICL lines; full lines: $3 \cdot 10^{-6} \text{ 1/s}$; dashed lines: $6 \cdot 10^{-6} \text{ 1/s}$; full symbols: $1 \cdot 10^{-5} \text{ 1/s}$)

In the following three sections, selected results from the oedometer testing will be shown for each clay separately, and the influence of strain rate and the comparison between natural and reconstituted Kreuzlingen clay will be discussed. Only a part of the test data have been plotted to give the overview. The discussion about the results is, however, based on all of the tests. The majority of tests were carried out with strain rates of $3 \cdot 10^{-6}$, $6 \cdot 10^{-6}$ and $1 \cdot 10^{-5}$ 1/s. Results of the slower tests with a strain rate of $1.8 \cdot 10^{-7}$ 1/s are added in the graphs dealing with the comparison of strain rates. Other topics, such as the comparison of the two natural clays on the basis of their plasticity characteristics, the influence of the drainage length and the results of the creep tests will be discussed later (Chapter 6).

The results have been discussed bearing in mind that the samples have experienced some disturbance and that not all tests plot above the ICL line. To facilitate the comparison of the test results, the void ratio e to mean effective vertical stress σ'_m graph have been normalised in respect of the initial void ratio e_0 .

Kreuzlingen

In Figures 5-38, 5-39 and 5-40, the compressibility and permeability characteristics are illustrated for the different strain rates of $3 \cdot 10^{-6}$, $6 \cdot 10^{-6}$ and $1 \cdot 10^{-5}$ 1/s.

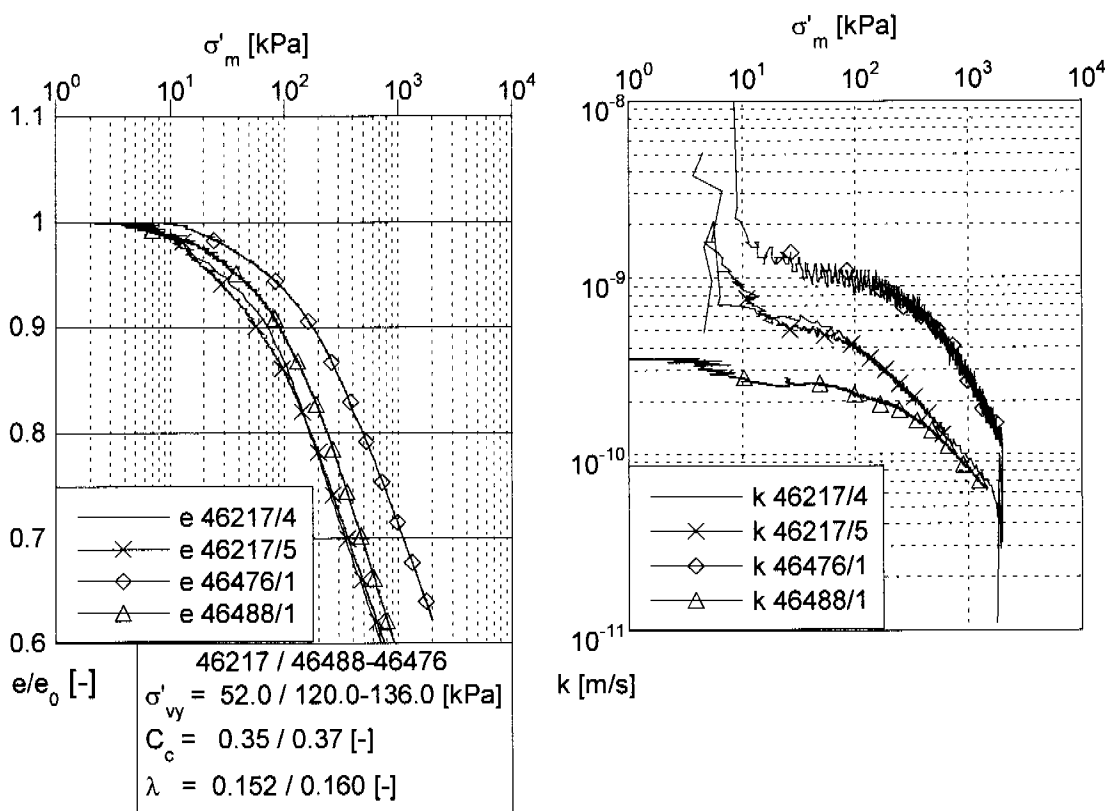


Figure 5-38: Results from tests with strain rate $\dot{\epsilon} = 3 \cdot 10^{-6}$ 1/s. Sample 46217 comes from Kreuz1, whereas samples 46476 and 46488 come from Kreuz2.

Figures 5-41 and 5-42 the normalised void ratio - effective stress curves and the permeability - effective stress curves measured by different strain rates are compared.

Kreuzlingen clay exhibits permeability k , which varies from $1 \cdot 10^{-9}$ m/s to $4 \cdot 10^{-11}$ m/s for mean effective vertical stresses σ'_m between 10 and 1000 kPa. Specimen 46217/1, tested with a strain rate of $1.8 \cdot 10^{-7}$ 1/s, displays a very low permeability (Figure 5-41), which can be due to a very low initial void ratio $e_0 = 0.85$ of this specimen.

From Figures 5-41 and 5-42, a strain rate dependency of the permeability k cannot be assumed with satisfactory reliability. Presumably the natural variability among the specimens is so high, that assessing the influence of strain rate is difficult. In future, strain rate stepping tests on the same specimen should be carried out in order to compare the effect of rate on the same specimen. In addition, the strain rates should be varied over at least 2 or 3 orders of magnitude.

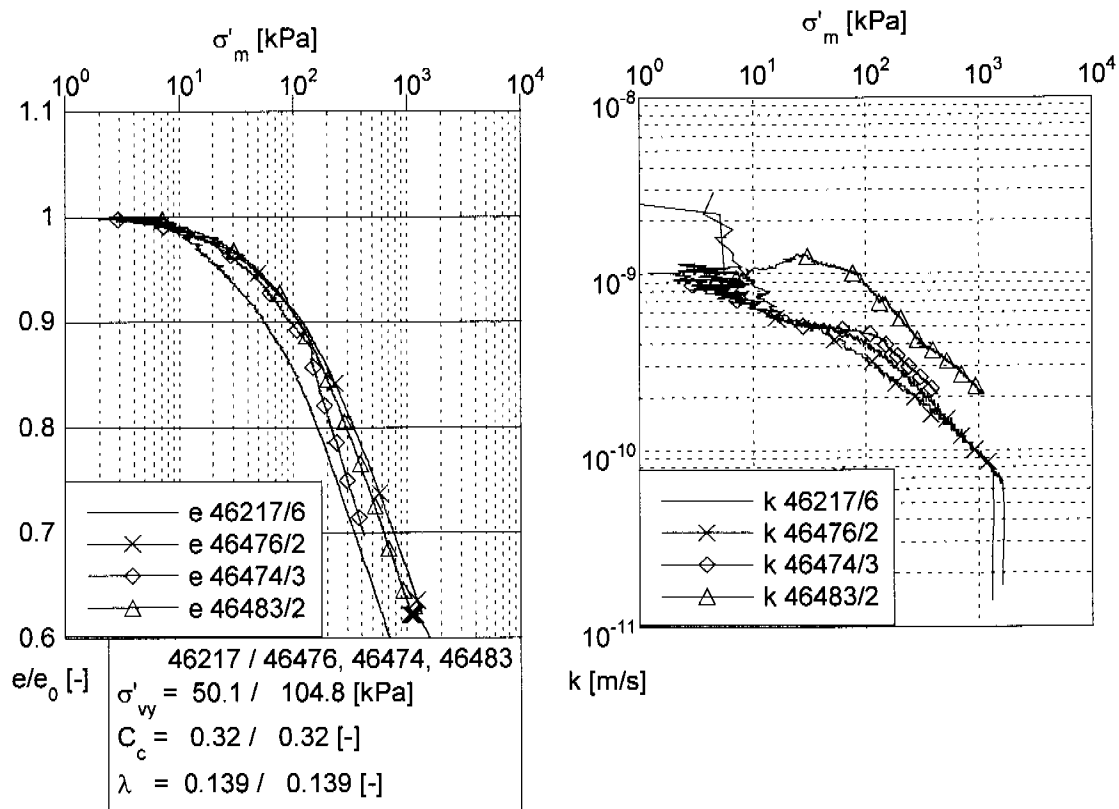


Figure 5-39: Results from tests with strain rate $\dot{\varepsilon} = 6 \cdot 10^{-6}$ 1/s. Sample 46217 comes from Kreuz1, whereas samples 46476, 46474 and 46483 originate from Kreuz2.

The mean effective stress σ'_m to normalised void ratio e/e_0 curves obtained at different strain rates are more or less superposed, and none of the curves show a sharp bend when reaching the vertical yield stress, which is therefore difficult to determine exactly. For the tests performed, it is in general difficult to separate strain rate influence from natural variability of the samples.

The bar graphs in Figure 5-43a and b are an attempt to investigate the influence of strain rate on the vertical yield stress σ'_{vy} and on the coefficient of compression C_c . The yield stress σ'_{vy} is approximately constant for strain rates from $3 \cdot 10^{-6}$ to $1 \cdot 10^{-5}$ 1/s, whereas σ'_{vy} values determined from plots of tests with strain rate $1.8 \cdot 10^{-7}$ 1/s are lower, indicating a slight influence of strain rate for

this clay. In Giudici Trausch et al. (2003), other tests were plotted, which showed a strain rate influence over the whole range of rates studied. It must be noted again that the chosen strain rates are too close to each other to indicate a distinct strain rate dependence.

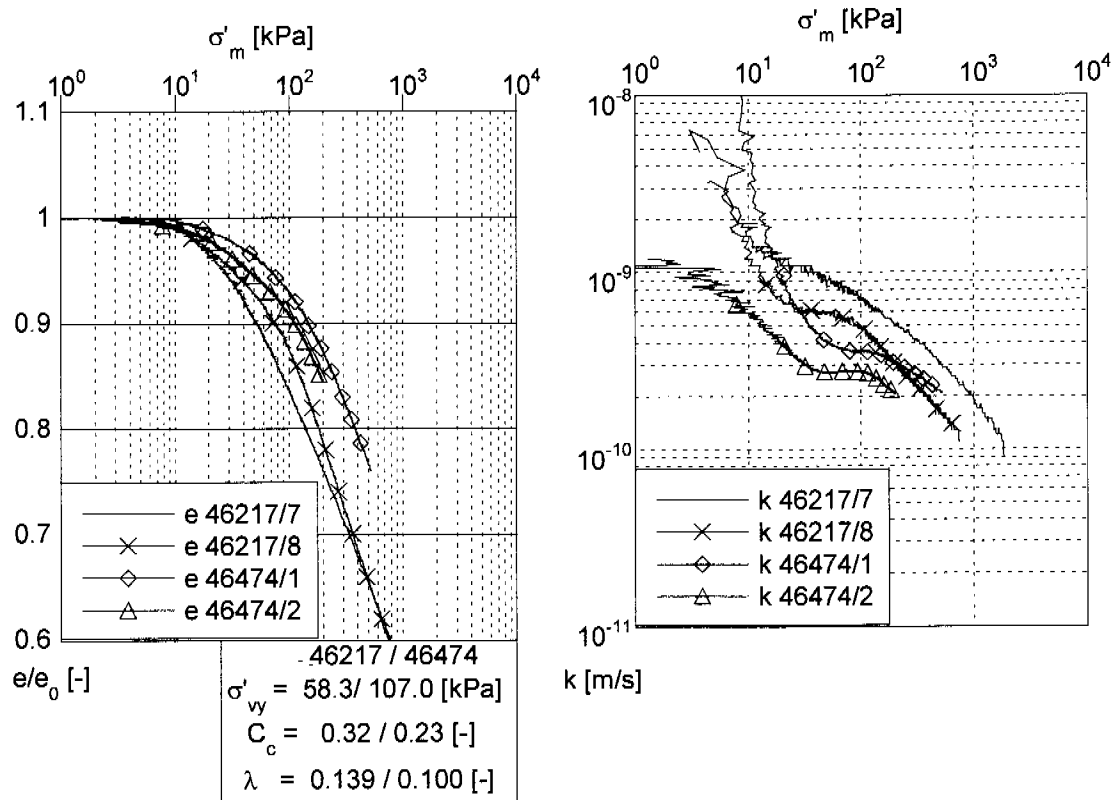


Figure 5-40: Results from tests with strain rate $\dot{\epsilon} = 1 \cdot 10^{-5} \text{ 1/s}$. Sample 46217 comes from Kreuz1, whereas sample 46474 originates from Kreuz2.

A clear difference in the vertical yield stress σ'_{vy} is however visible between samples from Kreuz1 and Kreuz2, although the specimens shown here come from approximately the same depth (specimens from Kreuz2 are from 6.4 m depth, sample 46217 from Kreuz1 is from 6.9 - 7.6 m). The in situ vertical effective stress σ'_v prior to sample extraction, has been estimated to ca. 65 kPa for Kreuz2 and to ca. 82 kPa for Kreuz1. The results indicate smaller σ'_{vy} values for Kreuz1 than would be expected for a normally consolidated clay from the in situ stresses, whereas Kreuz2 samples seem to have lower values of σ'_{vy} than the in situ stresses for a strain rate $1.8 \cdot 10^{-7} \text{ 1/s}$ and slightly higher values for higher strain rates.

The samples from the Kreuz2 site have been taken under a freshly built bridge, which was constructed top down under the existing railway line. If the Seebodenlehm deposits are considered to as geologically normally consolidated, then an explanation for its slight overconsolidation can be the construction of the bridge or the dynamic and static loads from the train service over the past 40 years. At the time of sample extraction, the bridge was being built over a period of two months. This period of time is too short to consolidate the Seebodenlehm deposit. The railway bed is usually 1.5 m high with a specific unit weight

of ca. 30 kN/m³. The Swiss Code SIA 260 (2003) models train loads either by 4 static concentrated loads of 250 kN each, at a distance of 1.60 m from each other, or by a static linear distributed load of 80 kN/m.

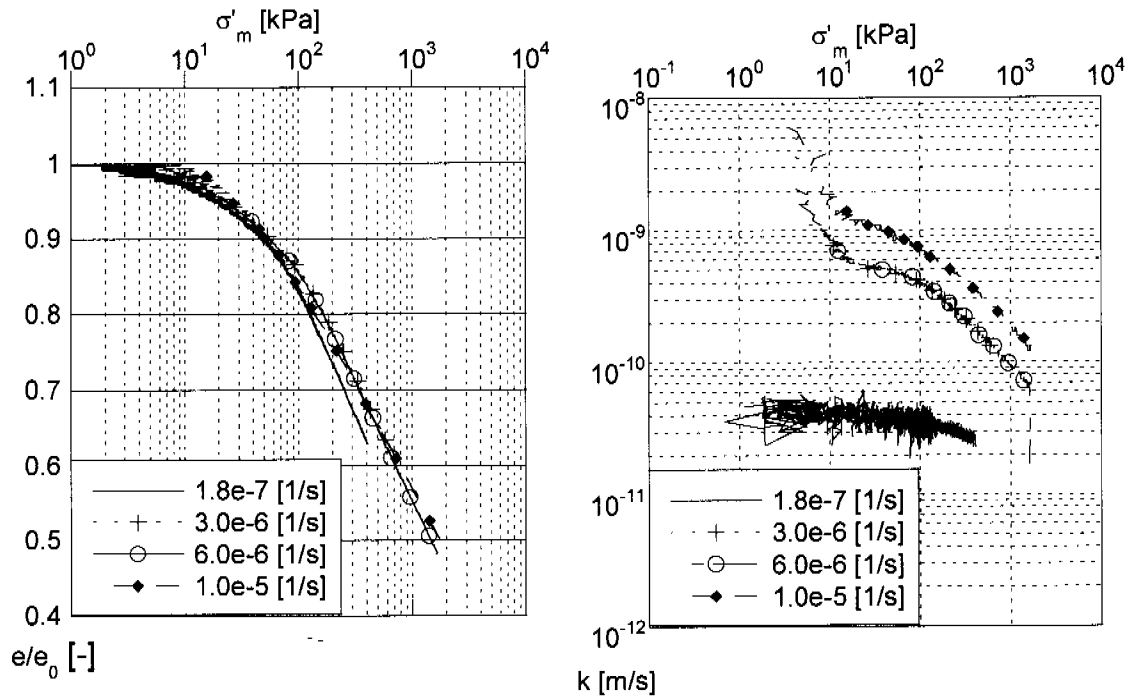


Figure 5-41: Comparison of strain rates for Kreuz1.

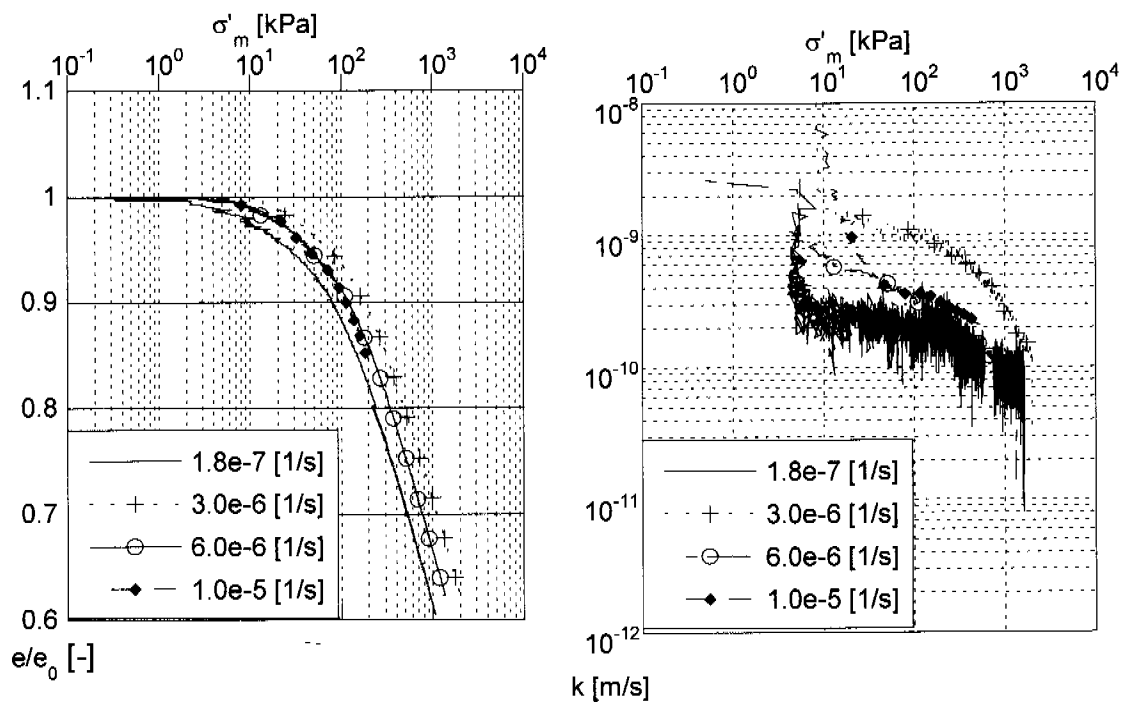


Figure 5-42: Comparison of strain rates for Kreuz2.

The linear distributed load of 80 kPa corresponds to a vertical stress of 8 kPa (elastic distribution of loads with depth, Boussinesq) at 6.4m depth, constituting the major load. This train load of 8 kPa constitutes a dynamic loading on the deposits, which has extended over years, leading probably to settlements and a slightly overconsolidation.

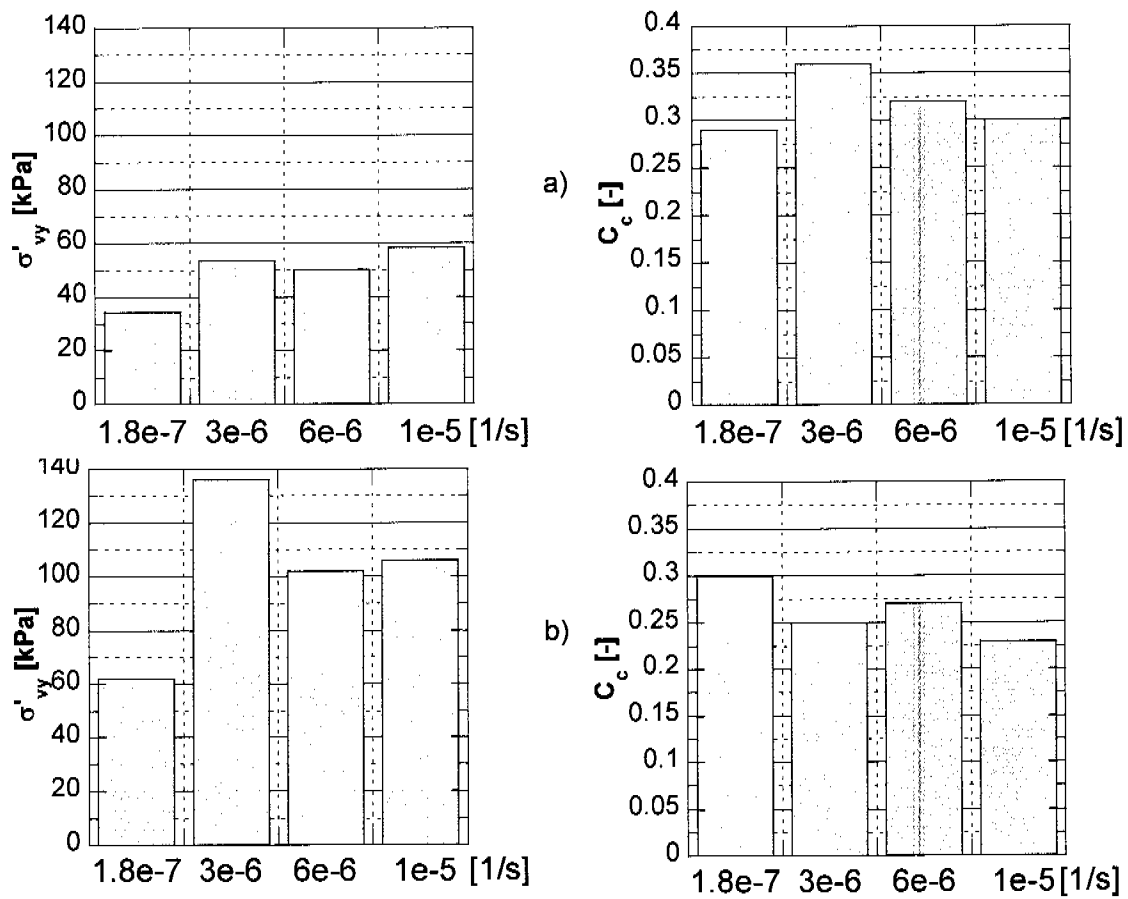


Figure 5-43: Influence of strain rate on σ'_{vy} and C_c : a) Kreuz1 b) Kreuz2.

Reconstituted Kreuzlingen clay

In Figures 5-44, 5-45 and 5-46, the results of the CRS tests on different specimens of the reconstituted Kreuzlingen clay are illustrated for each strain rate ($3 \cdot 10^{-6}$, $6 \cdot 10^{-6}$ and $1 \cdot 10^{-5}$ 1/s) separately in terms of the compressibility and permeability characteristics. Only the two specimens tested at a strain rate of $1.8 \cdot 10^{-7}$ 1/s show significantly lower k values than specimens tested at higher strain rates (Figure 5-47). In this case, the lower permeability is not due to a low initial void ratio e_0 of these specimens. For the higher strain rates, the reconstituted Kreuzlingen clay exhibits a permeability k which varies from $1 \cdot 10^{-9}$ m/s to $1 \cdot 10^{-10}$ m/s for mean effective vertical stresses σ'_m between 10 and 1000 kPa. Compared to the natural clay, the reconstituted clay shows lower permeability at low stresses and higher permeability at high stresses.

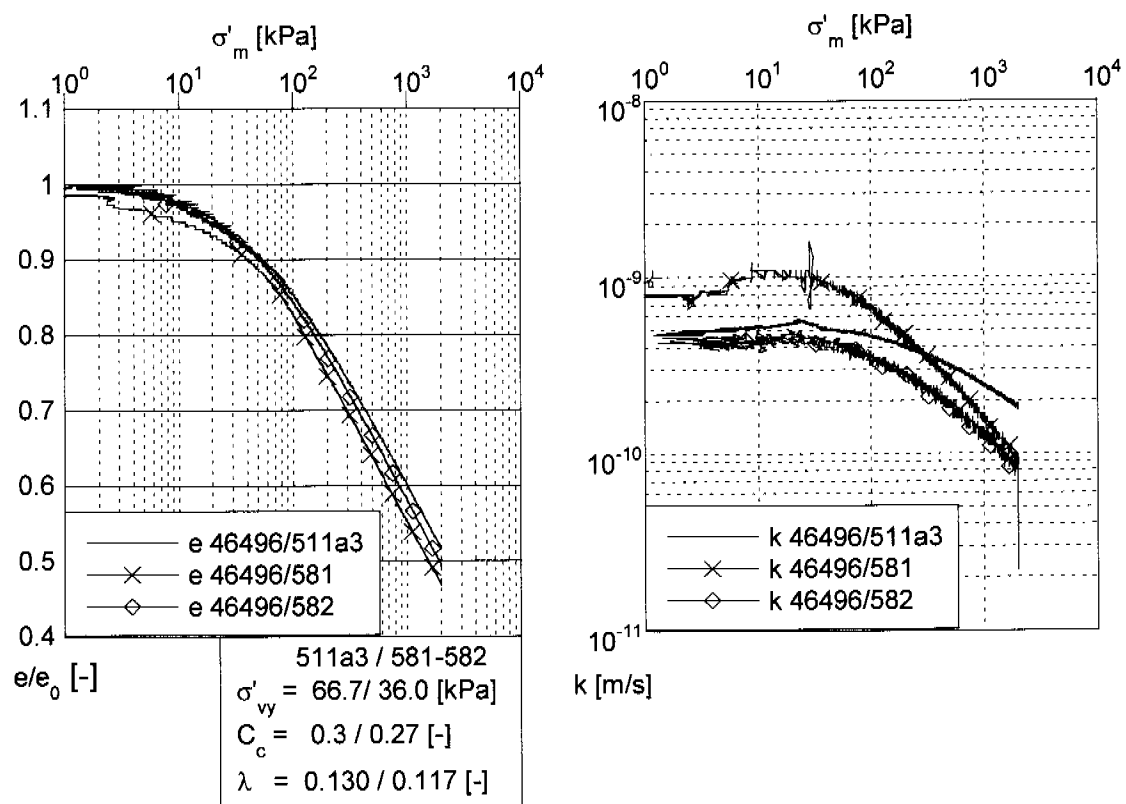


Figure 5-44: Results from tests on reconstituted Kreuzlingen clay with strain rate $\varepsilon = 3 \cdot 10^{-6}$ 1/s.

Sample 46496/511a has been tested by Basler (2001) and is, as indicated by the comparison with the ICL at the beginning of this chapter, a sample of better quality. This indicates what was assumed to be a better estimate of the vertical yield stress σ'_{vy} . The results of the tests performed on the various specimens from this sample, have therefore been used to plot the bar graph in Figure 5-48. Sample 46496/511a was not tested at strain rates slower than $3 \cdot 10^{-6}$ 1/s and therefore the results of tests on other specimens have been added to the graph for the strain rate of $1.8 \cdot 10^{-7}$ 1/s.

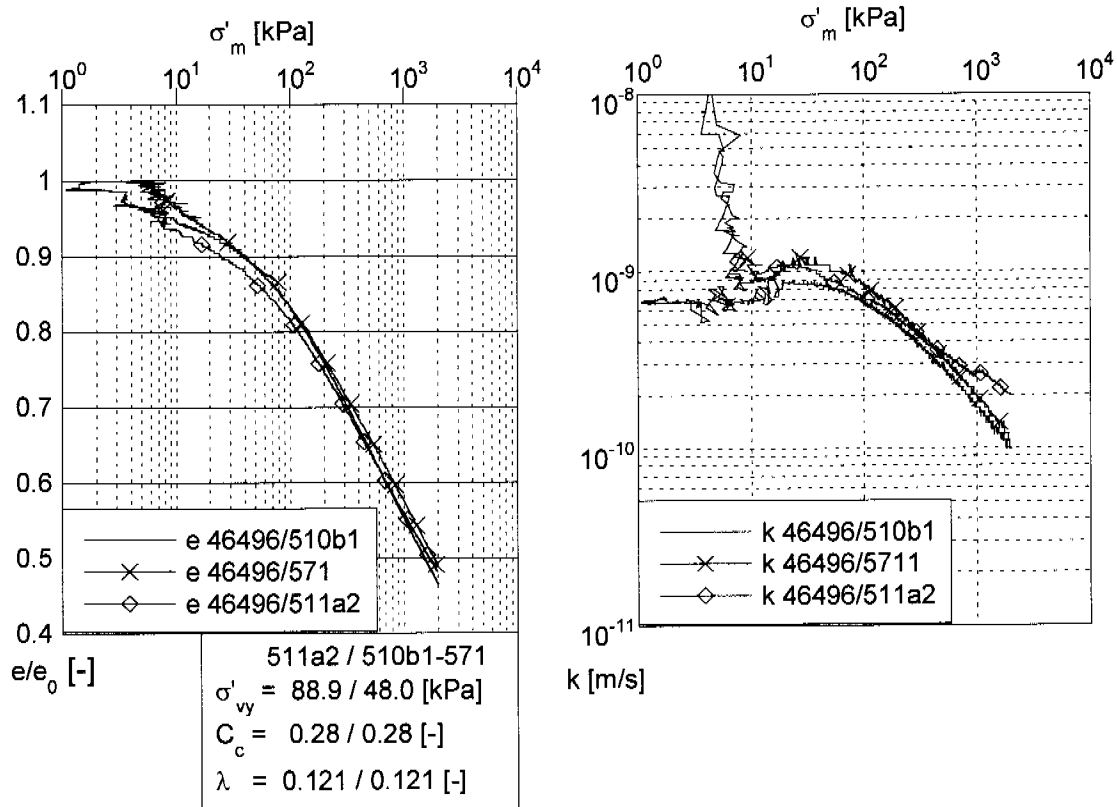


Figure 5-45: Results from tests on rec. Kreuz. clay with strain rate $\dot{\epsilon} = 6 \cdot 10^{-6}$ 1/s.

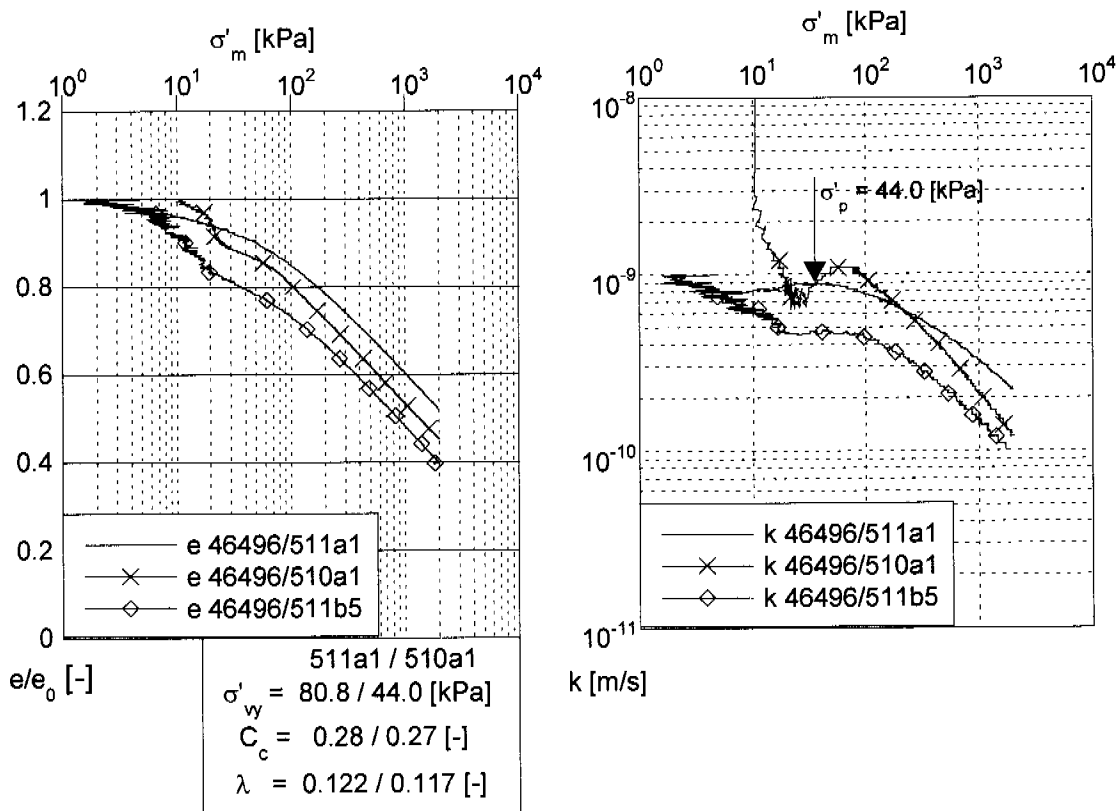


Figure 5-46: Results from tests on rec. Kreuz. clay with strain rate $\dot{\epsilon} = 1 \cdot 10^{-5}$ 1/s.

In this case the strain rate has an evident influence on the vertical yield stress, although the value of σ'_{vy} for the high strain rate is slightly lower than expected. In contrast, the C_c values are almost constant over the whole strain rate range.

In Figure 5-46, the vertical yield stress for specimen 46496/510a1 has been determined by the method proposed by Davison and Atkinson (1990), using the permeability k to mean effective stress σ'_m plot as the reference graph instead of a stiffness-stress graph. This is possible, because the stiffness moduli M_E and C_c are both related to the permeability k (Section 5.2.2 CRS test). The local minimum and maximum peaks indicate the change in stiffness, which occurs when the state of the sample moves from the reloading to the virgin normal compression line. The vertical yield stress is approximately mid-way between these two local extremes. Not all the permeability plots show such a distinct yield point. The comparison of the values of σ'_{vy} from compression curves and from stiffness-stress or permeability-stress curves may provide a more sensitive indication of the occurrence of yield during a CRS test.

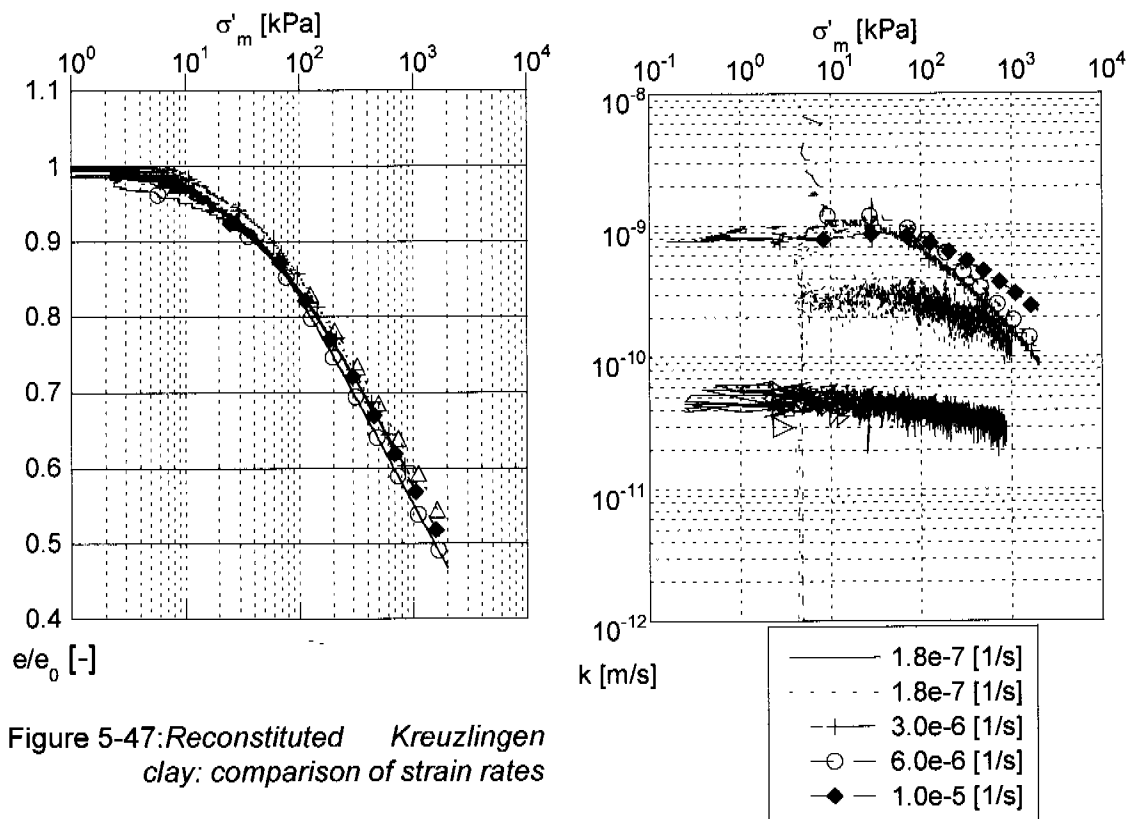


Figure 5-47: Reconstituted Kreuzlingen clay: comparison of strain rates

The comparison between the natural and the reconstituted clay under similar test conditions (Figure 5-49), i.e. same strain rate, does not show any evident difference, the compression lines being mostly congruent. The compression curve for an incremental loading test on natural Kreuzlingen clay has also been plotted in the graph corresponding to the lowest strain rate (Figure 5-49a, Kreuz1-IL). The end of primary consolidation (EOP) curve of the incremental loading oedometer is superimposed upon the $e/e_0 - \sigma'_m$ curve of the CRS, with no evident differences due to strain rate.

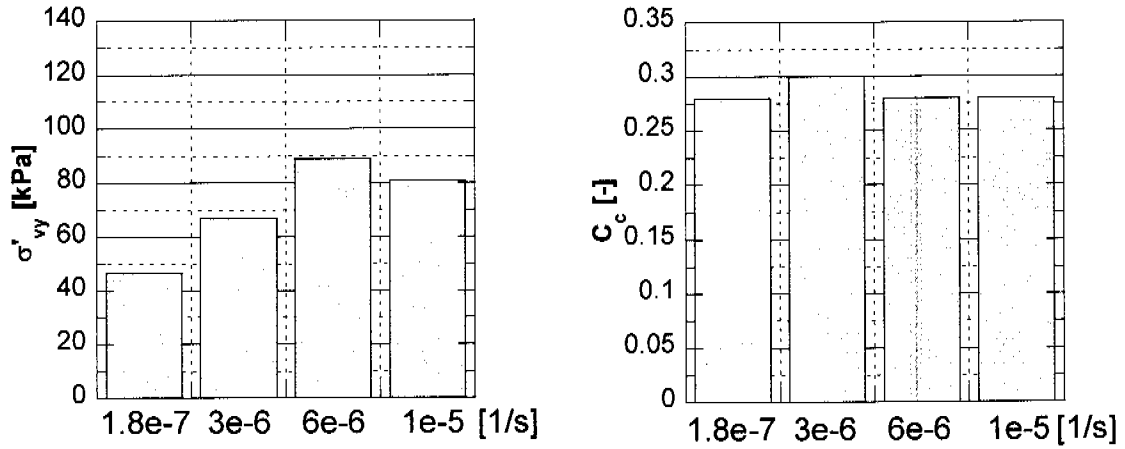


Figure 5-48: Influence of strain rate on σ'_{vy} and C_c for reconstituted Kreuzlingen clay.

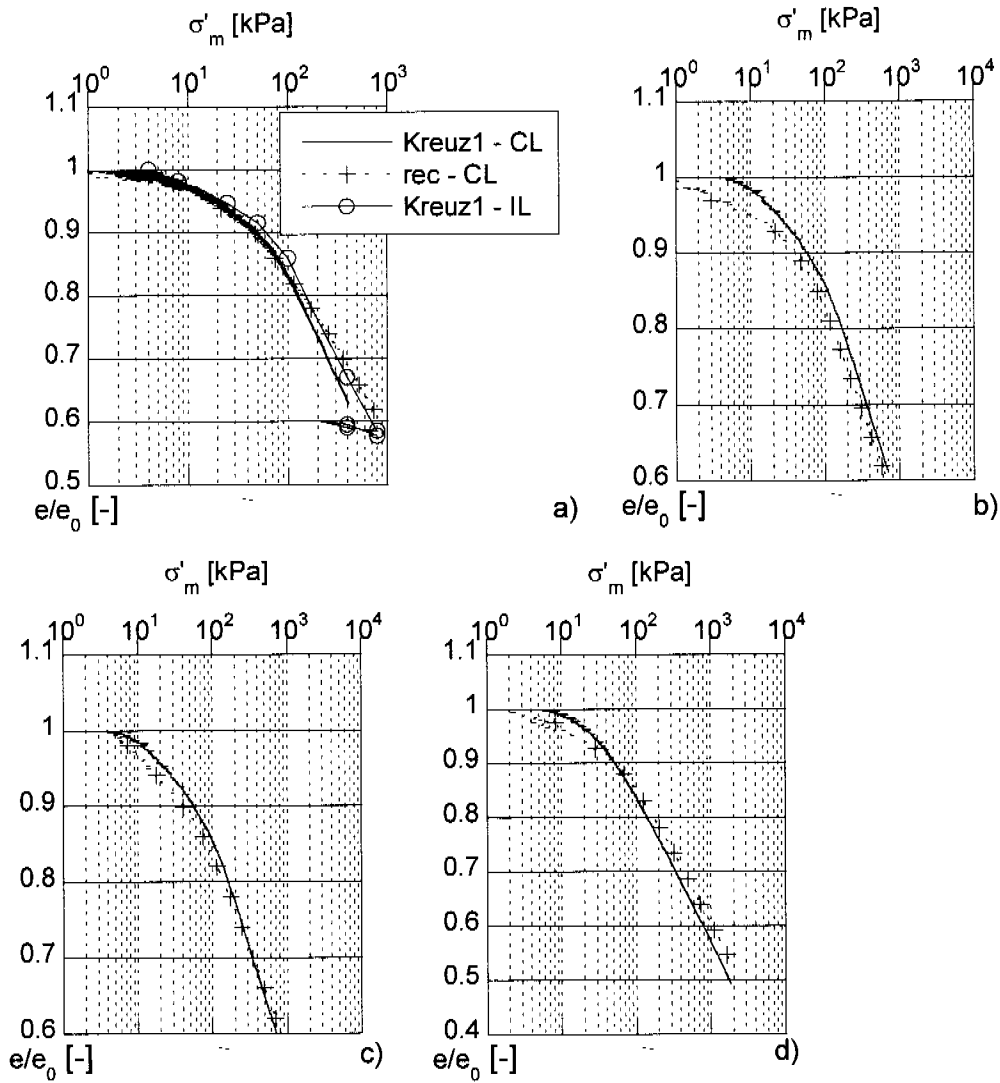


Figure 5-49: Comparison between natural and reconstituted Kreuzlingen clay: a) $\dot{\epsilon} = 1.8 \cdot 10^{-7}$ [1/s], b) $\dot{\epsilon} = 3 \cdot 10^{-6}$ [1/s], c) $\dot{\epsilon} = 6 \cdot 10^{-6}$ [1/s], d) $\dot{\epsilon} = 1 \cdot 10^{-5}$ [1/s]

Birmensdorf

Three samples from the Birmensdorf site were tested in the CL Oedometer. Sample 46292 comes from borehole Birm.1 at a depth of 8.0 to 8.8 m. Samples 46295 and 46296 come from borehole Birm.2 at a depth of 8.0 to 8.8 m and 5.0 to 5.65 m respectively. Therefore samples 46292 and 46295 can be compared to look at differences in vertical yield stress σ'_{vy} depending on the location of the borehole, and samples 46295 and 46296 can be compared to look at differences due to depth within the same borehole.

In Figure 5-50, 5-51 and 5-52, the compressibility and permeability characteristics are illustrated for the different strain rates of $3 \cdot 10^{-6}$, $6 \cdot 10^{-6}$ and $1 \cdot 10^{-5}$ 1/s. Birmensdorf clay shows a higher scatter in the results, largely because of greater heterogeneity of the natural samples. The permeability k of the Birmensdorf clay lies between $1 \cdot 10^{-9}$ and $8 \cdot 10^{-11}$ m/s for vertical effective stresses between 10 and 1000 kPa. These values of k are comparable with the permeability values for Kreuzlingen clay. Again, only the sample tested at $1.8 \cdot 10^{-7}$ 1/s (46292/1) shows lower k values over the whole range of stresses ($2 \cdot 10^{-10}$ to $1 \cdot 10^{-11}$ m/s) when compared to the results of tests with a higher strain rate (Figure 5-53).

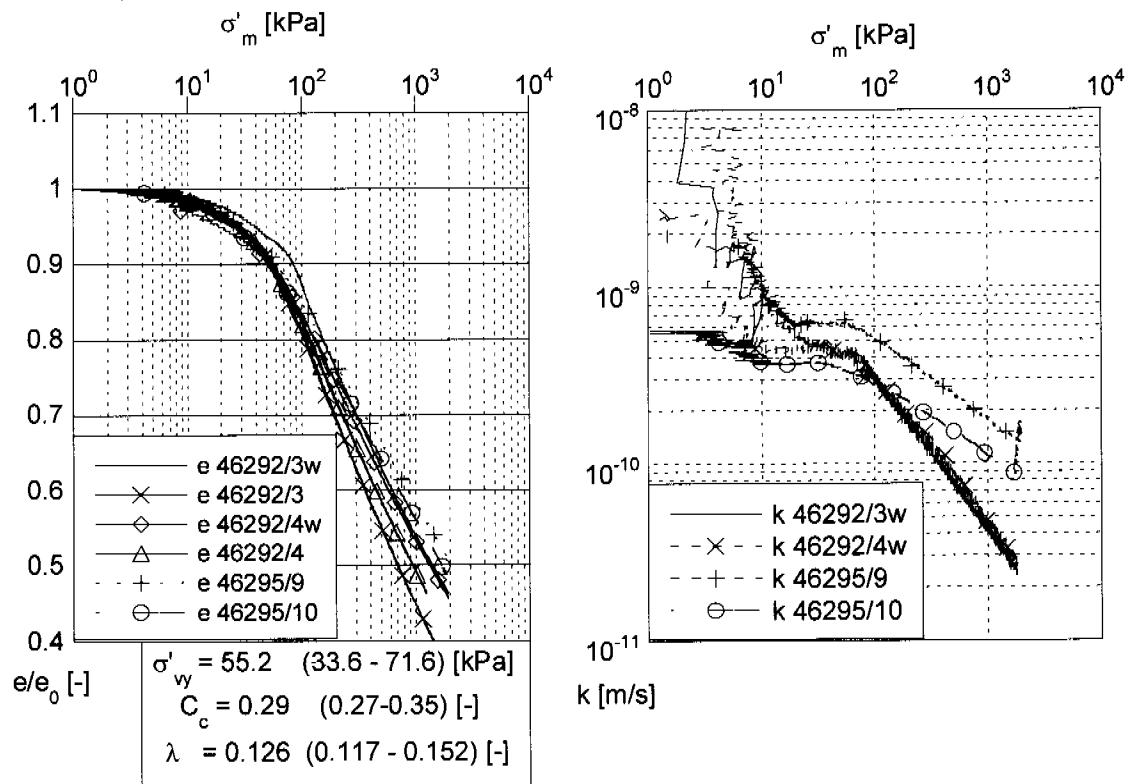


Figure 5-50: Results from tests on Birmensdorf clay with strain rate $\dot{\epsilon} = 3 \cdot 10^{-6}$ 1/s

There is a clear distinction between the test results of the three different samples for the middle strain rate of $6 \cdot 10^{-6}$ 1/s. The vertical yield stress σ'_{vy} increases from sample 46292 to 46295 and is greater for sample 46296, even if

this comes from a lower depth. The C_c value of 0.36 for sample 46292 indicates a less stiff soil, whereas the C_c values of samples 46295 and 46296 are almost the same with values of ca. 0.26.

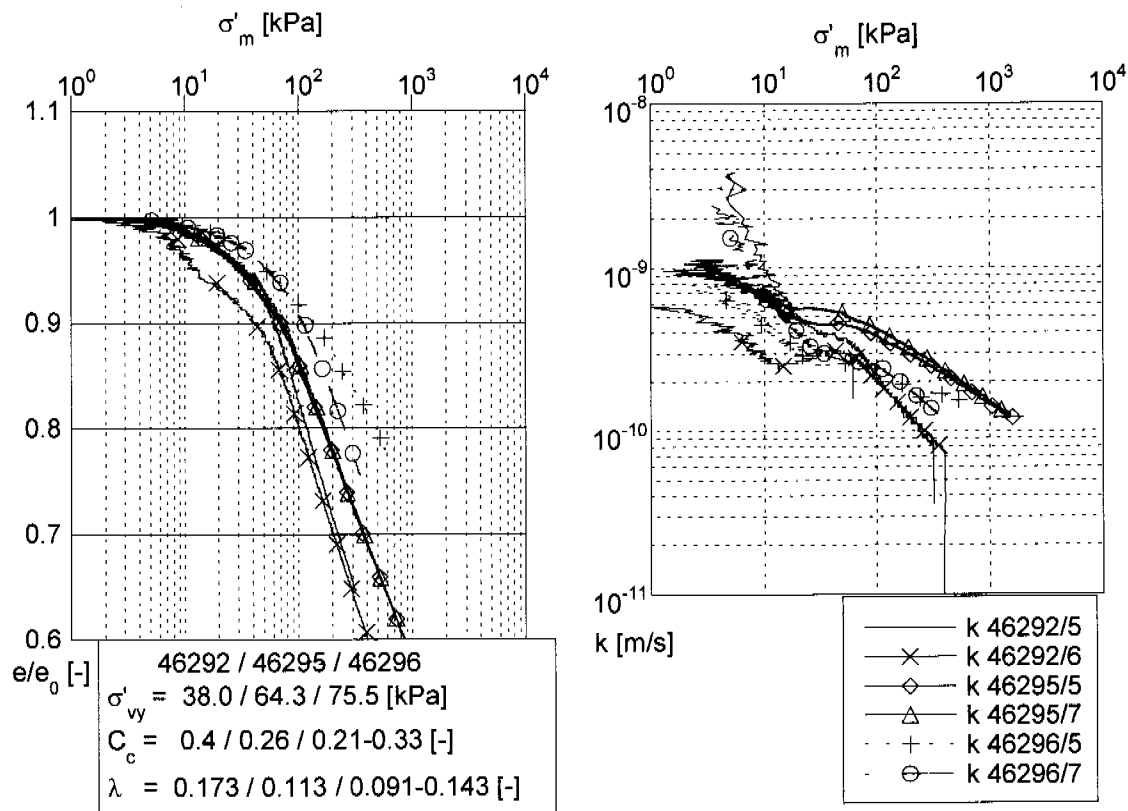


Figure 5-51: Results from tests on Birmensdorf clay with strain rate $\dot{\epsilon} = 6 \cdot 10^{-6} \text{ 1/s}$

The influence of strain rate on the vertical yield stress σ'_{vy} and on the coefficient of compression C_c can be investigated with the bar graphs in Figure 5-54. The results plotted are for sample 46295, except for those at a strain rate of $1.8 \cdot 10^{-7} \text{ 1/s}$, which are from sample 46292. It seems that for Birmensdorf clay, the vertical yield stress σ'_{vy} increases steadily with increasing strain rate. The C_c value measured at a strain rate of $1.8 \cdot 10^{-7} \text{ 1/s}$ is surprisingly high, indicating the presence of a more clayey specimen.

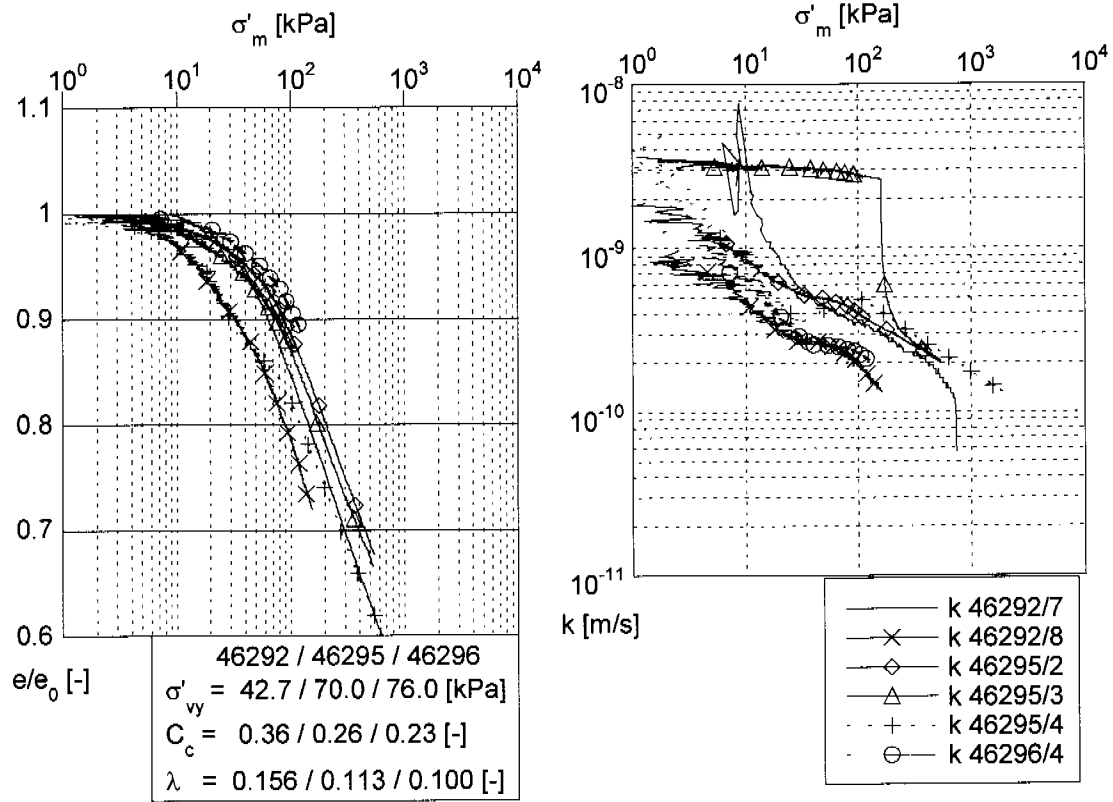


Figure 5-52: Results from tests on Birmensdorf clay with strain rate $\dot{\epsilon} = 1 \cdot 10^{-5} \text{ 1/s}$

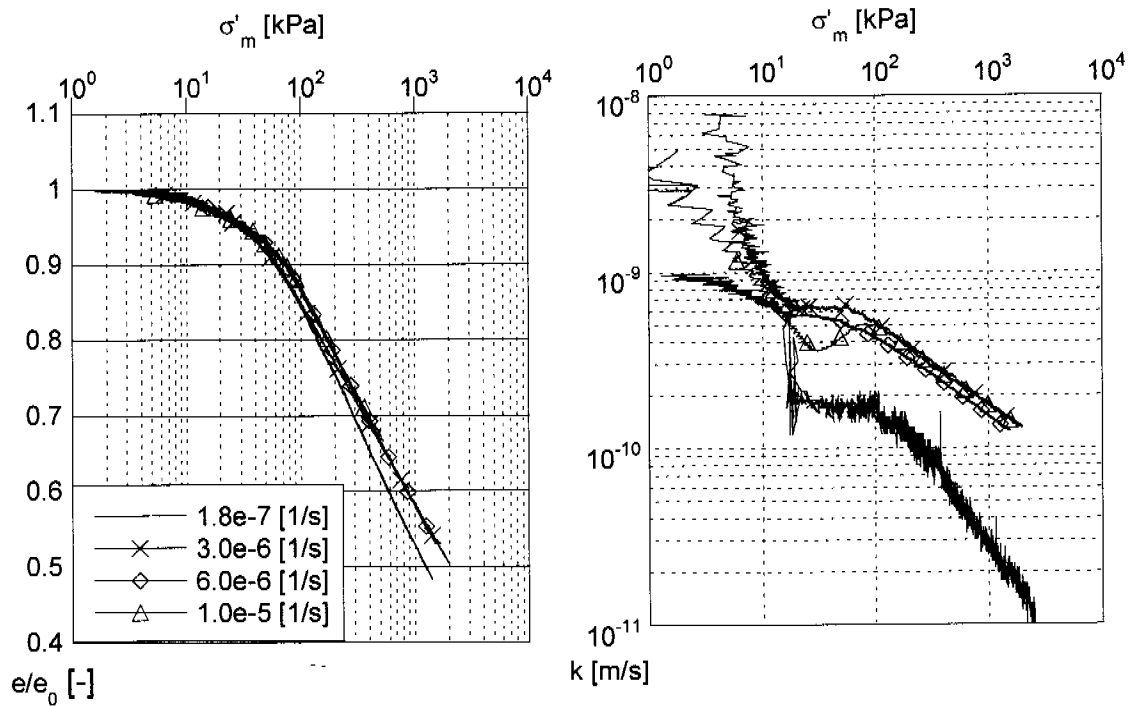


Figure 5-53: Birmensdorf: comparison of strain rates (46295 and 46292)

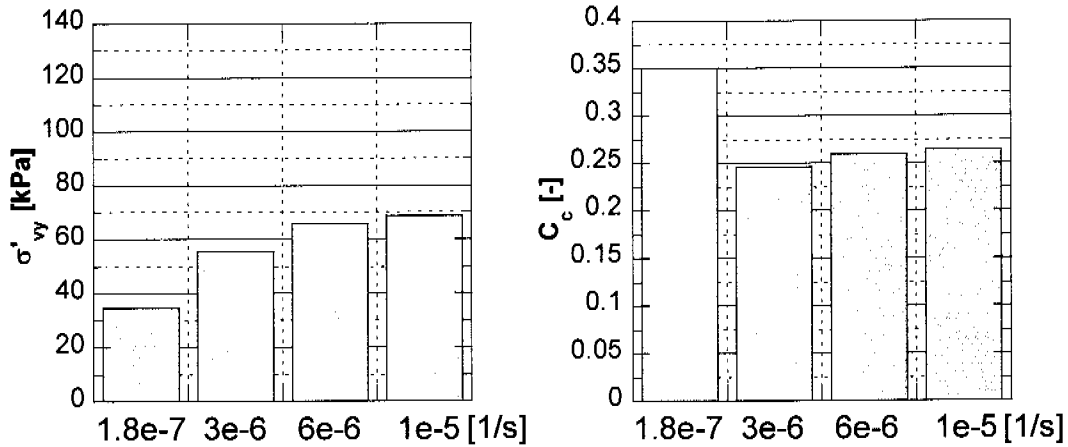


Figure 5-54: Influence of strain rate on σ'_{vy} and C_c for samples 46292 and 46295 (same depth, different boreholes).

CG tests

Figure 5-55 shows the strain rates measured during the CG tests on Bir-mensdorf clay from a depth of 5m. It can be seen that the test with controlled excess pore pressures at the base $\Delta u_{B2} = 30$ kPa, leads to higher strain rates than for $\Delta u_{B1} = 15$ kPa, and that the strain rates in the CG tests are greater than the fastest CRS strain rate of $1 \cdot 10^{-5} \text{ s}^{-1}$. Pronounced change in strain rate are needed in order to maintain the excess pore pressure $\Delta u_{B2} = 30$ kPa at the base of the specimen. In spite of the high difference in strain rates, the results of the CG tests were congruent with the results of the CRS tests. In this case the difference in strain rate are high enough to permit a statement about the strain rate influence for Seebodenlehm: it appears that the strain rate effect is relatively smaller for Seebodenlehm when compared with many other Canadian or Finnish soft clays.

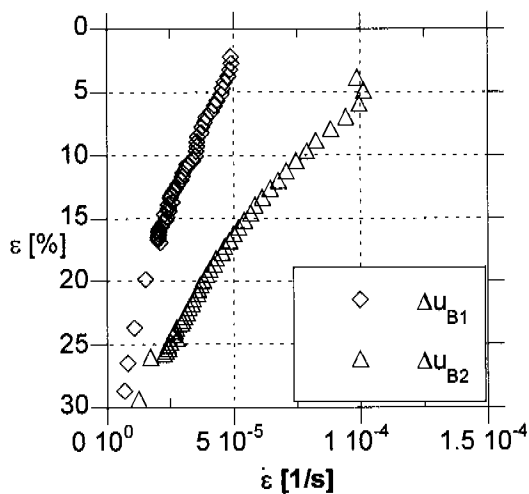


Figure 5-55: Strain rates measured during CG tests on Bir-mensdorf clay as a function of axial strain.

Stress - strain- strain rate relationship

Leroueil et al. (1985) showed that a unique stress-strain-strain rate relationship exists for natural clays, and they plotted the results of various CRS tests on different clays in a graph having the normalised yield stress as the y axis and the strain rate as x axis (Figure 2-12). A regression line could be plotted, which indicated an increase in the normalised yield stress with strain rate. The test results of the different clays plotted in a range of +/- 9% around this line. The unique stress-strain-strain rate relationship implies that at a given strain, the higher the strain rate, the higher the effective stress and that the vertical yield stress-strain rate relationship is unique. Test results on Finnish clay show very similar results. The clays considered by Leroueil et al. have sensitivities (from 22 to 125 from fall cone tests) and clay fraction contents (80%), which are significantly greater than those of the Seebodenlehm.

In Figure 5-56, the results of the CRS tests on Swiss Seebodenlehm are presented on a similar plot. The vertical yield stress of each test has been normalised with respect to the vertical yield stress σ'_{vy} ($3 \cdot 10^{-6}$ 1/s), obtained at the reference strain rate of $3 \cdot 10^{-6}$ 1/s for each particular clay. The value of σ'_{vy} ($3 \cdot 10^{-6}$ 1/s) is a mean value of the results of all tests for a particular clay at this strain rate.

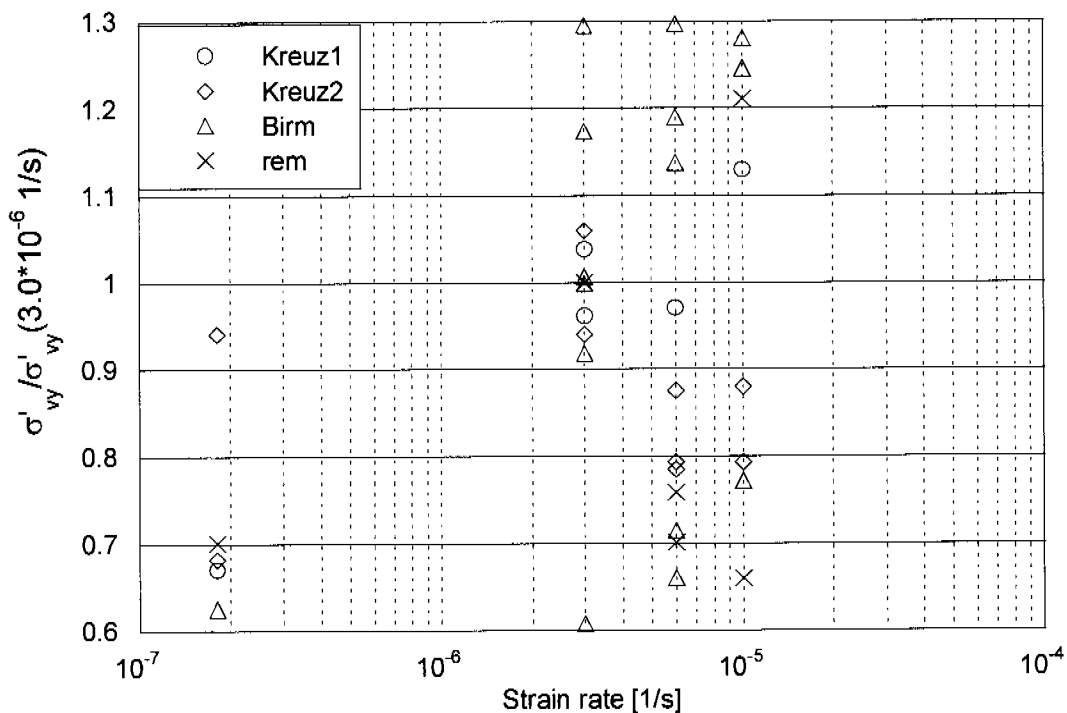


Figure 5-56: Normalized vertical yield stress-strain rate plot for Swiss Seebodenlehm (after Leroueil et al., 1985).

The data are spread over a range of 100% for the same strain rate, and absolutely no trend is visible in Figure 5-56. A slight increase of the vertical yield stress σ'_{vy} ($3 \cdot 10^{-6}$ 1/s) with strain can be depicted between the slowest strain rate of $1.8 \cdot 10^{-7}$ 1/s and the others. However, only few tests have been carried out for this strain rate, and this could have limited the differences in results due to the natural variability of the specimen.

Based on these results, it can be argued that the strain rate dependence of Seebodenlehm cannot be investigated with tests on different natural samples, because the influence of natural variability is high. As already stated above, strain rate stepping tests on the same specimen would be an improvement for the comparison of the effects of rate on compressibility. In addition, the strain rates should be varied over at least 2 or 3 orders of magnitude. These test specifications should be taken into account for future research.

It is worth indicating, however, that recent work on Resedimented Boston Blue Clay tested in a CRS and also in an IL oedometer (Sheahan and Wetters, 1997) suggests that the consolidation behaviour of non-cemented soils, such as the Resedimented Boston Blue Clay, may have a much weaker rate dependence than that observed in intact, cemented clay of eastern Canada and Scandinavia. The sensitivity is a good indicator of cementation and structure, and although the Swiss Seebodenlehm has a carbonate content of more than 30%, the sensitivity S_t measured with the fall cone tests is very low compared with the values of the eastern Canada marine clays studied by Leroueil (1985). The high carbonate content of Seebodenlehm does not result in an open-plan structure but results in the formations of distinct clumps, which acts as bigger silt particles. The Seebodenlehm acts for this reason as an uncemented soil with low sensitivity. It can be therefore stated that the strain rate effect is relatively smaller for Seebodenlehm than for many other soft clays. This is confirmed by the CG tests and correlates with the results of Sheahan and Wetters (1997).

Seite Leer /
Blank leaf

Data Analysis

6.1 Introduction

This chapter aims to link the tests performed to investigate the mechanical properties and the permeability of the soft clays from Kreuzlingen and Birmensdorf. The one dimensional compression of the clays is compared in Section 6.2 with the plasticity and liquidity indices of the clays. Sections 6.3 and 6.4 compare the undrained shear strength and the shear stiffness of the clays determined with in situ and laboratory tests. In Section 6.5 the yield curves of the two Seebodenlehm and their changes due to stress path history are estimated by the constitutive model S-CLAY1 and compared with the yield points determined from the triaxial stress path tests. Finally, the measurements of settlements, horizontal displacements and porewater pressures performed at the test fill embankment in Birmensdorf are analysed in Section 6.6.

6.2 Plasticity index

It was stated in Section 5.2.3 that the natural variability of the Seebodenlehm specimens did not allow the influence of strain rate on the results of strain controlled oedometer tests to be determined with any degree of certainty. The comparison of the two Swiss lacustrine clays and of the reconstituted material from Kreuzlingen is discussed in this Chapter on the basis of their plasticity properties.

Correlating engineering properties, such as the compression index C_c , with index properties assumes great importance, as the laboratory tests are time-consuming and expensive. So for preliminary design assumptions, it is advantageous to use correlation equations to estimate either the compressibility or the strength of a soil. Skempton (1944) gave following correlation for the C_c index with liquid limit w_L in % :

$$C_c = 0.007 \cdot (w_L - 10) \quad [6-1]$$

Different researchers have used various parameters for these correlations subsequently, including the natural water content w , the initial in situ void ratio e_0 , the dry specific weight γ_d , the plasticity index I_p , the liquid limit w_L or the void ratio

at liquid limit e_L . The plasticity index I_p , the void ratio at liquid limit e_L and the liquid limit w_L are constants for a given soil with constant mineralogy and composition, whereas all other parameters listed above are parameters, which describe the particular current state of a soil. It would be reasonable to expect a correlation between soil constants and the mechanical behaviour. Sridharan and Nagaraj (2000) investigated 10 different soils with different plasticity characteristics in incremental loading oedometers and found that the compression index has a good correlation with the shrinkage index I_s of the soil, where $I_s = w_L - w_S$. They also indicated that in the absence of the shrinkage index, the plasticity index can be used to predict the compressibility characteristics with a better correlation coefficient than the liquid limit.

In Giudici Trausch et al. (2003), the compressibility index C_c of three different Swiss lacustrine clays, deduced from CRS and CG tests, was plotted against the plasticity index I_p (continuous loading oedometer tests carried out by Basler (2002), Figure 6-1). The minimum C_c value that results for all clays is 0.2, independent of the strain rate. Samples from Birm-8m always behave stiffer than expected and samples from Birm-5m show a high heterogeneity. The results of the Controlled Gradient (CG) tests on Kreuzlingen and Birmensdorf clay are also shown on Figure 6-1. The C_c values from CG tests correspond well with the values from the CRS tests.

The best correlation was found for the results measured with a strain rate of $3 \cdot 10^{-6}$ 1/s (Equation 6-2). The correlation coefficient was 0.72.

$$C_c = 0.014 \cdot (I_p - 2.9) \text{ with } I_p \text{ in \%} \quad [6-2]$$

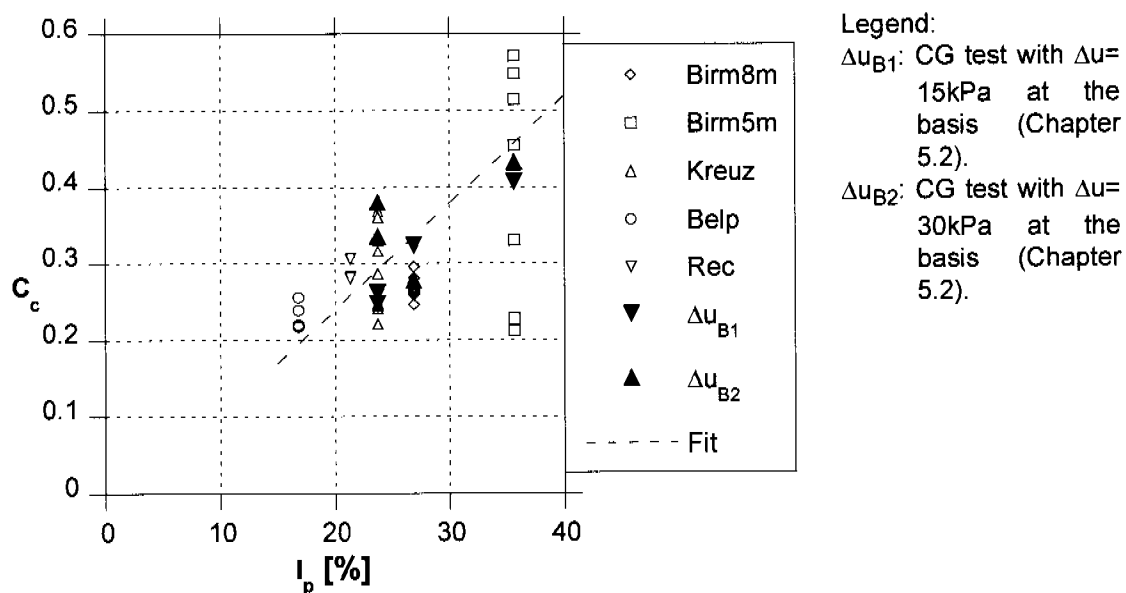


Figure 6-1: C_c - I_p graph for CRS and CG tests on Birmensdorf, Kreuzlingen and Belp natural clay and the reconstituted material from Kreuzlingen (Giudici Trausch et al., 2003). The dotted line "Fit" represents Equation 6-2.

The correlation for all data plotted in Figure 6-1 (irrespective of strain rate) was very poor with a coefficient of correlation of 0.3.

In this study, one I_p value was obtained for each of the core samples of 200 to 800 mm length. This I_p value was taken to be valid over the total length of the sample. In reality, the local values of I_p might vary according to the relative percentage of silt and clay for each specimen of the sample. In consequence, the samples of Birmensdorf clay that show C_c values lower or higher than may be expected in Figure 6-1, may indeed have contained a well defined silt layer, which would have produced a lower value of I_p than that assumed. For varved clays, therefore it is difficult to define the plasticity index as a soil constant. Instead the plasticity of a varved soil should be determined for soil specimens, whose dimensions have to be chosen according to the thickness of and distance between the varves present in the soil. For instance, a Birmensdorf clay specimen of 20 mm height can contain 2 to 3 silt layers up to 2mm thick, which affect the plasticity of the specimen.

In Figure 6-2, the compressibility index C_c is plotted against the plasticity index I_p for all continuous loading oedometer tests performed by the author (Chapter 5) in addition to the results of Basler (2002). The heterogeneity of the results is again evident from Figure 6-2, and no satisfactory correlation can be found between C_c and I_p . In Figure 6-2, the results of CRS tests on specimens with a height twice the standard oedometer height are plotted separately. It is evident that the results of the 40 mm specimens plot in the same cloud except for an I_p index of 35.6% (Birmensdorf clay, 5m depth), where they show higher compressibility than the 20 mm specimens. Here however the heterogeneity of the data is already very high due to the high silt layer content, so that no conclusion can be given with any reliability.

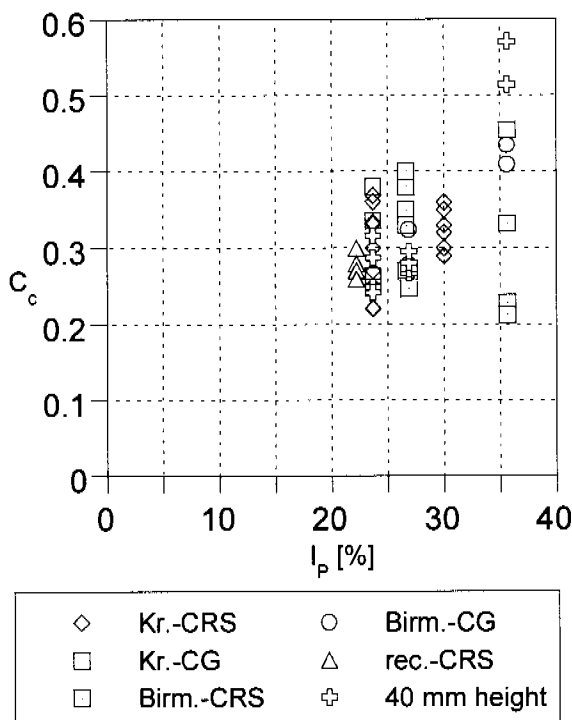


Figure 6-2: C_c - I_p graph for all oedometer tests.

Legend:

CRS: Constant Rate of Strain oedometer
CG: Controlled Gradient oedometer

6.3 Determination and comparison of the undrained shear strength s_u from laboratory triaxial tests and from in situ piezocone tests CPTU

Depending upon the nature of the soil deposits and the risk level of the designed construction, the suite of drilling and sampling, laboratory and in situ testing has to be implemented on the basis of available time and financial resources. The CPTU constitutes a high-capacity in situ test, which is often cheaper than drilling and sampling and the results offer the interpretation of various soil parameters, if it's applicable to the soil conditions. The tasks of parameter interpretation can be handled by empirical, closed-form analytical, numerical or experimental methods (Mayne, 2003). For instance, the determination of horizontal in situ permeability in Section 4.2.3 relied upon an analytical method, based on the cavity expansion theory, whereas the method used for determination of cone factor N_{KT} by calibration of the CPTU results against borehole vane tests or other laboratory tests, is an empirical method (Section 4.2.3), although numerical and analytical methods suggest similar N_{KT} values. Mayne (2003) gives an approach to determine s_u from CPTU test data, by calibration from different laboratory tests (Equation 6-3 and Table 6-1).

$$(s_u/(\sigma'_{v0})) = a_{rate} \cdot a_{OCR} \cdot a_{cont} \cdot (s_u/\sigma'_{v0})_{mode} \quad [6-3]$$

Table 6-1 describes the parameters included in Equation 6-3. The a-parameters in Equation 6-3 are negligible for both Swiss Seebodenlehm, as their end product reaches a value of 1.01, being $a_{rate} = 1.011$ with rate 1.3%/h, $a_{OCR} = 1$, as the CPTUs show that these clays are NC, and $a_{cont} = 1$ for intact, not fissured clays.

The equation of s_u/σ'_{v0} for CIUC test in Table 6-1 is based on critical state theory, which implies that undrained shear strength for normally consolidated soil in triaxial compression $s_{u,tc}$ is purely dependent on critical state parameters, such as M and $\Lambda = (\lambda - \kappa)/\lambda$ (which is described as the plastic volumetric strain ratio) and effective vertical stress. The parameter r is the ratio between the equivalent mean effective isotropic consolidation stress at failure p'_{of} (i.e. the value of p' (> 0) at $q = 0$, due to the yield surface at failure) and the effective mean stress at the critical state p'_f . The value of r equals 2.718 for the Original Cam Clay yield locus and 2 for Modified Cam Clay (MCC).

On the basis of the parameters reported in Table 5-8 for Kreuzlingen clay, the value of Λ ranges between 0.55 and 0.88, with a mean value of 0.73 and $s_{u,tc}/\sigma'_{v0}$ for Kreuzlingen clay would lie between 0.22 and 0.30 for an Original Cam Clay yield locus and between 0.26 and 0.36 for a Modified Cam Clay yield locus. Taking however the value of $M = 0.96$ for CIUC tests of Series 1, $s_{u,tc}/\sigma'_{v0}$ would then lie between 0.23 for original Cam Clay and 0.29 for Modified Cam Clay.

| Parameter | Mode | Expression |
|--|--|---|
| Undrained shear strength ratio (s_u/σ'_{v0}) | CIUC | $= 1/2 \cdot M \cdot (1/r)^\Lambda$ (1) |
| | PSC | $= \frac{\sin\phi'}{2 \cdot d_p} \cdot \left(\frac{d_p^2 + 1}{2}\right)^\Lambda$ (2) |
| | | where $d_p = 1/(2 - \sin\phi')$ |
| | CK ₀ UC | $= \frac{\sin\phi'}{2 \cdot d_t} \cdot \left(\frac{d_t^2 + 1}{2}\right)^\Lambda$ (3) |
| | | where $d_t = (3 - \sin\phi')/(3 - 4 \cdot \sin\phi')$ |
| | DSS | $= 1/2 \cdot \sin\phi'$ (4) |
| | PSE | $= (s_u/\sigma'_{v0})_{PSC} \cdot (I_P + 41)/118$ (5) |
| | CK ₀ UE | $= (s_u/\sigma'_{v0})_{CK0UC} \cdot (I_P + 37)/125$ (6) |
| Strain rate | | $a_{rate} = 1 + 0.1 \cdot \log(\partial\varepsilon/\partial t)$ with rate in% per hour |
| OC ratio | | $a_{OCR} = OCR^\Lambda$ with $\Lambda = 0.8$ for "normal" clays and $\Lambda = 1.0$ for structured clay |
| Continuity | | $a_{cont} = 1$ for intact clays, $= 2/3$ for moderately fissured clays and $= 1/3$ for highly fissured clays |
| CIUC: | isotropic consolidated undrained triax. compression test | |
| PSC/E: | plane strain compression / extension | |
| CK₀UC/E: | K₀-consolidated undrained triaxial compression /extension test | |
| DSS: | direct simple shear | |

Table 6-1: Parameters for Equation 6-3 from Mayne (2003) (I_P in%)

The value of Λ for Birmensdorf Seebodenlehm is equal to 0.66 on the basis of TSPT tests 46297/2 and 46297/3, whereas the value of M has been set equal to 1.02 from CIUC test 46294/5, as discussed in Chapter 5.1.3 (Table 5-9). With these assumptions, $s_{u,tc}/\sigma'_{v0}$ for Birmensdorf clay would lie between 0.26 for an original Cam Clay yield locus and 0.32 for a Modified Cam Clay yield locus.

The Λ value of Birmensdorf clay seems to be quite low but it is based on two tests only. The values for Kreuzlingen clay vary from 0.55 to 0.9 with an average value of 0.73. These values seems to be more similar to the average values known for clays.

Two direct shear tests were performed on samples of Birmensdorf Seebodenlehm, purported to be from an existing shear zone in the field. Although there were doubts about the quality of the samples, the results delivered a ϕ'_{mob} of 20°, which is higher than the value of residual shear strength obtained by Fauchère (2000) on reconstituted Birmensdorf clay ($\phi'_{res} = 15^\circ$), derived from

ring shear tests. The value of the angle of shearing resistance at peak ϕ'_{DSS} is thus available for the Birmensdorf Seebodenlehm deposit, and is equal to 20° . This gives, using Equation 4 in Table 6-1, $(s_u/\sigma'_{v0})_{DSS} = 0.17$.

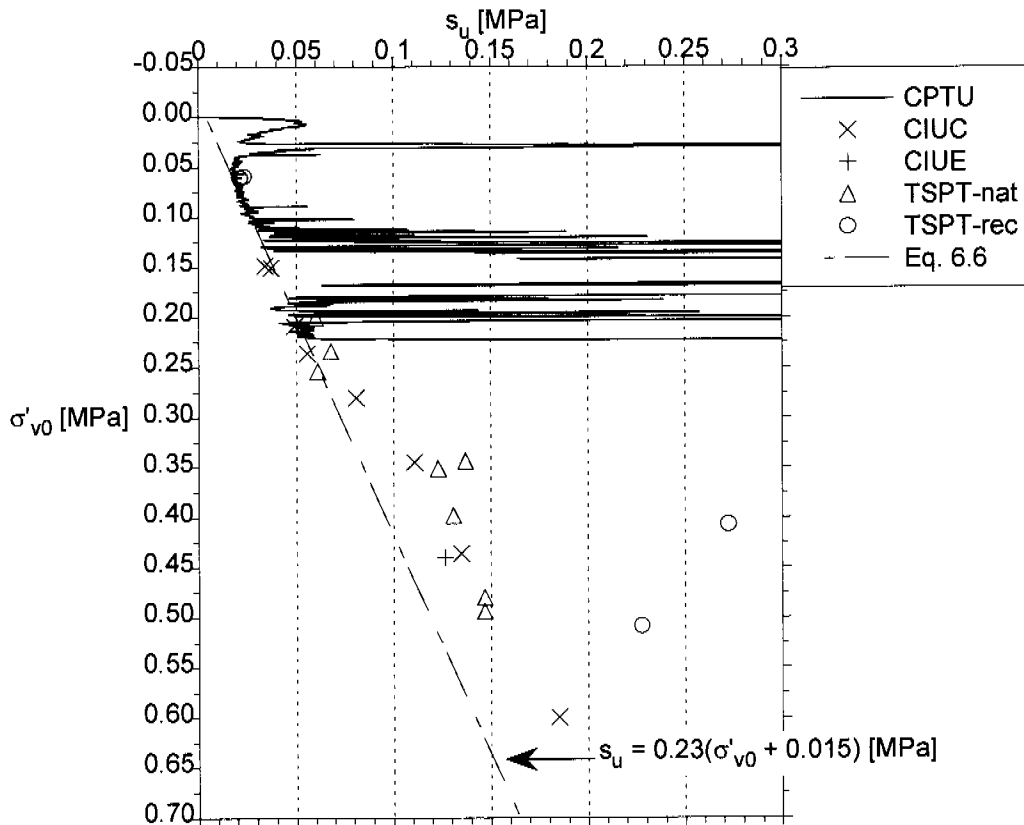


Figure 6-3: $s_u - \sigma'_{v0}$ from CPTU at B1 in Kreuzlingen with $N_{KT} = 17$, with results from triaxial tests.

In Section 4.2.3, an equation relating the variation of s_u with effective vertical stress σ'_{v0} was determined based on the choice of cone factor $N_{KT} = 17$ for both of the Kreuzlingen and Birmensdorf sites (Equation 6-4 and Equation 6-5). This value of the cone factor was assessed through correlation between CPTU and borehole vane and field vane tests (Heil, 1997 and Panduri, 2000).

$$s_u = 0.23 \cdot (\sigma'_{v0} + 15) \text{ [kPa]} \quad \text{for the Kreuzlingen site} \quad [6-4]$$

$$s_u = 0.28 \cdot (\sigma'_{v0} + 2) \text{ [kPa]} \quad \text{for the Birmensdorf site} \quad [6-5]$$

Equation 6-4 and Equation 6-5 agree quite well with the prediction given through critical state theory on the basis of isotropic consolidated triaxial compression tests CIUC. The prediction from the DSS tests underestimates the undrained shear strength for the Birmensdorf site, as given by Equation 6-5, which supports the doubts about the disturbance of the specimens.

The shear strength profile $s_u - \sigma'_{v0}$ for Kreuzlingen is shown in Figure 6-3, together with the results of the triaxial tests on natural and reconstituted clay samples. Each triaxial sample has been consolidated either isotropically or anisotropically to higher stresses than the relevant in situ condition, and so the figure shows the trend but not the exact values at the depth of sampling. It can be seen from Figure 6-3 that Equation 6-4 provides a reasonable fit to the CPTU

data and the CIUC results of test series 1 up to effective vertical stresses of 250 kPa, thereafter the equation underestimates the undrained shear strength given by the laboratory tests. This stress corresponds to a depth of ca. 25-30 m, which is probably within the typical scope of most geotechnical projects for which a prediction of undrained shear strength is needed. At higher stresses and depth, the prediction of s_u based on $N_{KT} = 17$ could represent a lower bound and safer design.

The triaxial test results on natural samples agree very well for effective vertical stresses between 150 kPa and 600 kPa, although the difference between strength in compression and extension is less than expected on the basis of work by Kulhawy (1993) with $s_{u,te} \sim 0.9 \cdot s_{u,tc}$. Two of the triaxial stress path tests on reconstituted Kreuzlingen material do not match the trend shown by the natural samples, and give undrained shear strengths that are significantly higher than expected in comparison with the natural samples. These tests are 46496/56 and 46496/57 and their s_u values reflect their unusual triaxial compression response described in Chapter 5.1.3, with strain hardening to a peak deviator stress occurring at 20% vertical strain. In contrast, specimens 46496/58 and 46496/510 fall in the expected range for the representative effective vertical stress of 60 kPa.

The shear strength profile $s_u - \sigma'_{v0}$ for the Birmensdorf site is shown in Figure 6-4, likewise together with the results of the various triaxial tests from Series 1 and 2. The values of the effective vertical stress σ'_{v0} for the triaxial samples plotted in Figure 6-4 are not the values at extraction depth, but are the equivalent value for the chosen consolidation pressure. Figure 6-4 shows that Equation 6-5 provides a good fit to the CPTU data and the triaxial test results on NC samples. This is valid also for the samples taken from the drilled core, which are labelled as dc in Figure 6-4. The triaxial test results on initially overconsolidated samples show higher values of s_u than expected at the equivalent depth. A good correlation between overconsolidation ratio OCR and s_u is given by Equation 6-6:

$$s_u / \sigma'_{v0} = a \cdot OCR^b \quad [6-6]$$

where empirical values of the constants are $a \sim \phi' / 100$ and $b = 0.6$ to 0.8 . This correlation has been used for creating suitable stress histories for reconstituted Kaolin samples, to achieve profiles of undrained shear strength in centrifuge model testing (Springman, 1993). It is also valid for the results on overconsolidated, disturbed samples of Birmensdorf clay. Taking $\phi' = 26^\circ$ from test 46294/5, Table 5-9, then a should be approximately equal to 0.26. The tests agree very well and show b equal to 0.73. These results for b lie in the given range.

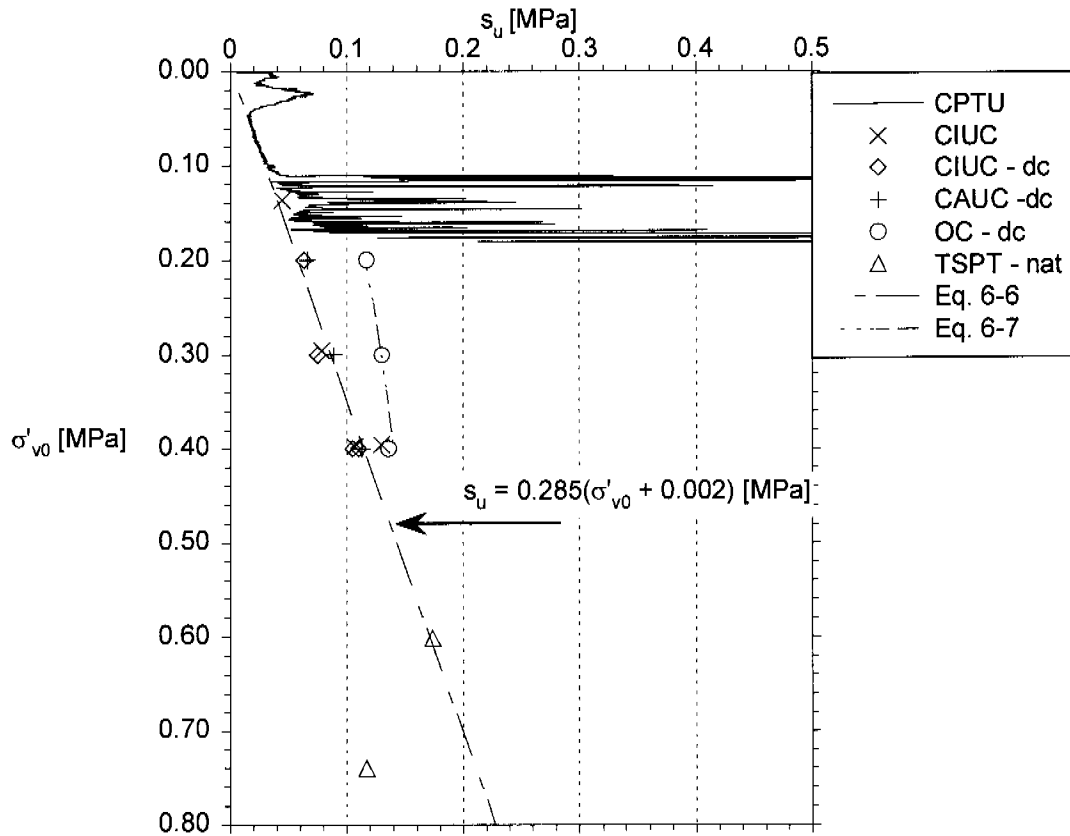


Figure 6-4: $s_u - \sigma'_{v0}$ from CPTU in Birmensdorf with $N_{KT} = 17$, with results from triaxial tests.

A theoretical solution for the cone factor N_{KT} is given by Teh and Houlsby (1991), which is based on an analysis of the quasi-static penetration of a cone penetrometer into clay. Equation 6-7 is an approximate expression for the cone factor N_{KT} , including the effect of the rigidity index I_r of the cone roughness α_f (roughness of cone face) and α_s (roughness of cone shaft) and the effect of in situ stress distribution Δ .

$$N_{KT} = N_s \cdot \left(1.25 + \frac{I_r}{2000} \right) + 2.4 \cdot \alpha_f - 0.2 \cdot \alpha_s - 1.8 \cdot \Delta \quad [6-7]$$

with $I_r = G/s_u$: rigidity index of the soil,

α_f, α_s : adhesion factors of cone face and shaft respectively,

$\Delta = \frac{\sigma'_{v0} \cdot (1 - K_0)}{2 \cdot s_u}$: in situ stress distribution factor,

$N_s = \frac{4}{3} \cdot [1 + \ln(I_r)]$: spherical expanding cavity factor.

Teh and Houlsby (1991) note that "Equation 6-7 requires an estimate of rigidity index and in-situ horizontal stress to be made before q_T can be used to estimate s_u and that the derived s_u may be then used to refine the calculation".

Further, they observe that their approach results in higher cone factors than have previously been derived theoretically and that the higher values of N_{KT} are closer to those observed in practice.

A representative value of G is required for the calculation of I_r . Jamiolkowski (2003) advises either to choose the value of G_{50} or even G_{80} , that is the value of the shear modulus G when 50 or 80%, respectively, of the undrained shear strength has been mobilized in a triaxial compression test. To evaluate N_{KT} for Kreuzlingen clay with Equation 6-7 for $\sigma'_{v0} = 200$ kPa, the G_{50} modulus measured in test 46216/1 has been used together with Equation 6-4 for s_u . The rigidity index I_r is then equal to 100. With this value, $\alpha_s = \alpha_f = 0.5$ and with $\Delta = 0.9$, $N_{KT} = 9.2$. Jamiolkowski (2003) proposes an evaluation of N_{KT} for a NC clay with $\Delta = 0.8$, $\alpha_s = \alpha_f = 0.5$ and $I_r = 400$, with a resulting value of $N_{KT} = 13.2$. If instead of G_{50} , the in situ measured stiffness is used (Chapter 4.3.3), then I_r assumes a value of 600 and this value leads to a N_{KT} factor around 14, which is nearer to the factor estimated with the comparison to the results from the in situ vane tests.

Figure 6-5 shows the s_u - σ'_{v0} profile for Kreuzlingen calculated with $N_{KT} = 14$, together with results of laboratory tests. A new equation relating the variation of s_u with effective vertical stress σ'_{v0} can be evaluated and is given by Equation 6-8.

$$s_u = 0.29 \cdot (\sigma'_{v0} + 18) \text{ [kPa]} \quad [6-8]$$

It can be seen from Figure 6-5 that Equation 6-8 provides a good fit to the CPTU data and the triaxial test results over the entire range of effective vertical stress displayed in the figure. In this case, the prediction of s_u based on $N_{KT} = 14$ could represent an upper bound and therefore a lower safety level for design.

To evaluate N_{KT} for Birmensdorf clay from Equation 6-7 for $\sigma'_{v0} = 600$ kPa, the G_{50} modulus measured in test 46297/2 has been used together with Equation 6-5 for s_u . The rigidity index I_r is then equal to 165. With this value, $\alpha_s = \alpha_f = 0.5$ and with $\Delta = 0.7$, $N_{KT} = 10.7$. The calculated N_{KT} indices are lower than those determined by empirical correlation with in situ vane tests and laboratory triaxial tests. Equation 6-5 correlates well with both in situ and laboratory tests and a new s_u - σ'_{v0} profile calculated with a lower N_{KT} value would overestimate the in situ undrained shear strength over the entire range of effective vertical stress.

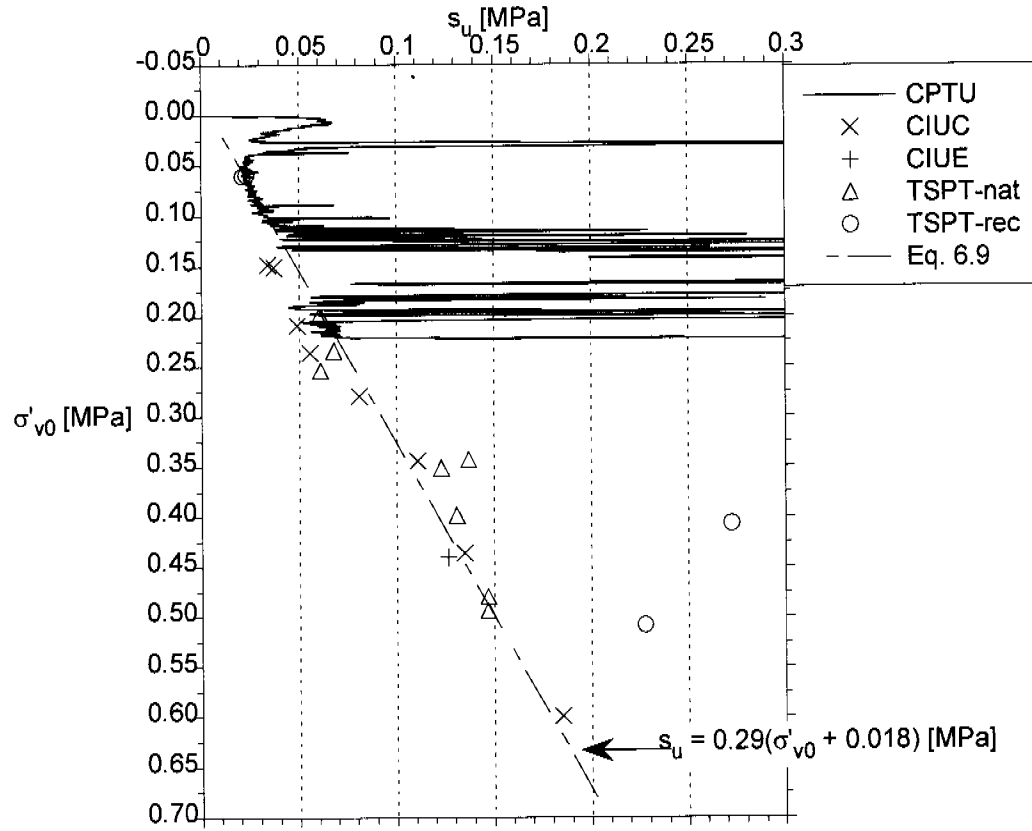


Figure 6-5: $s_u - \sigma'_{v0}$ from CPTU at B1 in Kreuzlingen, with $N_{KT} = 14$.

6.4 Determination and comparison of the shear modulus G from laboratory triaxial tests and from in situ seismic tests

Figure 6-6 a and b shows the variation of the small strain shear modulus measured by the bender elements G_{bender} , with mean effective stress p' during typical triaxial stress path tests. Both plots show that the stiffness increases almost linearly with mean effective stress. The bender element measurements leading to determination of the shear modulus for small strains are not automated and have been carried out, when possible, at constant time intervals during consolidation, i.e. two times a day. However, sometimes this schedule could not be kept, and so not as much G_{bender} data are available in some tests. The bender measurements during shearing were much more difficult to obtain because a tighter schedule is essential, particularly at the beginning of this stage. When comparing two tests with different measuring intervals, the shear modulus values correspond to different shear strain levels and different mean effective stress levels. In Mohsin and Airey (2003), an empirical approach has been proposed to automate the determination of G_{max} from bender elements during triaxial tests. The proposed method is computationally intensive and still requires a visual check at some stage of the test for the correct choice of the peak in the cross correlation. Moreover, the cross correlation is reliable only if the frequency is above some critical limit. However, the automated measurement of G_{max} has many advantages: this includes, primarily, the complete recording of the G - p' and G - ε_s behaviour of a soil specimen (for instance every minute).

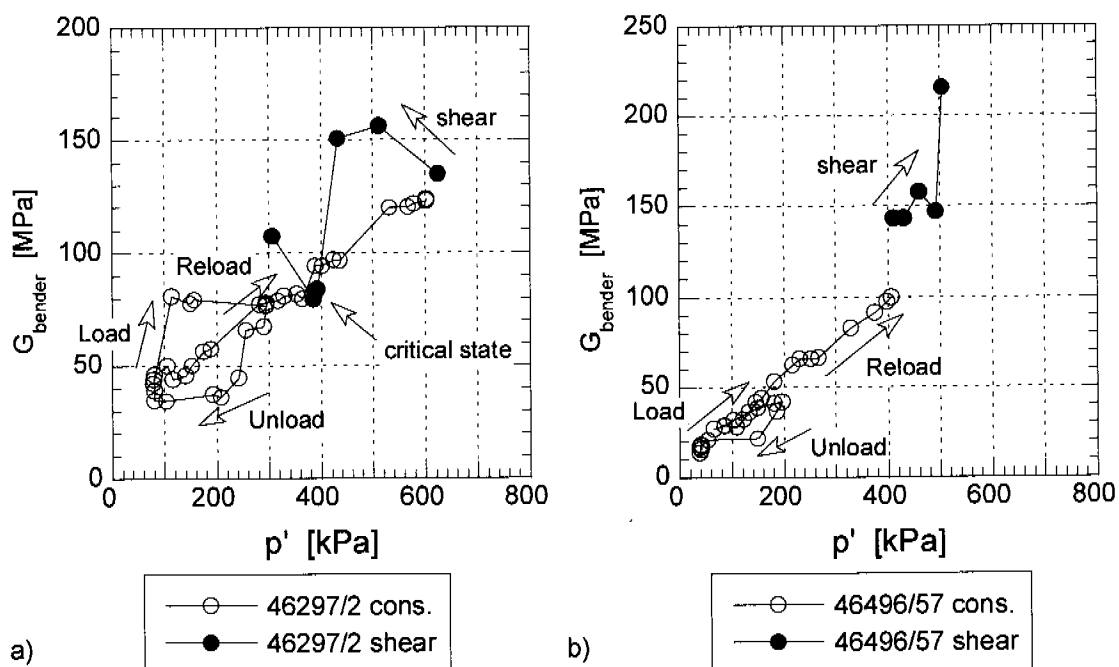


Figure 6-6: Variation of G_{max} measured with the bender element method during consolidation and during undrained shearing of two typical tests (a: Birmensdorf clay, b: reconstituted Kreuzlingen clay).

The Birmensdorf clay specimen 46297/2 was anisotropically consolidated to $p' = 300$ kPa with $\eta_1 = 0.3$, unloaded on the same stress path, isotropically reloaded to $p' = 600$ kPa and finally subjected to undrained shear in compres-

sion (Figure 6-6 a). Loading, unloading and reloading are distinguished clearly for specimen 46297/2: Figure 6-6 shows that the shear modulus jumps directly after loading with $\eta_1 = 0.3$ to values of ca. 80 MPa and stays constant until unloading, where G shows lower values than those for the same p' on loading. On reloading on the isotropic stress path with $\eta_2 = 0$, G_{bender} increases linearly with mean effective stress p' and reaches the previous maximum value of 80 MPa by the previous maximum p' of 300 kPa. Then the G_{max} values increase marginally up to $p' = 370$ kPa and then again more severely above this value. On shearing, the minimum value of G_{bender} is achieved at the critical state.

The reconstituted Kreuzlingen clay specimen 46496/57 was anisotropically consolidated with $\eta_1 = -0.3$ to $p' = 200$ kPa, unloaded on the same stress path and isotropically reloaded with $\eta_2 = 0$ to $p' = 400$ kPa. The load and reload response are indistinguishable in this plot (Figure 6-6 b), whereas again the unload response gives smaller G_{bender} values than on loading. During undrained shearing in compression, specimen 46496/57 shows a jump in G_{max} , which could correspond to the unusual behaviour observed in q - p' space (Figure 5-25).

The inclination of the stress path has no obvious influence on stiffness for specimen 46496/57 (Figure 6-6b), as load and reload paths have the same inclination. Both specimens in Figure 6-6 a and b show, however, a lower stiffness on unloading, i.e. by decreasing axial stresses, with lower stiffness values. It can be argued whether this is a consequence of the measurement device or if this reflects the soil behaviour. The bender elements protrude into the specimen by 2 mm on each side to assure optimal coupling with the soil. It can be called into question, if this coupling is also assured in extension tests, with decreasing axial stress. Equation 2-4 shows that by decreasing void ratio e , the values of G_{max} increase, assuming OCR, p' and the parameter A and k remain constant. In consequence, G should be higher on unloading than on loading as the soil behaves stiffer and e is smaller than on first loading. Figure 2-18 shows that the stiffness of Drammen plastic clay on unloading is higher than on loading and follows a G - σ'_a path almost parallel to that on loading. These observations could be verified with an automated measurement of G_{bender} in more triaxial stress path tests on natural and reconstituted specimens.

The reconstituted Kreuzlingen clay specimens 46496/58 and 46496/510 were loaded to the estimated previous consolidation stresses and left two weeks in this stress state to consolidate and creep. Specimen 46496/58 showed an axial strain of 3.5% by end of the consolidation stage, whereas specimen 46496/510 showed axial strains up to 12%. The $G_{\text{bender}} - p'$ plots shown in Figure 6-7 a and b are therefore related to very different strain levels, however they show clearly the stiffness increase during a constant stress stage. The increase in G_{bender} for 46496/58 is due to secondary effects (creep and ageing), whereas the porewater pressures in the middle of specimen 46496/510 are probably still dissipating, which leads to a greater change in the values of G_{bender} during this stage. This means also that the mean effective stress p' in the middle of the specimen is less than the computed p' , and therefore the first two points of Figure 6-7 b (at lower values of p' and G_{bender}) would plot more to the left. The final values of G_{bender} are however almost the same (ca. 25 MPa) for both specimens at the end of the constant stress stage.

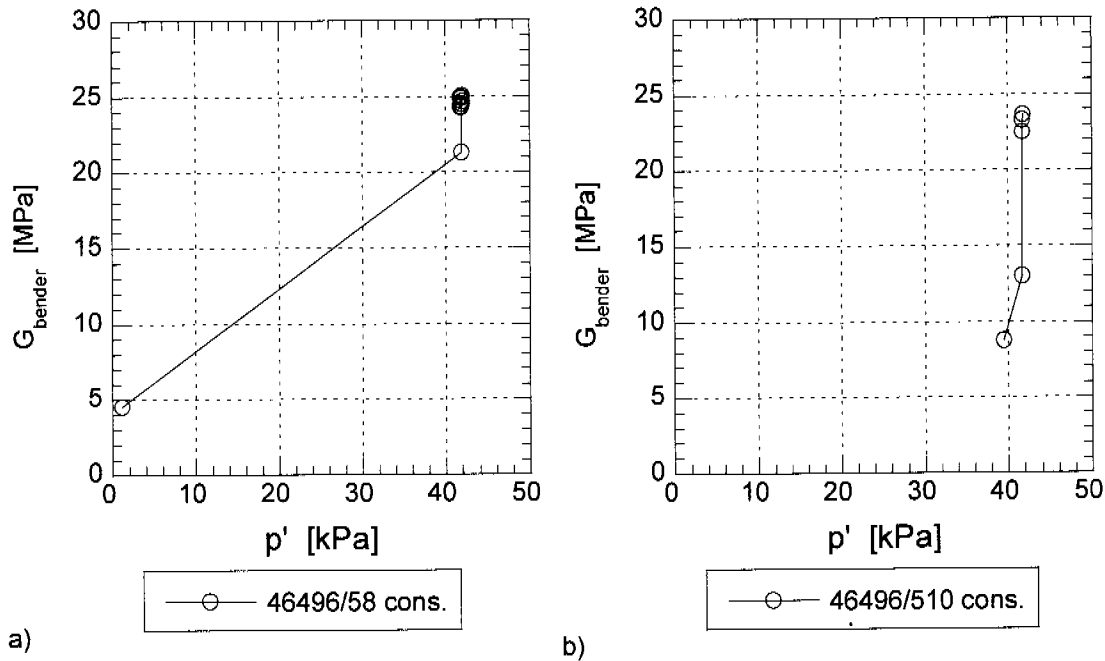


Figure 6-7: Variation of G_{max} measured with the bender element method during a constant stress stage on two reconstituted specimens.

The tangential stiffness during undrained triaxial shearing G_{tan} was calculated with discrete differences between data pairs (Chapter 5.1.2, Equation 5-13). This method is unreliable for data pairs too close to each others, where the subtraction and division of small numbers lead to errors. The Kondner hyperbola formulation of the modulus reduction curve was used to model the shear stiffness-shear strain variation during shear (Figure 6-8 and Figure 6-9). The a and b parameter of the Kondner hyperbola (Chapter 2.2) were determined from the interception of the $\gamma/\tau - \gamma$ plot at zero strain and the inclination of the $\gamma/\tau - \gamma$ plot respectively. The $G_{max,calc}$ value in figures 6-8 and 6-9 is therefore not a measured value, but is determined from a regression line of the $\gamma/\tau - \gamma$ plot extended to zero γ strain. Subsequently, it depends upon the number of data pairs included in the regression. In some cases, the first data pairs suffered under the measurement precision and did not show linearity but random values. In this case, it was not possible to obtain realistic a and b values for the Kondner hyperbola when taking into account these data pairs. As the $\gamma/\tau - \gamma$ curve can be influenced by the measurement precision, the Kondner hyperbola parameters were determined by comparing the results of different regressions on the basis of 10 to 100 data pairs, having the correlation coefficient $R^2 = 0.99$.

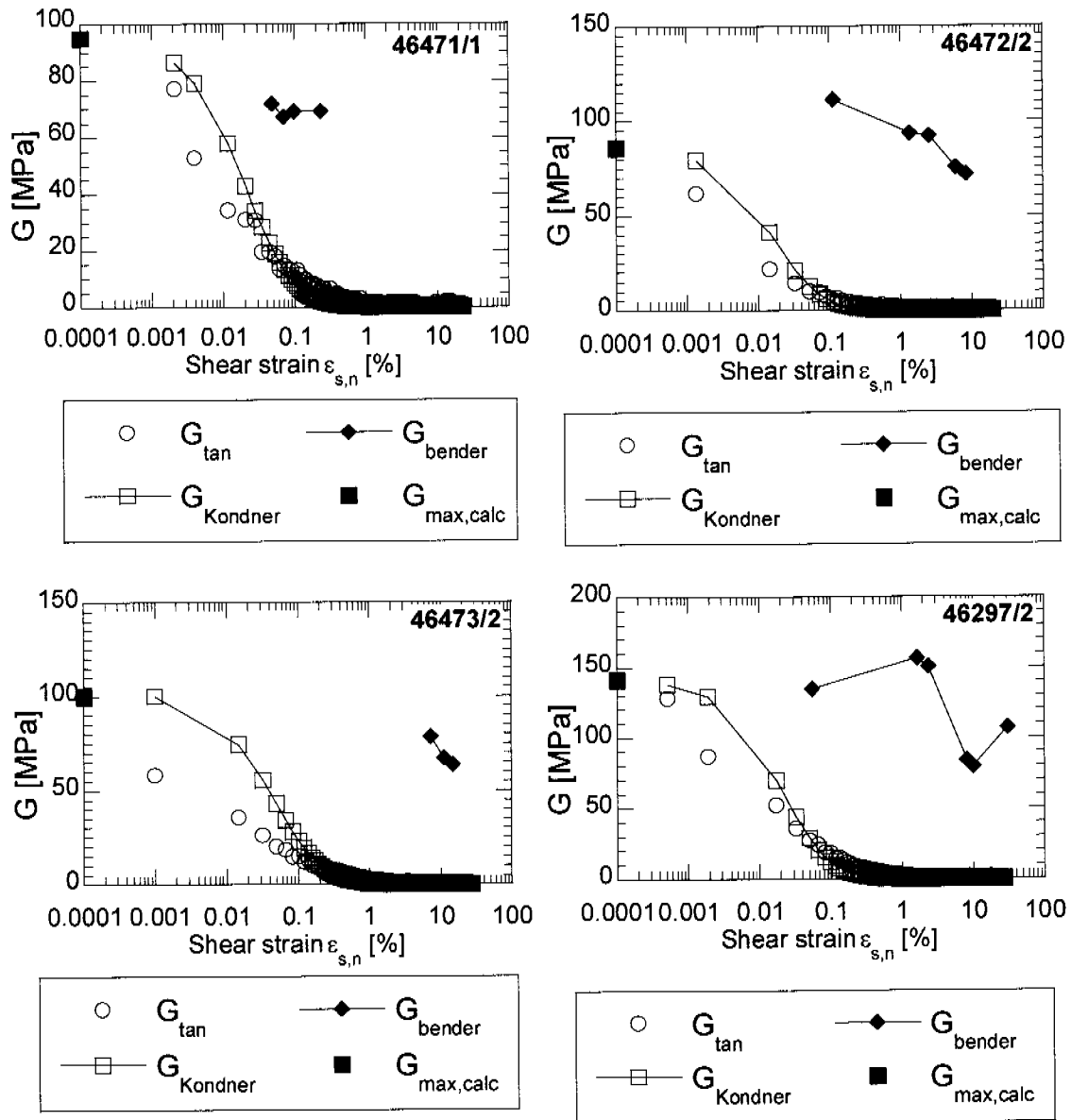


Figure 6-8: Stiffness-strain relationship during typical undrained triaxial shear tests on Kreuzlingen (46471/1, 46472/2 and 46473/2) and Birmensdorf (46297/2) Seebodenlehm: comparison between the calculated tangential shear modulus G_{tan} , the Kondner hyperbola approximation of maximum shear stiffness $G_{max,calc}$ of the modulus reduction curve $G_{Kondner}$ and the small strain shear modulus from bender element tests G_{bender}

Figure 6-8 and Figure 6-9 show that the calculated $G_{max,calc}$ and the measured G_{bender} agree in their order of magnitude, confirming the use of the Kondner hyperbola to model the modulus reduction curve. Figure 6-8 together with Figure 6-6 also show, that the values of G_{bender} are not influenced by the general strain level in the specimen, but only by the stress state during the test.

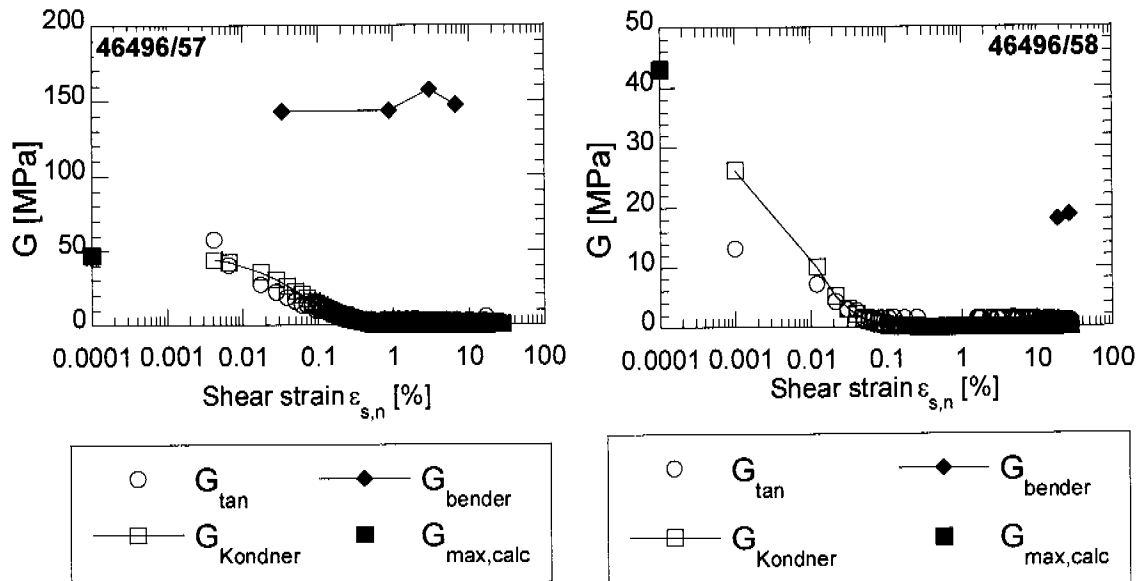


Figure 6-9: Stiffness-strain relationship during typical undrained shear tests on reconstituted Kreuzlingen Seebodenlehm: comparison between the calculated tangential shear modulus G_{tan} , the Kondner hyperbola approximation of $G_{max,calc}$ and of the modulus reduction curve $G_{Kondner}$ and the small strain shear modulus from bender element tests G_{bender} .

The Hashin-Shtrikman bounds presented in Chapter 5.1, Equations 5-6 to 5-10, can be used to estimate the shear modulus G_{max} for a mixture of soil grains and fluid. The shear stiffness moduli of the constituents can be taken from Mavko et al. (1998). As the shear modulus of water is 0, the lower bound describes the moduli of a suspension of grains in the pore fluid, which is consequently also 0. The upper bound of G was calculated to be 29950 MPa for Kreuzlingen clay and 21930 MPa for Birmensdorf clay. The predictive value of the Hashin-Shtrikman bounds is in this case very poor, because the constituents of the mixture are quite different (solid grains and water). Values of G_{max} for dry clays are reported in Mavko et al. (1998) and amount to 1400 MPa for Kaolinite up to 9000 MPa for "Gulf clays". These values are at least two orders of magnitude above the measured or calculated values for Seebodenlehm from triaxial tests.

In all tests, the Kondner hyperbola described the modulus reduction curve satisfactorily. The variation in the modulus reduction curves, modelled with the Kondner hyperbola and normalized with the appropriate $G_{max,calc}$ (Figure 6-10), is large, as the tests were carried out from different initial stress states (p' varied from 50 to 600 kPa, η from -0.3 to 0.5). It can, however, be gathered from Figure 6-10 that the Birmensdorf and Kreuzlingen plots are very similar. The reconstituted samples 46496/57 and 46496/56 plot above all other specimens. Sample 46216 from Kreuzlingen shows rather steeper modulus reduction curves, losing shear stiffness faster with strain than the other Kreuzlingen specimens.

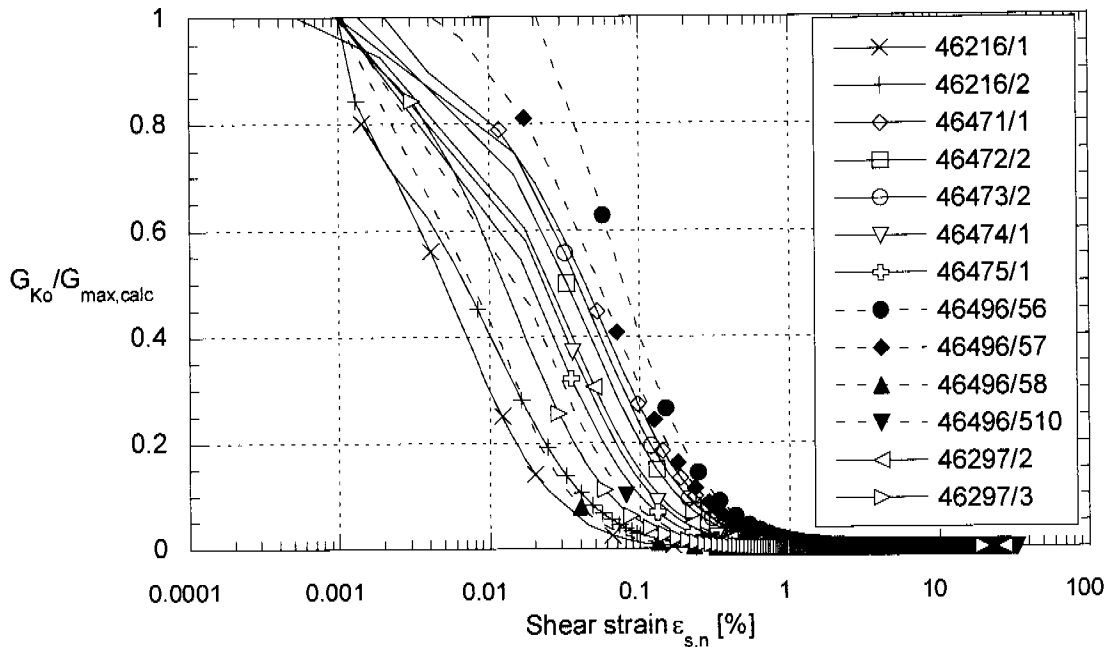


Figure 6-10: Normalized Kondner hyperbolae for all tests in series 2.

The b parameter of the Kondner hyperbola represents the maximum stress increase $\Delta\tau$ during shearing and $\Delta\tau = (\Delta q)/2$. Lämsivaara (1999) indicated that a method to verify the modelling with the Kondner hyperbola is to examine how well b predicts the maximum shear stress q_{max} in the tests (Equation 6-9 and Figure 6-11).

$$q_{max} = q_0 + \frac{2}{b} \tag{6-9}$$

with q_0 = deviator stress at the beginning of the shearing test.

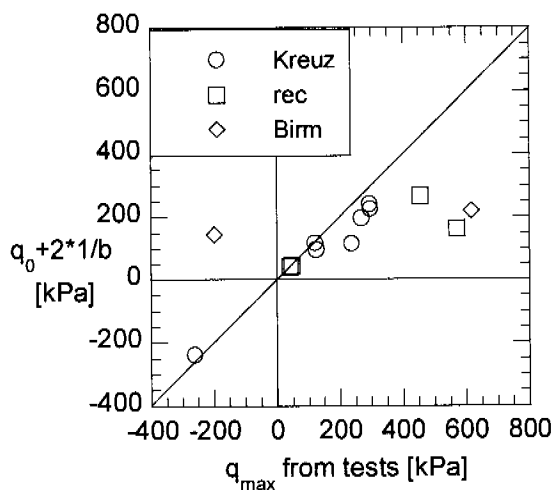


Figure 6-11: Comparison of the maximum deviatoric stress during undrained shear q_{max} and from the Kondner hyperbola.

Figure 6-11 shows a satisfactory correlation for Kreuzlingen clay specimens. Again, the reconstituted Kreuzlingen clay specimens 46496/58 and 46496/510 show behaviour equivalent to the natural specimens, whereas 46496/56 and 46496/57 reflect their unusual behaviour on shearing. In this case, the Kondner

hyperbola method underestimates the maximum stress increase during the test. The Kondner hyperbola underestimate q_{\max} also for the Birmensdorf specimens 46297/2 and 46297/3.

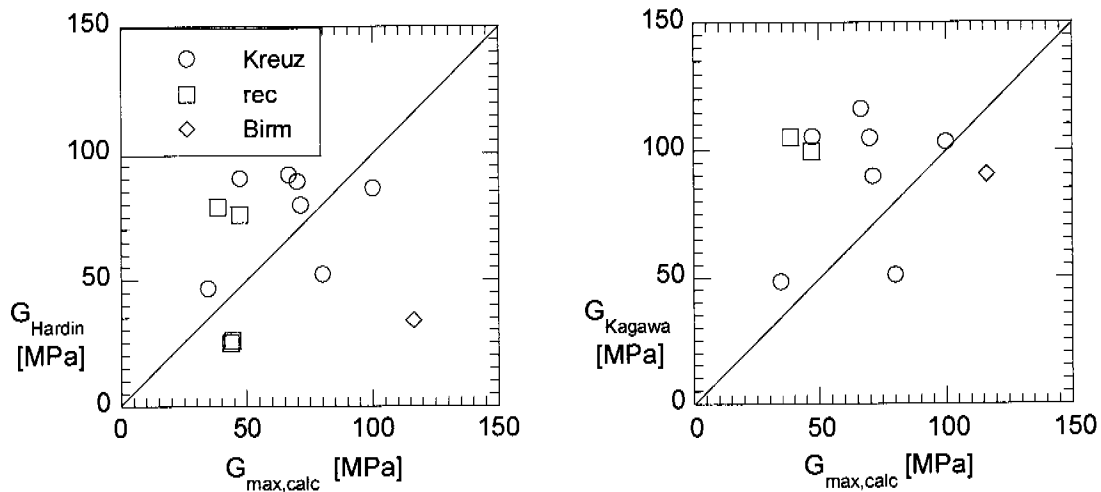


Figure 6-12: Maximum shear modulus $G_{\text{max,calc}}$ from the Kondner hyperbola compared to Equations 2-4 and 2-7 from Hardin (1978) and Kagawa (1992).

The maximum shear modulus can also be evaluated from Equations 2-4 and 2-8 from Hardin (1968) and Kagawa (1992). The value of parameter A in Hardin's equation was first evaluated for each test from the results, then the mean value of $A = 380$ was used to correlate G_{max} . The values of k and n were set to 0.15 and 0.5, respectively (after Hardin and Black, 1969). The correlation between the $G_{\text{max,calc}}$ values from the Kondner hyperbola approximation and the results from Equations 2-4 and 2-8 are presented in Figure 6-12. Both correlations are very poor, and indicate some inaccuracy in predicting the G_{max} from triaxial tests from these relationships.

Finally, the results of the seismic tomography experiment carried out in Kreuzlingen are compared with triaxial results (Figure 6-13 for test series 1 and Figure 6-14 for test series 2). To be able to compare stiffnesses measured at different stress levels, the G values have been normalized with respect to the undrained shear strength measured in the test. To normalize the in situ value of G_{max} , a mean undrained shear strength $s_{u,m}$ has been calculated from the CPTU for the entire deposit from 5 to 22 m depth. The calculated tangential stiffnesses in test series 1 showed large fluctuations, as these are based on an external measurement of displacement only. Therefore the G modulus has been calculated for series 1 as secant stiffness G_{sec} from the beginning of the test (Figure 6-13).

Both the triaxial test stiffness measurement in Figures 6-13 and 6-14 give an estimate of the modulus reduction curve, which tend asymptotically to the maximum shear stiffness measured in situ.

The secant shear stiffnesses calculated for series 1 show higher G values than the tangential stiffnesses of series 2 for the same strain level. For the same measurement in a triaxial test, the secant method for the calculation of stiffness is expected to give higher values than the tangential method. However the exter-

nal measurement of displacement performed during series 1 is highly unreliable and should therefore lead to an underestimation of stiffnesses when compared to the internal measurement of series 2. This is not the case here and this can be attributed perhaps to the storage time: samples of series 1 were tested during the 4 months after extraction, whereas the samples of series 2 were stored up to one year before testing.

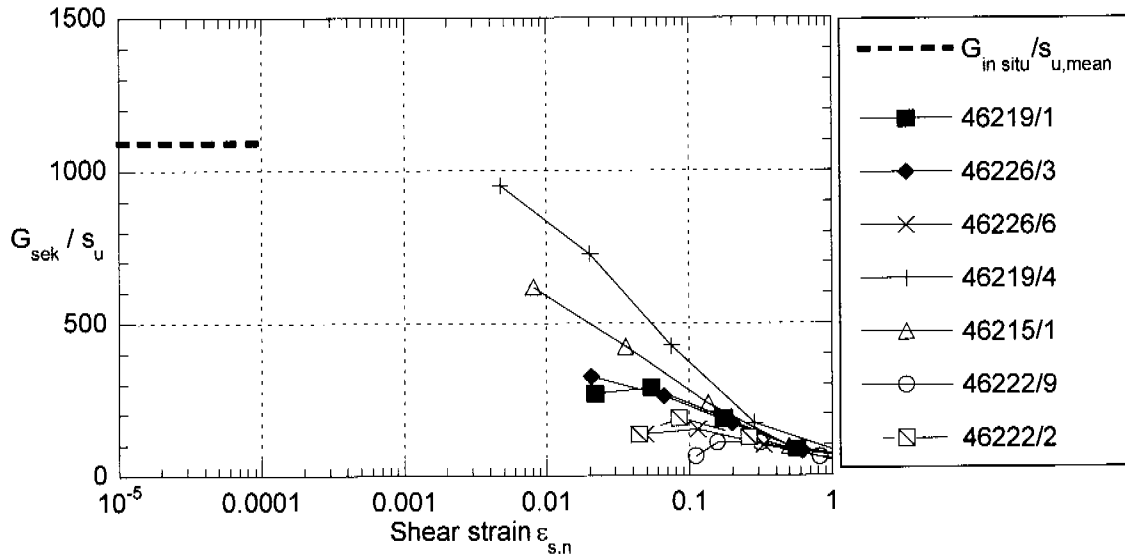


Figure 6-13: Shear stiffness - shear strain plot normalized with undrained shear strength s_u . Modulus reduction curves from measured tangential stiffness of test series 1, compared with the in situ stiffness from the seismic experiment.

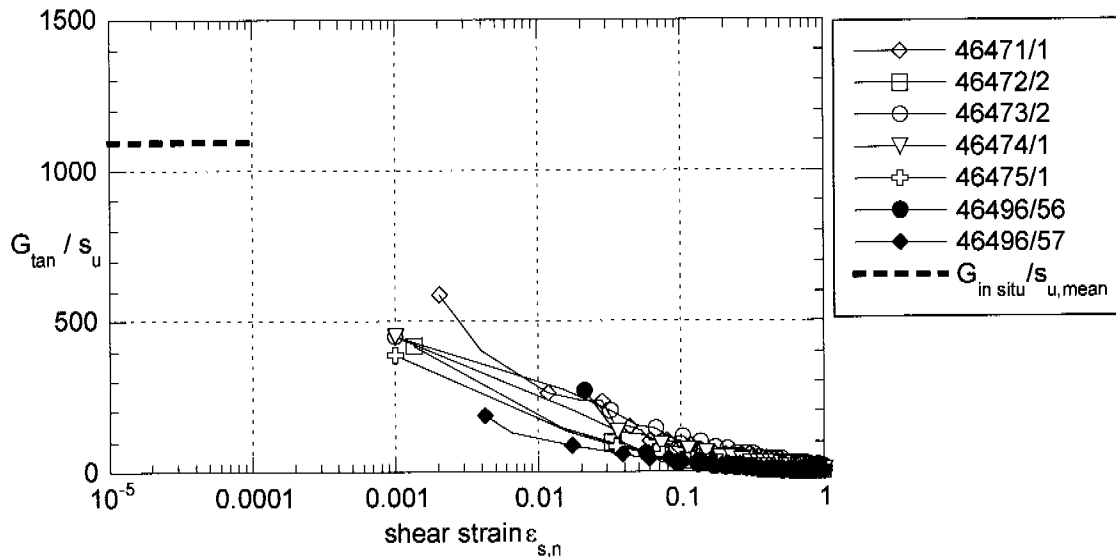


Figure 6-14: Shear stiffness - shear strain plot normalized with undrained shear strength s_u . Modulus reduction curves from measured tangential stiffness of test series 2, compared with the in situ stiffness from the seismic experiment.

Series 1 and 2 have subjected the triaxial specimens to different stress histories. In series 1, the undrained shear stage has been carried out after an isotropic consolidation stage at a mean effective stress p' well above the in situ value. In series 2, the specimens have been subjected to different anisotropic drained stress paths and their yield surface has also been extended well above its initial dimension. In both cases, the inclination of the yield surface has been rotated: in series 1, all undrained shear stages start from the isotropic axis and the yield locus is an almost horizontal ellipse. In series 2, each specimen has (at the beginning of the undrained shear stage), an inclined yield surface depending on the stress path followed (see Section 6.5). It is difficult to attest to what extent the stress path history has an influence on the measured stiffness for stress states on the boundary surface. The triaxial stress path tests carried out by Richardson (1988) and Stallebrass (1990) investigated the stress-strain behaviour of soil for stress states inside the boundary surface. Specimens 46471/1 and 46474/1 of series 2 have also been loaded isotropically before shearing; 46471/1 shows a slightly higher stiffness.

The values of G_{bender} are lower than $G_{\text{in situ}}$, but show extreme high values for sample 46216. From Equation 2-6 (Larsson and Mulabdic, 1991) values of G_{max}/s_u are equal to $504/w_L$. These values agree well with the normalized in situ stiffness $G_{\text{in situ}}/s_u$ (Figure 6-15).

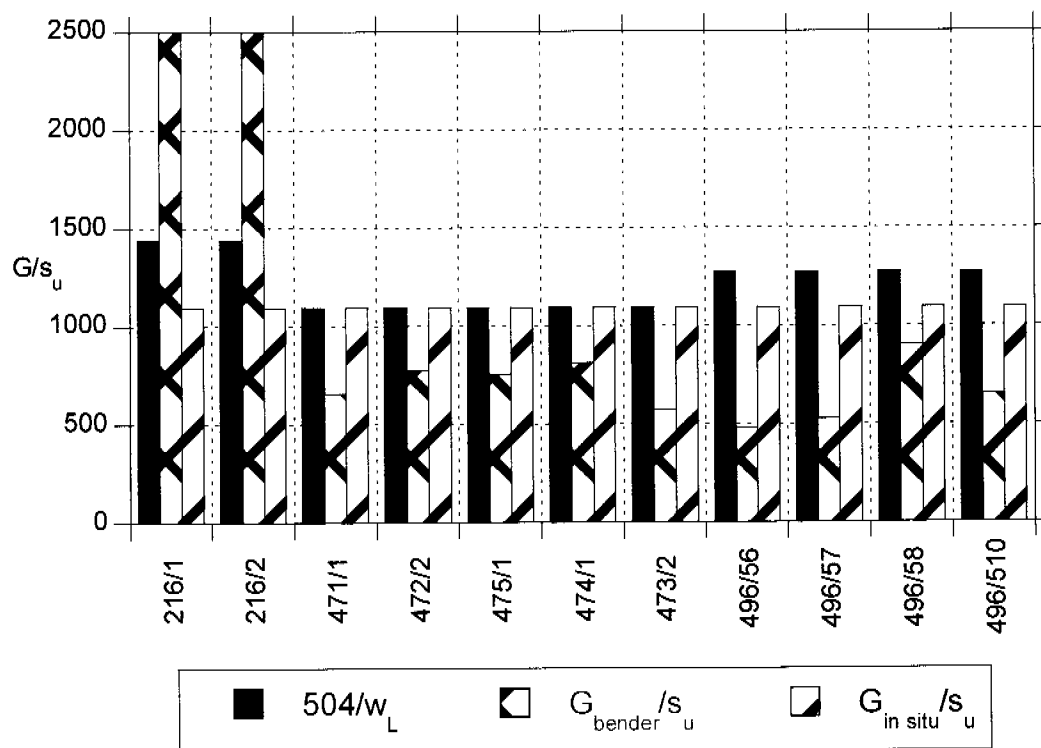


Figure 6-15: Comparison between the G values normalized with s_u from the Bender measurement and from the in situ measurement with Equation 2-7.

6.5 Determination of yield from TSPT and comparison with the predicted yield loci from S-CLAY1

As stated in Chapter 5.1.2, one of the main goals of the triaxial investigation was the determination of the yield surfaces for the clays investigated. The investigation of yield during triaxial drained loading on different stress paths, carried out on the basis of different strain and stiffness variables, can deliver a more sensitive indication of the occurrence of yield. The typical graphs used for yield determination (Figures 5-14 and 5-15) are compared in Table 5-7. The yield value identified from the $\ln p' - v$ plot was used to define the yield surface in $p' - q$ space.

Figures 6-16 and 6-17 show the yield points (Yield 1, Yield 2), the maximum stress reached during loading on a stress path (max) and the estimated in situ stresses for the different samples (insitu stress).

Equation 6-10 describes the yield surface proposed by Wheeler et al. (2003) for the constitutive model S-CLAY 1 (Section 2.3).

$$f = (q - \alpha \cdot p')^2 - (M^2 - \alpha^2) \cdot (p'_m - p') \cdot p' \quad [6-10]$$

where M is the critical state value of the stress ratio η , and p'_m and α define the size and inclination of the yield surface. Different values of M can be assumed for triaxial compression and extension.

Wheeler et al. (2003) report a simple procedure to estimate the in situ value of α for normally consolidated deposits, whose stress history is restricted to one dimensional straining (Equation 6-11).

$$\alpha_{K_0} = \frac{\eta^2_{K_0} + 3 \cdot \eta_{K_0} - M^2}{3} \quad [6-11]$$

where η_{K_0} is the stress ratio corresponding to K_0 conditions and K_0 can be estimated with Jaky's formula ($K_0 \approx 1 - \sin \phi'$ Jaky, 1944). Thus only the size of the ellipse defining the initial yield curve p'_m has to be selected by optimizing the fit to the experimental points. The maximum stress state reached during first loading (max) and the second yield point (Yield 2) detected during second loading are also shown in Figures 6-16 and 6-17. The expanded and rotated yield curve produced by first loading is fitted through the maximum stress point by changing the value of p'_m , while the value of α is selected so as to achieve a best fit to the various yield points Y2.

Figures 6-16d and 6-17a indicate a good agreement between the yield curves defined by Equation 6-10 and the experimental results based on stress paths with a significant difference in the η values. In Figures 6-16a to c and 6-17b, the SCLAY1 yield locus has also been fitted to the test results. In these tests however, the η values of the different stress paths were very similar and the data plotted in a small section of the yield curve.

The in situ yield curves for the four samples from Kreuz2 (Figure 6-16 c and d) have the same inclination α_{K_0} as defined by Equation 6-11, but not the same size. This may be due to inaccuracies in the determination of the yield points as well as to variability in the samples.

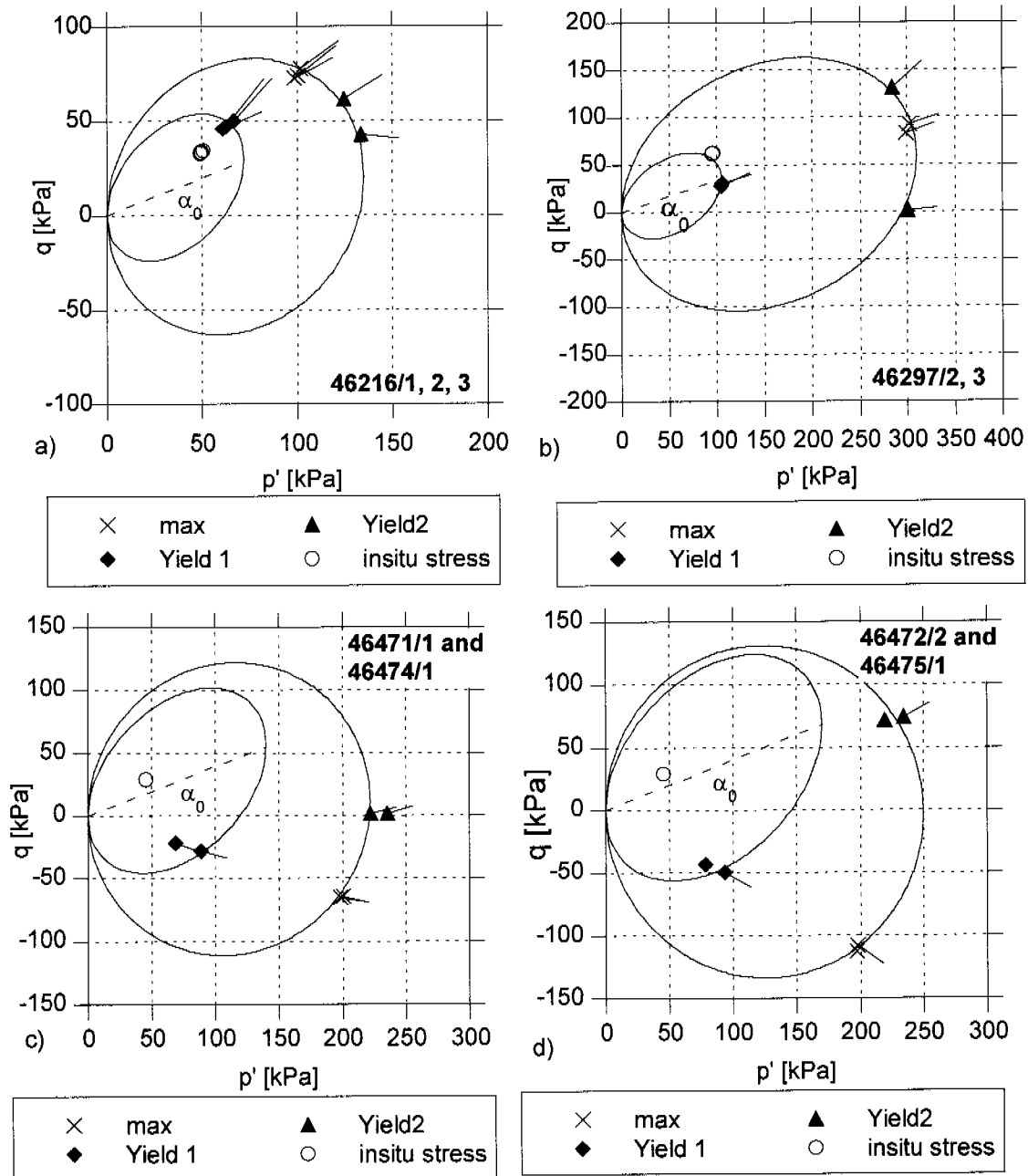


Figure 6-16: Yield points and maximum load stress obtained during triaxial stress path tests, estimated in situ stress and inclined yield surfaces estimated from S-CLAY 1: a) Kreuz1 - 46216, 3 specimens, b) Birm2 - 46297, 2 specimens, c) Kreuz2 - 46471 and 46474, d) Kreuz2 - 46472 and 46475.

The estimates of the in situ stresses, which are plotted as well in Figures 6-16 a, b, c and d, match the experimental in situ yield locus only for the Birmentsdorf sample (Figure 6-16b), whereas it lies inside the yield locus for both Kreuz1 and Kreuz2 sites. The difference between yield stresses and in situ stresses is particularly important for Kreuz2, for which a slightly overconsolidated behaviour was observed during CRS oedometer testing (Section 5.2.3).

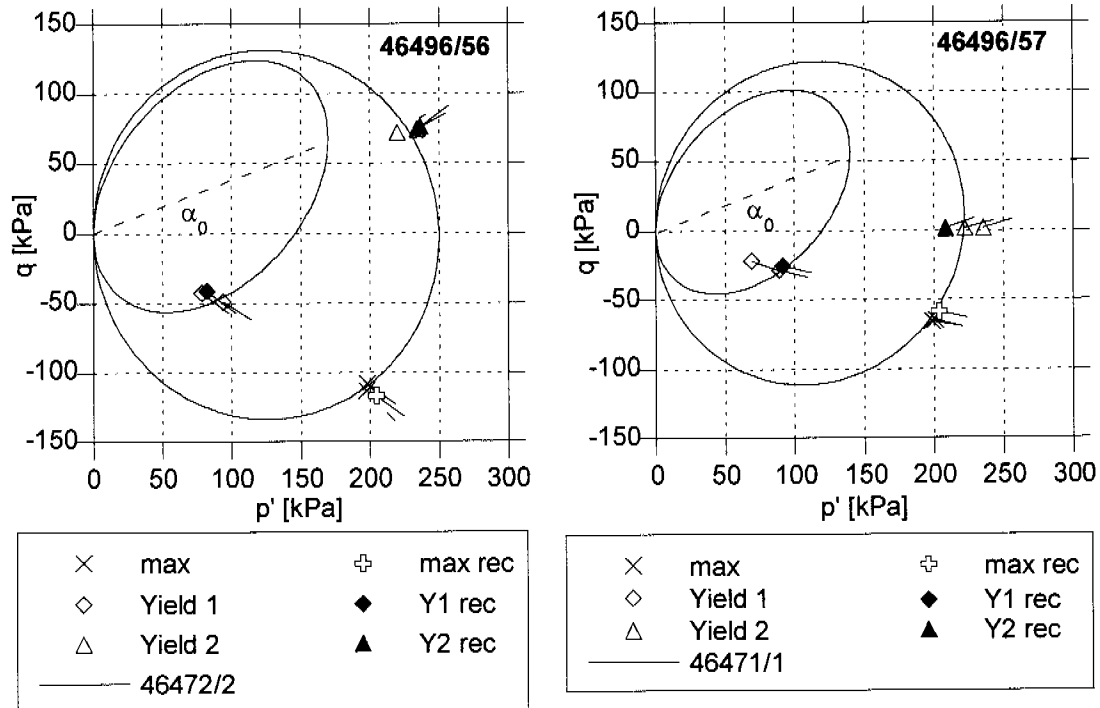


Figure 6-17: Yield points and maximum load stresses obtained during triaxial stress path tests for the reconstituted specimens 46496/56 and 46496/57 are compared to the relative tests on natural samples 46472/2 and 46471/1 respectively (Kreuz2).

It can be seen from Figure 6-16 and Table 6-2 that first loading at positive values of $\eta_1 < \eta_{k0}$ caused clockwise rotation of the yield curve (46216 and 46297), and that first loading in triaxial extension (negative values of η_1) can even drag α towards 0 (46471 to 46475). The Finnish Otaniemi clay showed a modest rotation from $\alpha_{k0} = 0.42$ to $\alpha_1 = 0.39$ for $\eta_1 = 0.75$ (Wheeler et al. (2003)), because the value of η_1 was close to η_{k0} for this clay and did not represent a radically new stress path. The value of η_{k0} for the Kreuzlingen Seebodenlehm is 0.66 and the critical value of η is equivalent to $M = 1.08$. The specimens 46216/1 to 3 have been loaded on a stress path with $\eta_1 = 0.75 > \eta_{k0}$ but also show a large clockwise rotation from $\alpha_{k0} = 0.4$ to $\alpha_1 = 0.15$. It seems that every inclination of the stress path tends to drag the yield locus to an isotropical state.

The yield points for the two reconstituted triaxial stress path tests (46496/56 and 46496/57) are compared to the similar tests (i.e. tests with same stress path history) on natural Kreuzlingen clay in Figure 6-17. The yield points of the reconstituted samples agree particularly well with the yield points of the natural samples, indicating that structure has, in this case, no influence on yielding for the Kreuzlingen Seebodenlehm, with the yield points of the young, reconstituted material comparable to those of the aged natural clay. The low sensitivity of this clay (Chapter 3) indicated already a lack of cementation and structure, although the carbonate content was $>30\%$.

| Sample No. | η_1 | $\alpha_{\kappa 0}$ | α_1 |
|-----------------|----------|---------------------|------------|
| 46216 / 1, 2, 3 | 0.75 | 0.4 | 0.15 |
| 46297 / 2, 3 | 0.3 | 0.34 | 0.19 |
| 46471/1 | -0.3 | 0.4 | 0.05 |
| 46472/2 | -0.5 | 0.4 | -0.01 |
| 46473/2 | 0 | 0.4 | 0.0 |
| 46474/1 | -0.3 | 0.39 | 0.08 |
| 46475/1 | -0.5 | 0.41 | -0.01 |
| 46496/56 | -0.5 | 0.38 | 0.05 |
| 46496/57 | -0.3 | 0.41 | 0.08 |

Table 6-2: Values of initial yield curve inclination $\alpha_{\kappa 0}$ and yield curve inclination after first loading α_1 .

Figure 6-17 shows that the ageing of the natural clay did not create a structure, which can offer higher resistance to yielding. Table 6-2 indicates that the rotation of the yield curve is almost the same for the natural and the reconstituted samples with same stress path history. The Kreuzlingen Seebodenlehm is more homogeneous than the Birmensdorf Seebodenlehm, where the varving pattern is more pronounced. The difference in rotation of the yield curve between natural and reconstituted Birmensdorf clay can be expected to be greater than for Kreuzlingen clay, because of the influence of the horizontal silt layers in the natural sample.

The rotational hardening law incorporated in S-CLAY1, describes the change of inclination of the yield curve produced by plastic straining and is directly dependent upon the plastic volumetric and shear strains (Equation 6-12 from Wheeler et al., 2003b).

$$d\alpha = \mu \cdot [(\chi_v(\eta) - \alpha) \langle d\epsilon_v^p \rangle + \beta \cdot (\chi_d(\eta) - \alpha) |d\epsilon_d^p|] \quad [6-12]$$

The soil constant β controls the relative effectiveness of plastic shear strain increments and plastic volumetric strain increments in determining the current target value of α , whereas the soil constant μ controls the rate at which α approaches its current target value (Wheeler et al., 2003b). It is assumed that plastic volumetric strain and plastic shear strain increments attempt to drag the value of α towards two different target values $\chi_v(\eta)$ and $\chi_d(\eta)$, which are both functions of the actual stress ratio η . The equilibrium value of α is the eventual inclination of the yield curve that would be reached after following a stress path with a new value of η , if this new stress path excursion extends sufficiently far beyond the previous yield locus. Therefore this is a function of the erasure of the past stress history.

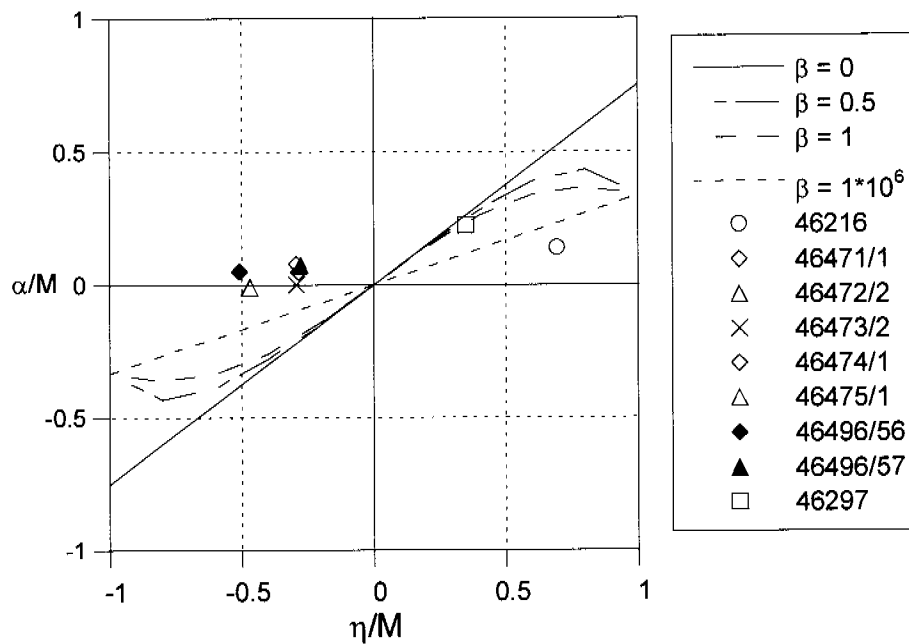


Figure 6-18: *Experimental versus theoretical values of α/M at equilibrium, data from series 2 for Swiss Seebodenlehm (Diagram as presented in Wheeler et al., 2003b).*

The suggested expressions for the target values $\chi_v(\eta)$ and $\chi_d(\eta)$ are given in Equation 6-13 and 6-14 (from Wheeler et al., 2003b).

$$\chi_v(\eta) = \frac{3 \cdot \eta}{4} \quad [6-13]$$

$$\chi_d(\eta) = \frac{\eta}{3} \quad [6-14]$$

Wheeler et al. (2003b) plotted the normalized experimental yield curve inclination α/M against the value of η/M from the first loading stage for different Finnish clays, together with theoretical predictions for α values for different values of β . An equivalent plot is produced in Figure 6-18 with the values for Swiss Seebodenlehm. This plot gives an estimate of how the value of α changes with stress path direction η , and a comparison between the analytical values (determined on the basis of SCLAY1) and the experimental values is possible.

The two tests on Birmensdorf clay 46297/2 and 46297/3 are the only ones that agree with the theoretical α values, with β between 0.5 and 1. Sample 46216 was tested with a very high value of η_1 , where the plastic shear strain are very high as η is approaching the critical value M .

All the tests that had first loading in extension and that involved a large re-orientation of the yield curve (Table 6-2) do not correspond at all to the theoretical values. Wheeler et al. (1999) showed, by using a numerical simulation, that the first loading path has to be continued much further in extension than in compression to rotate the yield surface completely to the new value of α , and therefore the measured values of α for $\eta_1 < 0$, are not the equilibrium values. This was

confirmed by Wheeler et al. (2003b) on the basis of test results on Otaniemi clay, although the discrepancies between theoretical and experimental values were smaller than for Swiss Seebodenlehm.

A physical model that could help to visualise this behaviour is the conceptual model of Simpson (1979). He idealises soil with a man walking around a room pulling behind him a series of bricks, each on a separate string of different length. The tests performed by Richardson (1988) and Stallebrass (1990) had shown that soils generally offer less resistance to continuation of straining in the direction they were previously following than they do to reversal of direction. Likewise, if the man pulling the bricks turns back, the bricks do not move initially; then the ones on shorter strings start to move, gradually followed by those on the longer strings (Simpson, 1979). This analogue may be either taken to represent plastic yield surfaces in stress space or strain vectors in strain space. A new stress path, which tries to drag the soil's state into a negative stress quadrant, has to extend far enough so that at least the first bricks (those on the shorter strings) start to move on the new direction.

As conclusion to these observations it can be said that SCLAY1 appears to be consistent with the test results, but there are at present time insufficient data to prove conclusively that the model is working for these soils. The issue about Seebodenlehm is its heterogeneity due to pronounced varving. It was shown in Chapter 5 that the varving influences the strength parameter M and ϕ' for specimens from the same undisturbed sample. In contrast SCLAY1 assumes an homogeneous shear strength for a clay type, so that it makes it difficult to choose the right parameter for simulation of Seebodenlehm for this model. Further the varving represent a structure which is more difficult to rearrange than the arrangement of clay particles in a more homogeneous clay. The varving represents probably a limit to the rotational hardening considered in SCLAY1 and therefore more data are needed to confirm the consistency of the model with test results on Seebodenlehm.

An associated flow rule is assumed within S-CLAY1. In this research, the total strain increment vectors are plotted at the appropriate yield points, with local axes (ε_s and ε_v) parallel to the main q and p' axes in Figure 6-16 and Figure 6-17. The common direct measurement of plastic strain increments requires significant expansion of the yield curve as it is based on a secant method, but during this process there may also be an important rotation of the yield curve. One way to avoid this problem is to check the correctness of the flow rule by comparing ε_s - ε_v strain paths from SCLAY1 simulations with measured ε_s - ε_v strain paths. This however implies that SCLAY1 is able to describe the behaviour of Seebodenlehm. For this research the strain path increment vectors were determined by a sliding regression to calculate the tangent to the ε_s - ε_v strain path: a straight line was fitted to 100 measured data pairs of the strain path and the gradient of this line was set as the tangent to the strain path in the middle of the data interval. The interval was then moved to the next data pair. The value of the tangent by stress reversal or yield points of the consolidation stage was then used to calculate the gradient of the total strain increment vectors at this points.

It was not possible to separate the plastic and elastic component of the strain increment vectors since no unload-reload cycles have been carried out to compute for the reversible strains. Therefore it is difficult to make a statement on the

validity of the associated flow rule for Swiss Seebodenlehm. What can be observed from Figure 6-17 is that the total strain vectors of similar tests (with the same stress path history) on different specimens are parallel, and that the total strain vectors seem to have the same inclination as the approaching stress path. This is also valid for the reconstituted specimens, which show total strain vectors very similar to those of the natural specimens with same stress path history (Figure 6-17).

6.6 In situ settlement: the Birmensdorf test fill

The results of a field test in Birmensdorf with three test fill embankments are evaluated in the report of the Geotechnischer Institut (1996). The data discussed in this chapter have been taken from this report and re-evaluated. Two of the test fills have been designed to test the influence of sand drains on settlement rate. This section considers only the measurements for the test fill without sand drains.



Figure 6-19: Picture of two of the test fill embankments in Birmensdorf (Tiefbauamt des Cantons Zürich, 1996)

The test fill (Figure 6-19 and 6-20) had a square plan area with a side length of 30 m at the base and a 1:1 vertical to horizontal slope, and was built up to a height of 6.25m. A drainage layer of gravel with 1m thickness was laid on the ground surface before the construction of the test embankment. The geotechnical profile under the test fill showed a 0.5m thick layer of top soil followed by a clay layer up to 18.5m depth. This layer is underlain by a clayey silt with sand and gravel, followed by the moraine. The ground water table was found between 0.5m and 1.5m depth. By the beginning of construction, the water level in the upper drainage layer was at a depth of 1.25m below the ground surface, while the groundwater pressure in the lower sandy silt layer corresponded to a depth of 2.8m below the ground surface. This indicates a downward hydraulic gradient of approximately 0.1 (0.087) in the clay layer.

The construction of the embankment started on 19th December 1994. 90 cm of fill material with a unit weight of 23 kN/m^3 were put in place before the Christmas holidays. The clay had the possibility to consolidate under this stress till 13th January 1995. The construction ended on 6th March 1995, with an equivalent total vertical stress acting on the ground surface of 144 kPa. Observations of pore water pressure and settlements under the test fill were continued during one year, until 26th March 1996.

The instrumentation was placed under the centre of the test fill (Figure 6-20). It consisted of 5 piezometers, placed at a depth of 4, 8, 12, 18 and 22 m under ground surface, and a sliding micrometer, which measured differential settlements in 1 m depth steps, up to a depth of 22 m. The sliding micrometer was fixed in the underlying moraine. In addition, a slope inclinometer up to 28 m

depth was placed 6 m away from the east side of the embankment along the centreline. The loading sequence, the evolution of differential settlement under the embankment, the total pore water pressure and the calculated excess pore water pressure are plotted in Figure 6-21. The plotted settlements correspond to the differential settlements measured by the sliding micrometer over a 1m interval at depths corresponding to the piezometer depth.

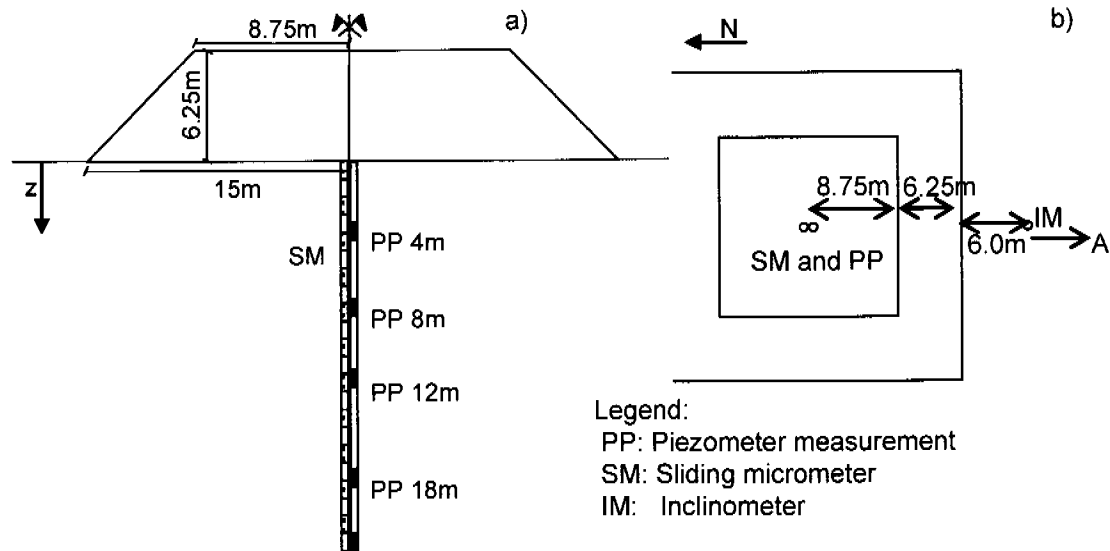


Figure 6-20: Sketch of the Birmensdorf test fill: a) section, b) plan.

The largest differential settlements are measured at 4m and 8m depth, whereas the highest excess pore pressure is measured at 8m and 12m depth. The differential settlements at 3m and 5m depth are also plotted in the settlement-time graph in Figure 6-21. The differential settlement value at 4m depth is smaller than at 3m and 5m depth, indicating the presence of a fine stiffer layer. This layer probably influences locally, with higher horizontal permeability, the excess pore pressure measurement, which also shows very low values of excess pore pressure at this depth. Moreover, only the layer at 4m depth seems to have reached secondary settlement after one year of consolidation time. The differential settlements are very small in the 1m layer at 12 and 18m depth until the end of monitoring, although the excess pore water pressure is greatest at 12m. On the basis of these measurements, the Birmensdorf clay deposit under this test fill cannot be considered homogeneous with respect to stiffness and permeability properties.

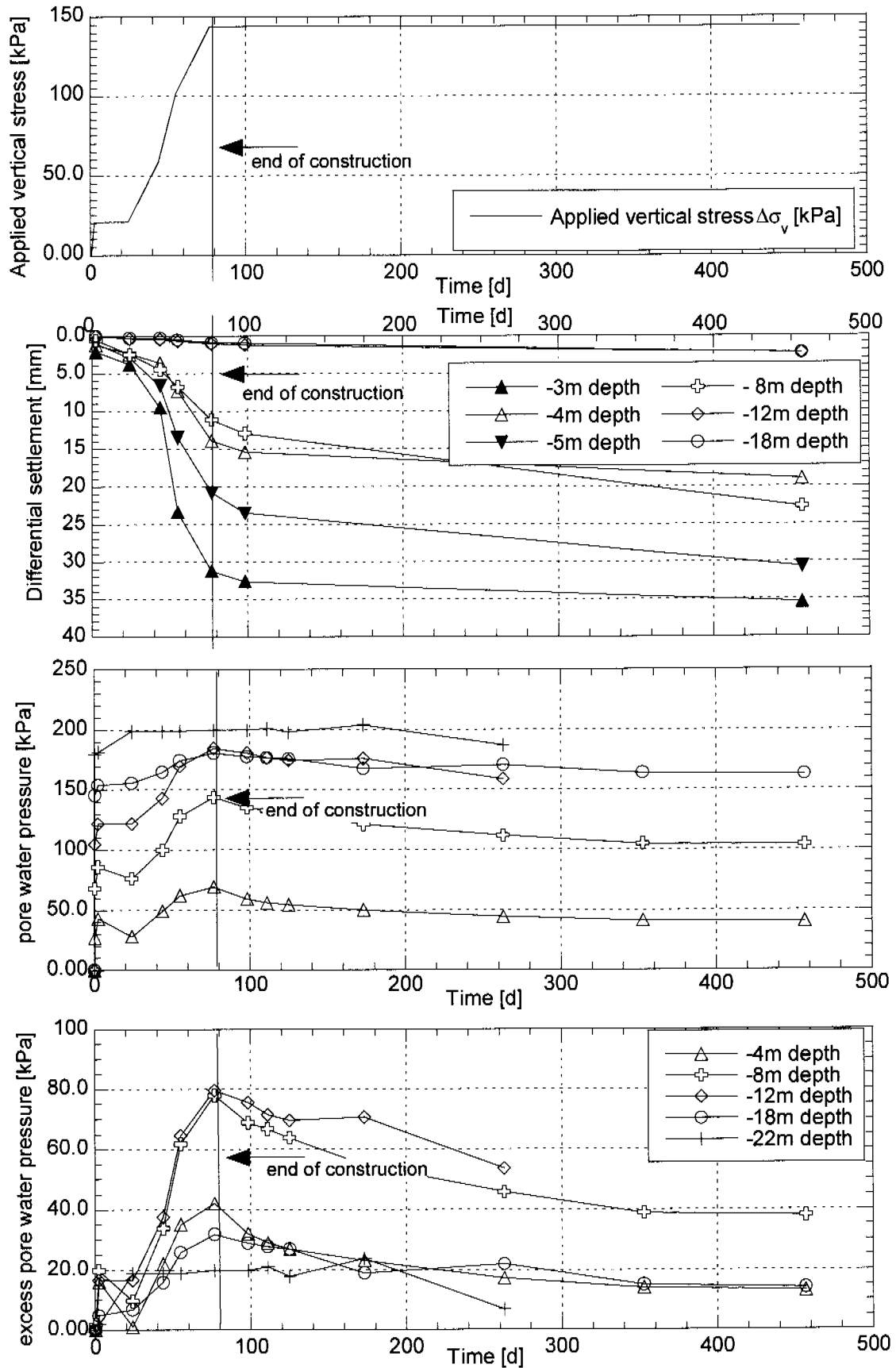


Figure 6-21: Applied load, settlement evolution, measured pore water pressure and calculated excess pore water pressure. (Technical failure of piezometers at 12m and 22m depth after 260 days)

The excess pore water pressure at the respective depth has been calculated from the piezometer measurement and the in situ pore water pressure distribution, based on a ground water level at 1.25m depth and a downward hydraulic gradient of approximately 0.1. The excess pore water pressure is reduced, during the monitored consolidation period (ca. 1 year), to half the maximum value measured at construction end (76.8 days) at 8m and 12m. In the stiffer layers above and beneath the clay (4m and 18m), Δu is reduced to less than one third of the maximum value measured at construction end. This indicates the expected parabolic pattern of excess pore pressure, with a quicker reduction of Δu at the upper and lower boundaries to the Seebodenlehm (Figure 6-22 a and b). In addition the horizontal layering of the Seebodenlehm also induces a difference in the anisotropy of the permeability parameter k_v and k_h between the layers. Indeed the rate of consolidation deduced from the measurement is far higher than that calculated with Terzaghi's one-dimensional consolidation theory, which only considers drainage.

Figure 6-22 a and b show the distribution of excess pore pressures under the embankment at different times, respectively during and after construction. The increase in excess pore pressure at 22 m depth after the Christmas Holidays (23.98 d) can be explained by an increase of the water level in the lower drainage layer, owing to large surface circulation of groundwater. The isochrones of the excess pore water pressure have an approximate parabolic shape between 4 and 18 m and show that the clay layer can drain in both directions towards the crust layer and towards the more permeable layers around 18m depth.

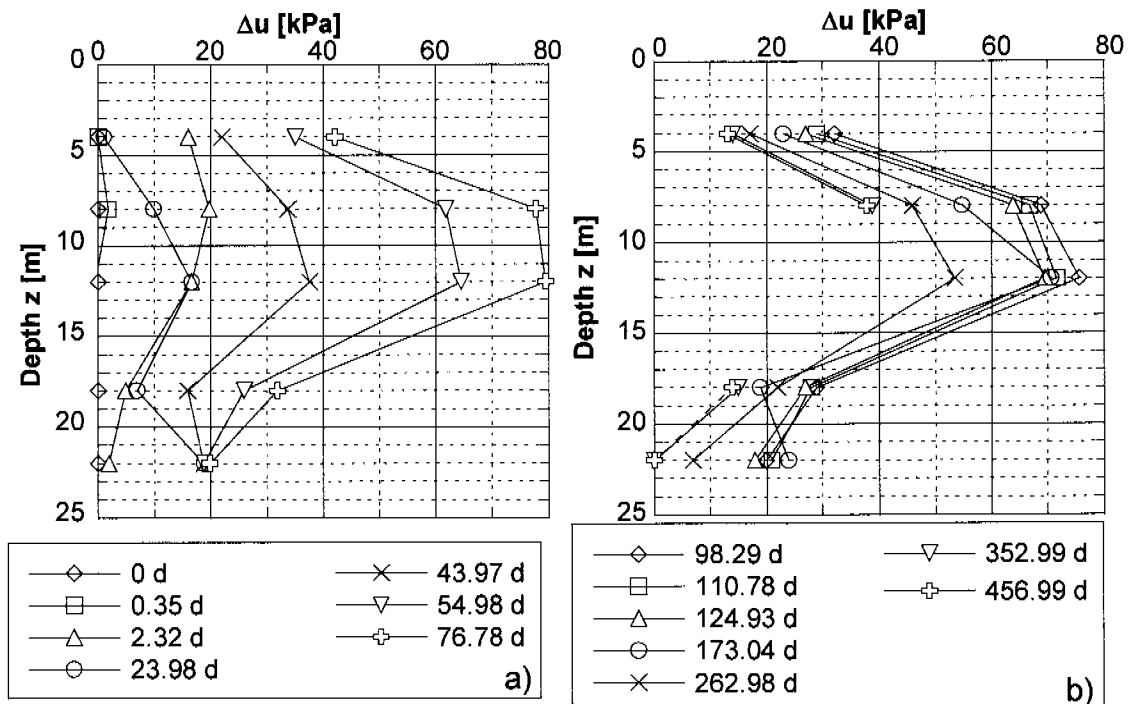


Figure 6-22: Isochrones of the measured excess porewater pressure with depth: a) during construction period, b) during consolidation time

The ratio between clay layer thickness and embankment side length is 0.6, which means that the boundary conditions for compression do not correspond to one dimensional conditions. Nonetheless, the total vertical applied stress has

been selected as a convenient stress component against which to compare the excess pore pressure, because it is the only one which can be considered rather insensitive to non-linear material properties (Berardi and Lancellotta, 2002). The pore pressure coefficient \bar{B} is then calculated as follows:

$$\bar{B}(t) = \frac{\Delta u(t, z)}{\Delta \sigma(t)} \quad [6-15]$$

where $\Delta \sigma(t)$ = total stress at ground level at a specific time t . $\Delta u(t, z)$ is the excess water pressure measured at the corresponding time t at the piezometer depths z . The development of excess pore pressure during the loading phases is plotted in Figure 6-23 together with dotted lines, which correspond to \bar{B} values of 1, 0.65 and 0.35 respectively. The local failure condition of $\bar{B} \geq 1$ is not reached in any of the layers. Berardi and Lancellotta (2002) showed that a sharp increase of the excess pore pressures measured by means of piezometers in a clay deposit loaded with oil tanks, indicated the onset of plastic straining, whereupon $\bar{B} \geq 1$ was found in all layers. This does not consider the reduction of the increment of vertical stress with depth, due to load-spreading effect. The \bar{B} value, as defined by Equation 6-15, is expected to reduce with depth because of the load-spreading effect but to be lowest at the boundary because of the lower Δu .

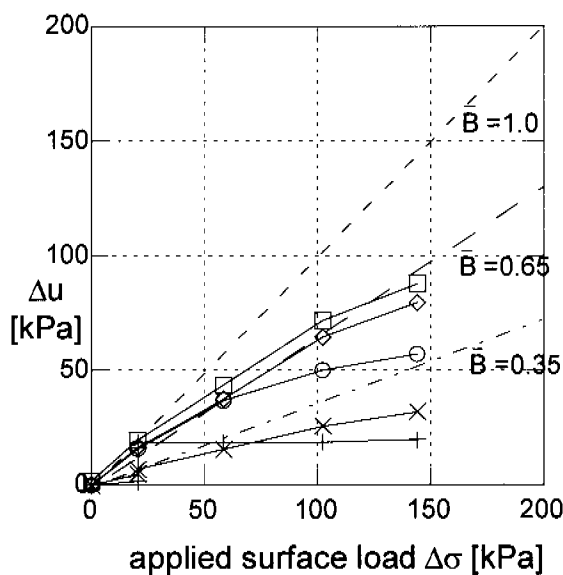
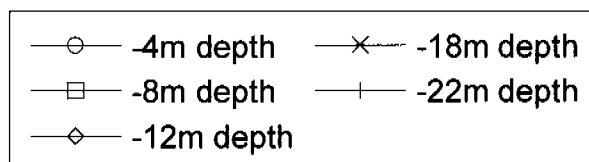


Figure 6-23: Pore pressure development during loading phases



The sliding micrometer measures settlement over each 1m segment of the micrometer tube. Assuming that the clay and the resulting vertical strains are homogeneous over this thickness, average vertical strains can be calculated for each segment of 1000 mm length. An elastic stress distribution was assumed under the centre of the embankment to take into account the load-spreading effect (Boussinesq). This assumption underestimates, however, the reduction of

the vertical load with depth. At the piezometer depths of 4, 8, 12 and 18 m, the pore pressure measurement leads to an evaluation of the effective vertical stress σ_m' (Equation 6-16),

$$\sigma_m' = \sigma_{v0} - \Delta\sigma_{\text{Boussinesq}} - U_{\text{measured}} \quad [6-16]$$

The mean effective in situ vertical stress σ_m' can be associated with the average vertical strain to provide an in situ vertical effective stress - vertical strain curve (Figure 6-24).

Typical results of CRS tests on specimens of Birmensdorf clay from a comparable depth are also presented in Figure 6-24, where the origin of strain is taken at $\sigma_m' = 78$ kPa, a stress equal to the vertical effective stress in the field at that depth, before embankment loading.

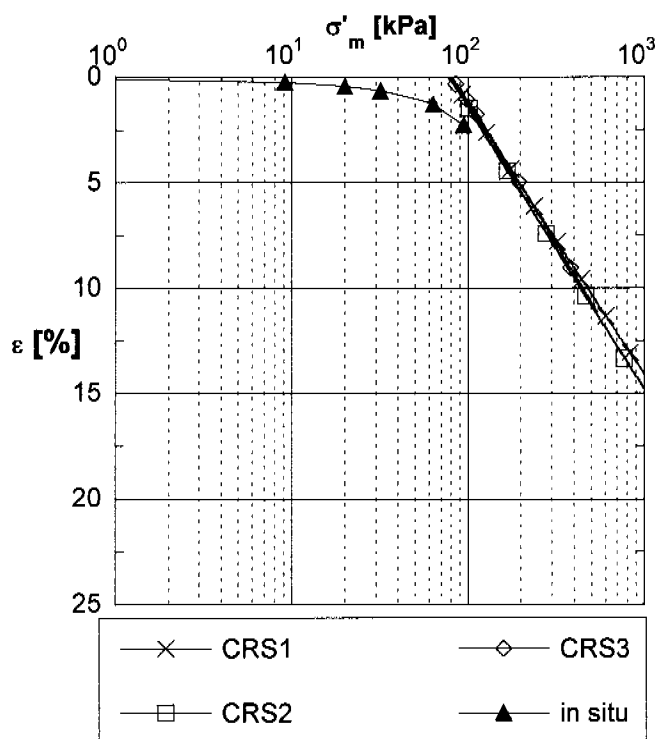


Figure 6-24: Vertical effective stress-vertical strain curves for in situ boundary conditions under the Birmensdorf test fill (8m depth) and for three CRS oedometer tests on Birmensdorf clay specimens from 8m depth.

Figure 6-25 shows the strain rates under the embankment, calculated from the settlements in the sliding micrometer and the elapsed time between two readings, and confirms that the strain rates at 4 and 8 m depth do not exceed $0.5 \cdot 10^{-8} \text{ s}^{-1}$ and are 600 times slower than the slowest strain rate in the CRS test ($3 \cdot 10^{-6} \text{ s}^{-1}$). Kabbaj et al. (1988) compared the in situ vertical effective stress - vertical strain curve for four embankments on soft clays from Canada, with laboratory vertical stress - vertical strain curves on undisturbed samples. They concluded that the laboratory tests underestimated the in situ strains and that this difference was mainly due to strain rate effects (in situ strain rate much slower than in laboratory test).

Therefore it can be expected that also for the Birmensdorf embankment the in situ stress-strain curve plots under the laboratory curves. From Figure 6-24 it is visible that the clay deposit barely reached the vertical yield stress σ'_{vy} under embankment loading. Monitoring has been interrupted too early in this case.

However, extrapolating the in situ curve for higher effective vertical stresses, it can be estimated that the in situ curve would plot slightly below the laboratory curves, which almost the same inclination in the normal consolidated region. Again the results show that the influence of strain rate on the stress-strain response of Seebodenlehm are minimal.

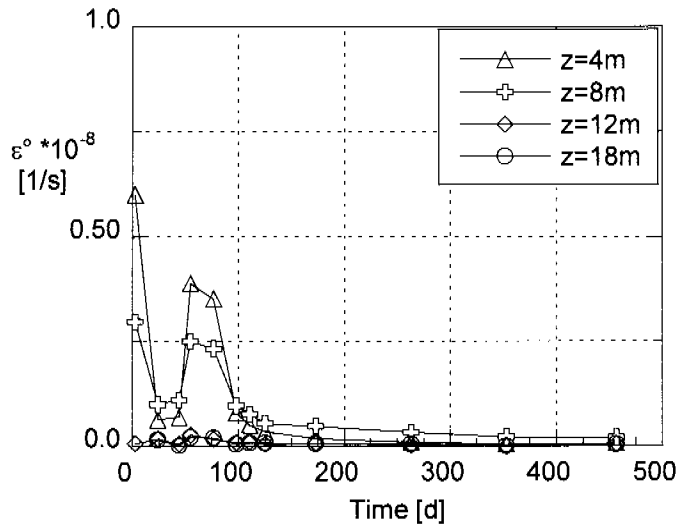


Figure 6-25: *In situ vertical strain rate under Birmensdorf test fill.*

The measured differential horizontal displacements, in direction A (Figure 6-20) perpendicular to the embankment site, at the inclinometer location, are displayed in Figure 6-26a. A change in displacement direction is detectable at 4m depth, indicating a local shear zone, which did not develop all along the eventual failure surface. The maximum integrated horizontal displacements amount to 30 mm at 4m depth.

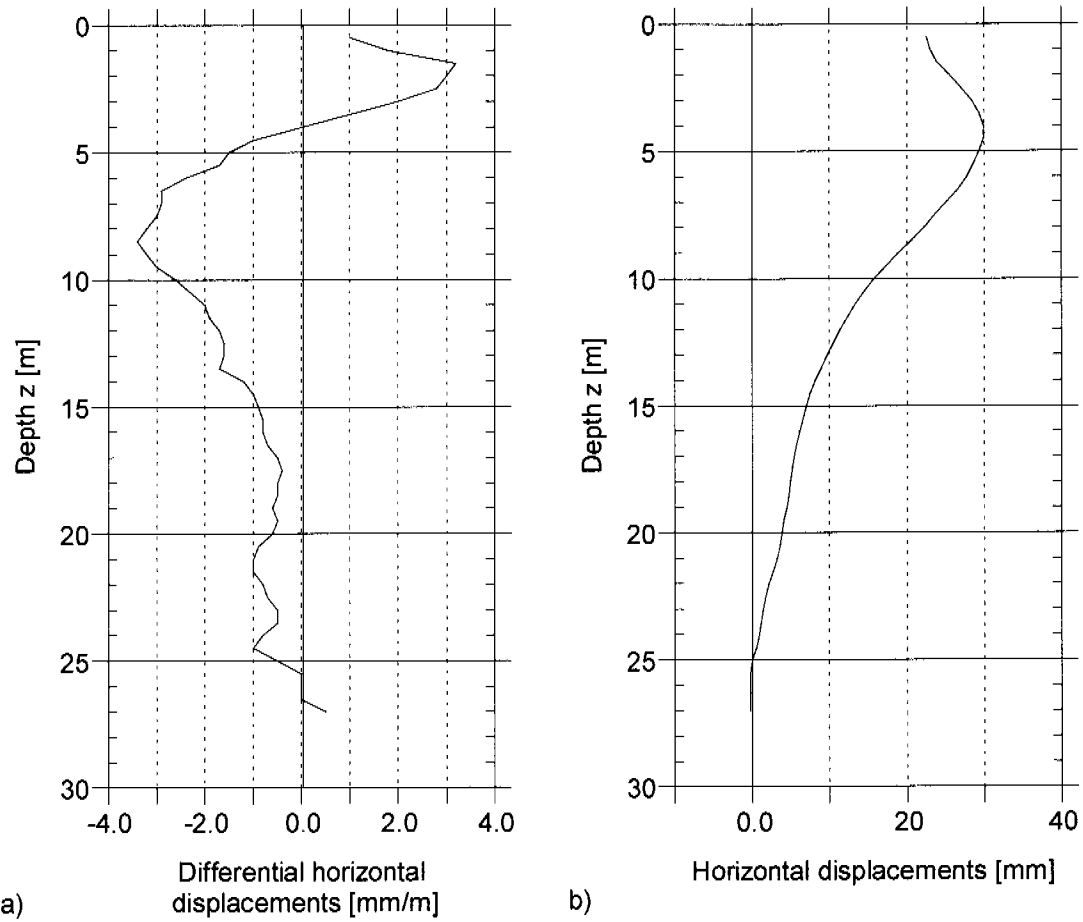


Figure 6-26: a) Measured differential horizontal displacements with depth and b) integrated horizontal displacements at the inclinometer location (Figure 6-20) by end of observation period.

Numerical Analysis

A simple numerical analysis has been carried out to model the behaviour under the test embankment with respect to the settlements, the horizontal displacements and the excess pore pressure development. The soil models used are the linear elastic -perfectly plastic Mohr Coulomb model for the embankment fill and the Modified Cam Clay (MCC) model for the clayey deposit. The analysis has been carried out using a β version of the FE program Plaxis, version 8.2 (Update pack 5), which contains the implementation of the MCC model. No updated manual was available for the β version, so that all references to the procedures of stress generation in advanced soil models are based on the manual PLAXIS 2D - Version 8. The analysis was carried out as a coupled consolidation analysis, where the loading sequence was modelled as shown Table 6-3. In this version of PLAXIS consolidation calculations have been extended to allow for staged construction in time.

The MCC idealises the soil as isotropic elasto-plastic, whereas the Seebodenlehm is thought to be an anisotropic material, with an inclined yield locus in p' - q space (Chapter 6.5). Ideally, it would have been better to have used an implementation of SCLAY1 to capture the anisotropy of the yield locus resulting from the past stress history of one dimensional consolidation. However this is not been possible since the planned implementation within Plaxis is not yet available. In summary, although the choice of the Modified Cam Clay model is not entirely satisfactory, the analysis has been carried out with this model to obtain first results and to investigate the choice of soil parameters from the laboratory and in situ tests carried out on the Birmensdorf Seebodenlehm. This analysis represents an advance on the other constitutive models available in Plaxis (e.g. linear elastic perfectly plastic, soft soil model) and a staging post towards the use of more appropriate anisotropic constitutive models.

Sharma (1994) investigated the behaviour of unreinforced and reinforced embankments on soft clay using the centrifuge modelling technique. The soft clay was modelled with one-dimensionally consolidated speswhite kaolin. The centrifuge model tests were then back-analysed at prototype scale. The clay foundation was divided into active, shear and passive zones on the basis of the anticipated direction of major principal stresses. An approximate modelling of anisotropy was achieved by specifying lower undrained shear strength in the direct shear and passive zones. In this way, good agreement was achieved between back-analyses and the measured values in the centrifuge model tests.

Figure 6-27 shows the geometry, the boundary conditions of the model and the mesh used to carry out the back-analysis of the embankment in Birmensdorf. The embankment has been modelled axi-symmetrically (i.e. as circular in plan) with corresponding radius at the crest of 9.9m and at the foot of 19.9m, with a boundary limit set at a radius of 40m from the centre of the embankment. The assumption of axi-symmetry provides a reliable estimation of settlements, as these are definitively spread axi-symmetrically around the centre of the embankment, whereas it does underestimate the failure load, particularly at the edges of the embankment, where 3D effects can increase the mobilised strength. As the aim of this simulation is the calculation of settlements only, the assumption is justifiable.

At the bottom boundary vertical and horizontal displacements are prevented, whereas at the vertical boundaries vertical displacements are allowed. Vertical and bottom boundaries are drainage boundaries, too, with $\Delta u=0$. The mesh was refined around the toe of the embankment using the "refine around point" tool of the PLAXIS program.

| Stage | | time [d] | accumulated time [d] | height of embankment [m] |
|-------|---------------|----------|----------------------|--------------------------|
| 1 | Load | 2 | 2 | 0.9 |
| 2 | Consolidation | 21 | 23 | 0.9 |
| 3 | Load | 2 | 25 | 2.5 |
| 4 | Consolidation | 18 | 43 | 2.5 |
| 5 | Load | 2 | 45 | 4.5 |
| 6 | Consolidation | 9 | 54 | 4.5 |
| 7 | Load | 2 | 57 | 6.3 |
| 8 | Consolidation | 400 | 456 | 6.3 |

Table 6-3: Stage data set

The analysis started with a sub-division into an upper and a lower clay layer. However further inspection revealed that this was unsatisfactory because the excess pore water pressure distribution was clearly affected by inhomogeneity in the sublayering.

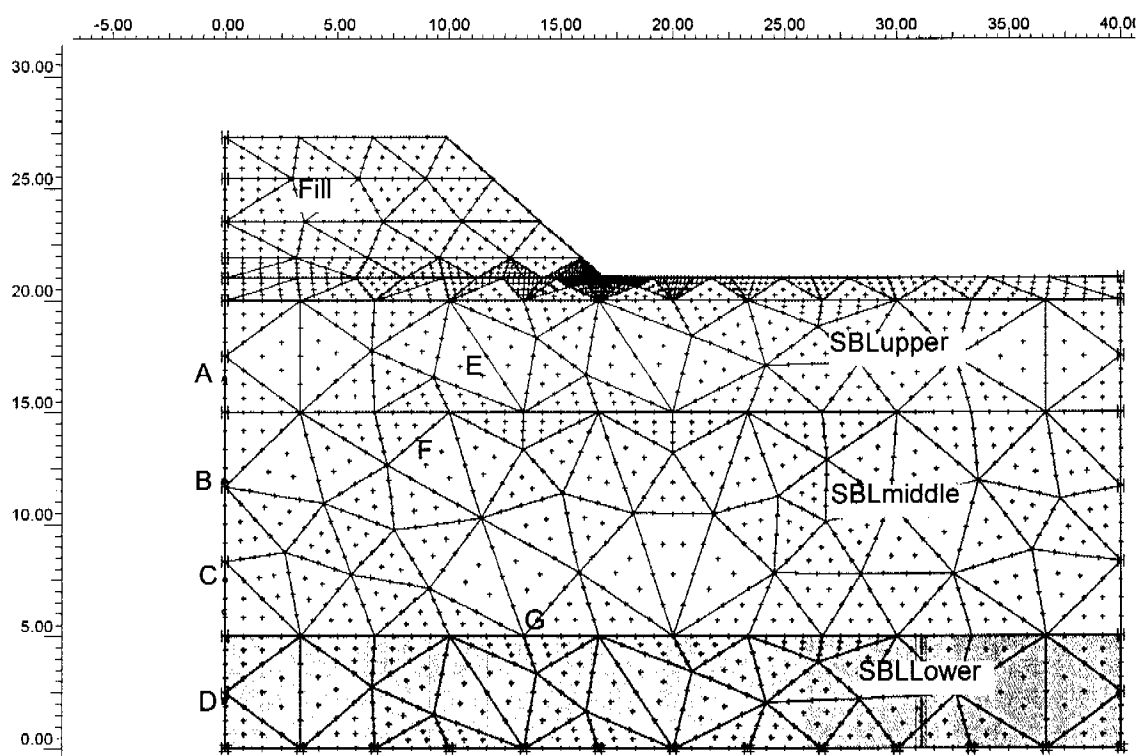


Figure 6-27: Geometry, boundary conditions and mesh of soil model used (scale in m).

Therefore the subdivision of the soil layer was changed as shown in Figure 6-27. The soil data sets of Table 6-4 correspond to this division. The drainage layer under the embankment was modelled for simplicity over the entire ground surface as an in situ soil layer.

It is worth noting that the stiffness parameters λ and κ are the same for the SBLupper layer and SBLlower layer and refer to the results of the TSPT test given in Table 5-9. The SBLmiddle layer corresponds to a softer layer and λ and κ are increased accordingly. The initial void ratio e_{init} , the critical state parameter M and the specific weights in saturated and unsaturated state γ_{sat} and γ_{unsat} are the same for all three layers and correspond to the results of the laboratory tests. The permeability in vertical and horizontal direction k_y and k_x indicate a difference in hydraulic anisotropy between the three layers: SBLupper has a ratio $(k_x/k_y)= 9.6$, SBLmiddle (k_x/k_y) of 50 and SBLlower $(k_x/k_y)= 100$. Preliminary calculations with lower values of k_x/k_y showed that the simulation was not able to match the reduction of the excess pore pressure with time measured in situ. Therefore these values were chosen for the model. The comparison of the horizontal permeability obtained from the CPTU to the the vertical permeability from the CRS tests shows that a ratio (k_x/k_y) up to 90 is possible for the Seebodenlehm.

It is essential in a numerical analysis to set up the in situ stresses and this is dependent on the past stress history and in particular on the maximum vertical stress ever supported by the soil layer, that is, the preconsolidation pressure. In PLAXIS it is possible to specify the initial stress state using the Pre-Overburden Pressure (POP) as an alternative to prescribing the overconsolidation ratio. The POP is defined as the difference between the vertical preconsolidation pressure σ'_{vy} and the overburden stress σ'_{v0} . With the use of the Pre-Overburden Pressure, the overconsolidation ratio OCR, defined as:

$$OCR = \frac{\sigma'_{vy}}{\sigma'_{v0}} \quad [6-17]$$

is not constant over the depth of a soil layer.

PLAXIS needs an equivalent isotropic preconsolidation stress p'_y to determine the initial position and size of a cap-type yield surface. The preconsolidation stress σ'_{vy} is used to compute p'_y on the basis of the effective stress state:

$$\sigma'_1 = \sigma'_{vy} \text{ and } \sigma'_2 = \sigma'_3 = (K_0^{NC} \cdot \sigma'_1) \quad [6-18]$$

where K_0^{NC} is the K_0 value associated with normally consolidated states of stress ($K_0^{NC}=1-\sin\phi'$).

| | | upper SBL | middle SBL | lower SBL | fill material | | |
|-------------------------|-------------------|---------------------|---------------------|---------------------|-------------------------|-------------------|-------|
| γ_{unsat} | kN/m ³ | 18.0 | 18.0 | 18.0 | γ_{unsat} | kN/m ³ | 23 |
| γ_{sat} | kN/m ³ | 18.5 | 18.5 | 18.5 | γ_{sat} | kN/m ³ | 25 |
| k_x | m/day | $8.6 \cdot 10^{-4}$ | $4.3 \cdot 10^{-4}$ | $8.6 \cdot 10^{-4}$ | k_x | m/day | 2 |
| k_y | m/day | $9 \cdot 10^{-5}$ | $8.6 \cdot 10^{-6}$ | $8.6 \cdot 10^{-6}$ | k_y | m/day | 2 |
| λ | - | 0.12 | 0.2 | 0.12 | c_{ref} | - | 1 |
| κ | - | 0.04 | 0.06 | 0.04 | E_{ref} | kN/m ² | 50000 |
| v' | - | 0.15 | 0.15 | 0.15 | v' | - | 0.35 |
| e_{init} | - | 1.8 | 1.8 | 1.8 | ϕ' | ° | 35 |
| M | - | 1.02 | 1.02 | 1.02 | | | |
| POP | kPa | 70 | 40 | 80 | | | |

Table 6-4: Soil data set

There are oedometer test data for Birmensdorf clay (Section 5.2.3) which indicate essentially that the Seebodenlehm deposit is normally consolidated. As already stated in Section 5.2.3, the soil samples have probably suffered disturbance due to sampling, storage and preparation prior to testing. Disturbance mostly results in a shrinkage of the yield surface and therefore in lower yield stress. Inspection of data for an initial scoping analysis, in which the soil was assumed to be entirely normally consolidated, indicated that the predicted vertical displacements were 3 times the measured values. Perhaps this zone was affected by the advances and retreats of the glacier during the end stage of the Würm ice age. The end moraines present in the Birmensdorf region (Figure 3-8) give evidence of the activity of the glacier. It was therefore assumed that the Birmensdorf Seebodenlehm is lightly overconsolidated in the layers SBLmiddle and SBLlower with maximum values of 1.5. The layer SBLupper will be affected with higher overconsolidation ratios to take into account the crust effect due to local changes in the ground water level. The preconsolidation was therefore chosen in the SBLlower layer to be POP=80 kPa, followed by the crust layer SBLupper (POP=70 kPa). These assumptions can be explained as follows:

- It is clear that the SBLlower is slightly older and may have been overrun by a glacier snout after its deposition and during the advances and retreats of the final stages of the Würm glaciation. SBLmiddle and SBLupper have been deposited during subsequent retreats of the glacier.
- Groundwater fluctuations or another overrun of a glacier snout can have produced a light overconsolidation SBLmiddle and higher overconsolidation of SBLupper. As SBLupper shows a higher permeability than SBLmiddle, this layer probably consolidated faster under the load and has therefore a higher preconsolidation pressure.

The value of the POP in the soft layer SBLmiddle is 40 kPa. This assumptions of the POP values lead to a distribution of the overconsolidation ratio as shown in Figure 6-28. The OCR values are highest in the layer SBLupper (up to 4.0 at the surface), gradually decreasing in SBLmiddle to OCR=1.26 to grow again up to OCR=1.5 in SBLlower. The OCR in Figure 6-28 have been calculated on the basis of the POP values and of the actual vertical overburden pressure (Equation 6-17).

In the overconsolidated stress range, the earth pressure coefficient at rest K_0^{OC} is larger than in the normally consolidated region. When generating the initial stresses, Plaxis calculates K_0^{OC} as follows (Plaxis Manual):

$$K_0^{OC} = \frac{\sigma'_{h0}}{\sigma'_{v0}} = K_0^{NC} \cdot OCR - \frac{\nu_{ur}}{1 - \nu_{ur}} \cdot (OCR - 1) \quad [6-19]$$

The K_0^{OC} values (Figure 6-28b) have also been calculated manually with Equation 6-19. Comparison with the ratio of horizontal to vertical effective stresses generated by PLAXIS in the initial phase, showed a satisfactory agreement, with a difference of 0.2 over the entire depth. With a value of $K_0^{NC}=0.561$ and a Poisson's ratio $\nu_{ur}=0.15$, the K_0^{OC} value calculated with Equation 6-19 will range from 0.7 to >1 (1.9). The principal direction of effective stresses is plotted in Figure 6-30 and corresponds to K_0^{OC} values >1 in the SBLupper layer. The results of the analysis are shown in Figures 6-28 to 6-36.

Figure 6-29 shows the values of the overconsolidation ratio after the observation period of ca. 400 days. It can be seen that the clay directly beneath the embankment is normally consolidated in the layer SBLupper and SBLmiddle. In the layer SBLlower, the soil shows OCR < 1.1 under the middle of the embankment. The zone farthest from the embankment shows OCR up to 1.4. The principal direction of effective stresses before loading and after the observation period is shown in Figures 6-30 and 6-31. The embankment loading causes the effective principal stresses to rotate from horizontal to vertical under the embankment with a transition zone under the shoulder to remaining horizontal in the far zone. The fact that the principal direction changes back to vertical next to the vertical boundary, indicates an interference of the boundary.

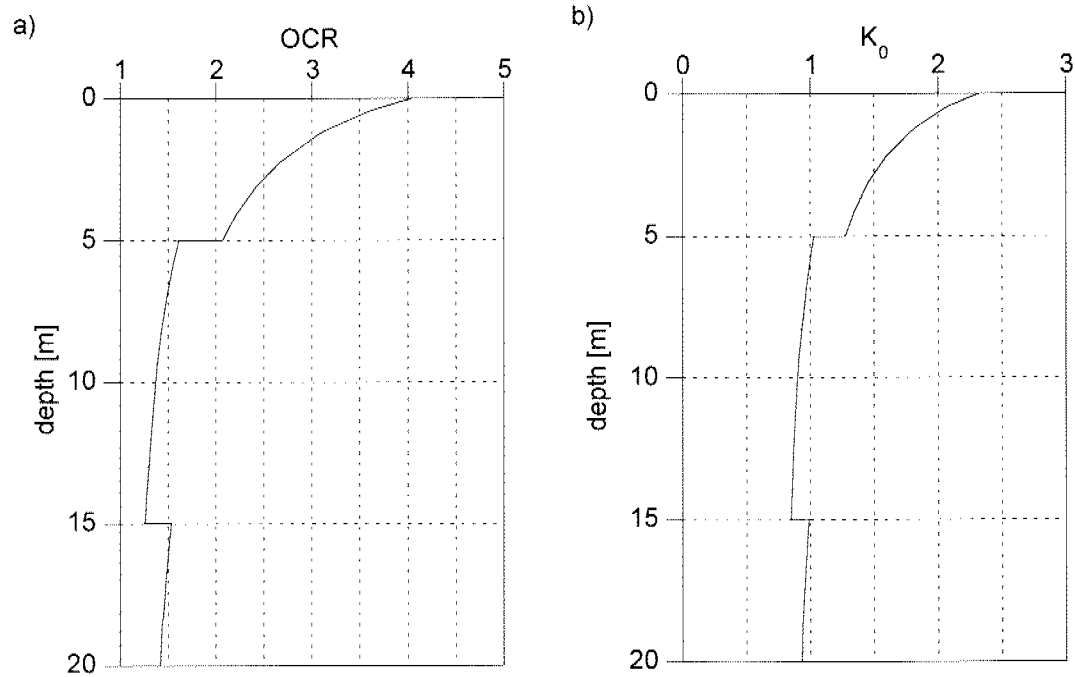


Figure 6-28: a) OCR values before loading, calculated on the basis of the POP values of Table 6-4 and the PLAXIS generated in situ stresses; b) Earth pressure coefficient at rest calculated with Equation 6-19.

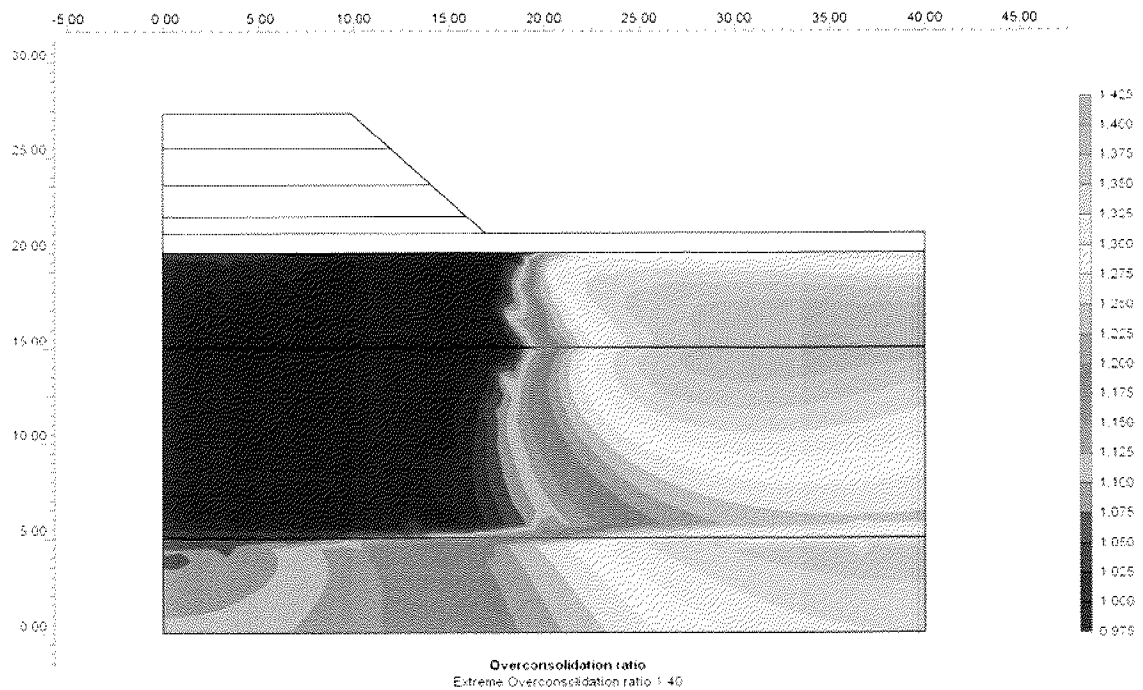


Figure 6-29: OCR values calculated at the end of the consolidation period (Scale from 1.0 to 1.425) and calculated as defined by Equation 6-17: $OCR = \frac{\sigma'_{vy}}{\sigma'_{v0}}$

The horizontal displacements at the end of the observation period are lower than anticipated with maximum values of 6 cm (Figure 6-32). As expected, the greatest lateral displacements occur under the embankment toe. The analysis

showed that without this layer, a local failure would have developed at the toe of the embankment. The distribution of horizontal displacements with depth at this stage at the inclinometer location (Figure 6-33) can be compared with the measured displacements (Figure 6-26b). The measured horizontal displacements reached 3 cm at ca. 4m depth, whereas the back-analysis shows 2 cm displacement at 5m depth. The inclinometer reached 28m depth and showed 5 cm displacement at 20m depth. The bottom boundary (with no displacement) was set in the model at a depth of 20m. Taking this difference into account, the agreement between the distribution of horizontal displacement with depth at this location and at this stage is satisfactory.

The points A, B, C and D in Figures 6-34 and 6-35 represent points under the middle of the embankment at the depth where the pore water pressures were measured (4m, 8m, 12m and 18m below ground surface, Figure 6-27). Figure 6-34 shows a total displacement at the end of the observation period of 20 cm at a depth of 4m. Surface settlements of 30cm were measured in situ. Figure 6-35 can be compared with the plot of excess pore pressure in Figure 6-21. There is a satisfactory agreement again between the measured and the back-analysed values. Particularly, point B at 8 m depth in the softer layer SBLmiddle, shows the highest Δu , which reaches almost the measured value. The reduction of excess pore pressure with time at points B and C are far slower than in point A, as was also observed from the measured values. This indicates that the choice of the anisotropic values for the permeability tends in the right direction. Point A shows high excess pore pressure when compared with the measured values.

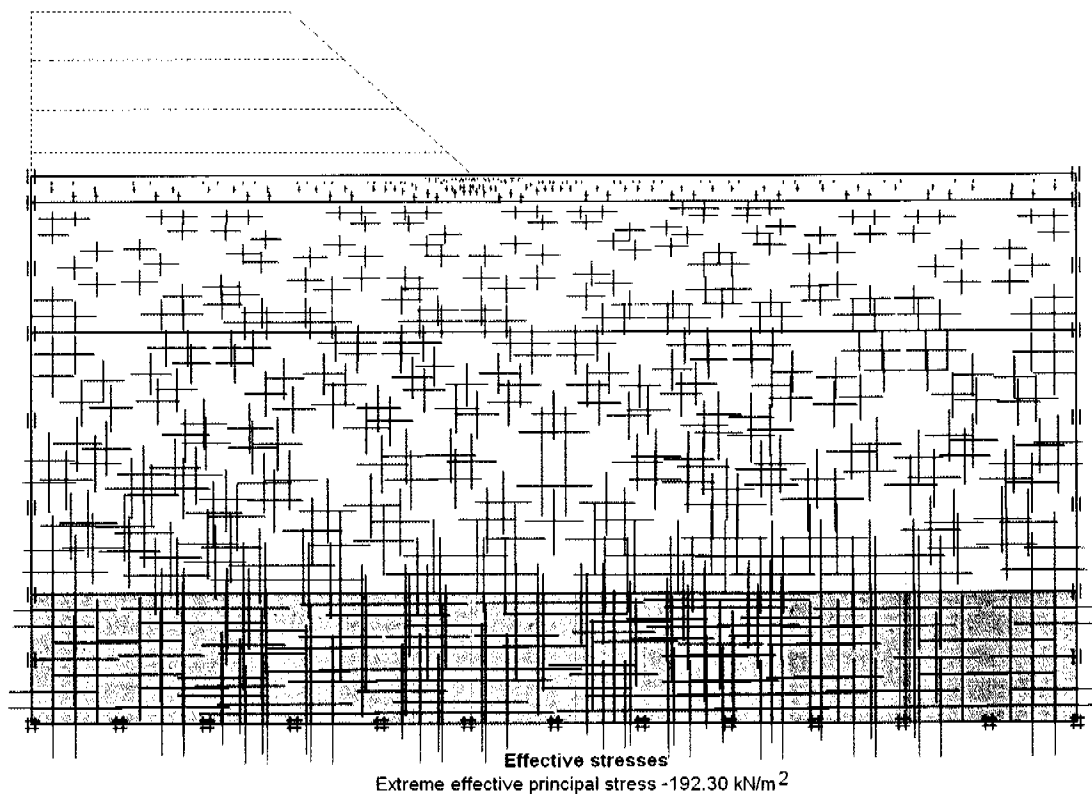


Figure 6-30: *Principal direction of effective stresses before loading.*

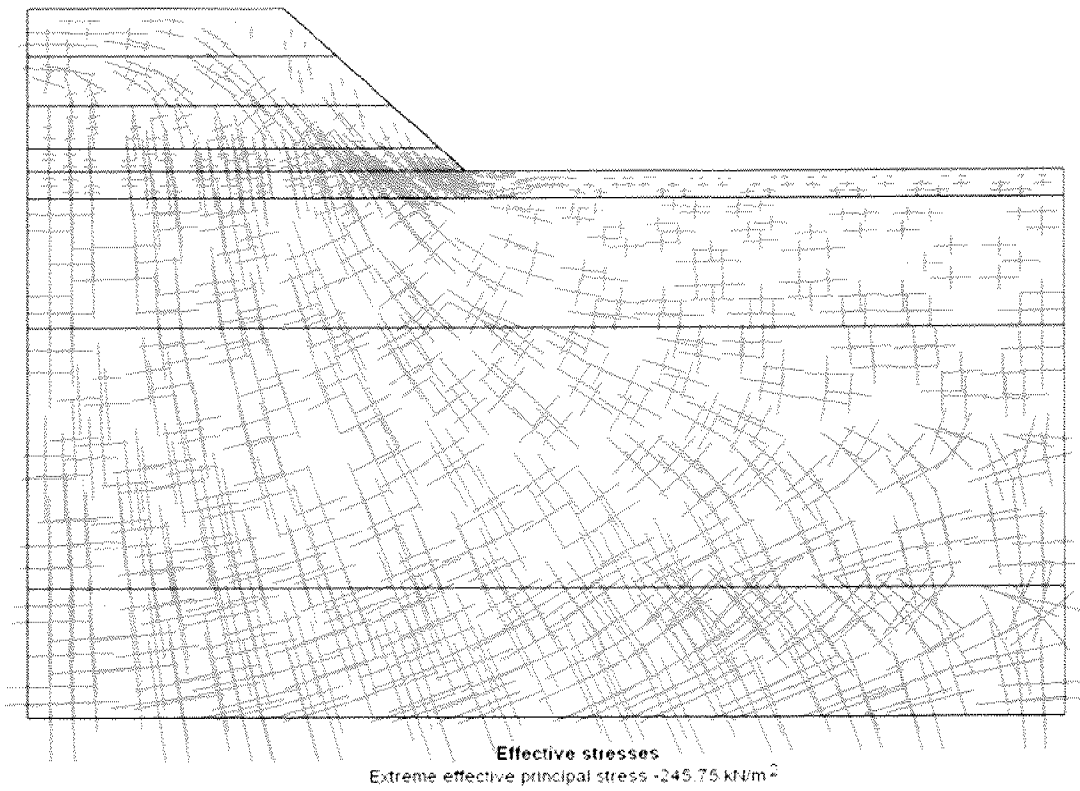


Figure 6-31: *Principal direction of effective stresses at the end of the observation period.*

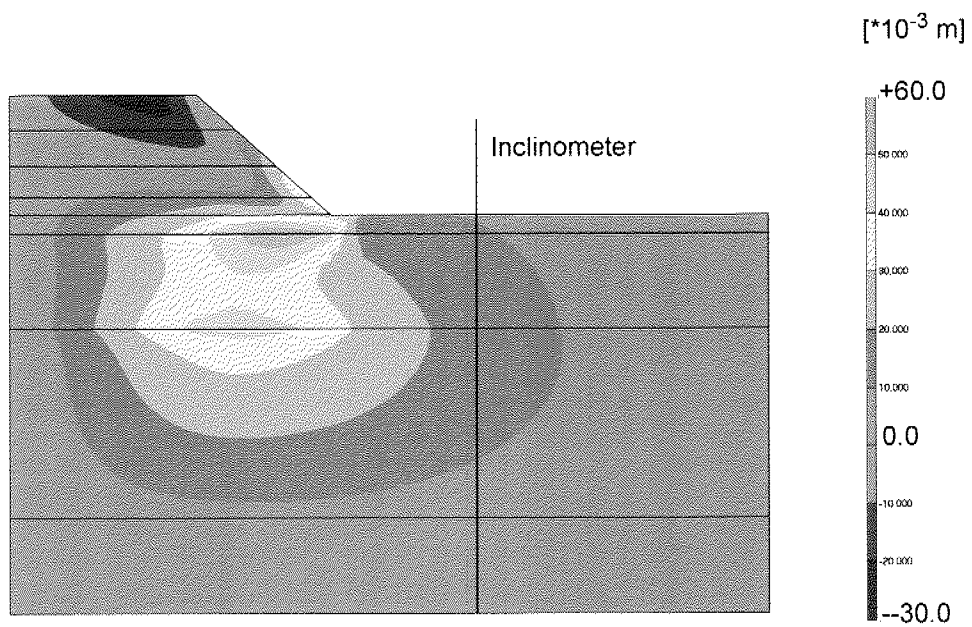


Figure 6-32: *Horizontal displacements at the end of the observation period.*

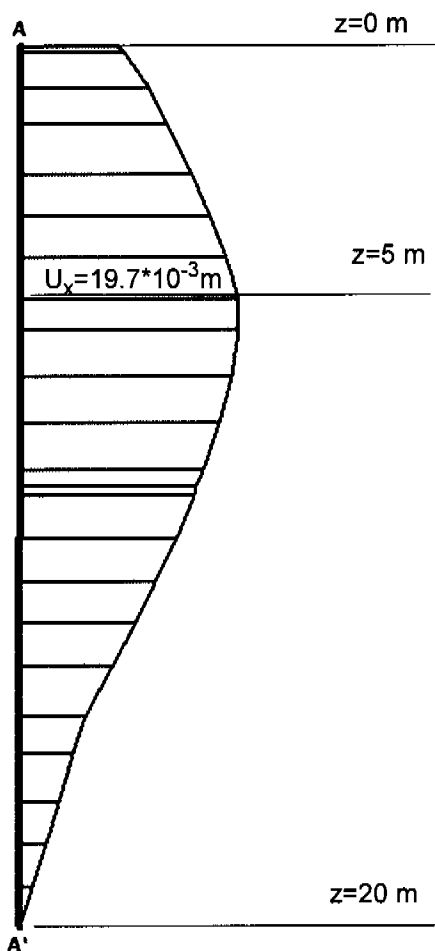


Figure 6-33: Horizontal displacements at inclinometer location A in m.

It was already pointed out, however, that the soil shows a lower compressibility at 4m depth than in adjacent layers at 3 and 5m depth, indicating the presence of a local stiffer layer. This layer has probably also influenced the development of excess pore pressure, with local higher horizontal permeability. The difference between the back-analysed and measured values is therefore due to a local inhomogeneity, which was not modelled in the numerical analyses. The values of Δu at 18m depth (point D Figure 6-35) for the last loading stage (nr. 7) are almost equal to the measured values. The reduction of Δu at this depth in the numerical model is too fast, indicating probably that the assumed ratio of k_x to k_y was too high.

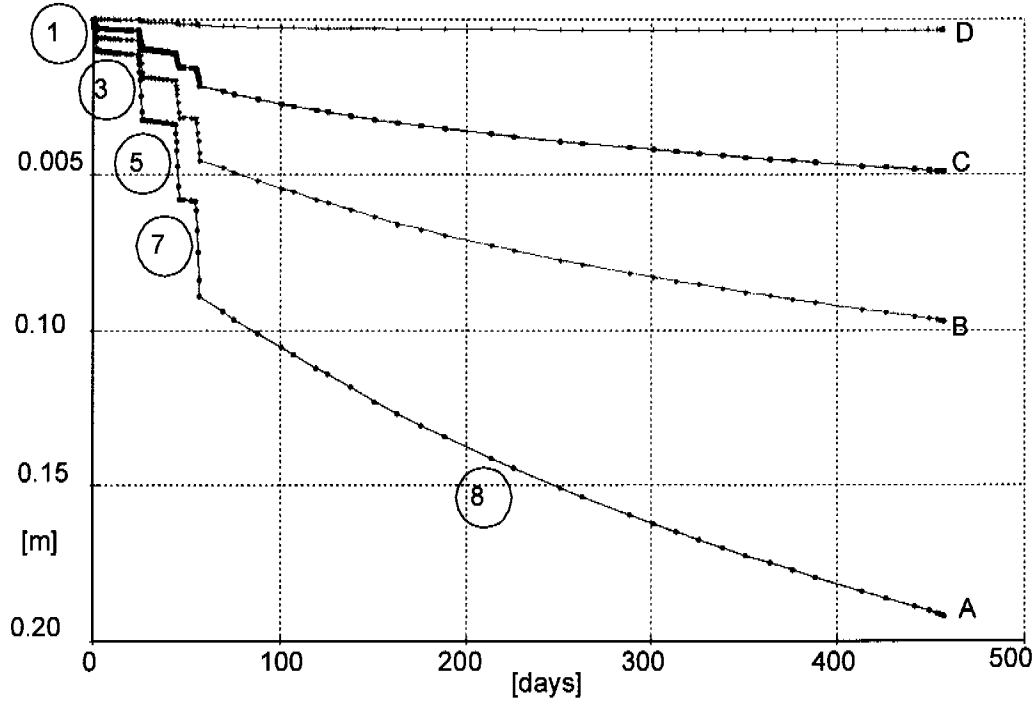


Figure 6-34: Evolution of cumulative settlements with time under the centre of the embankments at points A, B, C and D (respectively 4, 8, 12 and 18m depth) (the load phase number is encircled).

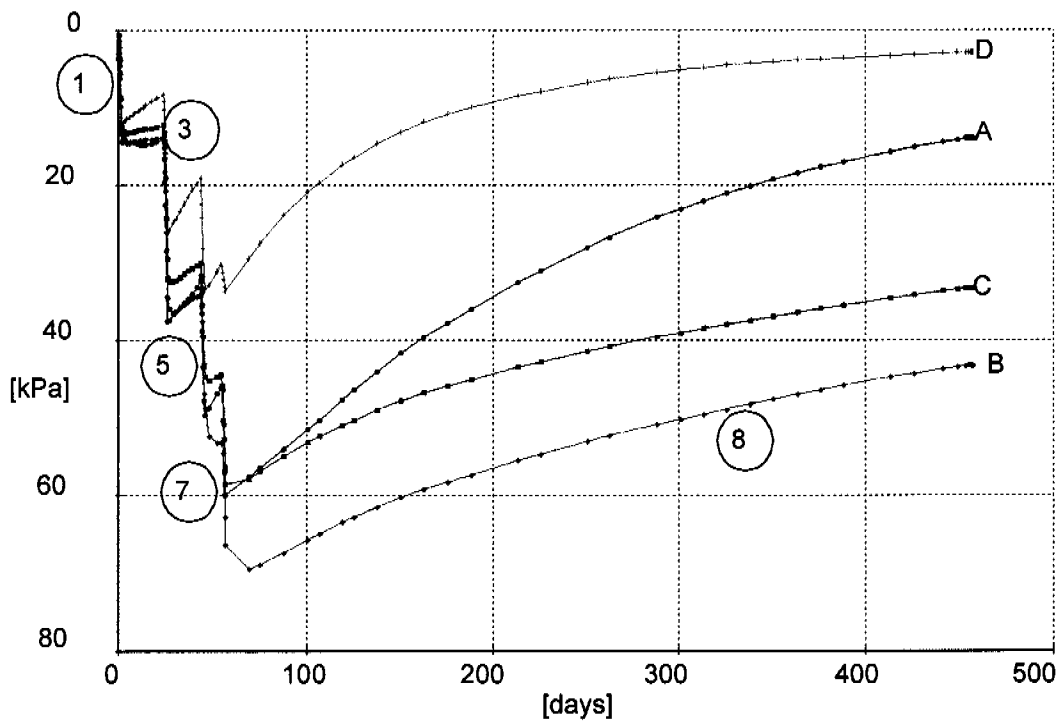


Figure 6-35: Evolution of excess pore pressures with time under the centre of the embankments at points A, B, C and D (respectively 4, 8, 12 and 18m depth) (the load phase number is encircled).

It is also interesting to follow the evolution of “cap” points (denoting reaching the yield locus) in the Seebodenlehm layers SBLupper, middle and lower (Figure 6-36). A cap point occurs if the Hardening Soil model or the Soft Soil model are used and the stress state in a point is equivalent to the preconsolidation stress, i.e. the maximum stress level that has previously been reached ($OCR = 1.0$) (PLAXIS manual). Accordingly, for the MCC model a “cap” point is reached when the isotropic preconsolidation stress p'_y is reached. No “cap” point develops in SBL layers until loading stage 5, at which the vertical total stress at the surface reaches 103 kPa. The zone of plastic points enlarges with load stage 7 ($\sigma'_v = 145$ kPa). It is visible that between stage 7 and 8, the consolidation process leads to a further enlargement of the plastic zone, due to the reduction of excess pore pressure and the consequent increase of effective stresses. The zone of plastic points corresponds to the zone with $OCR=1$ in stage 8 (Figure 6-29).

The increase of effective stresses during consolidation in stage 6 (Figure 6-36b) did not enlarge the number of plastic points reached. A redistribution of stresses is probably responsible for the stress states falling back inside the yield surface.

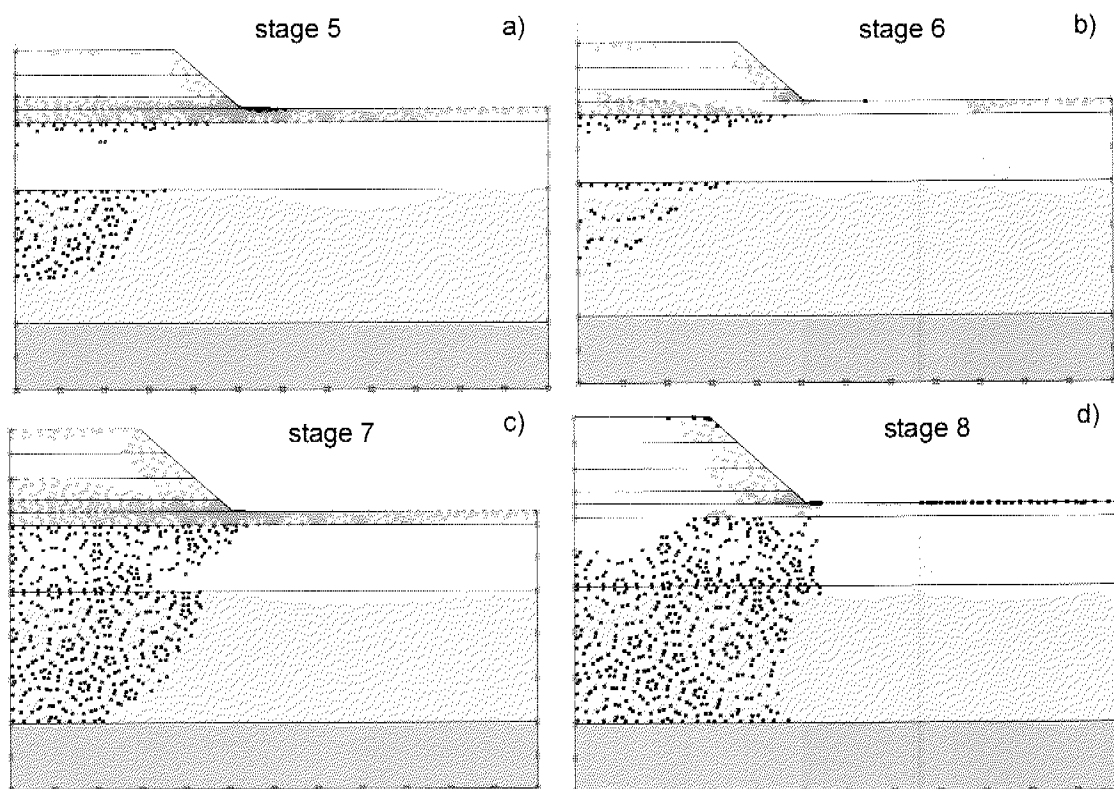


Figure 6-36: Plastic points in the Seebodenlehm deposit at the end of load stage 5 and 7 and at the end of the consolidation phases 6 and 8; a) phase 5; b) phase 6; c) phase 7; d) phase 8 (blue: “cap” points; red: Mohr Coulomb points).

The stress paths followed by the points E, F and G (Figure 6-27) are shown in Figure 6-37. The deviator stress is defined in PLAXIS as :

$$q = |\sigma'_1 - \sigma'_3| \quad [6-20]$$

The stress path followed by point E shows a reduction of q until the moment when the vertical stress becomes greater than the horizontal stress (i.e. $K_0^{OC} < 1$), because loading causes an increase of vertical stress. For point F and G, q increases steadily, as the value of K_0^{OC} was < 1 from the initial phase. For loading inside the yield locus ($OCR > 1$), the stress path is vertical, whereas it shows the typical pattern of an undrained compression test when the yield point has been reached (Point F, Figure 6-37, $OCR = 1$). During consolidation, the mean effective stress p' increases due to the decrease of Δu . At the same time also a small change in q is visible (net increase in q for points E and G, decrease in point F), probably due to a redistribution of stresses. This is enough for the stress states to fall back inside the newly developed yield surfaces.

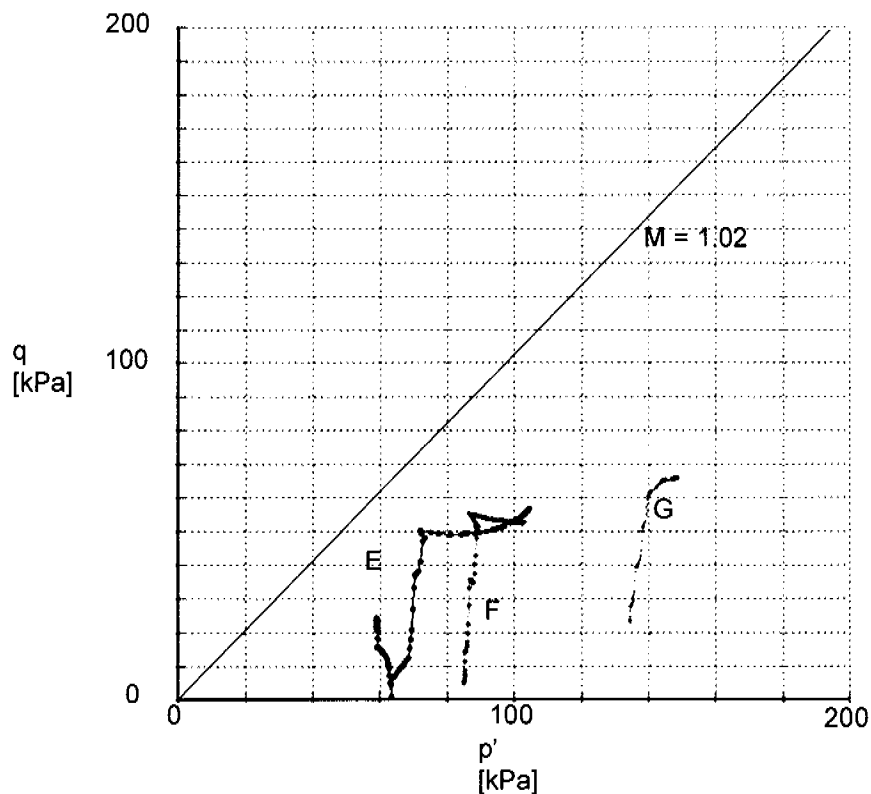


Figure 6-37: Stress paths followed by points E, F, and G.

Summary and conclusions

7.1 Summary

The stress-strain, strength and permeability properties of Swiss post-glacial lacustrine clays have been investigated using various in situ and laboratory tests. These deposits of soft varved lacustrine clays stretch along the highly populated Swiss Mittelland from the SW to the NE of the country. Sites in Kreuzlingen (on the shore of Lake Constance) and Birmensdorf (near Zürich) have been investigated, where extensive and complicated construction activity needed an improved site characterisation.

The mineralogical composition, the state and structure as well as the index properties of the soft varved clays from both sites have been characterised and discussed. The clay fraction ($< 2\mu\text{m}$) amounts to 40% for both sources in the bulk soil, but varies from 25% to 40% in separate silt and clay varves. The Birmensdorf clay shows a finer grain size distribution with a dominant particle size of $1\mu\text{m}$, a higher clay mineral content, higher plasticity index I_P (40%) and natural water content (42%). However the consistency in situ is less stiff for the Kreuzlingen clay, with a marginally higher liquidity index I_L . Both clays have a high carbonate content ($> 30\%$), but relatively low sensitivity S_t measured with the fall cone tests (4.0 for Kreuzlingen clay and 3.0 for Birmensdorf clay). Birmensdorf clay has a distinct macro-fabric with alternating silt and clay layers, whereas Kreuzlingen is more homogeneous, rather showing a coloured layering. The influence of the varving depends upon scale factors, which makes the laboratory testing of these soils and the subsequent interpretation of the tests results challenging.

The influence of structure and of soil sample preparation on the properties of the varved clays has been investigated by comparing the composition and the mechanical behaviour in triaxial and oedometer tests of the natural Kreuzlingen clay to those of the reconstituted Kreuzlingen clay. Thin tube samplers with inner clearance were used for the extraction of the natural samples and the specimens were prepared through wire cutting. To erase the structure and stress history of the clay, some samples of the natural soil were reconstituted at a liquidity index I_L of 3.0 and reconsolidated in a 40 cm diameter oedometer. The reconstituted

clay was very homogeneous and had equivalent index properties to the natural Kreuzlingen clay, but a lower sensitivity (2.1) and lower undrained shear strength, as expected from the effects of reconstitution and lack of aging.

The *adaptation of the prototype triaxial apparatus* for snow and frozen soils for use as a common soil stress path testing apparatus required several test runs for equipment development and calibration. A bender element testing device was added to the apparatus in the form of a top and bottom cap to the specimen. The testing methods, including sample preparation, testing programme adaptations and interpretation procedures, were developed over a period of about 1 year.

The *undrained shear strength* s_u of these Swiss soft clays have been investigated in situ using a piezocone (CPTU) and in the laboratory using standard and more advanced stress path triaxial tests, which also leads to determination of the angle of shearing resistance ϕ' . The CPTU constitutes a high-quality in situ test, which is often cheaper than drilling and sampling and its results offer the interpretation of various soil parameters. A linear equation relating the variation of s_u with effective vertical stress σ'_{v0} was determined for both the Kreuzlingen and Birmensdorf clay, based on correlation of CPTU results to borehole and field vane tests as well as to triaxial compression and extension tests. It was shown that these correlations represent a lower bound and a safe assumption for design, providing a reasonable fit to the triaxial test results for overburden stresses up to a depth of 30m.

The *angle of shearing resistance* ϕ' obtained from the triaxial tests varies between 24° and 27° for Kreuzlingen clay, and is 26° for a homogeneous Birmensdorf clay specimen, with more extreme variations for more varved specimens ($\pm 4^\circ$).

The *compressibility and the permeability* of Kreuzlingen and Birmensdorf clays has been investigated using continuous loading oedometer tests, where the vertical load is gradually increased with a low strain rate and the resulting pore pressure is measured at the base of the cell. No satisfactory correlation could be found between the compressibility and the plasticity of these soils. For these varved clays, it is difficult to define the plasticity index as a soil constant. Instead, the plasticity index should be determined for every soil specimen, whose dimensions should be chosen according to thickness and spacing between the varves present in the soil. Kreuzlingen clay exhibits a vertical permeability k varying from $1 \cdot 10^{-9}$ m/s to $4 \cdot 10^{-11}$ m/s for mean effective vertical stresses σ'_m between 10 and 1000 kPa, and coefficient of compression C_c of c. 0.25. The vertical permeability k of the Birmensdorf clay lies between $1 \cdot 10^{-9}$ and $8 \cdot 10^{-11}$ m/s for vertical effective stresses between 10 and 1000 kPa, the coefficient of compression C_c of Birmensdorf clay shows a higher scatter in the results, largely because of greater heterogeneity of the natural samples, varying from 0.25 to 0.35.

The *influence of loading rate* has been investigated by varying the strain rate in the continuous loading oedometer tests. The mean effective stress σ'_m to normalised void ratio e/e_0 curves obtained at different strain rates for both clays are more or less superimposed on each other and accurate determination of the relevant in situ vertical yield stress is difficult. Separating strain rate influence from natural variability of the samples is also challenging. The difference in strain rate

between CG and CRS tests are high enough to permit a statement to be made about the strain rate influence for Seebodenlehm: it appears that the strain rate effect is relatively smaller for Seebodenlehm when compared with many other Canadian or Finnish soft clays. Based on the results obtained, it can be argued that the strain rate dependence of Seebodenlehm cannot be investigated with tests on different natural samples, because the influence of natural variability is high. Strain rate stepping tests on the same specimen would be an improvement for the comparison of the effects of rate on compressibility. In addition, the strain rates should be varied over at least 2 or 3 orders of magnitude. These test specifications should be taken into account for future research.

A *stratigraphic profile* of the key soil layers, as well as *small strain estimates of the elastic parameters*, were obtained from a parallel seismic surface-to-borehole transmission experiment in Kreuzlingen (Maurer et al., 1998). The results from seismic measurements (dynamic moduli) are representative for large sub-surface volumes and can provide average small-strain stiffness values of these deposits. The initial or maximum shear modulus of a soil G_{\max} is an important parameter for a variety of geotechnical design applications. Body waves can also be produced (similar to those generated during a seismic measurement) by a trigger during a triaxial test and sent top to bottom through the specimen using piezoceramic bender elements. This test has been performed in the triaxial stress path tests to measure the travel time of the seismic waves and consequently to measure the small-strain stiffness G_{\max} . The triaxial testing of undisturbed borehole samples allows determination of the static shear modulus as well, but the results suffer from some inaccuracies in the small-strain domain. The accuracy of measurement of the static small-strain stiffness can be improved by using axially mounted local displacement transducers, which avoid end of sample bedding effects. The correlation between these two different measurements of the small-strain stiffness G_{\max} shows that the values of G_{\max} measured with the bender elements are not influenced by the general strain level in the specimen, but only by the stress state during the test. The Kondner hyperbola, used to model the static shear stiffness-shear strain behaviour during a triaxial shear test, describes the modulus reduction curve satisfactorily and shows that the non-linear stiffness-strain behaviour is similar for the two clays considered. The static stiffness measurement gives an estimate of the modulus reduction curve, which tends asymptotically to the maximum shear stiffness measured in situ. The dynamic shear stiffness measured during the triaxial tests is lower than the value measured with the seismic test in situ and the magnitude of this difference varies from test to test.

One of the main goals of the triaxial investigation was *the determination of the yield surfaces* for the clays investigated and investigation into applicability of an anisotropic elasto-plastic model with rotational hardening (SCLAY1) for Swiss soft clays. The investigation of yield during triaxial drained loading on different stress paths η , in deviatoric q and mean effective p' stress, was carried out on the basis of different strain and stiffness variables, to deliver a more sensitive indication of the occurrence of yield. The investigation indicates a good agreement between the yield curves defined by SCLAY1 and the yield points indicated by the triaxial tests, based on both stress paths with a significant difference in the η values and stress paths with a smaller difference in inclination. It can be said that SCLAY1 appears to be consistent with the test results, but there are insuffi-

cient data at the present time to prove conclusively that the model is working for these soils. SCLAY1 is based on one set of Critical State parameters representing a relatively homogeneous deposit, subjected to anisotropic deposition and subsequent loading. However the Critical State parameters of Seebodenlehm are dependent upon the varving. This makes it difficult to choose the right parameter for simulation of Seebodenlehm for this model. The varving probably limits the rotational hardening expected by SCLAY1 and therefore more data are needed to prove the consistency of the model with test results on Seebodenlehm. The tests on Swiss varved clay confirmed that the first loading path has to be continued much further in extension than in compression to rotate the yield surface completely to the new inclination. It was observed that the total strain vectors of similar tests (with the same stress path history η_1 and η_2) on different specimens are parallel, and that the total strain vectors seem to have the same inclination as the approaching stress path.

A simple numerical analysis has been carried out to model the behaviour under a test embankment in Birmensdorf. The analysis has been carried out with the Modified Cam Clay model to obtain first results and to investigate the choice of soil parameters from the laboratory and in situ tests carried out on the Birmensdorf Seebodenlehm, although this choice is not entirely satisfactory. This analysis represents an advance on the other constitutive models available in Plaxis (e.g. linear elastic perfectly plastic, softening soil model) and a staging post towards the use of more appropriate anisotropic constitutive models (e.g. SCLAY1).

7.2 Conclusions

The strength and permeability properties of the Swiss lacustrine clays from Kreuzlingen and Birmensdorf were estimated satisfactorily. However, some difficulties have been encountered during the evaluation due to the range of results obtained. This was due primarily to the variability of the natural specimens, which was more pronounced in samples from Birmensdorf.

The deposition modus was characterized in Birmensdorf by active water conditions and lakebed instabilities, whereas smaller variations in the water conditions dictated the deposition of the Seebodenlehm in Kreuzlingen. This was due to some extent to the different geomorphological situations and to the distance to the glacier front in Kreuzlingen (open, far) and Birmensdorf (valley, near). Birmensdorf Seebodenlehm shows a more pronounced macro-fabric with alternating silt and clay layers, whereas Kreuzlingen is more homogeneous. It has been shown that the thickness of, and distance between, the varves influence the shear strength obtained in triaxial tests, where the extent of the varving is important in terms of the dimensions and orientation of the specimen. This influence was consequently more pronounced in Birmensdorf Seebodenlehm, where the angle of shearing resistance ϕ' obtained from the triaxial tests showed variations of $\pm 4^\circ$.

Because the Birmensdorf clay had a higher content of swellable clay minerals than the Kreuzlingen Seebodenlehm, a lower friction angle could be expected. However the Birmensdorf Seebodenlehm showed a slightly higher angle of shearing resistance ϕ' . The explanation lies in the bedding formation and microstructure of the clay, in terms of the sample size, shape and orientation of layers, which affects the values of deviator stress mobilised throughout a triaxial stress path test, and from which a friction angle maybe deduced. The varving pattern can lead to an averaging of the mobilised shear properties if it lies mainly perpendicular to the major principal stress direction in the triaxial tests, whereas it can lead to a dramatic drop in shear strength in the case of inclined layers. Therefore it is not valid to define a failure parameter on the base of failure points of several tests for a varved or layered soft clay, when the structure of the material has such an influence on the test results. Before carrying out laboratory tests, it is important to define which is the appropriate test for the expected field case stress test path. For future research it is important to test natural Seebodenlehm samples in the ringshear apparatus to measure the shear resistance parallel to the varving.

The influence of structure was investigated by comparing the composition and the mechanical behaviour of the natural Kreuzlingen clay to those of the reconstituted Kreuzlingen clay. The test results indicated that the reconstitution process had no influence on the shear strength, the permeability and the compressibility characteristics as well as on the yielding of the young, reconstituted material, which were comparable to those of the aged natural clay. The low sensitivity of this clay had indicated a lack of cementation and structure. However a more pronounced difference between natural and reconstituted material can be expected for Birmensdorf Seebodenlehm, where the varving pattern is more pronounced.

The sensitivity is a good indicator of cementation and structure, and although the Swiss Seebodenlehm has a carbonate content of more than 30%, the sensitivity S_t measured with the fall cone tests is very low compared with the values of other clays. The high carbonate content of Seebodenlehm does not cause a regular "open" structure, but results in the formation of distinct clumps. The clumps influence the behaviour of the Seebodenlehm, which acts despite the high carbonate content as an uncemented soil with low sensitivity. It can therefore be stated that the strain rate effect is relatively smaller for Seebodenlehm than for many other soft clays. This is confirmed by the CG tests and correlates with the recent work on the consolidation behaviour of non-cemented soils, which shows that these soils may have a much weaker rate dependence than that observed in intact, cemented clay of eastern Canada and Scandinavia (Sheahan and Wetters (1997)).

For design calculations, although the dimensions of the object are orders of magnitude greater than the varves in the clay layer, the strength parameters have to be chosen on the basis of the expected varving in situ. In Birnensdorf, strength parameters from homogeneous samples can be used as a lower bound assumption, but a localisation of failure and a smaller value of the relevant shear resistance parameter, such as a residual shear strength, would still be possible due to the particular spatial arrangement of clay and silt layers. In Kreuzlingen, this is not likely to occur. Therefore in zones of post glacial deposition, where lakebed instability and active water conditions are likely to have occurred, an improved site characterisation has to be carried out. An improved site characterisation can allow a better spatial definition of layers, which can be used in numerical analysis with advanced constitutive models to investigate the influence of varying strength, stiffness and permeability parameters on the possible failure modes in situ. The consequences of possible failures have to be considered and weighted within a risk analysis, a suitable site monitoring programme has to be set up and emergency steps defined in advance.

An improved site and sample investigation also requires an optimal quality - cost relationship. The use of the CPTU techniques allows some of the expensive drilling and sampling to be avoided and offers the interpretation of various soil parameters. Miniature piezocones (Hird and Sills, 2003) are reported to be able to detect individual permeable layers as thin as 2 mm in normally consolidated clay deposits, provided their vertical spacing is at least two cone diameters and sufficiently fast data recording rate is used. The use of such a miniature cone in a deposit of Seebodenlehm could probably deliver a much more detailed data set about the varving in situ, especially their spacing, and improve site investigation. Seismic in situ tests, such as the transmission experiment carried out in Kreuzlingen, offer the possibility to determine the dynamic moduli of large sub-surface volumes and can provide average small-strain stiffness values of a deposits. The resolution of the seismic data was, however, insufficient to identify stratigraphy and stiffness unambiguously over ca. 20m depth. An improvement of this technique is represented by the seismocone, a piezocone which can also send body waves through the soil from different depths. The seismic waves are then received at the surface as seismographs. The analysis of the travel times of these waves can improve the resolution of the seismic data with depth. The Seebodenlehm deposits in Switzerland represent excellent soil conditions to carry out seismocone experiments. The bender element tests during mechanical labo-

ratory tests represent the counterpart to these in situ tests and offer the possibility of comparison between dynamic in situ and laboratory tests. The comparison will allow the influence of sample dimensions to be analysed, too. The bender element tests should now be automated, so that tests on different specimens can be compared at the same strain level, and the analysis has to account for the boundary conditions of a small specimen and seismic wave reflections at the sides of the specimens.

Sample disturbance was thought to have had some influence on the results of the oedometer tests. Disturbance could have occurred during the extraction and preparation process. The layering of the triaxial samples did not appear to show signs of disturbance (from visual inspection). Since the oedometer specimens are smaller, they are more affected by both the presence of silt layers and the preparation techniques. It is well known that block samples show less disturbance than those obtained from thin tube samplers, and ideally they should be used for the extraction of laboratory samples. It is very difficult to cut block samples from a cleared deposit of Seebodenlehm, due to very high negative pore pressures. The use of block samplers at depths of more than below excavation level is limited due to incompatibility with the engine used in practice to drill boreholes and to extract samples. In future, it would be useful to compare the effect of different samplers, such block samplers and larger diameter thin tube samplers. Larger thin tube samplers have probably the advantage to be easier applicable in practice. The use of larger specimens will reduce the effect of natural variability, too.

Seite Leer /
Blank leaf

References

- A. Keller AG. (1997). N7, Schwaderloh - Landesgrenze: Bahnunterführung Konstanzerstrasse: Geotechnischer Bericht. *Bericht Nr. S 9664*.
- Abbiss, C. P. (1981). Shear wave measurements of the elasticity of the ground. *Géotechnique, Vol. 31, 94-104*.
- Aki, K., and Richards, P.G. (1980). Quantitative Seismology. *Freeman & Co., San Francisco, U.S.A.*
- Al-Tabbaa, A. (1997). Permeability and stress-strain response of speswhite kaolin. *PhD Thesis University of Cambridge, UK*.
- Amann, P., and Heil, H. M. (1995). Cone Penetration Testing in Switzerland. *Proc. CPT '95, Linköping, Vol. 1, 35-242*.
- Amann, P, Bucher, F. and Heil, H. M. (1992). Untersuchung an Seebodenlehm. *Report 4391, Institute of Geotechnical Engineering*.
- Arenson, L. U. (2002). Unstable alpine permafrost: variations of geotechnical behaviour with time and temperature. (*ETH-Dissertation Nr. 14801. Zürich, 2002*) *Veröffentlichungen des Inst. für Geotechnik der ETH Zürich, Band 218, 271 p.*
- Arenson, U. L., Trausch-Giudici, J. L., Messerklinger, S., Zweidler, A., Bleiker, E. and Springman, S. M. (2004). A new computer controlled triaxial test apparatus for frozen soils and soft clays. *To be published*.
- Atkinson, J. H. and Bransby, P. L. (1978). The mechanics of soils: an introduction to Critical State Soil Mechanics. *McGraw Hill, p. 367*.
- Atkinson, J. H., Evans, J. S. and Ho, E. W. (1985). Non-uniformity of triaxial samples due to consolidation with radial drainage. *Géotechnique, Vol. 35 (3), 353-355*.
- Atkinson, J. H., Richardson, D. and Stallebrass, S. E. (1990). Effect of recent stress history on the stiffness of overconsolidated soil. *Géotechnique, Vol. 40 (4), 531-540*.

- Atkinson, J. H. and Salfors, G. (1991). Experimental determination of stress strain time characteristics in laboratory and in situ tests. *Proc. 10th Eur. Conf. Soil Mech., Florence 3*, 915-956.
- Atkinson, J. H. and Stallebrass, S. E. (1991). A model for recent history and non-linearity in the stress-strain behaviour of overconsolidated soil. *Computer Methods and Advances in Geomechanics, Beer, Booker & Carter (eds), Balkema, Rotterdam*, 555-560.
- Atkinson, J. H., Allman, M.A. and Böese, R.J. (1992). Influence of laboratory sample preparation procedures on the strength and stiffness of intact Bothkennar soil recovered using the Laval sampler. *Géotechnique, Vol. 42 (2)*, 349-354.
- Baligh, M. M. and Levadoux, J.N. (1980). Pore pressure dissipation after cone penetration. *MIT Research Report, MITSG 80-11*.
- Baligh, M. M. (1985). Strain Path Method. *Journal of Geotechnical Engineering, Vol. 111 (9)*, pp. 1108-1136.
- Baligh, M. M., Azzouz, A.S. and Chin, C.-T. (1987). Disturbances Due to "Ideal" Tube Sampling. *Journal of Geotechnical Engineering, Vol. 113 (7)*, pp. 739-757.
- Banerjee, P. K. and Yousif, N. B. (1986). A plasticity model for the mechanical behaviour of anisotropically consolidated clay. *Intern. Journ. for Num. and Anal. Meth. in Geomechanics, Vol. 10*, 521-541.
- Bartelt, P. and von Moos, M. (2000). Triaxial tests to determine a microstructure-based snow viscosity law. *Annals of Glaciology, Vol. 31*, 457-462.
- Basler, C. (2002). Seebodenlehme: CL-Oedometer. Diplomarbeit in Geotechnik, *Institut für Geotechnik, ETH Zürich*, 99p.
- Berardi, R. and Lancellotta, R. (2002). Yielding from field behaviour and its influence on oil tank settlements. *Journal of Geotechnical and Geoenvironmental Engineering, Vol. 128 (5)*, 404-415.
- Berre, T. and Iversen, K. (1972). Oedometer tests with different specimen heights on clay exhibiting large secondary compression. *Géotechnique, Vol. 22 (1)*, 53-70.
- Bishop, A. W. and Henkel, D. J. (1962). The measurement of soil properties in the triaxial test. *2nd. Edition, Edward Arnold, London*.
- Bjerrum, L. (1954). Geotechnical properties of Norwegian marine clays. *Géotechnique, Vol. 4 (1)*, 49-69.
- Bjerrum, L. (1973). Problems of soil mechanics and construction on soft clays and structurally unstable soils. *Proc. 8th. ICSMFE, Moscow, Vol 3*, 111-159.
- Blewett, J., Blewett, I. J. and Woodwark, P. K. (1999). Measurement of shear wave velocity using phase sensitive detection techniques. *Canadian Geotechnical Journal, Vol. 36*, 934-939.
- Blewett, J., Blewett, I. J. and Woodwark, P. K. (2000). Phase and amplitude responses associated with the measurement of shear-wave velocity in sand by bender elements. *Canadian Geotechnical Journal, Vol. 37*, 1348-1357.

-
- Bozzano, F., Marcoccia, S. and Barbieri, M. (1999). The role of calcium carbonate in the compressibility of pliocene lacustrine deposits. *Quarterly Journal of Engineering Geology*, Vol. 32, 271-289.
- Brignoli, E. and Gotti, M. (1992). Misure della velocità di onde elastiche di taglio in laboratorio con l'impiego di trasduttori piezoelettrici. *Riv. Ital. Geotec.*, Vol. 26 (1), 5-16.
- Brinkgreve, R. B. J. (ed.) (2002). PLAXIS Manual Version 8. A. A. Balkema.
- Brousseau, P. (1983). Etude de l'état limite et de la déstructuration d'argiles naturelles de Suède et du Québec. *Thèse de Maîtrise, Département de Génie Civil, Université Laval, Québec.*
- Büchi+Müller. (1996). N7, Schwaderloh - Landesgrenze: Bahnunterführung Konstanzerstrasse: Geologischer, hydrogeologischer und geotechnischer Bericht. *Bericht Nr.2347 B.5.*
- Burghignoli, A., Pane, V. and Cavalera, L. (1991). Modelling stress-strain-time behaviour of natural soils. Monotonic loading. *Proc. 10th Eur. Conf. Soil Mech., Florence 3*, 961-979.
- Burland, J. B. (1990). On the compressibility and shear strength of natural clays. *Géotechnique*, Vol. 40 (3), 329-378.
- Carrubba, C. and Maugeri, M. (1991). Written contribution: Threshold strain limits of two natural clays. *Proc. 10th Eur. Conf. Soil Mech., Florence 3*, 1299-1301.
- Clayton, C. R. I., Hight, D. W. and Hopper, R. J. (1992). Progressive destructuring of Bothkennar clay: implications for sampling and reconsolidation procedures. *Géotechnique*, Vol. 42 (2), 219-239.
- Cotecchia, F. and Chandler, R. J. (1997). The influence of structure on the pre-failure behaviour of a natural clay. *Géotechnique*, Vol. 47 (3), 523-544.
- Crawford, C. B. (1964). Interpretation of the consolidation test. *Journal of the Soil Mechanics and Foundations Division*, Vol. 90 (5), 87-102.
- Cummings, S. J., Sivakumar, V., Doran, I. G. and Graham, J. (2003). Deep sampling and testing in soft stratified clay. *Canadian Geotechnical Journal*, Vol. 40 (3), 575-586.
- Dafalias, Y. F. (1987). Anisotropic critical state clay plasticity model. In *Proc. 2nd Int. Conf. on Constitutive Laws for Engineering Materials, Tucson, Arizona, Elsevier*, Vol. 1, 513-521.
- Davies, M. C. R. and Newson, T. A. (1993). A critical state constitutive model for anisotropic soil. In *Predictive Soil Mechanics. Ed. G.T. Houlby and A. N. Schofield, Thomas Telford, London*, 219-229.
- Davison, L. R. and Atkinson, J. H. (1990). Continuous loading oedometer testing of soils. *Quarterly Journal of Engineering Geology*, Vol. 23, 347-355.
- DeGroot, D. J. and Lutenegro, A. J. (2003). Geology and engineering properties of Connecticut Valley Varved Clay. *Characterisation and engineering properties of natural soils. Tan et al. (eds), Swets & Zeitlinger, Lisse*, 695-724.

- Demberg, W. (1991). Über die Ermittlung des Wasseraufnahmevermögens feinkörniger Böden mit dem Gerät nach Enslin/Neff. *Geotechnik*, Vol. 14, 125-131.
- Desrues, J., Chambon, R., Mokni, M. and Mazerolle, F. (1996). Void ratio evolution inside shear bands in triaxial sand specimens studied by computed tomography. *Géotechnique*, Vol. 46 (3), 529-546.
- Diaz-Rodriguez, J. A. (2003). Characterisation and engineering properties of Mexico city lacustrine soils. *Characterisation and engineering properties of natural soils*. Tan et al. (eds), Swets & Zeitlinger, Lisse, 725-755.
- Diaz-Rodriguez, J. A., Leroueil, S. and Aleman, J. D. (1992). Yielding of Mexico City clay and other natural clays. *Journal of Geotechnical Engineering*, Vol. 118 (7), 981-995.
- Dumbleton, M. J. and West, G. (1966). The influence of the coarse fraction on the plastic properties of clay soils. *Road Research Laboratory, Report No. 36*.
- Dyvik, R. and Madshus, C. (1985). Laboratory measurements of G_{max} using bender elements. *Advances in the art of testing soils under cyclic conditions, proc. ASCE, Detroit, 186-196*.
- Dyvik, R. and Olsen, T. S. (1989). G_{max} measured in oedometer and DSS tests using bender elements. *Int. Conf. Soil Mech. and Found. Eng. Vol. 1. Rio de Janeiro. 39-42*.
- Enel.Hydro (2000). Manuale dell'operatore. Determinazione della velocità delle onde elastiche in laboratorio.
- Fearon, R. E. and Coop, M. R. (2000). Reconstitution: what makes an appropriate reference material? *Technical note, Géotechnique, Vol. 50 (4), 471-477*.
- Fleischer, P. (2000). Seebodenlehm Birmensdorf. Diplomarbeit in Geotechnik, *Institut für Geotechnik, ETH Zürich, 139p*.
- Gens, A. (1992) Stress-strain and strength characteristics of a low plasticity clay. *PhD Thesis, Imperial College of Science and Technology, University of London*.
- Gens, A. and Nova, R. (1993). Conceptual bases for a constitutive model for bonded soils and weak rocks. *Geomechanical engineering of hard soils and soft rocks, ed. Anagnostopoulos, Schlosser, Kallistos and Frank, Balkema, Rotterdam, Vol. 1, 485-494*.
- Geologischer Atlas der Schweiz 1:25000, 1992, Blatt 1091 Zürich.
- Geologische Generalkarte der Schweiz 1:200000, 1950, Blatt 3 Zürich-Glarus.
- Geotechnische Karte der Schweiz 1:1000000, 1963.
- Geotechnisches Institut, (1994). Dreieck Zürich-West: Geotechnische Berichterstattung. *Bericht Nr. 141.0440.001*.
- Geotechnisches Institut, (1994-1999). Dreieck Zürich-West: Kernbohrungen.
- Geotechnisches Institut, (1996). Versuchsschüttung mit Vertikaldrains. *Bericht Nr. 141.0440.014*

-
- Geotechnisches Institut, (1999). Dreieck Zürich-West: Konsolidationsschüttung, Vorbelastung Etappe 1. *Bericht Nr. 141.0440.040*.
- Giudici, J. and Springman, S. M. (1998a). N7, Schwaderloh-Landesgrenze. Kreuzlingen: Bahnunterführung Konstanzerstrasse. Probenuntersuchung. *Report 456, Institute of Geotechnical Engineering*.
- Giudici, J. and Springman, S. M. (1998b). N7, Schwaderloh-Landesgrenze. Kreuzlingen: Bahnunterführung Konstanzerstrasse. Drucksondierungen. *Report 456/1, Institute of Geotechnical Engineering*.
- Giudici Trausch, J., Basler, C., Weber, T. and Springman, S. M. (2003). Continuous loading oedometer testing on three Swiss lacustrine clays. *Proc. Deformation Characteristics of Geomaterials, Lyon, eds Di Benedetto, H., Doanh, T., Geoffroy, H. and Sauzéat C., 73-80*.
- Graham, J., Crooks, J. H. A. and Bell, A. L. (1983a). Time effects on the stress-strain behaviour of natural soft clay. *Géotechnique, Vol. 33 (3), 327-340*.
- Graham, J., Noonan, M. L. and Lew, K. V. (1983b). Yield states and stress-strain relationships in a natural plastic clay. *Canadian Geotechnical Journal, Vol. 20 (3), 502-516*.
- Gyger, M., Müller-von Moos, M. and Schindler, K. (1976). Untersuchungen zur Klassifikation spät- und nacheiszeitlicher Sedimente aus dem Zürichsee. *Schweizerische mineralogische und petrographische Mitteilungen, Heft 56, 387-406*.
- Hardin, B. O. (1978). The nature of stress-strain behaviour of soils. *Proc. of the ASCE Geot. Eng. Div. Specialty Conference, Earthquake engineering and soil dynamics., Vol. 1, 3-90*.
- Hardin, B.O. and Black, W.L. (1968). Vibration modulus of normally consolidated clay. *Journal of the Soil Mechanics and Foundations Division, Vol. 94 (SM2), 353-369*.
- Hardin, B.O. and Black, W.L. (1969). Closure to vibration modulus of normally consolidated clay. *Journal of the Soil Mechanics and Foundations Division, Vol. 95 (SM6), 1531-1537*.
- Head, K. H. (1994). Manual of soil laboratory testing, Vol. 2. *2nd. Edition, J. Wiley & Sons*.
- Head, K. H. (1985). Manual of soil laboratory testing, Vol. 3. *1st. Edition, J. Wiley & Sons*.
- Heil, H. M. (2001). Localisation and critical states. *Proc. Constitutive and Centrifuge modelling: two extremes. Ed. Springman, p. 379, S.M. Ascona, Switzerland, Balkema*.
- Heil, H. M., Huder, J. and Amann, P. (1997). Determination of shear strength of soft lacustrine clays. *Proc. 14th IC SMFE, Hamburg, Balkema Rotterdam, Vol. 1, 507-510*.
- Hight, D. W., Jardine, R. J. and Gens, A. (1987). The behaviour of soft clays. In *Embankments on Soft Clays, Special Publication Bulletin of the Public Works Research Centre, Ministry of the Environment, Physical Planning and Public Works, Athens, Greece*.

- Hight, D. W., Böese, R., Butcher, A.P., Clayton, C.R.I. and Smith, P.R. (1992). Disturbance of the Bothkennar clay prior to laboratory testing. *Géotechnique*, Vol. 42 (2), 199-217.
- Hird C. C., Johnson P., Sills G.C. (2003). Performance of miniature piezocones in thinly layered soils. *Géotechnique*, Vol. 53 (10), 885-900.
- Houlsby, G. T. and Wroth, C.P. (1991). The variation of shear modulus of a clay with pressure and overconsolidation ratio. *Soils and Foundations*, Vol. 31 (3), 138-143.
- Houlsby, G. T. and Sharma, R. S. (1999). A conceptual model for the yielding and consolidation of clays. *Géotechnique*, Vol. 49 (4), 491-501.
- Huder, J. and Groebli, M. (1959). Die Entnahme von ungestörten Bodenproben. *Mitteilungen der Versuchsanstalt für Wasserbau und Erdbau*, Nr. 46.
- Jâky, J. (1944). The coefficient of earth pressure at rest. *Journal of the Union of Hungarian Engineers and Architects*, 355-8.
- Janbu, N., Tokheim, O. and Senneset, K. (1981). Consolidation tests with continuous loading. *Proc. X ICSMFE, Stockholm*, Vol.1, 645-654.
- Janbu, N. (1985). Soil models in offshore engineering. *Géotechnique*, Vol. 35 (3), 241-282.
- Jamiolkowski, M. (2003). Soil properties evaluation from static cone penetration test. *Invited Lecture at the Institute of Geotechnical Engineering, ETH Zürich, November 2003*.
- Jardine, R. J., Potts, D. M., Fourie, A.B. and Burland, J. B. (1986). Studies of the influence of non-linear stress-strain characteristics in soil-structure interaction. *Géotechnique*, Vol. 36 (3), 377-396.
- Jovicic, V., Coop, M. R. and Simic, M. (1996). Objective criteria for determining G_{max} from bender elements tests. *Géotechnique*, 46(2), 357-362.
- Kabbaj, M., Tavenas, F. and Leroueil, S. (1988). In situ and laboratory stress-strain relationships. *Géotechnique*, Vol. 38 (1), 83-100.
- Kagawa, T. (1992). Moduli and damping factors of soft marine clays. *Journal of Geotechnical Engineering*, Vol. 118 (9), 1360-1375.
- Karlsrud, K. (1995). Provedforstyrrelse - siltig leire. *Proc. Norwegian Geotec. Soc.*, October 27.
- Kenney, T. C. and Folkes, D. J. (1979). Mechanical properties of soft soils. *State-of-the-Art Report to Session 2, Proc. 32nd Canadian Geotechnical Conference, Quebec City*, 51 p.
- Kenney, T. C. (1976). Formation and geotechnical characteristics of glacial-lakes varved soils. In *Laurits Bjerrum Memorial Volume - Contribution to soil mechanics*. Janbu, N., Jorstad F. and Kjaernsli, B. (eds), *Norwegian Geotechnical Institute Publication*, 15-39.
- Kenney, T. C. (1967). The influence of mineral composition on the residual strength of natural soils. *On shear strength properties of natural soils and rocks. Proc. Geotech. Conf. Oslo*. Oslo, NGI, 123-129.

-
- Kondner, R. L. (1963). Hyperbolic stress-strain response: cohesive soils. *Journal of the Soil Mechanics and Foundation Division, Vol. 89 (SM1)*, 115-143.
- Koskinen, M., Karstunen, M. and Wheeler, S. J. (2002a). Modelling destructuration and anisotropy of a natural soft clay. *Proc. 5. NUMGE, Paris*, 11-20.
- Koskinen, M., Zentar, R. and Karstunen, M. (2002b). Anisotropy and destructuration of natural POKO Clay. *Proc. VIII NUMOG, Rome*, 99-105.
- Kulhawy, F. H. (1993). Some thoughts on the evaluation of undrained shear strength for design. *Predictive Soil Mechanics, Thomas Telford, London*, 394-403.
- Küng, H. (2003). Undrainierte Scherfestigkeit an aufbereitetem Seebodenlehm. Diplomarbeit in Geotechnik. *Institut für Geotechnik, ETH Zürich*, 139p.
- Labhart, T. P. (1987). Geologie der Schweiz. *Hallwag Verlag*.
- Lacasse, S. (1995). Stress-strain behaviour: importance of mode and rate of load application for engineering problems. *Pre-failure deformation of geomaterials, Shibuya, Mitachi & Miura (eds), Balkema, Vol. 2*, 887-907.
- Lacasse, S. (1998). Contributions of research to improved safety: a geotechnical perspective from Norway. *Beitrag zum Festkolloquium Prof. H.-J. Lang: Stand und Entwicklung in der Geotechnik, 18. Oktober 1996, Band 211, 2/98, Zürich*, 35-39.
- Lacasse, S. and Lunne, T. (1982). Penetration tests in 2 Norwegian clays. *Proc. 2nd European Symposium on Penetration Testing, Amsterdam, Vol. 2*, 661-669.
- Lacasse, S., Hermann, S., Jensen, T. G. and Kvelde, V. (2002). Improved engineering solutions because of improved site characterization. *Proc. of the C.C. Ladd Symposium: Soil Behavior and Soft Ground Construction, October 5-6, 2001, Cambridge, Massachusetts, Germaine J. T., Sheahan T. C. and Whitman R. V. (eds)*, 239-254.
- Lämsivaara, T. (1999). A study of the mechanical behaviour of soft clay. *Thesis NTNU Trondheim, No 85*.
- Lämsivaara, T. (1995 a). A critical state model for anisotropic soils. *Proc. XI ECS-MFE, Copenhagen, Vol. 6*, 101-106.
- Lämsivaara, T. (1995 b). Stress- strain- strain rate relation in oedometer tests. *Proc. 70 Years of Soil Mechanics, International Symposium, Istanbul*, 109-118.
- Lang, H. J., Huder, J. and Amann, P. (2003). Bodenmechanik und Grundbau. 7. Auflage. *Springer Verlag*.
- Larsson, R. (1981). Drained behaviour of Swedish clays. *Swedish Geotechnical Institute, Linköping, Report No. 12*.
- Larsson, R. and Mulabdic, M. (1991). Shear moduli in Scandinavian clays. *Swedish Geotechnical Institute, Linköping, Report No. 40*.
- Leroueil, S. (1996). Compressibility of clays: fundamental and practical aspects. *Journal of Geotechnical Engineering, Vol. 122 (7)*, 534-543.

- Leroueil, S., Tavenas F., Bruzy F., et al. (1979). Behaviour of de-structured natural clays. *J. Geotech. Eng. -ASCE*, Vol. 105 (6), 759-778.
- Leroueil, S., Tavenas, F., Samson, L. and Morin, P. (1983). Preconsolidation pressure of Champlain clays. Part II. Laboratory determination. *Canadian Geotechnical Journal*, Vol. 20 (4), 803-816.
- Leroueil, S., Kabbaj, M., Tavenas, F. and Bouchard R. (1985). Stress-strain-strain rate relation for the compressibility of sensitive natural clays. *Géotechnique*, Vol. 35 (2), 159-180.
- Leroueil, S. and Tavenas, F. (1986). Discussion on: Effective stress path and yielding of soft clays below embankments. *Canadian Geotechnical Journal*, Vol. 23 (3), 410-413.
- Leroueil, S., Magnan, J-P. and Tavenas, F. (1990). Embankments on Soft Clays. *Ellis Horwood series in civil engineering*, ISBN 0-13-275736-2.
- Leroueil, S. and Vaughan, P. R. (1990). The general and congruent effects of structure in natural soils and weak rocks. *Géotechnique*, Vol. 40 (3), 467-488.
- Long, M. (2003). Characterisation and engineering properties of Athlone laminated clay. *Characterisation and engineering properties of natural soils*. Tan et al. (eds), Swets & Zeitlinger, Lisse, 757-790.
- Lo Presti, D. (1991). Behaviour of sand at small strain. *Proc. 10th Eur. Conf. Soil Mech., Florence 3*, 1229-1230.
- Lowe, J. III, Jonas, E. and Obrician, V. (1969). Controlled gradient consolidation test. *J. Soil Mechanics and Foundation Divisions*, No. 95, 77-97.
- Lunne, T., Berre, T. and Strandvik, S. (1997). Sample disturbance effects in soft low plasticity Norwegian clay. *Proc. Int. Symp. on Recent Development in Soil and Pavement Mechanics, Rio de Janeiro*, 81-92, Balkema.
- Lewin, P. I. (1973). The influence of stress history on the plastic potential. *Proc. Symp. on the Role of Plasticity in Soil Mechanics*, ed. A. C. Palmer, 96-105.
- Mancuso, C. and Vinale, F. (1988). Propagazione delle onde sismiche: teoria e misure in sito. *Atti del Convegno del Gruppo Nazionale di Coordinamento per gli Studi di Ingegneria Geotecnica, Monselice*, 115-138.
- Maurer, H., Giudici, J. and Springman, S. M. (1998). N7, Schwaderloh-Landesgrenze. Kreuzlingen: Bahnunterführung Konstanzerstrasser. Seismische Versuche. Report 456/2, *Institute of Geotechnical Engineering*.
- Maurer, H., Giudici Trausch, J., Roth, M., Hollinger, K., Springman, S. M. and van der Veen, M. (2000). Bestimmung elastischer Bodeneigenschaften bei kleinen Verformungen. *Felsbau, Rock and Soil Engineering*, Nr. 5, 129-133.
- Mavko, G., Mukerji, T. and Dvorkin, J. (1998). The rock physics handbook: tools for seismic analysis in porous media. *Cambridge University Press*, ISBN 0-521-62068-6.
- Mayne, P. W. (2003). Integrated ground behaviour: in-situ and lab tests. *Keynote Deformation characteristics of geomaterials, Lyon 2003, to be published*.
- Meier, L. P. and Kahr, G. (1999). Determination of the cation exchange capacity (CEC) of clay minerals using the complexes of copper (II) ion with triethylene-

-
- tetramine and tetraethylenepentamine. *Clays and Clay Minerals*, Vol. 47, 386-388.
- Mesri, G., Rokhsar, A. and Bohor, B.F. (1975). Composition and compressibility of typical samples of Mexico City clay. *Géotechnique*, Vol. 25 (3), 527-554.
- Mesri, G. and Godlewski, P. M. (1977). Time- and stress-compressibility relationship. *Journal of Geotechnical Engineering Division*, Vol. 103 (GT5), 417-430.
- Mesri, G. and Castro, A. (1987). C_{α}/C_c concept and K_0 during secondary compression. *Journal of Geotechnical Engineering*, Vol. 113 (3), 230-247.
- Messerklinger, S. (2003). Personal communication.
- Messerklinger, S., Kahr, G., Plötze, M., Giudici Trausch, J., Springman S.M., and Lojander, M. (2003). Mineralogical and mechanical behaviour of soft Finnish and Swiss clays. *Int. Workshop on Geotechnics of Soft Soils - Theory and Practice*. Vermeer, Schweiger, Karstunen & Cudny (eds.).
- Mohsin, A. K. M. and Airey, D. W. (2003). Automating G_{max} measurement in triaxial tests. *Proc. Deformation Characteristics of Geomaterials, Lyon*, eds. Di Benedetto, H., Doanh, T., Geoffroy, H. and Sauzéat C., 73-80.
- Mröz, Z., Norris, V. A. and Zienkiewicz, O. C. (1979). Application of an anisotropic hardening model in the analysis of elasto-plastic deformations of soils. *Géotechnique*, Vol. 29, 1-34.
- Muir Wood, D. (1990). Soil Behaviour and Critical State Soil Mechanics. *Cambridge University Press*.
- Müller-Vonmoos, M. et al. (1988). Tonmineralogie und Bodenmechanik: Tagung am 15. Mai 1997 and der ETH Zürich. *Mitteilungen des Instituts für Grundbau und Bodenmechanik, ETH Zürich*, Nr. 133.
- Müller-Vonmoos, M. and Loken, T. (1989). Das Scherverhalten der Tone. *Tagung: Tonmineralogie und Bodenmechanik, Mitteilungsheft Nr. 133, Institute for Geotechnical Engineering, Swiss Federal Institute of Technology, Zurich*, 23-39.
- Näätänen, A., Lojander, M., Wheeler, S. and Karstunen, M. (1999). Experimental investigation of an anisotropic hardening model for soft clays. *In Jamiolkowski, Lancellotta & Lo Presti (eds), Proc. 2nd. Int. Symp. On Pre-failure Deformation Characteristics of Geomaterials, Torino, 28-30 September 1999. Rotterdam: Balkema*.
- Näätänen, A. and Lojander, M. (2000). Modelling of anisotropy of Finnish clays. *Proc. 7th Finnish Symposium on Mechanics, Tampere, Finland, 25-26 May 2000*.
- Newson, T. A. (1995). Constitutive modelling of anisotropically consolidated clay. *Ph. D. Thesis, University of Wales*.
- Panduri, R. (2000). Seebodenlehm Birmensdorf: CPTU und triaxiale Scherversuche. Diplomarbeit in Geotechnik. *Institut für Geotechnik, ETH Zürich*, 142p.
- Parry, R. H. G. & Wroth, C. P. (1981). "Shear properties of soft clays." *Soft clay engineering, Elsevier, Amsterdam*, 311-364.

- Pestana, J. M. and Whittle, A. J. (1999). Formulation of an unified constitutive model for clays and sands. *International Journal for Numerical and Analytical Methods in Geomechanics*, Vol. 23, 1215-1243.
- Plötze, M. (2001). Personal communication.
- Plötze, M. (2003). Personal communication.
- Plötze, M., Giudici Trausch, J., Messerklinger, S. and Springman, S.M. (2003). Swiss Lacustrine Clay: mineralogical and mechanical characteristics. *Int. Workshop on Geotechnics of Soft Soils - Theory and Practice*. Vermeer, Schweiger, Karstunen & Cudny (eds.).
- Quigley, R. M. (1980). Geology, mineralogy and geochemistry of Canadian soft soils: a geotechnical perspective. *Canadian Geotechnical Journal*, Vol. 17, 261-285.
- Rey, R. (1994). Geotechnische Folgen der glazialen Vorbelastung von Seebodenablagerungen. *ETH-Dissertation Nr. 10631, Zürich*.
- Richardson, D. (1988). Investigations of threshold effects in soil deformations. *Ph. D. Thesis. The City University*.
- Robertson, P. K. (1990). Soil classification using the cone penetration test. *Canadian Geotechnical Journal*, Vol. 27, 151-158.
- Rösler, H. J. (1984). Lehrbuch der Mineralogie. *Verlag Grundstoffindustrie, Leipzig*.
- Salgado R., Mitchell J.K. and Jamiolkowski, M. (1998). Cavity expansion and penetration resistance in sand. *Journal of Geotechnical and Geoenvironmental Engineering*, 123 (4), 344-354.
- Salinero, I. S., Roesset, J. M. and Stokoe, K. H. (1986). Analytical studies of body wave propagation and attenuation. *Report GR 86-15. University of Texas at Austin*.
- Sällfors, G. (1975). Preconsolidation pressure of soft, high plastic clays. *Thesis Chalmers University of Technology, Geotechnical Department*.
- Seierstad, H-H. (2000). Provedorstyrreleise i leire vurdering av 75 stempelprovetaker. *Diploma Thesis, NTNU Trondheim, Autumn 2000*.
- Scherzinger, T. (1991). Materialverhalten von Seetonen - Ergebnisse von Laboruntersuchungen und ihre Bedeutung für das Bauen im weichen Baugrund. *Veröffentlichungen des Inst. für Boden- und Felsmechanik, Karlsruhe, Heft 122, p. 174*.
- Schofield, A. N. and Wroth, C. P. (1968). *Critical State Soil Mechanics. McGraw Hill, 306p*.
- Scholey, G. K., Frost, J. D., Lo Presti, D. C. F. and Jamiolkowski, M. (1995). A review of instrumentation for measuring small strains during triaxial testing of soil specimen. *Geotechnical Testing Journal*, Vol. 18 (2), 137-156.
- Sharma, J. (1994). The behaviour of reinforced embankments on soft clay. *PhD Thesis, Cambridge University*.

-
- Sheahan, T. C. and Watters, P. J. (1997). Experimental verification of CRS consolidation theory. *Journal of Geotechnical and Geoenvironmental Engineering*, 123 (5), 430-437.
- Skempton, A. W. (1953). The colloidal activity of clay. *Proc. of the 3d. ICSMFE, Switzerland, Vol.1, 57-61.*
- Simpson, B. (1979). A computer model for the analysis of ground movements in London clay. *Géotechnique, Vol. 29 (2), 149-175.*
- Simpson, B., O'Riordan, N.J. and Croft, D.D. (1992). 32nd Rankine Lecture. Retaining structure - displacement and design. *Géotechnique, Vol. 42 (4), 539-576.*
- Smith, N. D. (1978). Sedimentation processes and patterns in a glacier-fed lake with low sediment input. *Canadian Journal of Earth Sciences, Vol. 15, 741-756.*
- Smith, R. E. and Wahls, H. E. (1970). Consolidation under constant rates of strain. *Technical Paper No. 458. Engineering Progress of the University of Florida, 24(3), 519-539.*
- Soccodato, F. M., (2003). Geotechnical properties of Fucino clayey soil. *Characterisation and engineering properties of natural soils. Tan et al. (eds), Swets & Zeitlinger, Lisse, 791-807.*
- Springman, S. M., Giudici Trausch, J., Heil, H. M. and Heim, R. (1999). Strength of a soft swiss lacustrine clay: cone penetration and triaxial test data. *Journal of the Transportation Research Board 1675, 1-9.*
- Springman, S. M. (1993). Centrifuge modelling in clay: Marine applications. *Invited keynote lecture, 4th Canadian Conf. of Marine Geotechnics, Newfoundland, (ed J.L. Clarke et al.) Vol. 3, 853-896.*
- Sridharan, A. and Nagaraj, H. B. (2000). Compressibility behaviour of remoulded, fine-grained soils and correlation with index properties. *Canadian Geotechnical Journal, Vol. 37, 712-722.*
- Stallebrass, S. E. (1990). The effect of recent stress history on the deformation of overconsolidated soils. *PhD thesis, City University.*
- Stallebrass, S. E. and Taylor, R. N. (1997). The development and evaluation of a constitutive model for the prediction of ground movements in overconsolidated clay. *Géotechnique, Vol. 47 (2), 235-253.*
- Steiner, W. and Togliani, G. (1998). Experience from site investigations in glacial soils of the Alpine region. *1st IC on Site Characterisation, ISC'98, Atlanta, 1171-1176.*
- Steiner, W., Metzger, R, and Marr, W. (1992). An embankment on soft clay with an adjacent cut. *Proc. Stability and Performance of Slopes and Embankments II, GT Div/ASCE, Berkeley California, pp. 705-720.*
- Stokoe II, K. H., Hwang, S. K., Lee, J. N.-K. and Andrus, R. D. (1995). Effects of various parameters on the stiffness and damping of soils at small to medium strains. *Pre-failure deformation of geomaterials, Shibuya, Mitachi & Miura (eds), Balkema, Vol. 2, 785-816.*

- Tatsuoka, F. and Kohata, Y. (1995). Stiffness of hard soils and soft rocks in engineering applications. *Pre-failure Deformation of Geomaterials, Shibuya, Mitachi & Miura (eds), Balkema, Vol. 2, 947-1063.*
- Tavenas, F. and Leroueil, S. (1980). The behaviour of embankments on clay foundations. *Canadian Geotechnical J., Vol. 17 (2), 236-260.*
- Tiefbauamt des Kantons Zürich, (1996). N4/N20 INFO: Westumfahrung Zürich.
- Tey, C. I. and Houlsby, G. T. (1991). An analytical study of the cone penetration test in clay. *Géotechnique, 41 (1), 14-34.*
- Theron, M., Clayton, C. R. I. and Best, A. I. (2003). Interpretation of side-mounted bender element results using phase shift and group velocity. *Proc. Deformation Characteristics of Geomaterials, Lyon, eds. Di Benedetto, H., Doanh, T., Geoffroy, H. and Sauzéat C., 127-132.*
- Torstensson, B.-A. (1977). The pore pressure probe. *Archiwum Hydrotechniki, Vol. XXVI, Nr. 2, Warschau, 325-335.*
- Viggiani, G. and Atkinson, J. H. (1995). Interpretation of bender element tests. *Géotechnique, Vol. 45 (1), 149-154.*
- von Moos, M. (2002). Untersuchungen über das visko-elastische Verhalten von Schnee auf der Grundlage von triaxialen Kriechversuchen. (*ETH Dissertation Nr. 13725, Zürich, 2000*), *Veröffentlichungen des Inst. für Geotechnik der ETH Zürich, Band 214, vdf, 141p.*
- von Moos, M., Bartelt, P. Zweidler, A. and Bleiker, E. (2003). Triaxial tests on snow at low strain rate. Part I: experimental device. *J. Glaciol, 49(164), 81-90.*
- Wheeler, S. J. (1997). A rotational elasto-plastic model for clays. *In Proc. 14th ICSMFE, Hamburg, A.A. Balkema, Rotterdam, Vol 1, 431-434.*
- Wheeler, S. J., Karstunen, M., and Näätänen, A. (1999). Anisotropic hardening model for normally consolidated soft clays. *In (ed.), VII NUMOG, Graz: 33-40. A.A. Balkema, Rotterdam.*
- Wheeler, S.J., Cudny, M., Neher, H. P. and Wiltafsky, C. (2003a). Some developments in constitutive modelling of soft clays. *Int. Workshop on Geotechnics of Soft Soils - Theory and Practice. Vermeer, Schweiger, Karstunen & Cudny (eds.).*
- Wheeler, S.J., Näätänen, A., Karstunen, M. and Lojander, M. (2003b). An anisotropic elasto-plastic model for natural soft clays. *Canadian Geotechnical Testing Journal, Vol. 40 (3), 575-586.*
- Whittle, A. J. and Kavvas, M. J. (1994). Formulation of the MIT_E3 constitutive model for overconsolidated clays. *Journal of Geotechnical Engineering, 120 1), 199-224.*
- Wiltafsky, C. (2003). A Multilaminate Model for Normally Consolidated Clay. *Dissertation, Institute for Soil Mechanics and Foundation Engineering, Graz University of Technology.*
- Wong, P.K.K. and Mitchell, R.J. (1975). Yielding and plastic flow of sensitive cemented clays. *Géotechnique, Vol. 25 (4), 763-782.*

-
- Wroth, C. P. (1979). Correlation of Some Engineering Properties of Soils. *Proc. 2nd Intern. Conf. on Behaviour of Offshore Structures, London*, 121-132.
- Wroth, C. P. (1984). Interpretation of in situ soil tests. *Géotechnique, Vol. 34 (4)*, 449-489.
- Yu, H. S. and Mitchell, J. K. (1998). Analysis of cone resistance: review of methods. *Journal of Geotechnical and Geoenvironmental Engineering, Vol. 124 (2)*, 140-149.
- Zentar, R., Karstunen, M. and Wheeler, S. J. (2002). Influence of anisotropy and destructuration on undrained shearing of natural clays. *Proc. 5. NUMGE, Paris*, 21-26.

Seite Leer /
Blank leaf

Curriculum Vitae

Persönliche Daten

Name, Vorname: TRAUSCH-GIUDICI, Jolanda
 Anschrift: Limmattalstrasse 289
 8049 Zürich
 Geburtsdaten: 11. März 1973, Arzo (Ti)
 Staatsangehörigkeit: CH
 Zivilstand: verheiratet

Schulbildung

September 79 - Juni 84 Scuola elementare, Novazzano (Ti)
 September 84 - Juni 88 Scuola media, Chiasso (Ti)
 September 88 - Juni 92 Liceo Cantonale tipo D (neusprachlig), Mendrisio (Ti)
 Juni 92 Maturità Cantonale

Studium

Oktober 1992 – März 1997 Bauingenieurstudium an der ETH Zürich
 September 1993 Erstes Vordiplom
 September 1994 Zweites Vordiplom
 September 1996 Schlussdiplomprüfung
 Oktober 1996 - März 1997 Diplomarbeit und Abschluss des Studiums als diplomierte Bauingenieurin ETH
 Titel der Diplomarbeit:
 Grundbauliche Sanierung der Dreifaltigkeit-skirche in Konstanz

Praktikum und berufliche Tätigkeit während dem Studium

Februar - April 1995 Praktikum beim Consortium Cleuson-Dixence, Tunnelbaustelle
 September 1995 Praktikum Ingenieurbüro "Giani & Prada SA", Lugano

Berufliche Tätigkeit

April 1997 - März 1998 Assistenz am Institut für Geotechnik, ETH Zürich
 Seit April 1998 Doktorat am Institut für Geotechnik, ETH Zürich

Weiterbildungskurse

März 2001 - September 2002 Weiterbildungskurs "Risiko und Sicherheit", ETH Zürich
 23. September 2002 Abschluss als Sicherheitsingenieur gem. EKAS-Richtlinie
 Titel der Diplomarbeit:
 Die Sondermülldeponie in Bonfol: Arbeitssicherheit in kontaminierten Bereichen.